


2016

Synthesis and Characterization of Stable and Metastable Phases in Ni- and Fe-Based Alloy Systems by Mechanical Alloying

Ahmed Al-Joubori
University of Central Florida

 Part of the [Materials Science and Engineering Commons](#)
Find similar works at: <https://stars.library.ucf.edu/etd>
University of Central Florida Libraries <http://library.ucf.edu>

This Doctoral Dissertation (Open Access) is brought to you for free and open access by STARS. It has been accepted for inclusion in Electronic Theses and Dissertations, 2004-2019 by an authorized administrator of STARS. For more information, please contact STARS@ucf.edu.

STARS Citation

Al-Joubori, Ahmed, "Synthesis and Characterization of Stable and Metastable Phases in Ni- and Fe-Based Alloy Systems by Mechanical Alloying" (2016). *Electronic Theses and Dissertations, 2004-2019*. 5092.
<https://stars.library.ucf.edu/etd/5092>

SYNTHESIS AND CHARACTERIZATION OF STABLE AND METASTABLE PHASES IN Ni- AND Fe-BASED ALLOY SYSTEMS BY MECHANICAL ALLOYING

by

AHMED ABED QASSIM AL-JOUBORI

B.S., Technical University of Baghdad, Iraq, 2004

M.S., Technical University of Baghdad, Iraq, 2008

M.S., University of Central Florida, Orlando, U.S.A., 2015

A dissertation submitted in partial fulfillment of the requirements
for the degree of Doctor of Philosophy
in the Department of Materials Science and Engineering
in the College of Engineering and Computer Science
at the University of Central Florida
Orlando, Florida

Summer Term
2016

Major Professor: C. Suryanarayana

© 2016 AHMED ABED QASSIM AL-JOUBORI

ABSTRACT

Mechanical Alloying (MA) is a process that involves repeated cold welding, fracturing and rewelding of powder particles in a high-energy ball mill and has been used extensively to synthesize both stable (equilibrium) and metastable phases in a number of alloy systems. This is due to its ability to achieve many effects simultaneously, viz., reduction in grain size, introduction of a variety of crystal defects, disordering of the lattice, and modifying the crystal structures of materials; all these allowing alloying and phase transformations to occur in powders. In this Dissertation, we have synthesized a number of different alloy phases in Ni- and Fe-based alloy systems using MA.

The as-received, blended, and milled powders were characterized by X-ray diffraction (XRD), scanning electron microscopy (SEM), and transmission electron microscopy techniques to obtain information about the overall microstructure and chemical compositions. The NiX_2 ($\text{X} = \text{Ge}$ and Si) phases were synthesized in the Ni-Ge and Ni-Si systems. MA of Ni-Ge powder blends was investigated to study phase evolution as a function of milling time. On milling the powders for 5 h, the equilibrium NiGe phase started to form, and its amount in the powder increased with increasing milling time. On milling for about 60 h, the equilibrium intermetallic NiGe and Ge powder particles reacted to form the metastable NiGe_2 phase. However, on milling for a longer time (75 h), the metastable phase transformed back to the equilibrium NiGe phase.

Synthesis of the NiSi_2 intermetallic phase depended on the Si content in the initial powder blend. For example, while in the Ni-60 at.% Si powder blend, only the NiSi phase was present homogeneously, the powder blend of the Ni-67 at.% Si composition contained the NiSi phase along with a small amount of unreacted Si. But in the Ni-75 at.% Si and Ni-80 at% compositions,

the NiSi phase that had formed earlier (after 2 h of milling) and the remaining free Si powder reacted to form the equilibrium intermetallic NiSi₂ phase. This constitution in the milled powder has been attributed to a partial loss of Si content during MA. Formation of Ni(Si) solid solutions with a solubility of about 18.2 at.% and 20.6 at.% for the Ni-75 at.% Si and Ni-80 at.% Si powder blends, respectively, was also achieved in the early stages of MA.

In the Fe-C system, we were able to synthesize ferrite, cementite, and mixtures of the two phases. We were able to obtain the Fe-C solid solution phase (ferrite) with a BCC structure and the cementite phase with an orthorhombic structure in the eutectoid Fe-0.8 wt. % C composition, while a homogeneous cementite phase had formed at the higher carbon content of Fe-7.0 wt. % C after 30 h of milling time.

In the case of the Fe-18Cr-xNi (x = 8, 12, and 20) system, the current investigation showed that the phase constitution depended significantly on the Ni content in the powder blend. Whereas mostly the martensite or the ferrite and austenite phase mixture was present at lower Ni contents, a completely homogeneous austenite phase was present in the alloy with 20% Ni.

This Dissertation is dedicated to

My father, Abed

My mother, Souad

and

My wife, Mays

ACKNOWLEDGMENTS

Firstly, I would like to express my sincere gratitude to my advisor Prof. Dr. C. Suryanarayana for the continuous support of my Ph.D. study and related research, for his patience, motivation, and immense knowledge. His guidance helped me during the whole time of research and writing of this dissertation. I could not have imagined having a better advisor and mentor for my Ph.D. study.

Besides my advisor, I would like to thank the rest of my dissertation committee: Prof. Dr. Raj Vaidyanathan, Prof. Dr. Yuanli Bai, Prof. Dr. Jan Gou, and Prof. Dr. Kuo-Chi Lin for their insightful comments and encouragement, and for their valuable input in shaping up of my dissertation.

My sincere thanks also go to Dr. Yong-ho Sohn and Dr. Kevin Coffey, who provided me an opportunity to join their team as an intern, and who also gave access to the laboratory and research facilities. Without their precious support it would not be possible to conduct this research.

I am grateful to The Higher Committee for Education Development (HCED) in Iraq, Prime Minister's Office, Government of Iraq, for providing a scholarship to pursue my Ph.D. study in the United States of America.

Last but not the least, I would like to thank my family: my parents and my wife and to my brothers and sister for supporting me spiritually throughout writing this dissertation and my life in general.

TABLE OF CONTENTS

LIST OF FIGURES	x
LIST OF TABLES	xx
CHAPTER 1: INTRODUCTION	1
1.1 Mechanical Alloying.....	1
1.2 Mechanism of Alloying	3
1.3 Diffusion during Mechanical Alloying	9
1.4 Mechanical Alloying Parameters	11
1.4.1 Ball-to-Powder Weight Ratio	11
1.4.2 Process Control Agent	12
1.4.3 Milling Atmosphere	12
1.4.4 Milling Medium	13
1.4.5 Milling Temperature	13
1.5 Objectives	14
1.6 Dissertation Outline	15
CHAPTER 2: EXPERIMENTAL PROCEDURE.....	16
2.1 Starting Materials.....	16
2.2 Processing	17
2.3 Characterization Techniques.....	19
2.3.1 X-Ray Diffraction (XRD).....	19
2.3.1.1 Phase Proportions in Multi-Phase Mixtures	19
2.3.1.2 Lattice Parameter Calculations	21
2.3.1.3 Crystallite Size and Lattice Strain Measurements	22
2.3.2 Scanning Electron Microscopy (SEM)	24
2.3.3 Focused Ion Beam (FIB).....	24
2.3.4 Transmission Electron Microscopy (TEM)	26
2.4 Consolidation of Alloyed Powder.....	26
2.4.1 Spark Plasma Sintering (SPS).....	27
2.5 Heat Treatment.....	27
2.6 Mechanical Characterization	28
CHAPTER 3: SYNTHESIS OF METASTABLE NiGe ₂ BY MECHANICAL ALLOYING AND ITS REVERSION TO NiGe	30
3.1 Introduction.....	30
3.2 Results.....	34
3.2.1 X-Ray Diffraction (XRD).....	34

3.2.2	Scanning Electron Microscopy (SEM)	44
3.2.3	Energy Dispersive Spectroscopy (EDS).....	47
3.3	Discussion	49
3.3.1	Phase Formation.....	49
3.3.2	Solid Solution Formation.....	50
3.3.3	Formation of Intermetallics.....	51
3.3.4	Reversible Transformation.....	55
3.3.5	Microstructural Changes	58
3.4	Conclusions.....	61
CHAPTER 4: SYNTHESIS OF NICKEL-SILICIDE PHASES BY MECHANICAL ALLOYING.....		62
4.1	Introduction.....	62
4.2	Results.....	66
4.2.1	X-Ray Diffraction (XRD)	66
4.2.2	Scanning Electron Microscopy (SEM)	81
4.3	Discussion	85
4.3.1	Supersaturated Ni(Si) Solid Solutions	85
4.3.2	Crystallite Size and Lattice Strain.....	87
4.3.3	Formation of Stable NiSi and NiSi ₂ Intermetallic Phases	88
4.4	Conclusions.....	95
CHAPTER 5: SYNTHESIS OF Fe-C ALLOYS BY MECHANICAL ALLOYING		96
5.1	Introduction.....	96
5.2	Results.....	101
5.2.1	X-Ray Diffraction Investigations.....	101
5.2.2	Microstructural Investigation.....	114
5.2.3	Microhardness Investigation.....	126
5.3	Discussion	128
5.4	Conclusions.....	129
CHAPTER 6: SYNTHESIS OF AUSTENITIC STAINLESS STEEL ALLOY POWDERS THROUGH MECHANICAL ALLOYING.....		131
6.1	Introduction.....	131
6.2	Results.....	134
6.2.1	Evolution of X-Ray Diffraction Patterns	134
6.2.2	Lattice Parameter Calculations	142
6.2.3	Evolution of Microstructure.....	143
6.3	Discussion	149
6.4	Conclusions.....	152

CHAPTER 7: CONCLUSIONS	153
APPENDIX: <i>LIST OF PUBLICATIONS BY AHMED AL-JOUBORI</i>	155
REFERENCES	158

LIST OF FIGURES

Figure 1.1: Schematic representations of the four different types of milling machines [12].	5
Figure 1.2: Deformation characteristics of representative constituents of starting powders used in mechanical alloying. The ductile metal powders are flattened, while the brittle intermetallic and oxide particles are fragmented into smaller particles [5].	6
Figure 1.3: Ball-powder-ball collision of powder mixture during mechanical alloying [5].	7
Figure 1.4: Mechanism of MA.	10
Figure 2.1: Steps of sample preparation for TEM using FIB.	25
Figure 2.2: Schematic diagram of the SPS machine.	29
Figure 3.1: The Ni–Ge equilibrium phase diagram [37].	31
Figure 3.2: XRD patterns of the Ni-67 at.% Ge powder blend milled for different times. While the Ni and Ge peaks are clearly seen in the unmilled powder (0 h), formation of a solid solution started to occur on milling for 1 h. Simultaneously, the equilibrium NiGe intermetallic also started to form, and its amount increased with milling time. On milling the powder for 10 h, a new phase, identified as the metastable NiGe ₂ phase, started to form. An almost homogeneous NiGe ₂ phase had formed on milling the powder for 60 h.	36
Figure 3.3: Variation of the lattice parameter of the Ni(Ge) solid solution with Ge content based on Ref. [44, 52-54].	37
Figure 3.4: XRD pattern of the Ni-67 at.% Ge powder blend milled for 10 h showing formation of the equilibrium NiGe intermetallic phase. Note that a small amount of Ge, and even a smaller amount of NiGe ₂ , are also present in the powder at this stage.	39

Figure 3.5: XRD pattern of the Ni-67 at.% Ge powder blend milled for 60 h showing an almost homogeneous formation of the metastable NiGe ₂ phase.	40
Figure 3.6: XRD patterns showing the reversibility of the formation of NiGe on milling the powders. Whereas an almost homogeneous NiGe ₂ phase was found to form on milling the powder blend for 60 h, continued milling to 65 h showed the re-formation of the NiGe phase. The amount of the NiGe phase continued to increase on milling to 75 h at the expense of the metastable NiGe ₂ phase.	42
Figure 3.7: Scanning electron micrographs of the powder blend in the (a) as-blended (unmilled) condition showing elemental Ni and Ge powder particles, (b) formation of the NiGe phase at 5 h, and (c) after milling for 60 h, when an almost homogeneous NiGe ₂ phase had formed. Chemical analysis of the particles through EDS confirms these observations.	45
Figure 3.8: Secondary-electron and back-scattered images of the Ni-67 at.% Ge powder blend milled for 5 h. While the secondary-electron image (a) shows the general morphology of the large powder particle, the back-scattered image (b), shows the atomic number contrast where the heavier metal (Ge) appears brighter and the lighter metal (Ni) dark. Because of a reasonably uniform distribution of the dark and bright areas, (b) clearly confirms that alloying has occurred between Ni and Ge.	46
Figure 3.9: SEM images and EDS spectra of the Ni-67 at.% Ge powder blend milled for (a and b) 0 h, (c and d) 5 h and (e and f) 60 h. Whereas Ni and Ge are present in the unmilled powder (0 h), the powder contains predominantly the equilibrium NiGe phase on milling the powder for 5 h, and the metastable NiGe ₂ phase on milling for 60 h.	48

Figure 3.10: Schematic showing the structural evolution in the Ni-Ge powder blend on MA. (a) The soft Ni particles get plastically deformed and form lamellar structures, while the brittle Ge particles get fragmented on milling. (b) The brittle Ge particles get impregnated into the soft particle surfaces or along lamellar boundaries. (c) – (e) show that agglomeration, fracturing and rewelding of powder particles occur as milling continues. (f) The final stage of milling when fine alloy particles form with the same composition as the starting composition of the powder blend.

..... 60

Figure 4.1: The Ni–Si equilibrium phase diagram [65] 63

Figure 4.2: XRD patterns of the Ni-60 at.% Si powder blend milled for different times. The Ni and Si peaks are clearly seen in the unmilled powder (0 h). The equilibrium NiSi intermetallic started to form at 5 h of milling time, and its amount increased with milling time. 67

Figure 4.3: Plot of crystallite size and lattice strain for Ni-60 at.% Si as a function of milling time. 68

Figure 4.4: XRD patterns of the Ni-67 at.% Si powder blend milled for different times. The Ni and Si peaks are clearly seen in the unmilled powder (0 h). Formation of the equilibrium NiSi phase started at 2 h of milling time. Note that a small amount of Si is present along with NiSi in the powder milled even for 30 h. 70

Figure 4.5: Plot of crystallite size and lattice strain for the Ni-67 at.% Si powder blend as a function of milling time..... 71

Figure 4.6: XRD patterns of the Ni-75 at.% Si powder blend milled for different times. The Ni and Si peaks are clearly seen in the unmilled powder (0 h). Formation of the equilibrium NiSi phase started to occur at 2 h of milling, and its amount increased with milling time..... 73

Figure 4.7: XRD patterns of the Ni-80 at.% Si powder blend milled for different times. The Ni and Si peaks are clearly seen in the unmilled powder (0 h). Formation of the equilibrium NiSi phase started to occur at 2 h of milling, and its amount increased with milling time.....	74
Figure 4.8: Variation of the lattice parameter of Ni(Si) solid solution with Si content based on the results of Klement [44].	76
Figure 4.9: XRD patterns of the Ni-75 at.% Si powder blend milled for different times. On milling the powder for 10 h, a new equilibrium intermetallic NiSi ₂ started to form. An almost homogenous NiSi ₂ phase had formed on milling the powder for 15 h.	78
Figure 4.10: XRD patterns of the Ni-80 at.% Si powder blend milled for different times. On milling the powder for 10 h, a new equilibrium intermetallic NiSi ₂ started to form. An almost homogenous NiSi ₂ phase had formed on milling the powder for 15 h.	79
Figure 4.11: Plot of crystallite size and lattice strain for the Ni-75 at.% Si powder blend powder blend as a function of milling time.	80
Figure 4.12: Plot of crystallite size and lattice strain for the Ni-80 at.% Si powder blend as a function of milling time.	81
Figure 4.13: (a) and (b): Scanning electron micrographs of pure Ni and Si powders showing the spiky and faceted morphologies, respectively.	82
Figure 4.14: (a): Scanning electron micrograph of the Ni-60 at. % Si powder blend in the as-blended (unmilled) condition showing elemental Ni and Si powder particles. (b): Scanning electron micrograph of the Ni-60 at. % Si powder blend after milling for 5 h. showing the presence of both NiSi and Si phases. (c): Backscattered image of the Ni-60 at.% Si powder shows the atomic number contrast where the lighter phase (Si) appears dark and the heavier phase (NiSi) appears	

bright (d): Scanning electron micrograph of the Ni-60 at. % Si powder blend after milling for 20 h showing uniform grains size of NiSi phase.	83
Figure 4.15: Scanning electron micrograph of Ni-67 at. % Si after milling for 5 h. showing the presence of both NiSi and Si phases (b): Scanning electron micrograph of Ni-67 at. % Si after milling for 30 h showing. Showing NiSi and small amount of Si phases.	84
Figure 4.16: Plot of intensity for 111_{Si} peak in Ni-60 at.% Si and Ni-67 at.% Si powder blends as a function of milling time.	90
Figure 4.17: Plot of intensity for 112_{NiSi} peak in Ni-60 at.% Si and Ni-67 at.% Si powder blends as a function of milling time.	91
Figure 5.1: XRD patterns of Fe-0.8 wt.% C powder blend as a function of the milling time.	102
Figure 5.2: XRD pattern of the Fe-0.8 wt.% C powder blend milled for 30h, showing formation of the Fe_3C phase coexisting with $\alpha\text{-Fe}$	103
Figure 5.3: XRD patterns of the Fe-7.0 wt.% C powder blend as a function of the milling time.	104
Figure 5.4: XRD pattern of the Fe-7.0 wt.% C powder blend milled for 30 h, showing homogenous formation of the Fe_3C phase.	105
Figure 5.5: Plot of crystallite size and lattice strain for (a) Fe-0.8 wt. % C and (b) Fe-7.0 wt. % C powder blends as a function of milling time.....	106
Figure 5.6: XRD pattern of the Fe-0.8 wt.% C powder milled for 30 h after sintering at 600 °C for 15 min under a pressure of 70 MPa showing formation of the Fe_3C phase coexisting with $\alpha\text{-Fe}$	107

Figure 5.7: : Variation of the lattice parameter of the Fe (C) solid solution with C content based on ref. [128].	108
Figure 5.8: Changes in the carbon content with milling time for (a) Fe-0.8 wt.% C powder blend and (b) Fe-7.0 wt.% C powder blend, as a function of milling time.	109
Figure 5.9: XRD pattern of the Fe-7.0 wt.% C powder milled for 30 h, after sintering at 600 °C for 15 min under a pressure of 70 MPa showing formation of only the Fe ₃ C phase.	110
Figure 5.10: XRD pattern of the Fe-0.8 wt.% C after annealing at 900 °C for 1 h showing increase in the sharpness of the α -Fe and Fe ₃ C phase peaks.	111
Figure 5.11: XRD pattern of the Fe-0.8 wt.% C after quenching in water showing only the martensite phase.	112
Figure 5.12: c/a ratio vs. carbon content of quenched martensite in Fe-C steels [129].	113
Figure 5.13: XRD pattern of the Fe-7.0 wt.% C of sintered sample after annealing at 900 °C for 1 h showing decomposition of the Fe ₃ C phase to form α -Fe.	114
Figure 5.14: Scanning electron micrographs of the powder blend in the (a) as-blended (unmilled condition) showing elemental Fe and C powder particles, (b) after milling for 5 h, showing both large and small sized particles distributed non-uniformly, and (c) after 30 h of milling, when the powder particles became more homogeneous.	115
Figure 5.15: (a) Low magnification scanning electron micrograph of Fe-0.8 wt.%C after spark plasma sintering showing fully dense sample (b) high magnification scanning electron micrograph showing α -Fe and Fe ₃ C phases.	116

Figure 5.16: Low magnification (a) bright field and (b) dark field TEM micrograph of sintered Fe-0.8 wt.% C. High magnification (c) bright field and (d) dark field TEM micrograph of sintered Fe-0.8 wt.% C sample.	117
Figure 5.17: Selected area diffraction pattern of Fe-0.8 wt.% C after sintering, showing the presence of the α -Fe and Fe_3C phases.	118
Figure 5.18: Scanning electron micrographs of Fe-0.8 wt.% C after annealing at 900 °C for 1 h (a) Low magnification micrograph with large area of pearlitic structure, and (b) high magnification micrograph clearly showing the lamellar structure of pearlite.	119
Figure 5.19: EDS elemental concentration profiles along with scan line of the Fe-0.8 wt.% C sample after annealing at 900 °C for 1 h. Increasing and decreasing C contents can be clearly identified in the lamellar structure of pearlite (Fe_3C and α -Fe, respectively).	120
Figure 5.20: TEM micrographs of the Fe-0.8 wt.% C sample after annealing at 900 °C for 1 h (a) bright field (b) dark field, showing the lamellar structure of pearlite (α -Fe and Fe_3C).	121
Figure 5.21: Scanning electron micrographs of Fe-0.8 wt.% C after quenching in water (a) Low magnification micrograph and (b) high magnification micrograph showing the lenticular structure of martensite.	122
Figure 5.22: TEM micrograph of Fe-0.8 wt.% C after quenching in water (a) bright field (b) dark field micrographs showing the lenticular structure of martensite.	123
Figure 5.23: (a) Low magnification scanning electron micrograph of Fe-7.0 wt.% C after spark plasma sintering showing fully dense sample (b) high magnification secondary-electron image showing the general morphology.	124

Figure 5.24: (a) TEM micrograph of sintered Fe-7.0 wt.% C, (b) selected area diffraction pattern, showing only the Fe ₃ C phase, (c) TEM micrograph of Fe-7.0 wt.% C after annealing at 900 °C for 1 h, and (d) selected area diffraction pattern after annealing, showing the both α-Fe and Fe ₃ C phases.....	125
Figure 5.25: Optical microscope images of Vickers hardness impressions of as-sintered samples in (a) Fe-7.0 wt.% C and (b) Fe-0.8 wt.% C.....	127
Figure 6.1: XRD patterns of the Fe-18Cr-8Ni powder blend milled for different times. The Fe, Cr and Ni peaks are clearly seen in the unmilled powder (0 h). Formation of the metastable α phase started to form at 5 h of milling. After 15 h of milling, the metastable α phase transforms to the γ phase, and its amount increased with increasing milling time.....	135
Figure 6.2: XRD patterns of the Fe-18Cr-8Ni powder blend milled for different times. After 40 h of milling, the γ (austenite) phase has transformed to the α phase. On continued milling of the powder to 45 h, only the α phase (martensite) is present.	136
Figure 6.3: XRD patterns of the Fe-18Cr-12Ni powder blend milled for different times. The Fe, Cr and Ni peaks are clearly seen in the unmilled powder (0 h). The γ phase started to form at 10 h of milling. After 15 h of milling, the metastable α phase transforms to the γ phase, and its amount increased with milling time.....	138
Figure 6.4: XRD patterns of the Fe-18Cr-20Ni powder blend milled for different times. The Fe, Cr and Ni peaks are clearly seen in the unmilled powder (0 h). The γ phase started to form at 10 h of milling. After 15 h of milling, the metastable α phase transforms to the γ phase, and its amount increased with milling time.....	139

Figure 6.5: XRD patterns of Fe-18Cr-8Ni, Fe-18Cr-12Ni, and Fe-18Cr-20Ni powders milled for 30 h.....	140
Figure 6.6: XRD patterns of Fe-18Cr-8Ni, Fe-18Cr-12Ni, and Fe-18Cr-20Ni powders after annealing the milled powders at 600 °C for 1 h.	141
Figure 6.7: Variation of lattice parameter with milling time.	143
Figure 6.8: Low magnification scanning electron micrograph of the Fe-18Cr-8Ni powder blend in the as blended (unmilled) condition showing elemental Fe, Cr and Ni powder particles. (c): high magnification scanning electron micrograph (unmilled condition) showing the morphology of the pure Fe particles which are spheroidal in shape, Cr particles which are bulky and random in size and pure Ni particles which have spiky needle-like. (c): Scanning electron micrograph of Fe-18Cr-8Ni powder blend after 5 h of milling showing both large and small sizes particle distributed non-uniformly (d): Scanning electron micrograph of the Fe-18Cr-8Ni powder blend after milling for 30 h showing uniform particles.....	144
Figure 6.9: SEM images and EDS spectra of the Fe-18Cr-8Ni powder blend milled for (a) 5 h and (b) 30 h.	146
Figure 6.10: (a) Low magnification transmission electron micrograph, (b) selected area diffraction pattern, and (c) high-resolution transmission electron micrograph of Fe-18Cr-8Ni powder blend milled for 30 h. Both the austenite and martensite phases are present. The fast Fourier transformation diagrams (as insets in (c)) show that regions 1 and 2 represent the austenite phase and region 3 the martensite phase.	147

Figure 6.11: (a) Low magnification transmission electron micrograph, (b) selected area diffraction pattern, and (c) high-resolution transmission electron micrograph of the Fe-18Cr-20Ni powder blend milled for 30 h. Only the austenite phase is present in this powder.	148
Figure 6.12: The effect of Cr and Ni contents on the stability of the austenite phase in Fe-Cr-Ni alloys, thin (black) line according to [158] and the proposed boundary as indicated by the thick (red) line. The compositions investigated in the present investigation are indicated by asterisks.	151

LIST OF TABLES

Table 1.1: Attributes of mechanical alloying.....	3
Table 2.1: Elemental powders used in the present study.	16
Table 2.2: Nominal compositions used in the present study.	17
Table 2.3: Milling parameters used in the current study.	18
Table 3.1: Crystal structures and lattice parameters of the different phases in the Ni–Ge system [37-39, 43].....	32
Table 3.2: Peak positions and their intensities of milled Ni-66.7 at.% Ge powder blend at milling times of 10, 60, 65, and 75 h.....	43
Table 4.1: Crystal structures and lattice parameters of equilibrium phases in the Ni-Si system [39, 65].	64
Table 5.1: Microhardness measurements of Fe-0.8 wt.% sample.	126
Table 5.2: Microhardness measurements of Fe-7.0 wt.% sample.	127
Table 6.1: Proportions of the different phases in the as-milled and annealed (600 °C/1 h) Fe-18Cr-xNi (x = 8, 12, and 20) powders.	142
Table 6.2: Chemical analyses of the Fe-Cr-Ni powder at 30 h of milling.....	145

CHAPTER 1: INTRODUCTION

1.1 Mechanical Alloying

Mechanical alloying (MA) is a powder processing technique by which homogenous materials could be produced, starting from blended elemental powder mixtures. This technique has been in use for nearly fifty years and has been employed to synthesize a variety of materials that include those that have not been possible to synthesize by any other methods. The technique of MA was developed by John Benjamin and coworkers in 1966 at the International Nickel Company (INCO) laboratories. The first attempt was to synthesize a novel nickel-based superalloy for gas turbine applications that needed the combination of high temperature strength of oxide dispersion and intermediate temperature strength of gamma-prime precipitate [1-3]. This approach has been subsequently extended to Fe-based ODS alloys as well [4]. It was later realized that MA can also be used to synthesize a variety of both equilibrium and non-equilibrium materials at room temperature [5-8].

MA is the generic term used to express processing of blended elemental metal powders in high-energy ball mills. However, more specifically, it describes the process when mixtures of powders (of different metals or alloys/compounds) are milled together and material transfer is involved in forming a homogeneous alloy. Thus, if powders of pure metals A and B are milled together to synthesize alloys, the process is referred to as MA. On the other hand, when powders of uniform (often stoichiometric) composition such as pure metals, intermetallics, or prealloyed powders, are milled in a high-energy ball mill, the process has been termed Mechanical Milling (MM). When a mixture of two intermetallics is processed, and then alloying occurs, this will be

referred to as MA since material transfer is involved. But, if a homogeneous material is processed only to reduce the particle (or grain) size and increase the surface area, then it will be referred to as MM, since material transfer is not involved. Also, if a phase transformation occurs in a single-phase material under mechanical action, this also will fall under the category of MM. The destruction of long-range order in intermetallics to produce either a disordered intermetallic (solid solution) or an amorphous phase has been referred to as Mechanical Disorder (MD).

MA is a non-equilibrium solid-state powder processing method which involves severe plastic deformation of powder particles in a high-energy ball mill. The two most important actions involved in MA are cold working and fracturing of powder particles and these events get repeated until a homogenous powder is produced. Alloying is considered completed when the rate of these two events balances and the average particle size remains relatively constant and the composition of the powder is the same as that of the starting powder blend [6, 9].

MA is normally a dry, high-energy ball milling technique that has been used to produce a variety of commercially useful and scientifically interesting materials. The formation of an amorphous phase by mechanical grinding of a Y-Co intermetallic compound in 1981 [10] and its formation in the Ni-Nb system in 1983 by ball milling of blended elemental powder mixtures [11] brought about the recognition that MA is a potential non-equilibrium processing technique. Subsequently, a large number of equilibrium and non-equilibrium phases including supersaturated solid solutions, crystalline and quasicrystalline intermediate phases, and amorphous alloys have been synthesized using this technique. It has also been recognized that powder mixtures can be mechanically activated to induce chemical reactions, at room temperature or at least at much lower temperatures than normally required, to produce pure metals, nanocomposites, and a variety of

commercially useful materials. Due to all these special attributes, this simple, but effective, processing technique has been applied to metals, ceramics, polymers, and composite materials. The attributes of MA are summarized in Table 1.1.

Table 1.1: Attributes of mechanical alloying.

1	Production of fine dispersion of second phase particles (usually oxides)
2	Extension of solid solubility limits
3	Refinement of grain sizes down to nanometer range
4	Synthesis of novel crystalline and quasicrystalline phases
5	Development of amorphous (glassy) phases
6	Disordering of ordered intermetallics
7	Possibility of alloying immiscible metals
8	Inducement of chemical reactions at low temperatures
9	Scalable process

1.2 Mechanism of Alloying

MA involves loading the desired proportions of the blended elemental powders mixed with the grinding medium (usually steel or tungsten carbide balls) into a vial and subjecting the powder to severe plastic deformation in a high-energy ball mill. Milling is usually carried out in one of four common mill configurations [5, 12, 13]. The first one is a vibratory mill such as a SPEX shaker mill (Figure 1.1(a)). The vial is shaken in a complex motion which combines back-and-

forth swings with short lateral movements several hundred times a minute. This machine can produce small quantities of powder (about 10-20 g) at a time in relatively short times. A second configuration is a vertical ball mill such as an attritor mill, which can be used to produce large quantities of powder (from about 0.5 to 40 kg) at a time in a moderate milling time. As shown in Figure 1.1(b), the sealed cylindrical tank contains many grinding balls which are activated by a vertical shaft having a set of horizontal impellers attached to it. The impellers energize the ball charge, causing the powder size reduction as a result of impacts between the balls and the container wall, the agitator shaft, the impellers and the balls themselves. Another popular mill is the planetary ball mill (referred to as Pulverisette) in which a few hundred grams of powder can be milled at a time (Figure 1.1 (c)). The centrifugal force produced by the containers rotating around their axes and that produced by the rotating support disk both act on the powder to be milled and the grinding balls. A conventional horizontal ball mill, Figure 1.1(d), is a relatively large machine which can be charged with large volumes of powder and milling is carried out over long periods of times.

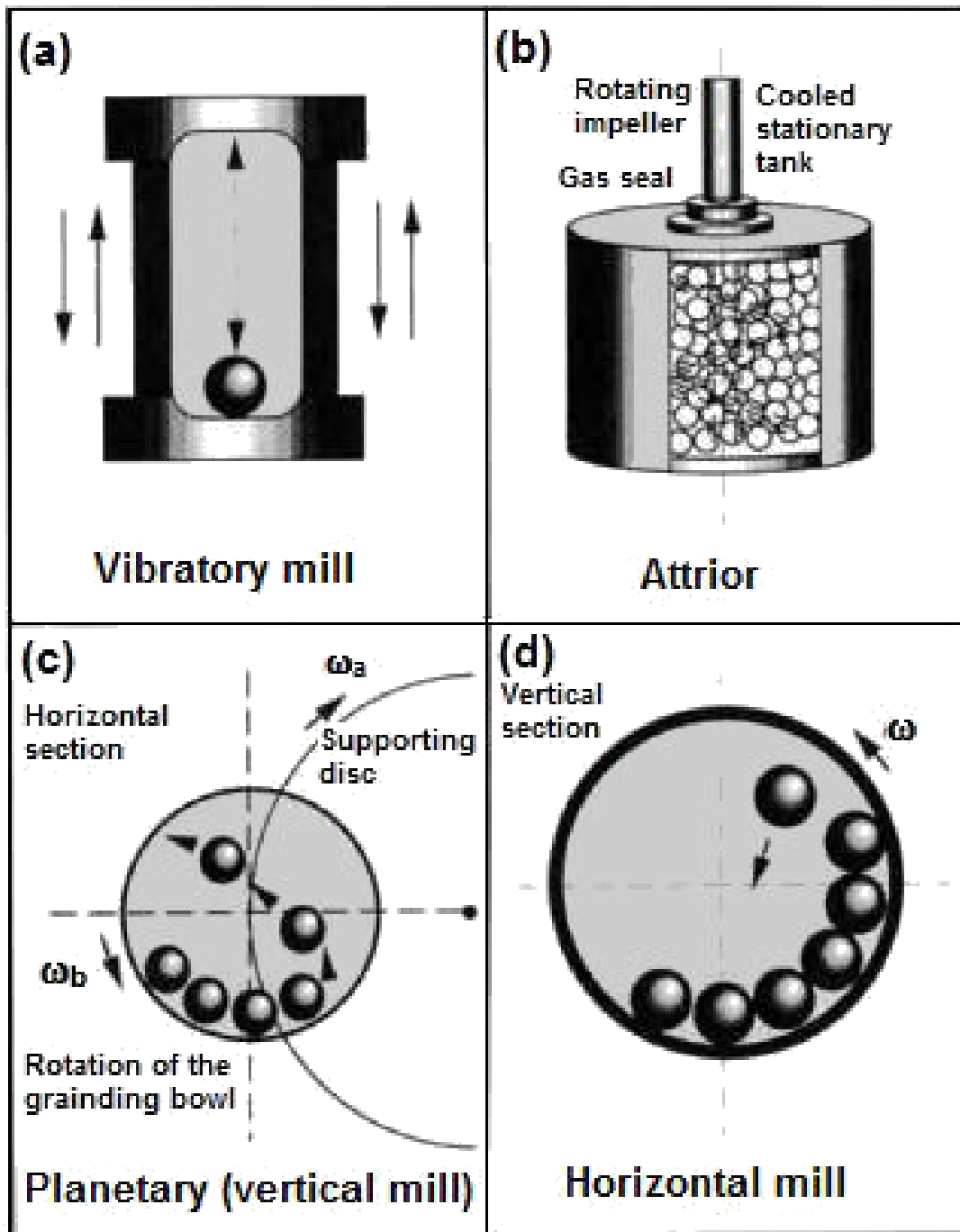


Figure 1.1: Schematic representations of the four different types of milling machines [12].

The effects of a single collision on each type of constituent powder particles are shown in

Figure 1.2.

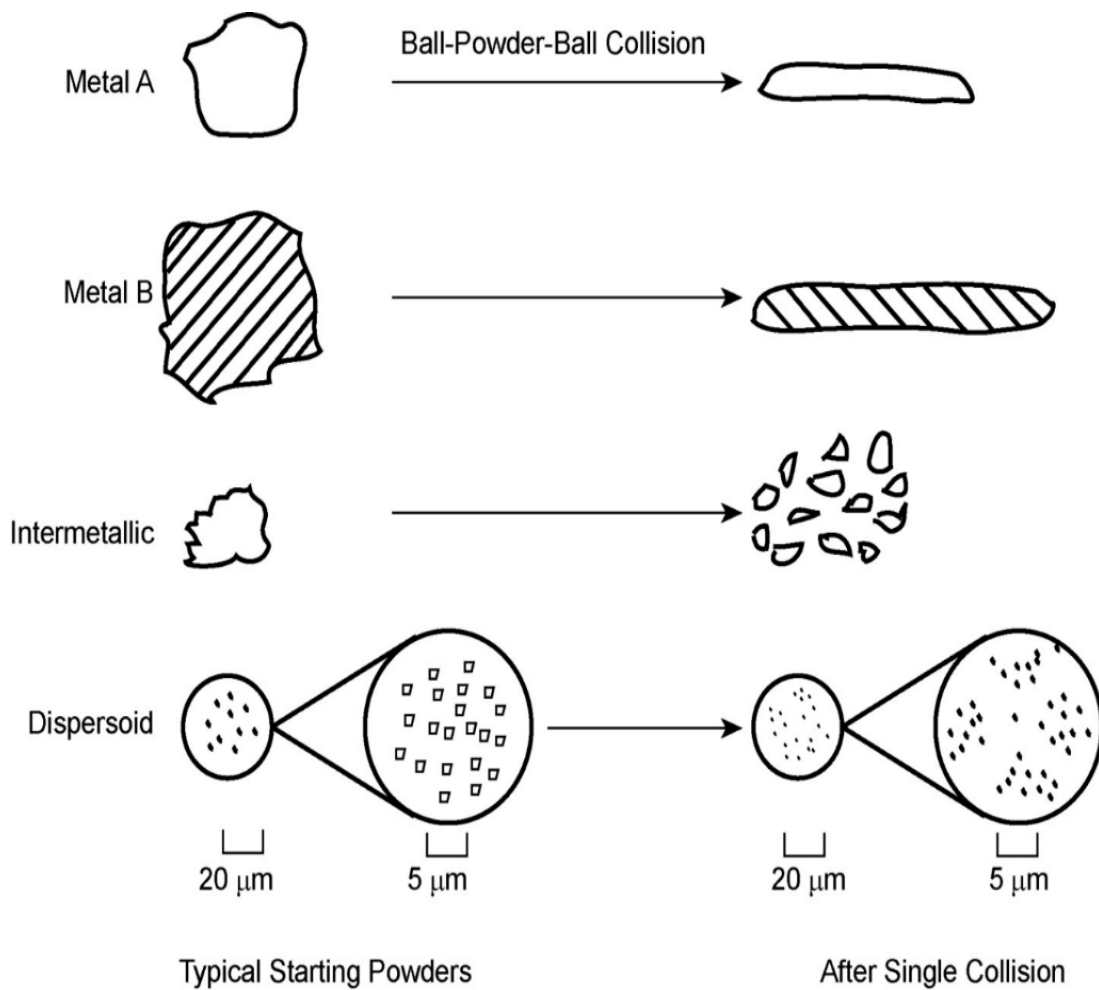


Figure 1.2: Deformation characteristics of representative constituents of starting powders used in mechanical alloying. The ductile metal powders are flattened, while the brittle intermetallic and oxide particles are fragmented into smaller particles [5].

The initial impact of the grinding balls causes the ductile metal powders to flatten and work harden. The severe plastic deformation experienced by the powders increases their surface-to-volume ratio and ruptures the surface films of adsorbed contaminants. The brittle intermetallic powder particles get fractured and are refined in size. The oxide particles added are comminuted more severely.

Whenever two grinding balls collide, a small amount of the powder being milled is trapped in between them. Typically, around 1000 particles with an aggregate weight of about 0.2 mg are trapped during each collision [5] (Figure 1.3)

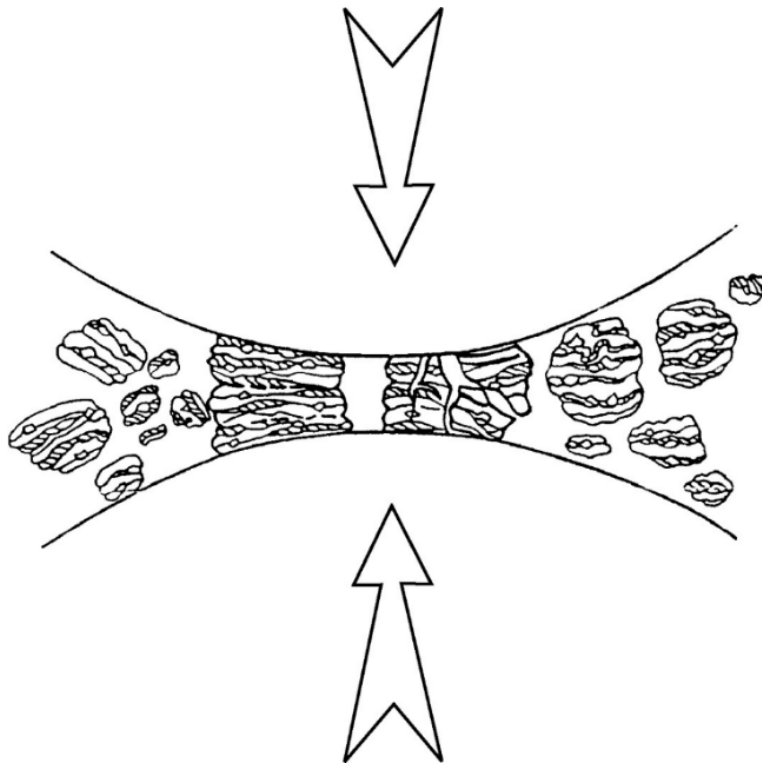


Figure 1.3: Ball-powder-ball collision of powder mixture during mechanical alloying [5].

During this process, the powder morphology can be modified in two different ways, depending on whether we are dealing with ductile-ductile, ductile-brittle, or brittle-brittle powder combinations. If the starting powders are soft metal particles, the particles get flattened and the flattened layers overlap and form cold welds. This leads to formation of layered composite powder particles consisting of various combinations of the constituent metals. The composite powder particles get work hardened with increasing milling time. Consequently, the hardness and brittleness of the particles will increase, and the particles become fragmented with more equiaxed shapes forming. With increasing milling time, the elemental lamellae of the welded layer and both fine powder particles become convoluted rather than being linear. On the other hand, the more brittle constituents (such as the oxide particles) tend to become occluded by the ductile constituents and trapped in the composite. The work-hardened elemental or composite powder particles may fracture at the same time. These competing events of cold welding (with plastic deformation and agglomeration) and fracturing (size reduction) continue repeatedly throughout the milling period. After milling for a certain length of time, steady-state equilibrium is attained when a balance is achieved between the rate of welding, which tends to increase the average particle size, and the rate of fracturing, which tends to decrease the average composite particle size. The particle size distribution at this stage is narrow, because particles larger than average are reduced in size at the same rate that fragments smaller than average grow through agglomeration of smaller particles. Eventually, a refined and homogenized microstructure is obtained and the composition of the powder particles is the same as the proportion of the starting constituent powders.

1.3 Diffusion during Mechanical Alloying

Diffusion is the main process during mechanical alloying that leads to the formation of alloy phases. Diffusion is driven in any system by a decrease in Gibbs free energy or chemical potential difference. There are two major mechanisms by which atoms can diffuse through a solid, viz., the interstitial or substitutional mechanisms and are referred to as lattice diffusion. Conventional solid-state reactions involve formation of one or more product phases between solid reactants. The factors on which the possibility and rate of a solid state reaction depend include reaction conditions, structural properties of the reactants, the initial contact areas of the solids, their reactivity and the thermodynamic free energy change associated with the reaction [14, 15]. However, most solid-state reactions have limited diffusion rates. Therefore, solid-state reactions are mainly temperature dependent. This is not the situation for MA, since the reaction rate may actually increase with increasing milling time resulting in the formation of new phases [5, 6, 16]. Because of the nature of MA, the particles are always in contact with each other with atomically clean surfaces and significantly reduced diffusion distances. As a result, reaction areas are increased, permitting an increase in chemical reactivity during MA.

The presence of defect structure in the milled powder (dislocations, grain boundaries, stacking faults, vacancies, etc.) enhances the diffusivity of solute elements in the matrix. Further, the refined microstructural features decrease the diffusion distances. Additionally, the slight rise in temperature during milling further aids the diffusion behavior, and consequently, true alloying takes place amongst the constituent elements. While this alloying generally takes place nominally at room temperature, sometimes it may be necessary to anneal the mechanically alloyed powder at a slightly elevated temperature for alloying to be achieved. This is particularly true when

formation of intermetallics is desired. The particular times required to synthesize a given phase in any system would be a function of the initial particle size and characteristics of the compositions as well as the specific equipment used for conducting the MA process and the operating parameters of the equipment. The mechanism of MA is schematically shown in Figure 1.4.

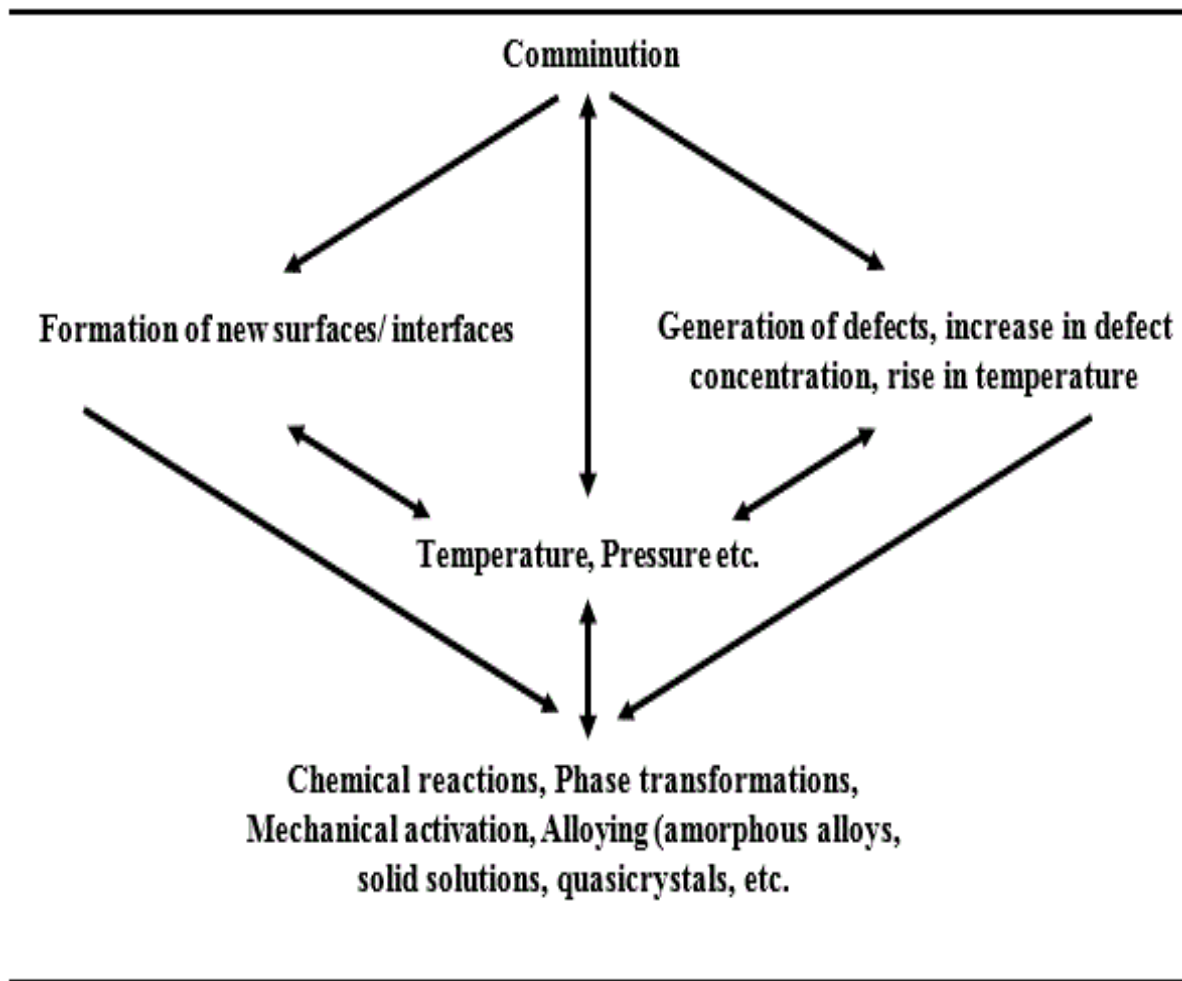


Figure 1.4: Mechanism of MA

1.4 Mechanical Alloying Parameters

MA is a complex process that involves optimization of a number of parameters to produce the desired phase, microstructure and properties. A brief description of some of the important process parameters that have an influence on the final constitution of the milled powder is presented below.

1.4.1 Ball-to-Powder Weight Ratio

The ratio of the weight of grinding balls to the powder (BPR), also referred to as charge ratio (CR), is a crucial parameter in the milling process. Generally, the ratio depends upon the alloy system under study and has been as low as 1:1 [17] or as high as 1000:1 [18]. Milling the powder in a small capacity mill such as a SPEX mill, employs a BPR of 10:1 most commonly.

The effect of BPR on milling time which is required to achieve a specific phase in the powder being milled is significant. High BPR infers higher rate of collisions and consequently, more energy is transferred to the powder particles and alloying occurs faster. Since alloying occurs due to impact forces of balls applied on the powder particles, it is important that there should be enough space for the balls and the powder particles to move freely in the container. Therefore, the amount of filling the milling container with the powder and balls is important. If the quantity of the balls and the powder is very small, then the production rate is very low. However, if the quantity is large, then there is not enough space for the balls and powder to move around so the energy of the impact is less. Generally, around 50% of the container is left empty for best results.

1.4.2 Process Control Agent

Due to the heavy plastic deformation, the powder particles get cold welded to each other during milling. However, true alloying among powder particles can take place only when equilibrium is maintained between cold welding and fracturing of particles. The main purpose of adding a process control agent (PCA) to the powder mixture during milling is to act as a surface active agent to avoid or reduce the effect of excessive cold welding between powder particles and the powder and walls of the container. The PCA could be solid, liquid, or gas. The PCA adsorbs on the surface of the powder particles and minimizes cold welding between powder particles and thereby prevents agglomeration. The nature and quantity of PCA have a significant effect on the final shape, size and purity of the powder particles. One study shows that use of 1 wt. % of PCA increases the particle size to about 500 μm , whereas use of 3 wt. % of PCA reduces the particle size to about 10 μm [19]. Also, it is reported that a homogeneous distribution of particle sizes can be easily achieved when the PCA is in the liquid state than when it is in the solid state.

1.4.3 Milling Atmosphere

The main purpose of milling the powders under vacuum or in an inert gas such as argon or helium is to prevent or minimize oxidation and/or contamination of the milled powder. Normally, powder handling such as loading, unloading and weighting is conducted inside atmosphere-controlled glove boxes, which are usually repeatedly evacuated and refilled with argon gas.

For certain purposes, different atmospheres have been used during milling. For example, hydrogen atmosphere was used to synthesize hydrides [20]. Also, nitrogen or ammonia atmosphere has been used to synthesize nitrides [21, 22].

1.4.4 Milling Medium

The most common types of materials used for the milling medium are hardened steel, tool steel, hardened chromium steel, tempered steel, stainless steel or WC-Co. The density of milling medium (balls) should be high enough to generate enough impact force that could be transferred to the powder during milling. The density of the milling medium also has an influence on alloying efficiency. High impact forces will be transferred to the powder particles by the high density (large size) of the balls.

Generally, only one size of the milling medium is used in the studies. But, it has been shown that the highest kinetic energy could be obtained when the balls with different sizes are used [23]. In the early stages of milling, the powder gets coated onto the surface of the milling medium and also gets cold welded. This is useful because it prevents excessive wear of the milling medium and also prevents contamination of the powder due to wear and tear of the milling medium. However, the disadvantage of this effect is that it is difficult to detach this powder and so the powder yield is low. So, it is important to combine large and small diameter balls during milling to minimize the amount of cold welding and the amount of powder coated onto the surface of the balls [24]. Also, use of different sizes of balls during milling creates shearing forces that may help to detach the powder from the surface of the balls.

1.4.5 Milling Temperature

The temperature of milling has a significant effect in any alloy system since diffusion processes are involved in the formation of alloy phases regardless of whether the final phase is solid solution, intermetallic, nanostructure, or an amorphous phase. A few studies reported where

the temperature of milling has been intentionally varied. This was done by either dripping liquid nitrogen on the milling container to lower the temperature or electrically heating the milling container to increase the temperature of milling. These studies were used to investigate the effect of milling temperature on the variation in solid solubility levels, or to determine whether an amorphous phase or a nanocrystalline structure forms at different temperatures [5].

1.5 Objectives

The objectives of the present investigation are.

1. To identify and synthesize stable and metastable phases in different alloy systems using high-energy ball milling.
2. To investigate structural behavior using characterization techniques such as X-ray diffraction (XRD), scanning electron microscopy (SEM), transmission electron microscopy (TEM), energy dispersive X-ray spectroscopy (EDS) and electron energy loss spectroscopy (EELS).
3. To synthesize NiX and NiX₂-type of phases (X=Si,Ge) starting from blended elemental powders.
4. To investigate the mechanical properties and phase transformations after consolidating the Fe-0.8 wt.% C, and Fe-7.0 wt.% C powder blends in the Fe-C system and Fe-18Cr-8Ni, Fe-18Cr-12Ni and Fe-18Cr-20Ni powder blends in Fe-Cr-Ni system using spark plasma sintering (SPS) method.

1.6 Dissertation Outline

The dissertation is presented in seven different chapters. Following a general introduction, here, in Chapter 1, Chapter 2 describes the experimental procedures used to synthesize and characterize the different phases in the Ni-Ge, Ni-Si, Fe-C, and Fe-Cr-Ni elemental powder blends. The characterization techniques used in the present investigation include X-ray diffraction (XRD), scanning electron microscopy (SEM), focused ion beam (FIB), energy dispersive spectroscopy (EDS), and transmission electron microscopy (TEM).

In Chapter 3, we report investigations on the synthesis of a metastable phase NiGe₂ at room temperature and atmospheric pressure, which is normally present at high temperatures and high pressures. And, we will discuss the reversible transformation from equilibrium phase NiGe to metastable phase NiGe₂ which then reversion back to the equilibrium NiGe phase with continued milling.

Chapter 4 reports on formation of NiSi phase in the Ni-Si system in the composition range of 60-67 at.% Si. Furthermore, studies on the formation of nickel disilicide (NiSi₂) in the compositions of 75 and 80 at.% Si were also conducted.

Chapter 5 reports the production of different steel alloys, for example, eutectoid (Fe-0.8 wt.% C) steel and cementite (Fe-7.0 wt.% C) using MA. Chapter 6 focuses on the synthesis of austenitic stainless steel by MA and study the phase transformations in the as-milled condition and after heat treatment. Finally, the dissertation ends with Chapter 7 which provides a summary of the present study.

CHAPTER 2: EXPERIMENTAL PROCEDURE

This chapter describes the experimental procedures employed to synthesize and characterize the Ni-Ge, Ni-Si, Fe-C, and Fe-Cr-Ni alloys starting from blended elemental powders by MA. A full description of the starting materials, processing of the powders, and the individual powder characterization techniques are detailed in the sections to follow.

2.1 Starting Materials

Table 2.1 gives detailed information on the purity and size of the elemental powders used in this study. Powder blends of pure elemental powders, corresponding to the nominal compositions of different alloy systems (Table 2.2), were milled in a high-energy SPEX CertiPrep 8000D shaker mill. These compositions were selected so as to investigate the formation of stable and metastable phases, and specifically in the Ni-based systems, formation of disilicides and digermanides.

Table 2.1: Elemental powders used in the present study.

Element	Powder purity (%)	Powder size (μm)
Fe	99.9	<10
C	-	-
Cr	99.95	74
Ni	99.9	3-7
Si	99.5	44
Ge	99.9	80

Table 2.2: Nominal compositions used in the present study.

Alloy	Composition	
	wt. %	at. %
Steel	Fe _{99.2} C _{0.8}	Fe _{96.39} C _{3.61}
	Fe ₉₃ C ₇	Fe _{74.08} C _{25.92}
Stainless steel	Fe ₇₄ Cr ₁₈ Ni ₈	Fe _{73.31} Cr _{19.15} Ni _{7.54}
	Fe ₇₀ Cr ₁₈ Ni ₁₂	Fe _{69.48} Cr _{19.19} Ni _{11.33}
	Fe ₆₂ Cr ₁₈ Ni ₂₀	Fe _{61.77} Cr _{19.26} Ni _{18.96}
Ni-silicide	Ni _{58.21} Si _{41.79}	Ni ₄₀ Si ₆₀
	Ni _{51.06} Si _{48.94}	Ni _{33.3} Si _{66.7}
	Ni _{41.06} Si _{58.94}	Ni ₂₅ Si ₇₅
	Ni _{34.32} Si _{65.68}	Ni ₂₀ Si ₈₀
Ni-germanide	Ni _{28.74} Ge _{71.26}	Ni _{33.3} Ge _{66.7}

2.2 Processing

MA was carried out in a high-energy SPEX CertiPrep 8000D shaker mill. About 2 wt.% of stearic acid (CH₃(CH₂)₁₆COOH) was used as a process control agent (PCA) to reduce the effect of excessive cold welding between powder particles and the powder and the walls of the container. For each experiment, 10 g of the blended elemental powder mix and 100 g of stainless steel balls or tungsten carbide balls were loaded into the hardened steel vial, thus maintaining a ball-to-powder weight ratio (BPR) of 10:1 during milling. Around 50% of the vial space was left empty to give enough space for the balls and powder particles to move around freely in the milling

container. Powder handling was done in an argon-filled glove box to avoid/minimize contamination. Milling was conducted for different times up to a total of 75 h in the Ni-Ge system, which was the longest milling time used. Milling was interrupted for 30 min after every 2 h of milling to minimize the powder temperature rise. It was observed that the powder tends to stick to the walls of the container, especially in the early stages of milling, thus preventing the expected phases from forming. To minimize this effect, the container was opened at regular intervals, inside the glove box, the powder was scraped off the walls of the container, and milling was resumed. MA was interrupted after selected time intervals and a small amount of the milled powder was removed for structural and microstructural characterization.

Table 2.3: Milling parameters used in the current study.

Parameter	Value
Weight of powder	10 g
BPR	10:1
PCA	2.0 wt.% of Stearic acid
Atmosphere	Argon
Milling medium	(4 and 9.5 mm diameter) Stainless steel or tungsten carbide balls
Type of mill	SPEX CertiPrep 8000D

2.3 Characterization Techniques

The mechanically alloyed powders were analyzed by X-ray diffraction (XRD), scanning electron microscopy (SEM), energy dispersive X-ray spectrometry (EDS), and transmission electron microscopy (TEM) techniques. MA was interrupted after selected time intervals and a small amount of the milled powder was removed for structural and microstructural characterization.

2.3.1 X-Ray Diffraction (XRD)

X-ray diffraction was used to follow the structural evolution in the milled powder, and to study the variation of crystallite size and lattice strain as a function of milling time, and also to identify the crystal structures of the phases and calculate the lattice parameter(s). X-ray diffraction (XRD) for structural characterization was conducted in a Rigaku-DXR 3000 diffractometer using Cu K α radiation ($\lambda = 0.154056$ nm) at 40 kV and 30 mA settings. Diffraction patterns were recorded in the 2θ range from 20° to 90° with a step size of 0.05° and the dwell time of 3 s. The phases present were identified and their lattice parameters calculated using standard XRD procedures [25, 26]. Identification of the phases was done by comparing the diffraction angles and intensities of the different diffraction peaks with the standard XRD patterns reported in the literature.

2.3.1.1 Phase Proportions in Multi-Phase Mixtures

The intensity of the diffraction peak of a particular phase in a mixture of phases depends on the absorption coefficient of the mixture and this itself varies with the phase fraction. Therefore, peak positions and their intensities were employed to determinate the amounts of the different

phases using the following procedure [25, 26]. The integrated intensity of a diffraction peak is given by:

$$I = \left(\frac{I_0 e^4}{m^2 c^4} \right) \left(\frac{\lambda^3 A}{32 \pi r} \right) \left(\frac{1}{v^2} \right) \left[|F|^2 p \left(\frac{1 + \cos^2 2\theta}{\sin^2 \theta \cos \theta} \right) \right] \left(\frac{e^{-2M}}{2\mu} \right) \quad (2.1)$$

where

I = integrated intensity per unit length of the diffraction line

I_0 = intensity of the incident beam

e, m = charge and mass of the electron

c = velocity of light

λ = wavelength of the incident radiation

r = radius of the diffractometer circle

A = cross-sectional area of the incident beam

v = volume of the unit cell

F = structure factor

p = multiplicity value

θ = Bragg angle

e^{-2M} = temperature factor

μ = linear absorption coefficient

When we put

$$K = \left(\frac{I_0 e^4}{m^2 c^4} \right) \left(\frac{\lambda^3 A}{32 \pi r} \right) \quad (2.2)$$

and

$$R = \left(\frac{1}{v^2} \right) \left[|F|^2 p \left(\frac{1 + \cos^2 2\theta}{\sin^2 \theta \cos \theta} \right) \right] (e^{-2M}) \quad (2.3)$$

the diffraction peak intensity in equation (2.1) is given by

$$I = \frac{K R}{2\mu} \quad (2.4)$$

where K is a constant, independent of the kind and amount of the diffraction substance, and R depends on θ , hkl , and the kind of substance.

The amounts of the two phases in a two-phase mixture, for example A and B , can be determined using the following procedure:

$$I_A = \frac{K R_A c_A}{2\mu} \quad (2.5)$$

$$I_B = \frac{K R_B c_B}{2\mu} \quad (2.6)$$

where c_A and c_B represent the volume fraction of A and B phases. Division of these two equations yields

$$\frac{I_A}{I_B} = \frac{R_A c_A}{R_B c_B} \quad (2.7)$$

The value of c_A/c_B can be calculated from a measurement of I_A/I_B and calculation of R_A and R_B .

Once c_A/c_B is obtained, the value of c_A or c_B can be calculated from the additional relationship

$$c_A + c_B = 1 \quad (2.8)$$

2.3.1.2 Lattice Parameter Calculations

The lattice parameter(s) were calculated from the interplanar spacing calculated from the XRD patterns using Bragg's equation which relates the wavelength of the x-ray beam and the atomic plane spacing:

$$\lambda = 2d \sin \theta \quad (2.9)$$

where

λ = wavelength of the incident radiation

θ = Bragg angle

d = interplanar spacing

The interplanar spacing can be obtained from a measurement of the θ values and knowing the λ value. Further, the values of the lattice parameters can be calculated using the following relationships.

$$\frac{1}{d^2} = \frac{h^2+k^2+l^2}{a^2} \quad (\text{cubic}) \quad (2.10)$$

$$\frac{1}{d^2} = \frac{h^2+k^2}{a^2} + \frac{l^2}{c^2} \quad (\text{tetragonal}) \quad (2.11)$$

$$\frac{1}{d^2} = \frac{h^2}{a^2} + \frac{k^2}{b^2} + \frac{l^2}{c^2} \quad (\text{orthorhombic}) \quad (2.12)$$

2.3.1.3 Crystallite Size and Lattice Strain Measurements

A number of factors contribute to B , the width of a diffraction peak. These include instrumental effects, small crystallite size, lattice strain, dislocations, stacking faults, etc. Amongst these, the most important are usually crystallite size and lattice strain. Thus, the total broadening can be expressed as:

$$B_{\text{Observed}} = B_{\text{Instrumental}} + B_{\text{crystallite}} + B_{\text{strain}} \quad (2.13)$$

We can rewrite the above equation:

$$B_{\text{crystallite}} + B_{\text{strain}} = B_{\text{Observed}} - B_{\text{Instrumental}} \quad (2.14)$$

$B_{\text{Instrumental}}$ is usually determined using well-annealed powders

Peak broadening was utilized to calculate the crystallite size and lattice strain by measuring the peak width B , in radians, at an intensity equal to half the maximum value, called the full width at half maximum (FWHM). The peak width, B_c is related to the crystallite size, L , through the Scherrer equation:

$$L = \frac{k\lambda}{B_c \cos \theta} \quad (2.15)$$

where

L = crystallite size

k = shape factor, with a value of about 0.9

λ = wavelength of the X-ray beam

B_c = broadening of the XRD peaks due to small crystallite size

θ = Bragg angle

It is important to realize that the Scherrer formula provides a lower bound on the particle size.

The lattice strain induced during MA also causes broadening of diffraction peaks, which is given by

$$B_{strain} = \eta \tan \theta \quad (2.16)$$

where η is the strain in the material

Since both lattice strain and small particle size cause peak broadening simultaneously in the milled powders, the total broadening is expressed as:

$$B = B_{crystallite} + B_{strain} = \frac{k\lambda}{L \cos \theta} + \eta \tan \theta \quad (2.17)$$

which can be rewritten as:

$$B \cos \theta = \frac{k\lambda}{L} + \eta \sin \theta \quad (2.18)$$

Thus, by plotting ($B \cos \theta$) against ($\sin \theta$), a straight line is obtained. It is then possible to obtain the crystallite size and lattice strain from the intercept on the Y-axis ($B \cos \theta$) and the slope (η) of the straight line, respectively [27, 28].

2.3.2 Scanning Electron Microscopy (SEM)

Scanning electron microscopy (SEM) was conducted in a Zeiss Ultra 55 microscope at an acceleration voltage of 10 kV to observe the microstructural changes using both secondary-electron and backscattered imaging modes. Energy dispersive x-ray spectroscopy (EDS) was used to evaluate the chemical compositions of the milled powders and correlate them with the XRD results. The average sizes of the particles or microstructural features in the SEM micrographs were determined using quantitative metallography methods. In this method, the linear dimensions of a large number of particles in different directions were measured and the average particle size was calculated by averaging out the total length over the number of particles [29].

2.3.3 Focused Ion Beam (FIB)

The focused ion beam (FIB) technique was conducted in a Zeiss Crossbeam 1540XB FIB unit to prepare thin samples for TEM investigations. The samples of Fe-0.8 wt.% C and Fe-7.0 wt.% C, after compacting the mechanically alloyed powders into bulk form, were prepared using FIB employing the In-situ FIB technique. Platinum metal was sputter-deposited on top of the thin sample area in order to protect it from damage by high energy Ga ion beam (Figure 2.1 (a)). The next step is including extraction of the sample from its trench with “U”-shaped cuts (Figure 2.1

(b)). The cut partially surrounds the target. Then the probe is fixed to the released sample (Figure 2.1 (c)). The sample dimensions were about 20 μm in length and 1.2 μm in width. In FIB, a variable current, starting from 2 nA to ending with 50 pA, at a voltage of 30 kV was used during the preparation of TEM specimens.

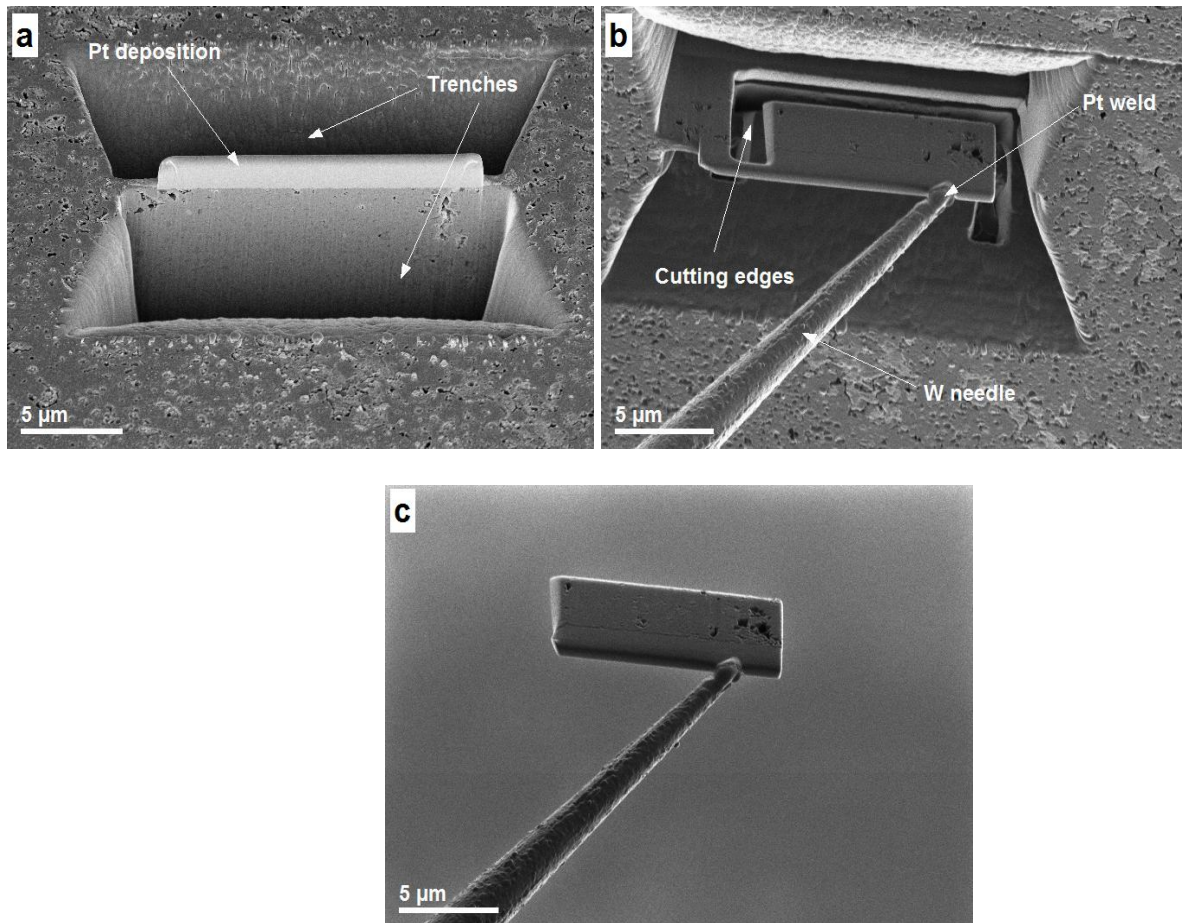


Figure 2.1: Steps of sample preparation for TEM using FIB.

2.3.4 Transmission Electron Microscopy (TEM)

Transmission electron microscopy of the mechanically alloyed powders and compacted samples was carried out using an FEI Tecnai F30 TEM, operating at an acceleration voltage of 300 kV. The main purpose of TEM analysis was to characterize the microstructures of the phases, crystal structure, and chemical composition. The phases were identified with the electron diffraction patterns using Digital Micrograph software. Many techniques of TEM, bright-field, dark-field, selected area diffraction patterns (SADP) and high resolution transmission electron microscopy (HRTEM), were also used to investigate the internal microstructure of the mechanically alloyed powder in both the as-milled and after sintering into bulk form conditions. Electron energy loss spectroscopy technique (EELS) was used to determine the chemical compositions of the sintered sample. Since EELS tends to work best at relatively low atomic number elements ranging from carbon through the 3d transition metals, we used this technique to evaluate the carbon content in the steel alloys in the both as-sintered and after heat treatment conditions.

2.4 Consolidation of Alloyed Powder

Following 30 h of mechanical alloying, the Fe-C (Fe-0.8 wt.% C and Fe-7.0 wt.% C) and Fe-Cr-Ni (Fe-18Cr-8Ni, Fe-18Cr-12Ni and Fe-18Cr-20Ni) powders were consolidated by spark plasma sintering (SPS) to produce bulk samples. Brief details of the process are mentioned in the following paragraphs.

2.4.1 Spark Plasma Sintering (SPS)

Spark Plasma Sintering (SPS) consolidation technique was used for compacting the powders into bulk form. The SPS technique is also known as Field Assisted Sintering Technique or Pulsed Electric Current Sintering Technique. The main feature of SPS is that pulsed DC current directly passes through the graphite die and the conductive powder compact. This produces a very high heating or cooling rate, resulting in fast sintering of the samples. SPS has the potential of densification of nano-sized powders without grain growth from occurring or glassy materials from crystallizing. It has been experimentally shown that densification is improved by the use of pulsed DC current.

About 10 g of powder samples were loaded in a graphite die (10 mm diameter) and punch unit. Samples were sintered at 600°C and a pressure of 70 MPa for 15 min, in a vacuum controlled environment. Figure 2.2 shows a schematic drawing of the SPS unit.

2.5 Heat Treatment

The bulk consolidated samples of the Fe-C and Fe-Cr-Ni (as-milled and after SPS) systems were heat treated under an inert gas atmosphere to study the effect of heat treatment and the cooling rate on the phase transformation behavior and mechanical properties. In the case of the Fe-0.8 wt.% C composition, the bulk sample was heat treated at 900 °C for 1 h in argon atmosphere to prevent oxidation of the samples. Following heat treatment, the samples were cooled down to room temperature at different rates, either in the furnace, or in air or quenched in water, whereas the Fe-7.0 wt.% C composition bulk sample was cooled down in the furnace only. Further, the as-milled Fe-Cr-Ni (Fe-18Cr-8Ni, Fe-18Cr-12Ni and Fe-18Cr-20Ni) powders were also heat treated at 600

°C for 1 h in argon gas and cooled in the furnace. After heat treatment, the samples were taken out for XRD, SEM, EDS and TEM studies to investigate the phases formed after heat treatment.

2.6 Mechanical Characterization

Mechanical characterization of the consolidated Fe-C alloys was carried out by measuring the Vickers microhardness. The hardness measurements were done using Leco LV700 Vickers hardness tester. The device is equipped with a typical diamond indenter in the form of a pyramid with square base and an included angle of 136° between the opposite faces. Indentations were carried out with an applied load of 1 kgf and a dwell time of 10 s. The hardness values reported are the average of eight measurements.

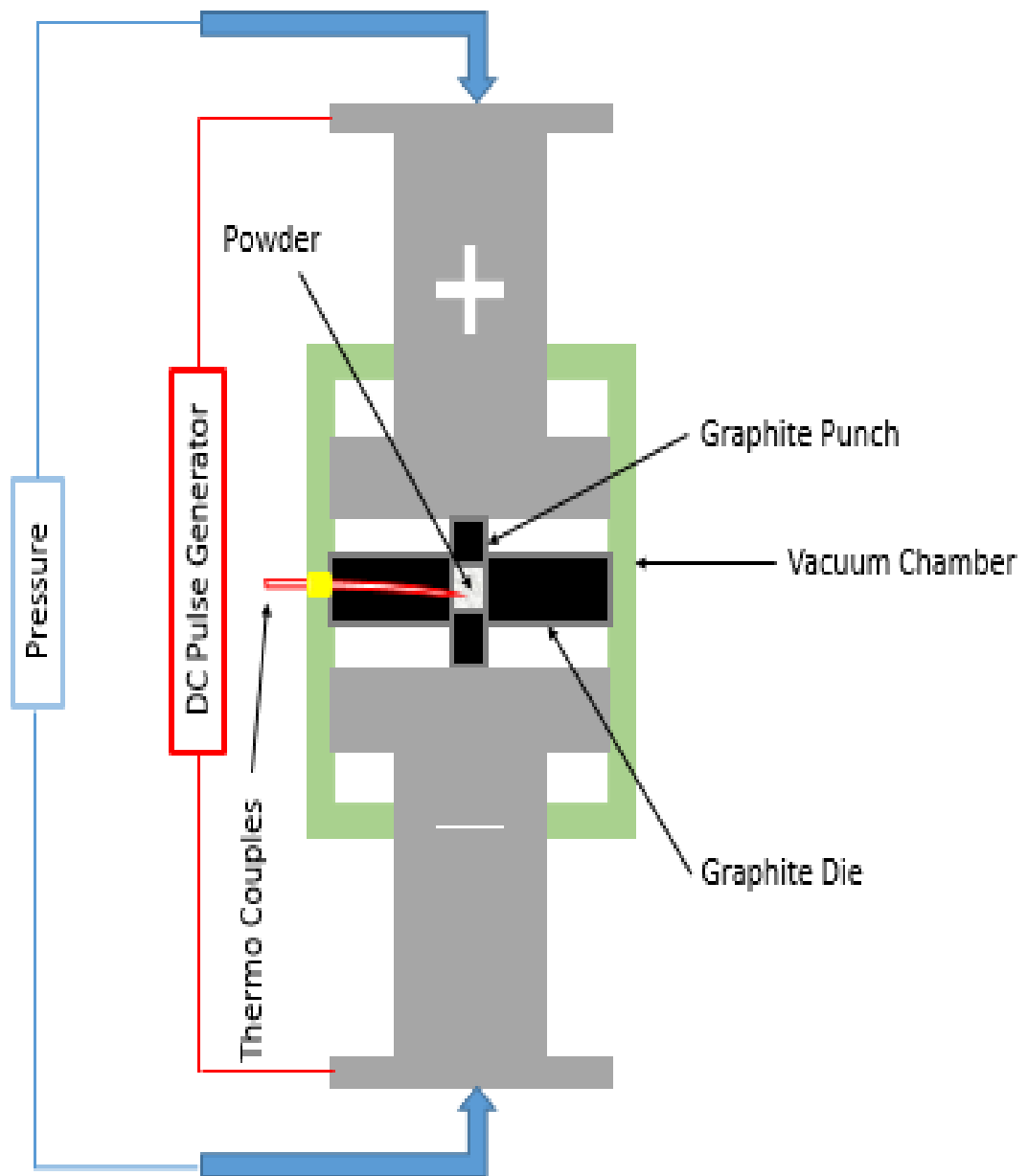


Figure 2.2: Schematic diagram of the SPS machine.

CHAPTER 3: SYNTHESIS OF METASTABLE NiGe₂ BY MECHANICAL ALLOYING AND ITS REVERSION TO NiGe

3.1 Introduction

Transition metal (TM)-germanides are interesting materials for semiconductor applications because of the variety of electrical and magnetic properties they exhibit [30-36]. Ni-based germanides can be synthesized at a low processing temperature of around 270 °C by using rapid thermal processing, while titanium germanides and cobalt germanides can be formed only at higher temperatures of >800 °C and >500 °C, respectively. Such a low processing temperature is effective in preventing degradation of germanium.

The most Ge-rich phase in majority of the TM-Ge binary equilibrium phase diagrams is TMGe₂ or TMGe_{2-x}. One of the exceptions to this observation is the Ni-Ge system, in which no intermetallic phase containing more than 50 at.% Ge exists in the equilibrium phase diagram. In the Ni-Ge system, the most Ge-rich phase is NiGe.

Details of the constitution of Ni-Ge alloys have been recently investigated and the Ni-Ge equilibrium phase diagram is shown in

Figure 3.1 [37]. The Ni-Ge system contains nine intermediate phases, in addition to two terminal phases, and the details of the crystal structures of all these phases are listed in Table 3.1 [37-43]. The Ge-rich part (≥ 50 at. % Ge) of the equilibrium phase diagram (NiGe-Ge part) exhibits a simple eutectic reaction with the eutectic point at 762°C and 67 at. % Ge. No intermediate phase exists in this region of the Ni-Ge phase diagram.

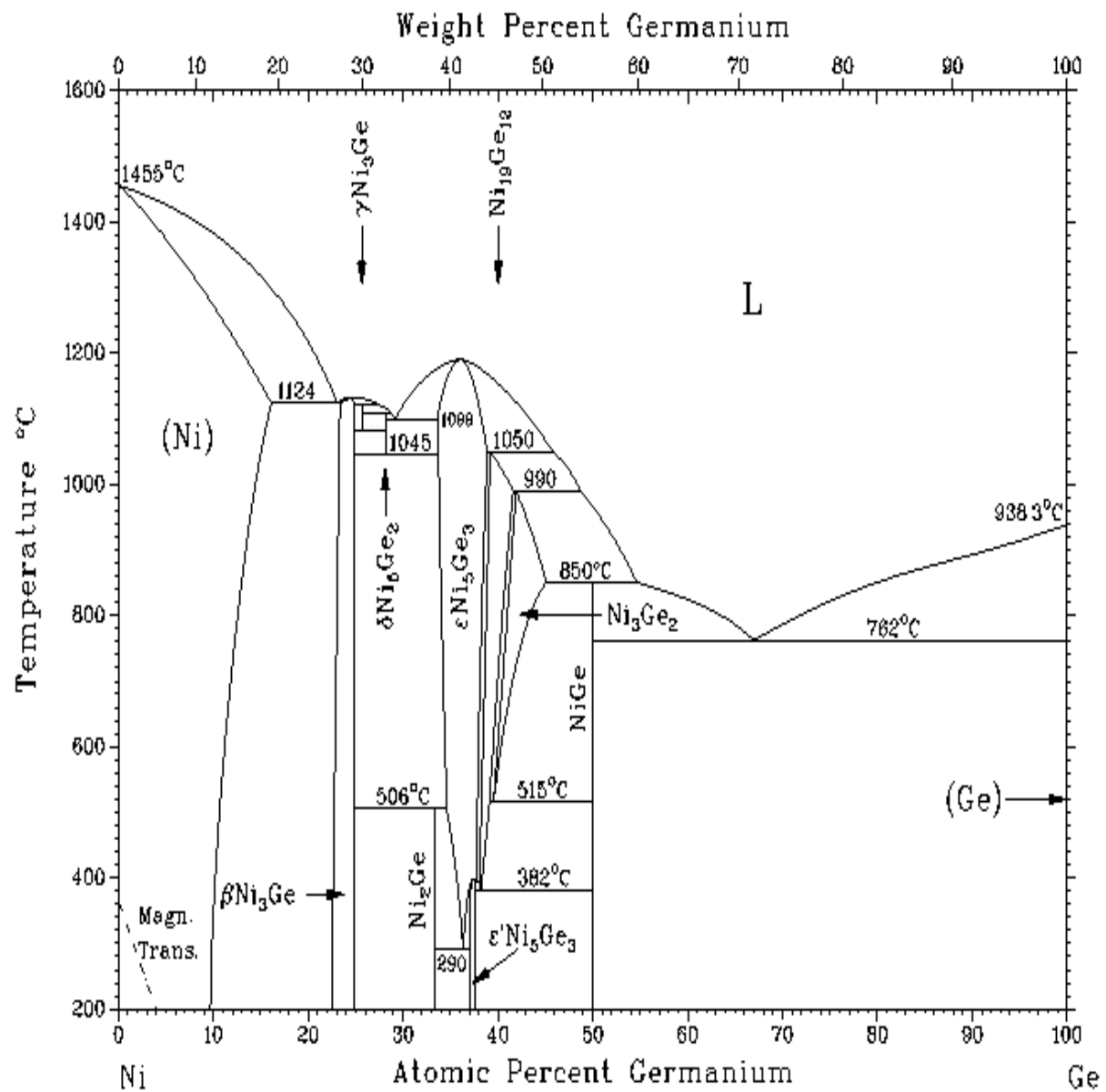


Figure 3.1: The Ni-Ge equilibrium phase diagram [37].

Table 3.1: Crystal structures and lattice parameters of the different phases in the Ni–Ge system [37-39, 43].

Phase	Crystal structure	Pearson symbol	Space group	Structure type	Lattice parameters				
					a (nm)	b (nm)	c (nm)	c/a	β (°)
(Ni)	Cubic	<i>cF4</i>	<i>Fm$\bar{3}m$</i>	Cu	0.3523	-	-	-	-
β -Ni ₃ Ge	Cubic	<i>cP4</i>	<i>Pm$\bar{3}m$</i>	Cu ₃ Au	0.357	-	-	-	-
γ -Ni ₃ Ge	Cubic	<i>cP4</i>	NaT1	0.35731	-			-
δ -Ni ₅ Ge ₂	Hexagonal	<i>hP84</i>	<i>P 6₃/mmc</i>	Pd ₅ Sb ₂	0.6827	-	1.2395	1.816	-
Ni ₂ Ge	orthorhombic	<i>oP12</i>	<i>Pnma</i>	Co ₂ Si	0.7264	0.511	0.383	-	-
ϵ -Ni ₅ Ge ₃	Hexagonal	<i>hP4</i>	<i>P 6₃/mmc</i>	NiAs	0.3622	-	0.5013	1.384	-
ϵ' -Ni ₅ Ge ₃	Monoclinic	<i>mC32</i>	<i>C2</i>	Ni ₅ Ge ₃	1.1682	0.6715	0.6364	-	52.1
Ni ₁₉ Ge ₁₂	Monoclinic	<i>mC62</i>	<i>C2</i>	Ni ₁₉ Ge ₁₂	1.1638	0.6715	1.0048	-	90
Ni ₃ Ge ₂	Hexagonal	<i>hP4</i>	<i>P 6₃/mmc</i>	NiAs	0.386	-	0.500	1.295	-
NiGe	Orthorhombic	<i>oP8</i>	<i>Pnma</i>	MnP	0.581	0.538	0.343	-	-
* NiGe ₂	Orthorhombic	<i>oP24</i>	<i>Cmca</i>	CoGe ₂	1.083	0.5763	0.5762	-	-
Ge	Cubic	<i>cF8</i>	<i>Fd$\bar{3}m$</i>	C	0.56575	-	-	-	-

* metastable phase

There have been some investigations on the synthesis of non-equilibrium phases in the Ni-Ge system using methods such as rapid solidification processing and mechanical alloying. Klement [44] had rapidly solidified Ni-Ge melts in the composition range of 5.48 to 20.55 at.% Ge. By measuring the variation of the lattice parameter of the rapidly solidified alloys with Ge content, he concluded that the maximum solid solubility of Ge in Ni was increased to about 20 at.% from the equilibrium value of <10 at.%. He noted that the lattice parameter of the Ni solid solution increased

with increasing Ge content at a rate of 1.94×10^{-4} nm per at.% Ge. Polesya and Slipchenko [45] also reported an increased solid solubility of up to 21.3 at.% Ge in Ni in their rapidly solidified alloys. Grigorieva et al. [46] reported a maximum solid solubility of 26 at.% Ge in Ni by mechanical alloying methods. Ellner and Predel [47] reported formation of a glassy phase in rapidly solidified Ni-Ge melts, which transformed to the Ni₃Ge phase on crystallization.

Benameur and Yavari [48] subjected prealloyed and fully ordered Ni₃Ge to mechanical attrition and noted that the fully ordered alloy became disordered with a nanocrystalline structure in the beginning and then had transformed to an amorphous phase after milling for longer times. A maximum of about 20 vol.% of the amorphous phase had formed on milling for 160 h. Benameur et al. [49] had also investigated Ni-Ge powder blends in the composition range of 25 to 50 at.% Ge after subjecting them to MA for different milling times. They reported formation of the equilibrium NiGe phase in Ni₆₀Ge₄₀ after 20 h of milling. In the case of Ni₅₀Ge₅₀, the NiGe phase formed in the early stages of milling, but, at longer milling times, a significant amount of the amorphous phase had formed. They had also reported heavy Fe contamination from the milling medium before amorphization occurred, suggesting perhaps that Fe contamination played an important role in the observed amorphization.

On mechanically alloying Ni and Ge powders with the composition Ni₆₂Ge₃₈, Antolak et al. [50] noted formation of Ni-Ge solid solution in the early stages of milling and formation of the Ni₅Ge₂ phase after 20 h of milling.

Some attempts have been made in the past to synthesize the NiGe₂ phase in a metastable condition at room temperature, but have not been completely successful. Starting from a stoichiometric mixture of Ni and Ge, Takizawa et al. [43] synthesized the NiGe₂ phase by reacting

Ni and Ge powders at a high pressure of 5.5 GPa and a high temperature of 700 °C and quenching the sample to room temperature before releasing the applied pressure. Lim et al. [35] sputtered 15 nm Ni layers on a Ge-on-Si substrate and subjected them to laser annealing and rapid thermal annealing. Using different characterization techniques, they observed Ge-rich NiGe₂ phase coexisting with NiGe or Ge phases. By depositing alternate layers of Ni and Ge and allowing the reaction to take place between them, Ly et al. [51] reported the possible formation of a metastable cubic NiGe₂ phase. But, there have been no reports on the formation of homogeneous NiGe₂ phase at low temperatures and at atmospheric pressure. The main objective of this Chapter is to report on the conditions under which the NiGe₂ phase can be synthesized by MA and also determine its stability on continued milling.

3.2 Results

3.2.1 X-Ray Diffraction (XRD)

Figure 3.2 presents the XRD patterns of the Ni-67 at.% Ge powder mixture after milling for different times. The XRD pattern of the unmilled powder blend (for 0 h of milling) indicates the presence of diffraction peaks of pure crystalline Ni (ICDD-PDF # 4-0850) and Ge (ICDD-PDF #65-0333), with the Ge peaks showing a much higher intensity than those of Ni peaks; a consequence of the higher amount of Ge present in the powder blend.

XRD patterns of the powder milled for 1 h showed that both the Ni and Ge peaks became slightly broader and that their peak intensities decreased. Additionally, it was noted that the relative intensities of the 111_{Ni} and 220_{Ge} and 200_{Ni} and 311_{Ge} peaks were reversed, suggesting that perhaps some interdiffusion took place between the two elements. The fact that alloying did occur was

confirmed by observing the back-scattered electron images in the SEM, when interdiffusion between Ni and Ge was observed through X-ray mapping. A slight shift in the positions of the Ni diffraction peaks to lower angles suggests that some solid solubility of Ge in Ni occurred at this stage. Simultaneously, a new peak representing formation of the NiGe phase (ICDD-PDF #65-6716) started appearing at this stage at a 2θ value of about 34.8° . This trend of increased peak broadening, reduction in peak intensity, and more number of diffraction peaks of the NiGe phase, continued with milling time.

The lattice parameter of the Ni(Ge) solid solution was calculated from the 111_{Ni} peak position as a function of the milling time. The lattice parameter increased from 0.3522 nm for pure Ni in the as-blended condition to 0.3529 after 2 h of milling the Ni-67 at. % Ge powder blend, and to 0.3546 nm after milling for 5 h. This increase in the lattice parameter confirms formation of the Ni(Ge) solid solution. Dissolution of Ge atoms ($r_{\text{Ge}} = 0.125 \text{ nm}$), which are smaller than those of Ni ($r_{\text{Ni}} = 0.149 \text{ nm}$) in substitutional positions in the Ni lattice is expected to decrease the lattice parameter of the Ni(Ge) solid solution. However, the observed increase in the lattice parameter suggests that the Ge atoms have dissolved in the interstitial positions. In this condition, the Ni lattice is expected to expand. The continuously increasing lattice parameter observed with milling time suggests that more and more Ge was getting incorporated into the Ni lattice with continued milling. From the standard variation of the lattice parameter of the Ni(Ge) solid solution as a function of the Ge content in the Ni-Ge system, shown in Figure 3.3 [44, 52-54], the Ge content in the solid solution was estimated to be about 11.9 at.%, on milling the powder for 5h. Since the maximum solid solubility of Ge in Ni under equilibrium conditions is less than about 10 at.%, it can be concluded that MA processing has increased the solid solubility limit in this alloy system.

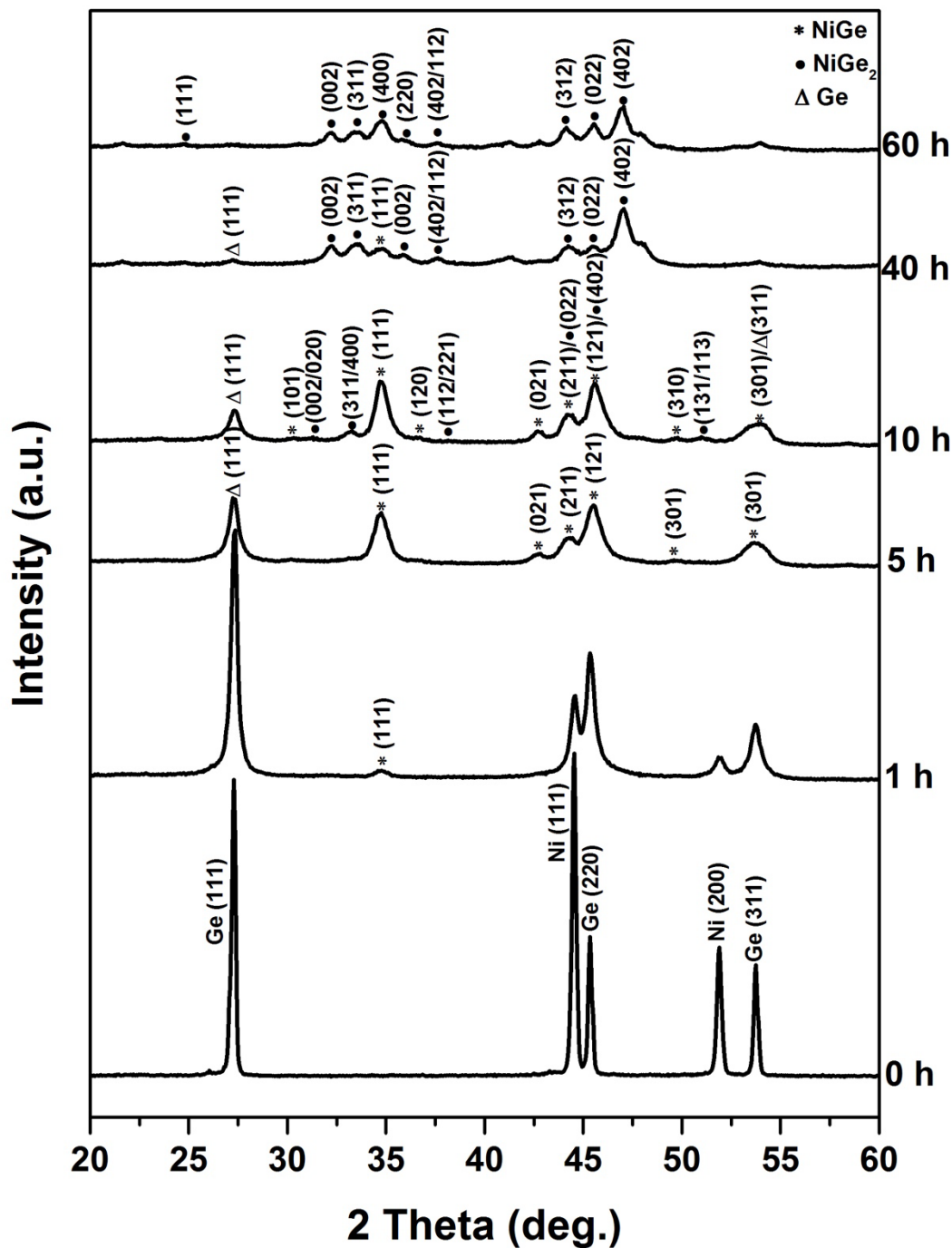


Figure 3.2: XRD patterns of the Ni-67 at.% Ge powder blend milled for different times. While the Ni and Ge peaks are clearly seen in the unmilled powder (0 h), formation of a solid solution started to occur on milling for 1 h. Simultaneously, the equilibrium NiGe intermetallic also started to form, and its amount increased with milling time. On milling the powder for 10 h, a

new phase, identified as the metastable NiGe_2 phase, started to form. An almost homogeneous NiGe_2 phase had formed on milling the powder for 60 h.

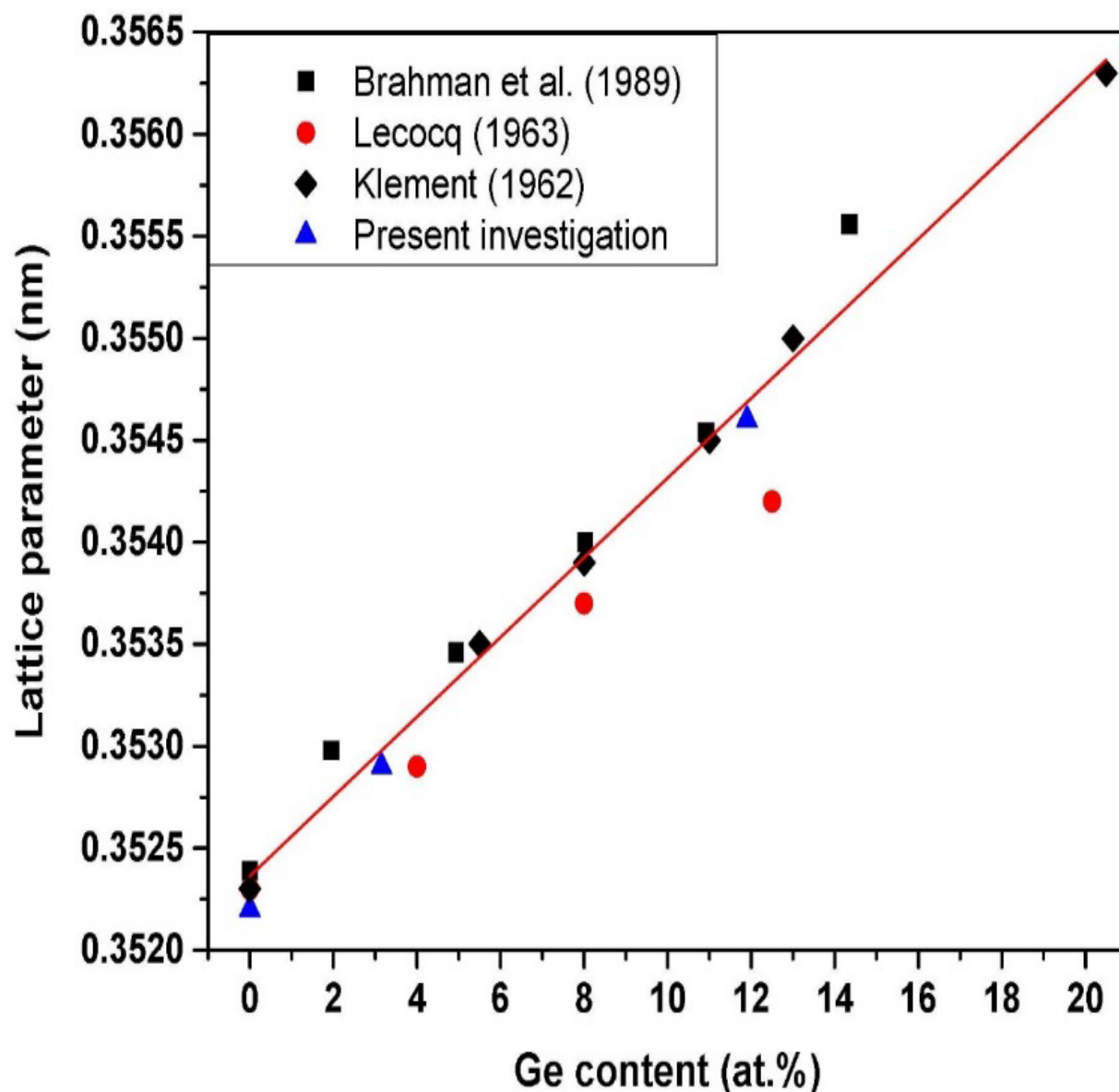


Figure 3.3: Variation of the lattice parameter of the Ni(Ge) solid solution with Ge content based on Ref. [44, 52-54].

The Ni peaks completely disappeared on milling the powder blend for 5 h, and at this stage we observe only peaks from the NiGe and Ge phases, noting that the amount of the NiGe phase increased with increasing milling time, as indicated by the increase in the number and intensity of the diffraction peaks. For example, the 111_{NiGe} peak became more intense with milling time, suggesting an increased amount of NiGe in the milled powder, and this continued up to 10 h of milling. Figure 3.4 shows an enlarged view of the XRD pattern of the powder milled for 10 h from which it is clear that the NiGe phase coexists with a small amount of Ge and a very small amount of NiGe₂. The NiGe phase has the orthorhombic crystal structure with the lattice parameters $a = 0.581$ nm, $b = 0.538$ nm, and $c = 0.343$ nm. Increasing the milling time up to 10 h led to the formation of another phase, identified as the metastable NiGe₂ phase (ICDD-PDF # 70-3928). Even at this stage, a small amount of unreacted Ge existed in the milled powder. On increasing the milling time to 40 h, the metastable NiGe₂ phase had formed through a reaction between the equilibrium NiGe phase and the unreacted Ge powder and the amount of this phase was higher at this time than it was at 10 h. Moreover, XRD patterns indicated that the NiGe₂ peaks became more prominent on milling for 60 h, as shown in Figure 3.5.

XRD patterns clearly indicate that the increase in the amount of the NiGe₂ intermetallic compound is associated with a sharp decrease in the Ge content with continued milling. This confirms that the NiGe₂ phase has formed as a result of the interaction between NiGe and Ge. However, there appears to be a difference in the lattice parameters of the NiGe₂ phase formed in the early stages of milling and at later stages. While the crystal structure at both the stages is orthorhombic, belonging to the space group *Cmca* (No. 64), the lattice parameters at the early stages of milling are $a = 1.0830$ nm, $b = 0.5763$ nm, and $c = 0.5762$ nm, similar to those reported

by Takizawa et al. [43]. On the other hand, the lattice parameters of the NiGe_2 phase obtained at the later stages of milling are $a = 1.0303$ nm, $b = 0.5829$ nm, and $c = 0.5402$ nm. The reasons for this difference are not clear, but could be caused by the heavy deformation experienced by the powder particles.

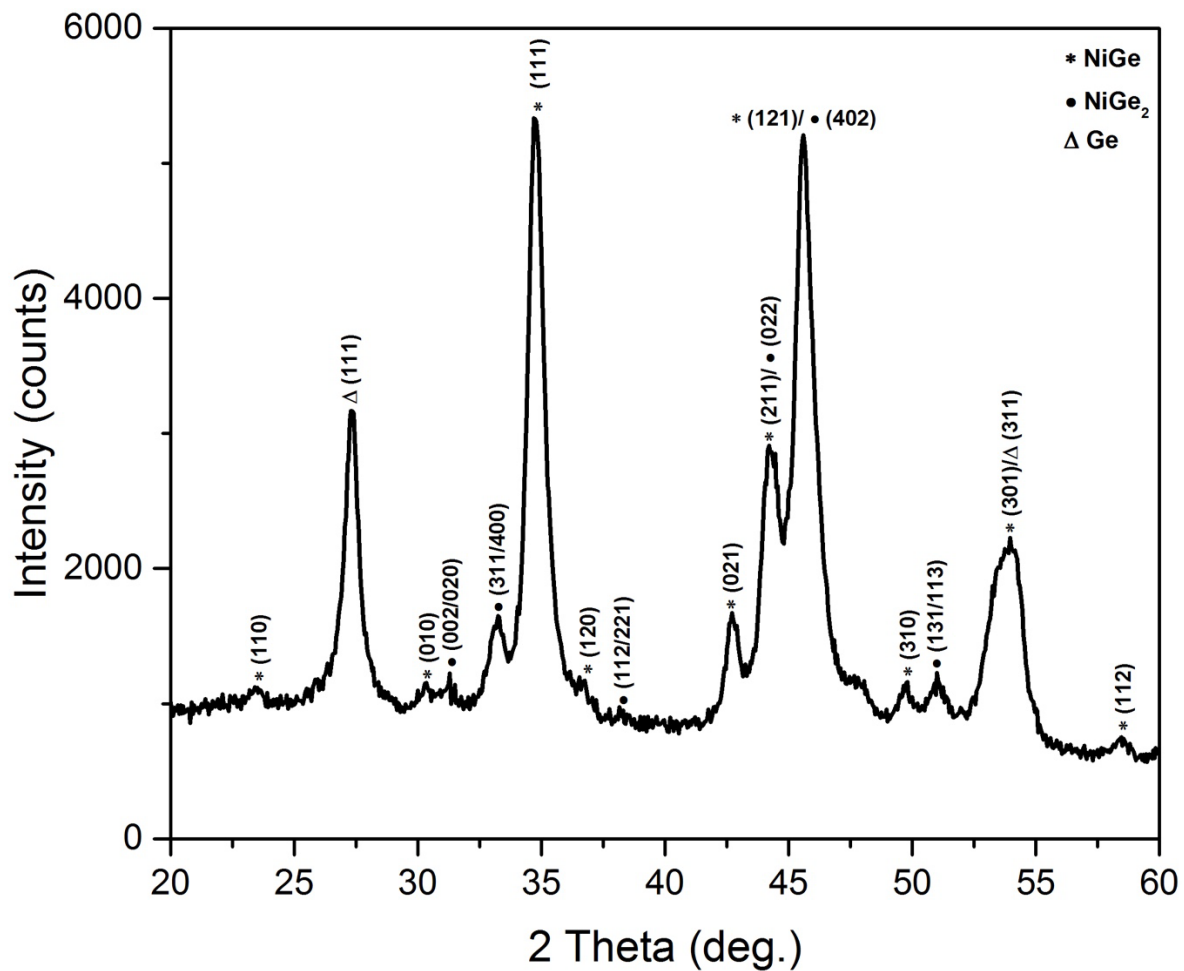


Figure 3.4: XRD pattern of the Ni-67 at.% Ge powder blend milled for 10 h showing formation of the equilibrium NiGe intermetallic phase. Note that a small amount of Ge, and even a smaller amount of NiGe_2 , are also present in the powder at this stage.

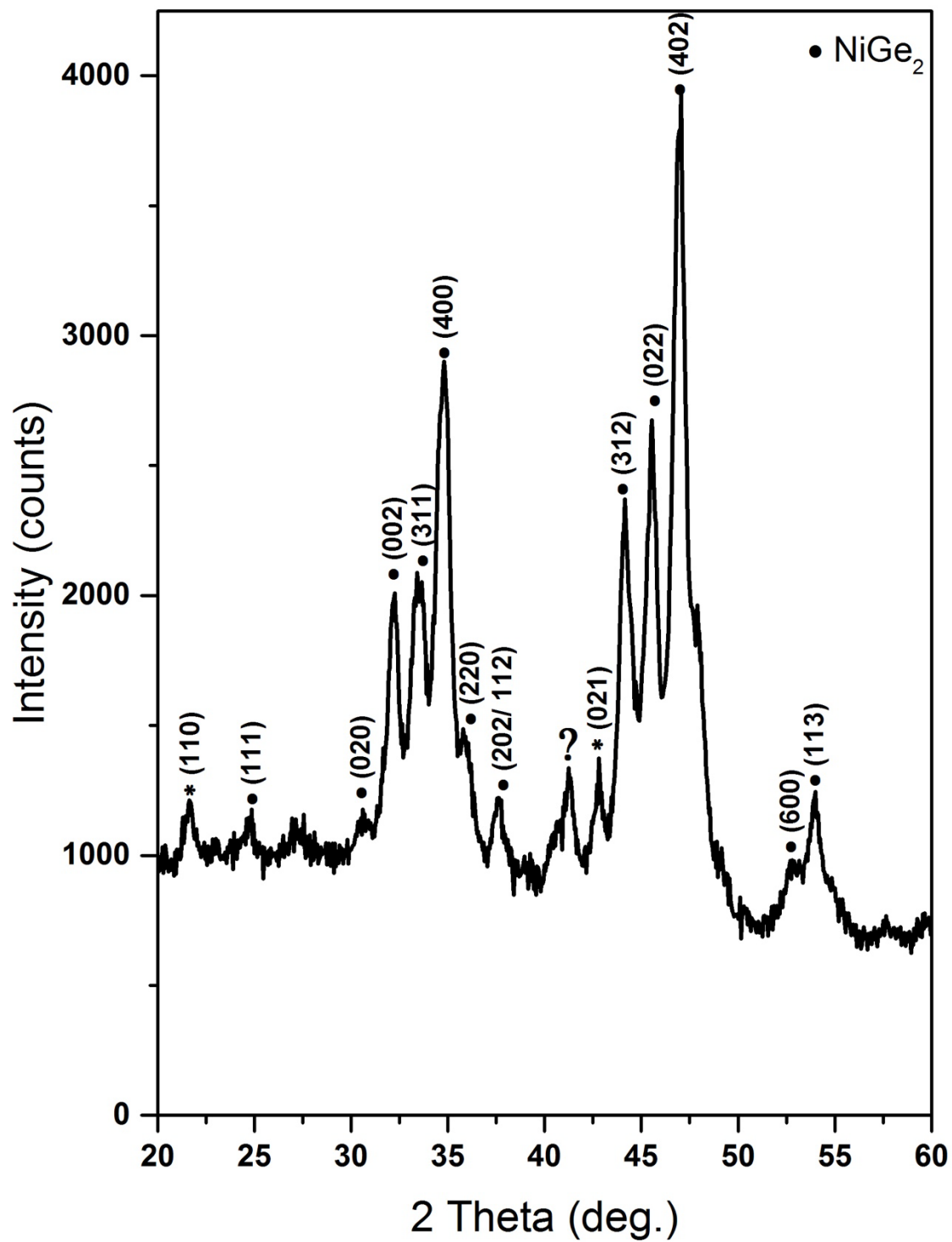


Figure 3.5: XRD pattern of the Ni-67 at.% Ge powder blend milled for 60 h showing an almost homogeneous formation of the metastable NiGe_2 phase.

An interesting observation that was made during milling of the powder blend was the reversibility of the NiGe phase formation. Figure 3.6 shows the XRD patterns of the powders milled for 60, 65, and 75 h. While the powder milled for 60 h contained essentially the NiGe₂ phase, the powder milled for 65 h and beyond contained both the NiGe₂ and NiGe phases. That is, the amount of the NiGe phase started increasing with milling time with a concomitant decrease in the amount of the NiGe₂ phase. This trend continued on milling the powder up to 75 h, when the amount of the NiGe phase is substantially higher than at 65 h of milling and this occurred at the expense of the NiGe₂ phase. Thus, it appears that there is a reversal in the formation of the NiGe phase suggesting that NiGe starts to transform to the NiGe₂ phase and then reverts back to the NiGe phase.

The reversibility of the transformation becomes clear from Table 3.2 where the diffraction peak positions and their intensities from the XRD patterns of powders milled for 10, 60, 65, and 75 h are presented. The intensities have been calculated using the JADE-7 software available with the XRD machine. For example, it may be noted that the intensities of some of the diffraction peaks from the NiGe phase are reasonably strong at 10 h of milling. These intensities then decrease up to 60 h of milling, and on subsequent milling their intensities again increase.

This trend may be particularly noted for 111, 021, 310, 301, and 112 peaks. Similarly, the intensities of the diffraction peaks from the NiGe₂ phase are noted to continuously decrease from 60 to 75 h of milling. For example, the 420 peak which has a relative intensity of 100 at 60 h, has an intensity of only 26.7 at 65 h, and 7.4 at 75 h of milling. Similarly, the 002 peak which has a relative intensity of 29.9 at 60 h became weak with a relative intensity of 8.3 at 65 h and 5.7 at 75 h of milling. Further, the relatively weak reflections such as 112 and 313 observed at 60 h have

completely disappeared at 75 h of milling. These trends clearly show that reversibility of the phase transformations is actually occurring.

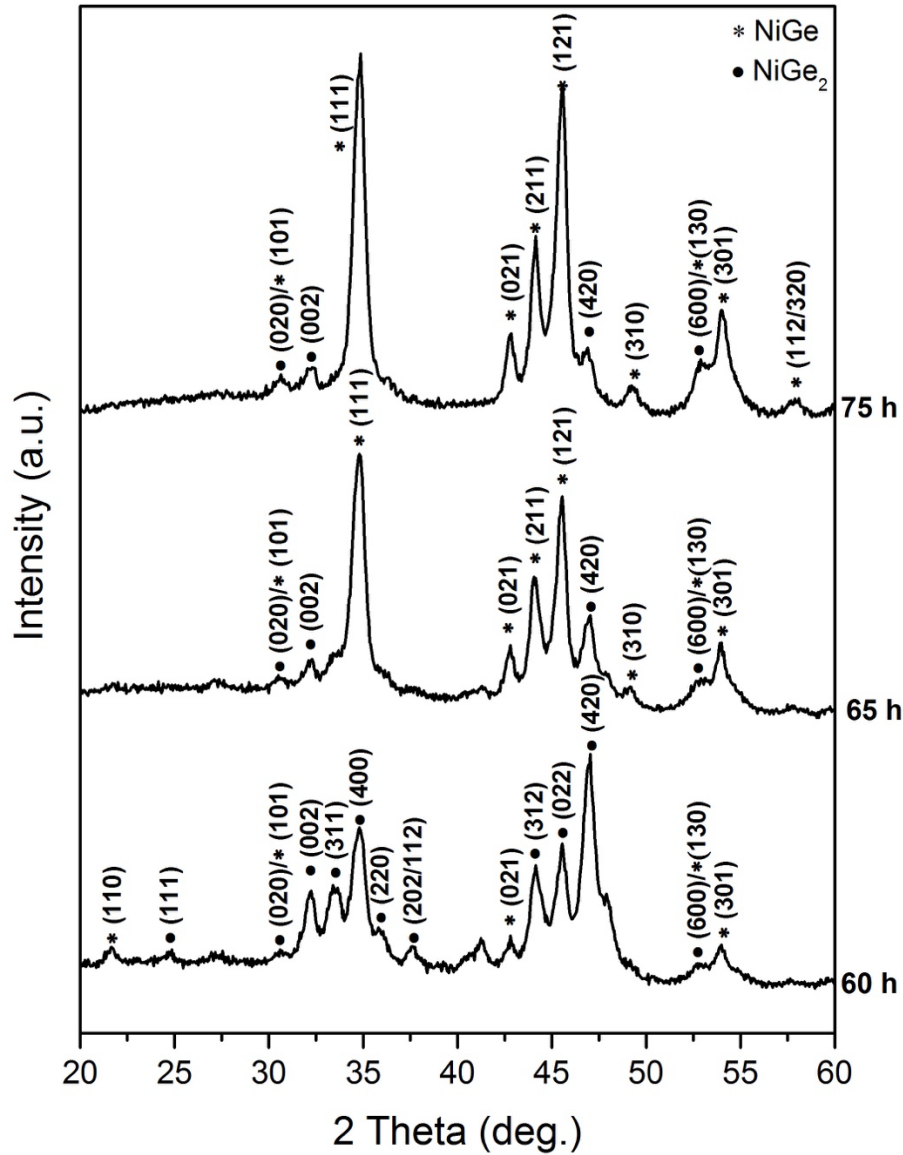


Figure 3.6: XRD patterns showing the reversibility of the formation of NiGe on milling the powders. Whereas an almost homogeneous NiGe₂ phase was found to form on milling the powder blend for 60 h, continued milling to 65 h showed the re-formation of the NiGe phase. The amount of the NiGe phase continued to increase on milling to 75 h at the expense of the metastable NiGe₂ phase.

Table 3.2: Peak positions and their intensities of milled Ni-66.7 at.% Ge powder blend at milling times of 10, 60, 65, and 75 h.

Peak No.	Milling Time																
	10 h					60 h				65 h				75 h			
	2 θ (°)	I%	hkl			2 θ (°)	I%	hkl		2 θ (°)	I%	hkl		2 θ (°)	I%	hkl	
			Ge	NiGe	NiGe ₂			NiGe	NiGe ₂			NiGe	NiGe ₂			NiGe	NiGe ₂
1						21.655	10	110									
2	23.412	3			111	24.843	7.5		111								
3	27.304	50.2	111														
4	30.335	2.9		101		30.609	5	101	020	30.493	3	101	020	30.639	4.9	101	020
5	31.277	4.6			002/020	32.244	29.9		002	32.286	8.3		002	32.303	5.7		002
6	33.246	9.7		020	400/311	33.399	23.4	020	311								
7	34.703	100		111	021	34.800	60.3	111	400	34.8	100	111	400	34.849	100	111	400
8						35.828	5.5		220								
9	36.742	2.9		120													
10	38.172	2.5			112/221	37.605	10.4		202/112								
11						41.255	14.5	unidentified		41.297	3.6	unidentified					
12	42.697	13.3		021		42.799	13.9	021		42.793	18.3	021		42.837	16	021	
13	44.202	25.2		211	022	44.148	45	211	312	44.052	40.2	211	312	44.147	34.8	211	312
14	45.600	81.7	220	121	402/420	45.549	46.8	121	022	45.052	76.6	121	022	45.551	79.8	121	022
15						47.044	100		420	47.044	26.7		420	46.899	7.4		420
16	49.783	5.5		310						49.151	5	310		49.2	7	310	
17	50.969	7.1			113/131												
18						52.795	4.5	130	600	53.185	3.5	130	600	52.892	5.8	130	600
19	54.049	24.7	311	301		53.995	15.3	301	113	53.995	21.7	301	113	54.002	21	301	113
20	58.45	3.4		112/320	132					57.763	3.2	112/320		58.090	4.4	112/320	
21						59.643	4.8	131	313								

3.2.2 Scanning Electron Microscopy (SEM)

Figure 3.7 (a) shows the SEM image of the as-blended Ni-Ge powder mixture. It can be seen from the image that the pure Ni particles are roughly spheroidal in shape and that the average particle size is around 6 μm whereas Ge particles have thin plate-like or massive structures with an average size of about 80 μm .

Figure 3.7 (b) shows the micrograph of the Ni-67 at.% Ge powder mixture milled for 5 h. Due to agglomeration in the early stages of milling, the morphology and distribution of the powder particles is inhomogeneous showing both large and small sizes of particles distributed non-uniformly. XRD results (Figure 3.2) have also confirmed that the NiGe phase has formed at this stage of milling. Additionally, it may be noted that some free Ge is present in the powder at this time of milling. The morphology of the powders has changed to be more homogeneous on milling the powder for 60 h (Figure 3.7 (c)). The powder particle size is also fine and very little agglomeration is noted at this stage.

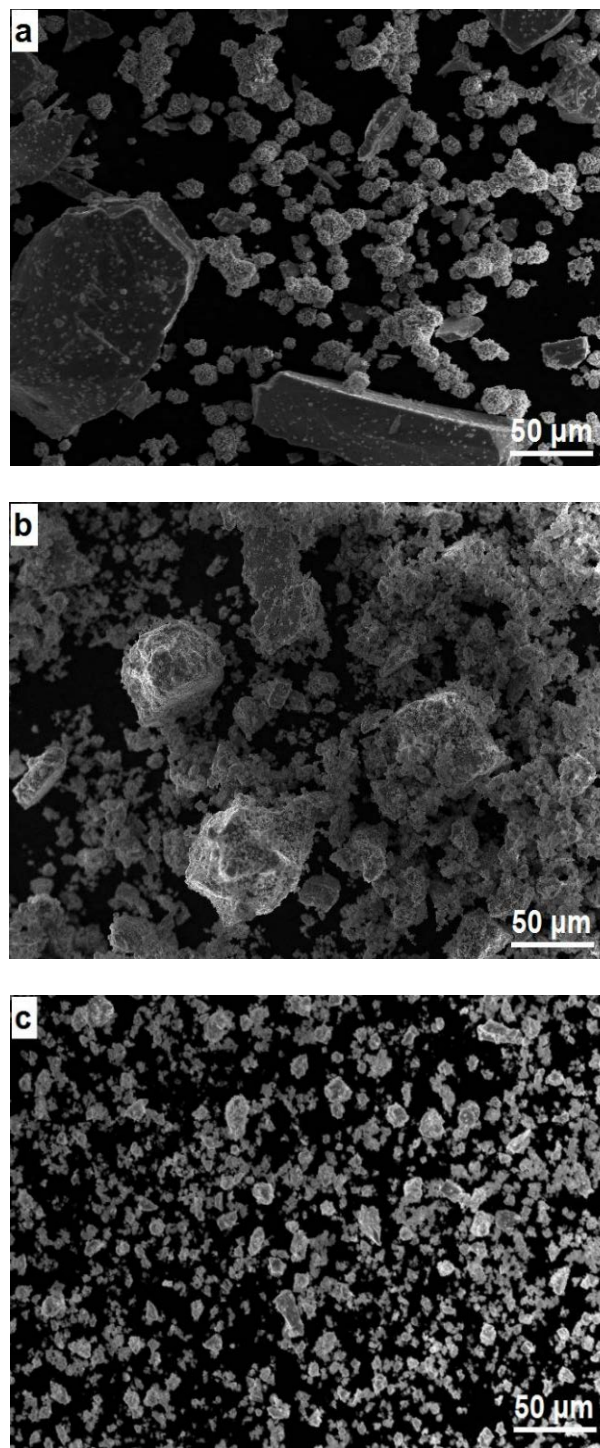


Figure 3.7: Scanning electron micrographs of the powder blend in the (a) as-blended (unmilled) condition showing elemental Ni and Ge powder particles, (b) formation of the NiGe phase at 5 h, and (c) after milling for 60 h, when an almost homogeneous NiGe₂ phase had formed. Chemical analysis of the particles through EDS confirms these observations.

The fact that structural changes are occurring in the milled powder was also confirmed through SEM studies. Figure 3.8 shows the backscattered and secondary-electron images of the Ni-67 at.% Ge powder milled for 5 h. The secondary electron micrograph (Figure 3.8(a)) shows the general morphology of one large powder particle and it may be noted that there appears to be some internal structure. However, on observing the backscattered micrograph (Figure 3.8(b)), which shows the atomic number contrast, it becomes clear that interdiffusion between Ni and Ge has taken place and that structural changes have occurred, resulting in the formation of the NiGe intermetallic. In the backscattered images, the phase with a higher average atomic number appears brighter and the one with a lower atomic number appears darker. Accordingly, the heavier phase Ge appears brighter and the lighter phase NiGe appears darker as shown in Figure 3.8(b).

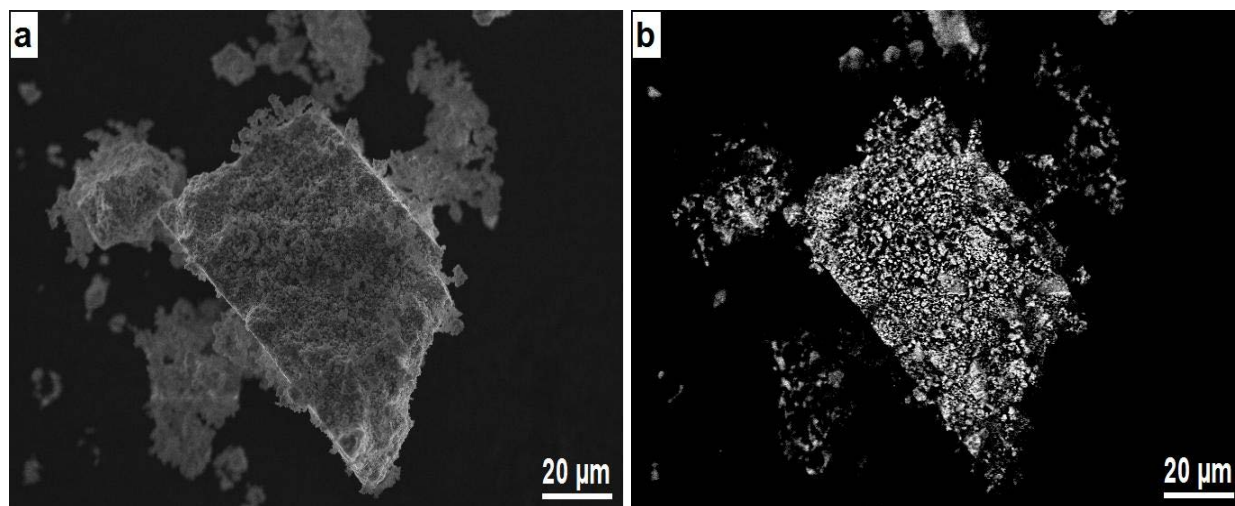


Figure 3.8: Secondary-electron and back-scattered images of the Ni-67 at.% Ge powder blend milled for 5 h. While the secondary-electron image (a) shows the general morphology of the large powder particle, the back-scattered image (b), shows the atomic number contrast where the heavier metal (Ge) appears brighter and the lighter metal (Ni) dark. Because of a reasonably uniform distribution of the dark and bright areas, (b) clearly confirms that alloying has occurred between Ni and Ge.

3.2.3 Energy Dispersive Spectroscopy (EDS)

Figure 3.9(a) and (b) show the EDS analyses of the as-blended Ni-Ge powder mixture. EDS analysis of the particles clearly confirms that the spheroidal particles are Ni and that the plate-like or massive particles are Ge. Furthermore, Figure 3.9(c) and (d) show that the chemical composition is different in different regions of the Ni-67 at.% Ge powder mixture milled for 5 h. In some regions of the powder, the Ge content in the powder is about 49.01 ± 0.88 at. %, which is the value expected for the equilibrium NiGe phase.

The powder milled for 60 h showed that the powder particles now have about 66.95 ± 0.63 at. % Ge (Figure 3.9(e) and (f)). This composition is what is expected for the NiGe₂ phase, which was also seen to form at this time of milling, interpreted from the XRD patterns (Figure 3.5). Further, it was noted that the powder contained about 6.6 ± 0.28 at. % Fe, which is incorporated into the milled powder, due to the wear and tear of the steel grinding balls and the milling vial at long milling times. Another point of interest is that no free Ge is present in the powders at this stage of milling.

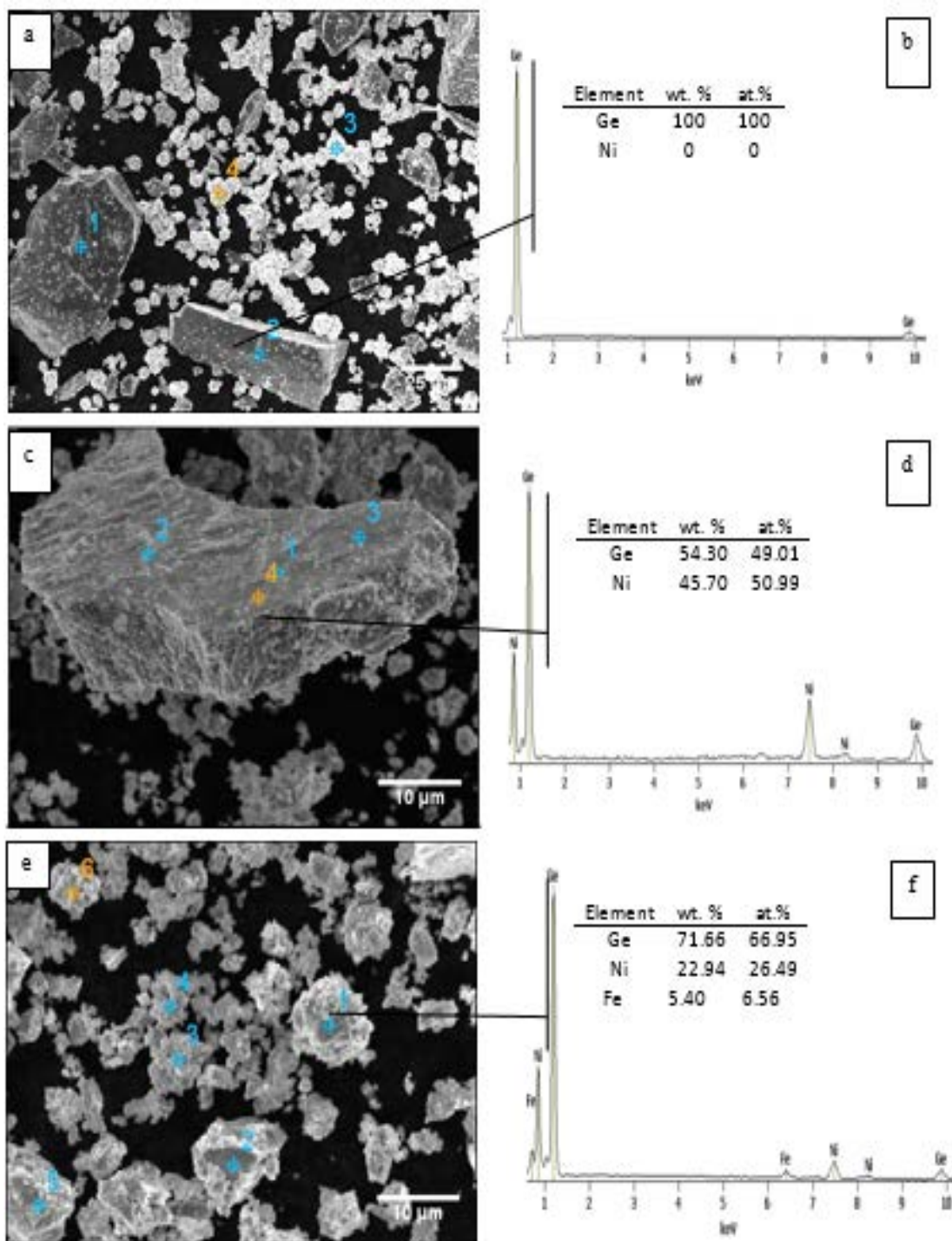


Figure 3.9: SEM images and EDS spectra of the Ni-67 at.% Ge powder blend milled for (a and b) 0 h, (c and d) 5 h and (e and f) 60 h. Whereas Ni and Ge are present in the unmilled powder (0 h), the powder contains predominantly the equilibrium NiGe phase on milling the powder for 5 h, and the metastable NiGe₂ phase on milling for 60 h.

3.3 Discussion

3.3.1 Phase Formation

As shown in Figures 3.2 and 3.4, the sequence of structural evolution in the Ni-67 at.% Ge milled powder was that alloying occurred between Ni and Ge resulting in the formation of an Ni(Ge) solid solution in the early stages of milling, followed by the formation of the equilibrium NiGe intermetallic and eventually the metastable NiGe₂ phase. This NiGe₂ phase reverted to the equilibrium NiGe phase on continued milling. According to the equilibrium phase diagram, one would have expected to observe the NiGe and Ge phases at this composition if alloying occurred between the blended elemental Ni and Ge powders, since both of them are the equilibrium phases. However, according to the present result, we ended up with the formation of the Ni(Ge) solid solution and the NiGe intermetallic phase before eventually forming the metastable NiGe₂ phase and then the NiGe phase again.

As is well known, MA is a high-energy ball milling process involving repeated cold welding, fracturing, and rewelding of powder particles. A variety of stable and metastable solid solutions, intermetallic phases, and amorphous alloys have been synthesized using this technique in a number of alloy systems [5, 6]. Mechanisms for the formation of alloy phases have been described earlier in the literature [5, 6]. In brief, due to the intense plastic deformation experienced by the powder particles, the powder particles store lot of energy. This could be in terms of a variety of crystalline defects including dislocations, grain boundaries, stacking faults, vacancies, etc, which induce lot of lattice strain. Additionally, due to the processes of cold working and recovery, grain refinement occurs leading to the formation of very fine grains, often with nanometer dimensions. Further, a slight rise in temperature also occurs. All these effects put together –

increased defect concentration and consequent lattice strain, small grain sizes, and a slight rise in temperature – significantly increase the diffusivity of solute elements into the solvent lattice and hence alloying occurs. Therefore, it is only natural to expect formation of solid solutions. However, since the two constituent elements, Ni and Ge, do not satisfy the Hume-Rothery rules for complete solid solution formation, there was only a limited solid solubility of Ge in Ni, and formation of other intermetallic phases.

3.3.2 Solid Solution Formation

The equilibrium solid solubility of Ge in Ni was reported to be 13 at.% at 800 °C and 16 at.% at 1124 °C, the eutectic temperature [38]. The solid solubility at room temperature is reported to be less than about 10 at.%. During MA, it was noted that the lattice parameter of Ni increased with milling time. This trend can be easily rationalized if we consider the equilibrium between the solid solution and the neighboring intermetallic phase. From the known variation of lattice parameter of the Ni(Ge) solid solution with Ge content [44, 52-54], it is estimated that the maximum Ge content in the Ni solid solution increased to about 12 at.% on milling the powder for about 5 h, suggesting that an equilibrium is established between the Ni(Ge) solid solution and the NiGe intermetallic that has formed. It is important to realize that NiGe is not the equilibrium intermetallic to coexist with the Ni(Ge) solid solution according to the binary Ni-Ge phase diagram, but NiGe was the only intermetallic that had formed during milling.

Different investigators have reported different extents of solid solution formation in mechanically alloyed Ni–Ge powder blends. These results varied from about 12 at.% Ge in the present investigation to 20 to 26 at.% Ge [44-46]. Rapid solidification studies have shown [5] that

the maximum solid solubility is limited by the high-temperature solubility limit, which is 16 at.% Ge at the eutectic temperature of 1124 °C. It is also known in mechanically alloyed systems [5, 6] that the maximum solid solubility extension achieved is related to the thermodynamic equilibrium between the solid solution and the neighboring intermetallic compound, which is Ni₃Ge in the present case. Therefore, the maximum possible limit is expected to be 25 at.% Ge, which is close to the values reported in the literature. However, the solid solubility limits also depend on the energy input into the powders during milling and this could be the reason for the different solubility limits reported in the literature.

3.3.3 *Formation of Intermetallics*

As mentioned earlier, two intermetallics, viz., NiGe and NiGe₂, had formed on mechanically alloying the Ni-67 at.% Ge powder blend. It is clear from Figure 3.2, that the NiGe phase had started to form as early as 1 h of milling, but an appreciable amount of the phase had formed on milling the powder for 5 h. Since the starting powder had 67 at.% Ge, the milled powder contained a mixture of the NiGe phase and some free Ge, according to the reaction:



It is known that in the early stages of milling a mixture of ductile-brittle components such as in the Ni-Ge system, the ductile Ni powder particles get flattened to platelet/pancake shaped cold welds by the ball-powder-ball collisions. On the other hand, the brittle Ge powder particles get fragmented and get occluded into these cold welds and form the Ni-Ge composite. Because of the severe plastic deformation experienced by the powder particles, the spacing between the cold welds decreases and the increased defect concentration enhances the diffusivity via short circuit

paths. This results in alloy formation. However, since intermetallics have a much lower free energy than the solid solution phases, the equilibrium NiGe intermetallic phase has formed at this stage. It is also reported that in several alloy systems, an intermetallic phase forms first during MA, even if a solid solution is the most stable phase at that composition [46, 55].

Since the starting powder contained 67 at.% Ge, it is natural to expect formation of the stoichiometric NiGe₂ phase in the milled powder according to the reaction:



But, the equilibrium phase diagram did not exhibit the presence of this phase; it occurs only under metastable conditions. Earlier investigators had synthesized this phase on subjecting the powder mixture to a high pressure of 5.5 GPa and a high temperature of 700 °C [43]. Therefore, it may appear unusual that this high-pressure and high-temperature metastable phase has formed in the as-milled powder.

Formation of metastable phases, including intermetallics, is of common occurrence in mechanically alloyed powders [5, 6]. The intermetallics synthesized by MA include those that exist under equilibrium conditions and those that are metastable such as quasicrystalline phases, high-temperature phases, and high-pressure phases. The NiGe₂ phase synthesized in this study is known to be a high-pressure and high-temperature phase.

As mentioned earlier, there is some rise in temperature in the milled powder. Reports on the maximum temperature reached during milling (either by estimation or interpretation based on experimental microstructural observations) differ significantly from a few degrees to a few hundred degrees. But, it is fairly well accepted now that the maximum temperature reached in the milled powder is only about 200 °C, even though it may reach a much higher temperature in a

highly localized region. It has also been recognized that the energy supplied during MA can be considered as equivalent to an increase in temperature [5]. Consequently, continuous milling of the powder may be considered as subjecting the powder to high temperatures. Since the synthesis of NiGe₂ requires a temperature of about 700 °C under pressure, it is unlikely that the modest temperature rise reached during MA alone is responsible for the formation of the NiGe₂ intermetallic phase in the mechanically alloyed powder mixture.

Normally, both high temperatures and high pressures are required for the formation of the NiGe₂ phase. During milling, the powder particles are also subjected to high pressures since they experience very high collision pressures from the grinding balls. It has been suggested that these high pressures could reach about 6 GPa [13, 56], which are high enough for the formation of the NiGe₂ phase, if sufficiently high temperatures are also simultaneously present.

As mentioned above, during milling, the individual powder particles get refined and get intimately mixed together to form a homogeneous mixture. Because of the presence of short circuit diffusion paths such as a large number of grain boundaries in the fine-grained material and increased defect density, diffusion takes place rapidly. As a result, a number of chemical reactions, that normally require high temperatures, occur at relatively lower temperatures, if not at room temperature. In the present system, it is possible that the combination of a homogeneous distribution of the fine constituent powders, high pressures, and modest temperatures is highly conducive to the formation of the metastable NiGe₂ phase in the as-milled condition.

The crystal structure of the metastable NiGe₂ phase has been reported differently by different authors. Ly et al. [51] reported the crystal structure to be cubic based on their grazing incidence XRD studies on alternately deposited Ni and Ge layers. All the others, based on either

XRD or electron diffraction studies reported the crystal structure to be orthorhombic [35, 43]. Based on a detailed analysis of the XRD data on samples subjected to high pressures and high temperatures, Takizawa et al. [43] determined the crystal structure to be orthorhombic. They had also determined the space group, atomic environments, and the interatomic distances between Ni and Ge and the bond angles in the NiGe₂ structure. Our results are in conformity with those of Takizawa et al. [43], even though the lattice parameters are slightly different, possibly due to the heavy plastic deformation experienced by the powders.

Formation of the NiGe₂ phase from a mixture of the NiGe and Ge phases is not possible at room temperature and atmospheric pressure due to the higher free energy of the NiGe₂ phase. That is:

$$\Delta G_{\text{NiGe}} + \Delta G_{\text{Ge}} < \Delta G_{\text{NiGe}_2} \quad (3.3)$$

However, the relative thermodynamic stabilities of the phases could be different at different temperatures and pressures. Also, in thin film or powder conditions, the system is under non-equilibrium conditions and therefore NiGe₂ can be made stable. For example, in the present situation, due to the severe plastic deformation of the metal powders, additional interfacial energy (due to creation of fresh surfaces, grain boundaries, stacking faults, etc.) and strain energy terms are introduced and therefore, the free energy in this condition could be:

$$\Delta G_{\text{NiGe}} + \Delta G_{\text{Ge}} + \Delta G_{\text{interfaces}} + \Delta G_{\text{strain}} > \Delta G_{\text{NiGe}_2} \quad (3.4)$$

Since the free energy of the NiGe₂ phase is now lower than the phase mixture of NiGe + Ge and the additional factors, the NiGe₂ phase becomes stable.

It may appear strange that the final phase to form on mechanically alloying the powders is a metastable NiGe₂ phase formed after the formation of the equilibrium NiGe phase. But, as

explained above the combination of fine grain sizes, high pressures and a slight rise in temperature is responsible for this observation. It is possible that this metastable phase will transform to the equilibrium phase constitution on annealing the milled powder. It may also be noted that this metastable NiGe₂ phase starts reverting back to the equilibrium NiGe phase on continued milling.

The additional energy input into the system allows the metastable phases, which are otherwise unstable, to be stabilized at room temperature and at atmospheric pressure. It is also possible that the enthalpy of formation for the NiGe₂ phase is not high and that is why under the non-equilibrium conditions of MA, this phase had formed. The formation of a very large number of metastable phases has been reported in the literature on MA, including amorphous alloys [6, 55, 57]. It is also repeatedly noted that even if the final phase obtained is a solid solution, the system forms intermediate phases in the early stages of milling [55, 58]. The reason for the formation of the intermediate phases is their lower energy (higher thermodynamic stability) in relation to the solid solution phases.

3.3.4 *Reversible Transformation*

Let us understand why the equilibrium NiGe phase transformed to the metastable NiGe₂ phase and then reverted back to the stable NiGe phase.

The introduction of a variety of crystalline defects (plus disorder and nonstoichiometry) raises the free energy of the system above that of the equilibrium phase and so the metastable phase gets stabilized. A metastable phase can transform to the equilibrium phase by releasing the additional energy that is stored in it. This is possible, for example, by increasing the temperature, which provides the needed thermal activation energy for the transformation.

There have been some examples in the MA literature where a metastable phase transformed to the equilibrium phase on continued milling. For example, amorphous phases formed either by rapid solidification processing [59] or by MA [60, 61] have been shown to crystallize on milling the powder mixture, a phenomenon referred to as “mechanical crystallization”. This has been reported mostly in Fe-based alloys. Reversible amorphous–crystalline–amorphous transformations have also been reported in some Co-Ti alloy compositions [62-64]. Even though the observation in the present investigation is not about crystallization of an amorphous alloy, but transformation from a metastable to a stable state, the transformation is similar because a metastable crystalline phase is transforming to the equilibrium crystalline phase just like a glass (metastable) is transforming into a crystalline (equilibrium) phase.

Transformation of a metastable crystalline phase to an equilibrium phase can involve transformation from (a) a high-temperature phase to a low-temperature phase or (b) a high-pressure phase to a low-pressure phase. The literature has many such examples [5, 6]. But, in the present case, we are dealing with a situation when a high-pressure and high-temperature phase is transforming to a stable phase, just by mechanical milling. A transformation of the above type requires that the pressure is released from the high-pressure phase and that the necessary thermal energy is provided to transform the high-temperature phase to the low-temperature phase.

Several reasons are possible for the transformation of a metastable phase to an equilibrium phase. Firstly, the equilibrium phase has a lower free energy than the metastable phase and therefore, the equilibrium phase is more stable. However, this transformation requires activation energy to be supplied, and consequently, the transformations take place only at elevated temperatures. But, in the present case, the transformation is taking place at near-room temperature.

During MA, the powder particles get fragmented and become smaller and smaller until the steady state condition is reached when the particle size remains virtually constant. Because fresh surfaces are constantly created during milling, the pressure experienced by the powder during milling could be released, resulting in the formation of the equilibrium phase.

But, a more interesting observation made in this investigation is the reversibility of the NiGe phase. As shown in Figure 3.6, milling up to 60 h resulted in the formation of the metastable NiGe₂ phase, and on further milling, the NiGe₂ phase transformed back to the NiGe phase. Such a transformation is possible when we realize that NiGe₂ is a metastable phase. Since this is a high temperature, high-pressure phase, it is also possible that the “stability” of this metastable phase at room temperature and at atmospheric pressure is not very high. Therefore, the phase transforms to the more stable equilibrium NiGe phase. A transformation from the metastable to stable phase requires provision of sufficient activation energy in terms of either pressure or temperature.

However, another and more plausible explanation is that the powder experiences high temperatures during milling because of the severity of deformation. But, in the present investigation, MA was conducted at room temperature and therefore it is not possible that the powder has experienced a high temperature. In fact, it has been clearly shown that the maximum temperature experienced by powders during MA is not more than about 200 °C [5, 6], a temperature too low for the transformation to occur in the present investigation. It has been suggested earlier [5] that the energy supplied during MA can be considered as equivalent to an increase in temperature. Consequently, continued milling of the powder may be considered as subjecting it to high temperatures and this could be the reason why the metastable NiGe₂ phase transformed to the NiGe phase. It is also possible that the activation energy for the transformation

from NiGe₂ to NiGe is not very high and therefore it has been relatively easy to go from the metastable to the equilibrium state.

As a final note, it should be realized that, under equilibrium conditions, the constitution of the Ni–66.7 at.% Ge powder should be a mixture of the NiGe and Ge phases. However, on milling the powder for 75 h, we have observed a mixture of the NiGe₂ and NiGe phases and the presence of Ge was not noted. This suggests that the transformation from the metastable NiGe₂ phase to stable phases has just started, but not completed. Accordingly, we observe only the NiGe phase but not Ge. Longer milling and/or high-temperature annealing of the milled powder will lead to complete equilibration.

3.3.5 *Microstructural Changes*

Figure 3.10 represents a schematic of the microstructural changes that take place during MA. During milling, the repeated collisions that occur between the powder particles and the grinding balls and the grinding vial result in severe plastic deformation of the powder particles. If the metal powders involved are soft, they get elongated and, due to convolution effects, lamellar structures consisting of alternate layers of the constituent metals are formed. On the other hand, brittle and hard particles get fragmented into smaller particles (Figure 3.10 (a)).

In the present case, however, Ge is relatively harder (and brittle), and therefore, it will not be possible to have a lamellar structure forming alternate layers of Ni and Ge. Instead, the hard Ge particles get dispersed along the lamellar boundaries of the soft Ni phase and/or get impregnated into the softer powder particles (Figure 3.10 (b)). With continued milling, these lamellar structures of the softer metal with the hard metal particles along the interfaces get convoluted and the hard

particles get slowly distributed uniformly (Figure 3.10 (c)). Due to the continued milling beyond this stage, work hardening of the powder particles takes place and these get fragmented again into smaller particle sizes (Figure 3.10 (d)). Since fresh surfaces are created at this stage due to fragmentation, these are very reactive and therefore agglomeration of powder particles takes place leading to the formation of larger particles (Figure 3.10 (e)). These repeated fracturing and cold welding events during milling result in a particle size distribution such that there is a peak at an intermediate stage and in the final stages of milling, when steady-state conditions are obtained, very fine particles result (Figure 3.10 (f)). The SEM micrographs presented in Figure 3.8 confirm that the powder particle sizes follow the above trend.

During milling, the powder particles get refined, a high density of crystalline defects such as dislocations, vacancies, and grain boundaries are introduced, and simultaneously, there is also a slight increase in powder temperature. All these effects lead to increased diffusivity and consequently alloying occurs [5, 6]. Therefore, it is not surprising that intermediate phases have formed during MA from blended elemental Ni and Ge powders.

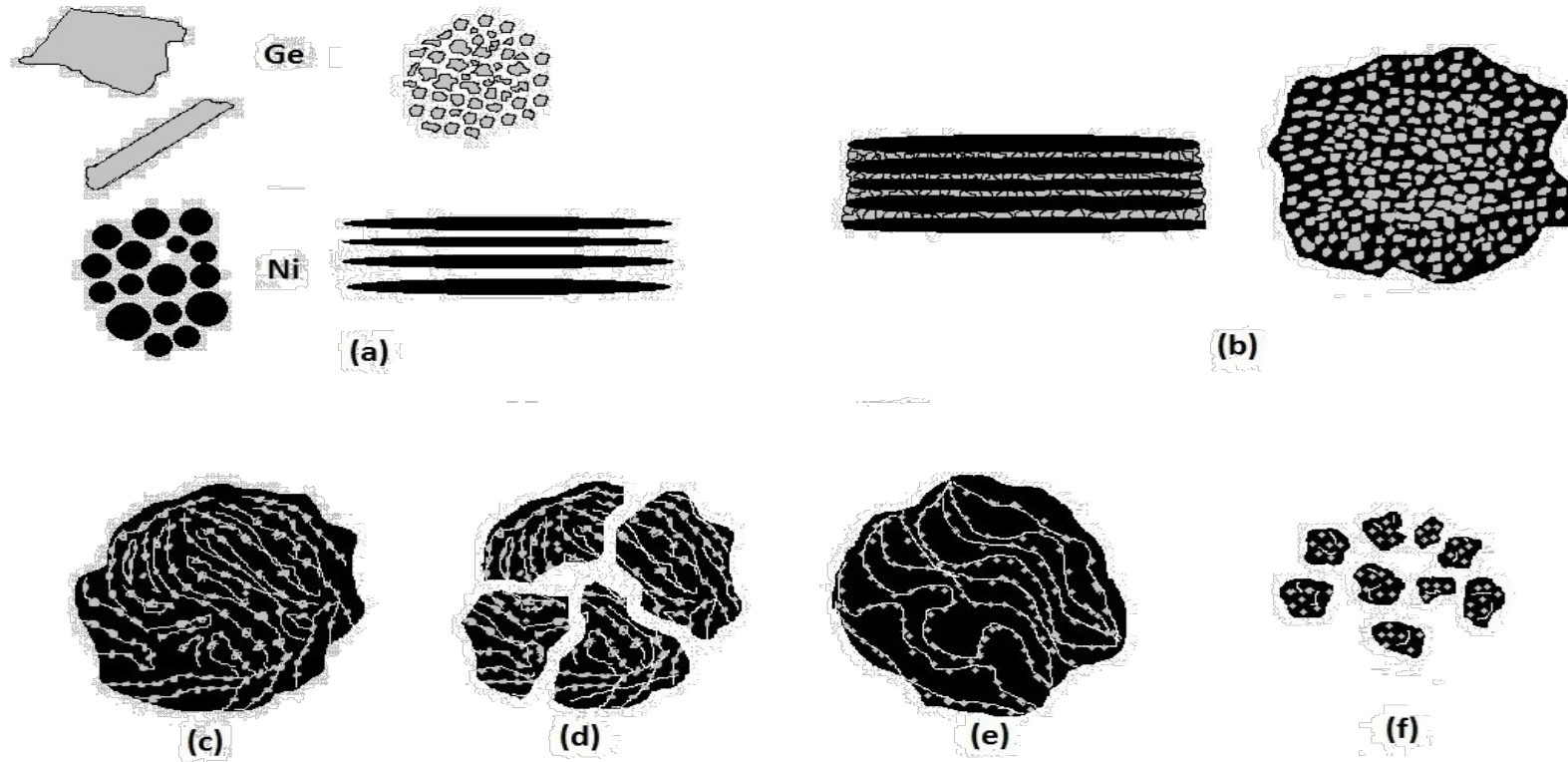


Figure 3.10: Schematic showing the structural evolution in the Ni-Ge powder blend on MA. (a) The soft Ni particles get plastically deformed and form lamellar structures, while the brittle Ge particles get fragmented on milling. (b) The brittle Ge particles get impregnated into the soft particle surfaces or along lamellar boundaries. (c) – (e) show that agglomeration, fracturing and rewelding of powder particles occur as milling continues. (f) The final stage of milling when fine alloy particles form with the same composition as the starting composition of the powder blend.

3.4 Conclusions

Mechanical alloying of Ni-67 at.% Ge powder mixture was conducted at room temperature. In the early stages of milling a supersaturated solid solution of Ge in Ni had formed followed by the formation of the NiGe intermetallic at 5 h of milling. A small amount of unreacted Ge was also present at this stage. The amount of the NiGe phase formed increased with increasing milling time. On continued milling, the NiGe intermetallic and remaining Ge reacted to form the NiGe₂ phase. This is a metastable phase normally present at a high temperature of 700 °C and a high pressure of 5.5 GPa. The factors that helped in the formation of the NiGe₂ phase at atmospheric pressure and under near-room temperature conditions are (i) a homogeneous mixture of the fine constituent phases with small dimensions, (ii) achievement of a reasonably high pressure during milling, and (iii) a modest temperature increase.

Most surprisingly, just by milling for a longer period of time, this metastable phase started to decompose to form the equilibrium NiGe phase, thus moving toward equilibrium. The possible reasons for the formation of the stable and metastable phases during milling, the process of equilibration, and the reversibility of the NiGe → NiGe₂ → NiGe transformations have been explained on the basis of the thermodynamic stabilities of the different phases and the microstructural features of the milled powders.

CHAPTER 4: SYNTHESIS OF NICKEL-SILICIDE PHASES BY MECHANICAL ALLOYING

4.1 Introduction

The important attributes of transition metal silicide alloys for commercial applications are their high melting points, high electrical conductivity, excellent oxidation and corrosion resistance, and low density. However, most of these silicide phases have narrow homogeneity ranges and high melting points, and therefore their synthesis by conventional methods of melting and casting is quite difficult.

The Ni-Si equilibrium phase diagram, shown in Figure 4.1, contains six intermediate phases under equilibrium conditions [65]. Details of the crystal structures of these phases are listed in Table 4.1 [39, 65]. The Si-rich part (≥ 50 at.% Si) of the equilibrium phase diagram exhibits a congruent melting phase NiSi at 50 at.% Si and the non-congruent melting phase NiSi₂ at 67 at.% Si. These Ni-silicides are currently being investigated extensively due to their high-temperature performance and applications in the microelectronics industry.

There have been some investigations on the synthesis of non-equilibrium phases using methods such as solid-state reaction between Ni and Si multilayers during annealing [66-72]. Further, some investigations have also been conducted on Ni-rich Ni-Si alloys through MA, mostly to produce Ni-rich Ni-Si solid solutions, intermetallics, and amorphous phases. Omuro and Miura [73] studied Ni-Si powder blends in the composition range of 24 to 50 at.% Si by milling them up to 200 h, and reported formation of equilibrium Ni₃₁Si₁₂ (γ) and Ni₂Si (δ) phases after milling for 10 h. These phases had subsequently transformed into an amorphous phase after continued milling

up to 200 h, except for the compositions Ni-24 at.% Si and Ni- 50 at.% Si. This observation suggests that the intermediate compositions corresponding to $\text{Ni}_{31}\text{Si}_{12}$ and Ni_2Si became amorphous after 200 h of milling. Formation of the equilibrium NiSi phase was not reported.

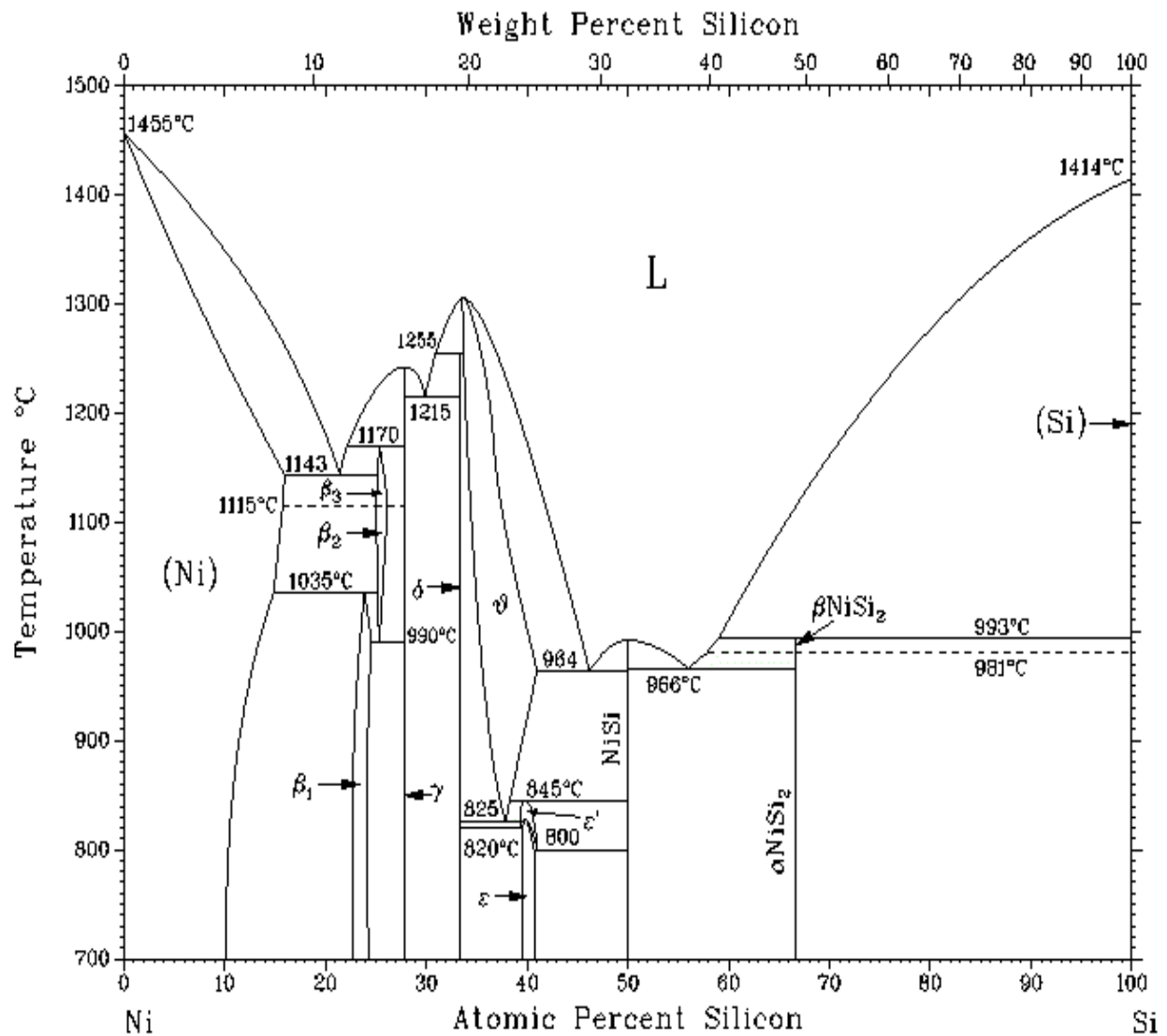


Figure 4.1: The Ni–Si equilibrium phase diagram [65] .

Table 4.1: Crystal structures and lattice parameters of equilibrium phases in the Ni-Si system [39, 65].

Phase	Crystal structure	Pearson symbol	Space group	Structure type	Lattice parameters			
					a (nm)	b (nm)	c (nm)	c/a
(Ni)	Cubic	<i>cF4</i>	<i>Fm$\bar{3}m$</i>	Cu	0.3523	-	-	-
β_1 -Ni ₃ Si	Cubic	<i>cP4</i>	<i>Pm$\bar{3}m$</i>	Cu ₃ Au	0.350	-	-	-
γ -Ni ₃₁ Ni ₁₂	Hexagonal	<i>hP14</i>	-	-	0.667	-	1.228	1.841
δ -Ni ₂ Si	Orthorhombic	<i>oP12</i>	-	Co ₂ Si	0.706	0.499	0.372	-
ε -Ni ₃ Si ₂	Orthorhombic	<i>oP80</i>	-	-	-	-	-	-
NiSi	Orthorhombic	<i>oP8</i>	<i>Pnma</i>	MnP	0.562	0.518	0.334	-
α -NiSi ₂	Cubic	<i>cF12</i>	<i>Fm$\bar{3}m$</i>	CaF ₂	0.5406	-	-	-
(Si)	Cubic	<i>cF8</i>	<i>Fd$\bar{3}m$</i>	C (diamond)	0.54306	-	-	-

Other researchers [74-82] investigated the effects of MA on the ordered L1₂-Ni₃Si by ball milling. They showed that milling of the ordered Ni₃Si compound resulted in its disordering leading to the formation of an fcc solid solution of Si in Ni on milling for 60 h.

Jang et al. [74] investigated Ni-Si powder blends with the nominal composition of 24 at.% Si. The authors reported formation of a homogeneous fcc solid solution of Si in Ni, as inferred by the absence of Si peaks in the XRD pattern. The ordered Ni₃Si phase with the L1₂ structure was obtained on annealing the powder milled for 24 h at 600 °C under vacuum.

Omuro and Miura [80] showed that the final milled powder exhibited the equilibrium Ni₂Si and Ni₃₁Si₁₂ phases for the elemental powder blend of Ni-30 at.% Si milled for 200 h. Datta et al. [81, 82] investigated MA of Ni-Si powder blends over a wide composition range in the Ni-Si

system (10 to 75 at.% Si). They reported that only congruent melting phases, viz., $\text{Ni}_{31}\text{Si}_{12}$, Ni_2Si , and NiSi formed during MA, while formation of the noncongruent melting phases, Ni_3Si , Ni_3Si_2 and NiSi_2 , did not occur. They did not observe formation of the NiSi_2 phase even when the Si content was as high as 75 at.%. These phases have, however, formed after the milled powders were annealed. The authors explained that the nanocrystallization reaction of the congruent melting phases, produced by MA, is quite similar to the eutectic or polymorphous nanocrystallization reaction from an amorphous phase. Consequently, the reaction favors formation of the congruent melting phases over noncongruent melting phases because of lower interfacial energy that plays a critical role in the stability of phases in the nanocrystalline state. They had also reported that the congruent melting phases, $\text{Ni}_{31}\text{Si}_{12}$ and NiSi became unstable and reacted with other phases available in the milled powder like $\text{Ni}(\text{Si})$ and Si , respectively, during annealing to form the equilibrium noncongruent melting phases Ni_3Si and NiSi_2 . It was also reported that grain growth in the noncongruent phases was faster than that in the congruent melting phases.

On the other hand, Iwamoto and Uesaka [83] showed that it is relatively easy to synthesize the silicide phases in the Ni-Si system when subjected to MA. They successfully synthesized the congruent and noncongruent melting phases such as Ni_3Si (25 at. % Si), Ni_2Si (33 at. % Si), NiSi (50 at. % Si) and NiSi_2 (67 at. % Si), after 30 h of MA.

In this work, we report on the successful synthesis of the equilibrium NiSi and NiSi_2 phases through high energy ball milling starting from a mixture of Ni and Si elemental powders with different Si compositions ranging from 60 to 80 at.% . We will demonstrate that it is possible to synthesize line compounds (such as NiSi and NiSi_2) using the non-equilibrium processing method of MA. The NiSi_2 phase has also been shown to exist over a slightly wider composition range,

unlike the equilibrium phase, which is a line compound. As a byproduct of milling, we were also able to obtain supersaturated solid solutions of Si in Ni, much beyond the equilibrium solubility levels.

4.2 Results

4.2.1 X-Ray Diffraction (XRD)

Figure 4.2 shows the X-ray diffraction (XRD) patterns of the Ni-60 at.% Si powder mixture after milling for different times. The XRD pattern of the unmilled powder blend (for 0 h of milling) indicates the presence of diffraction peaks of only pure crystalline Ni (ICDD-PDF # 4-0850) and Si (ICDD-PDF # 27-1402). The lattice parameters of Ni and Si calculated from the XRD patterns match very well with those listed in the literature.

After milling for 5 h, diffraction peaks corresponding to the starting elements (Ni and Si) were still observed, Figure 4.2. However, the peaks of both the elements were broadened and their intensities decreased, a result of the reduced crystallite size and increased lattice strain introduced into the powder during milling. Additionally, we can notice the presence of new diffraction peaks in the XRD pattern suggesting possible formation of a new phase. By comparing the peak positions and intensities of these new peaks with those of the possible phases, it could be concluded that the additional diffraction peaks correspond to the NiSi phase (ICDD-PDF # 70-2626).

On milling the powder blend for 10 h, the Ni peaks completely disappeared, suggesting that, at this stage of milling, the powder contained only peaks from the NiSi and Si phases. It may also be noted that the amount of the NiSi phase increased with increasing milling time, as indicated by the increase in the number and intensity of the diffraction peaks. For instance, the intensities of the

peaks 211_{NiSi} and 112_{NiSi} which are the most intense in the standard XRD pattern, became more intense with milling time, indicating an increased amount of NiSi in the milled powder. Simultaneously, the intensity of 111_{Si} , the most intense peak in the XRD pattern, decreased with increasing milling time, suggesting consumption of Si in the formation of the NiSi phase, and this continued up to 20 h of milling. Only the NiSi phase was found to be present in the powder milled for 20 h.

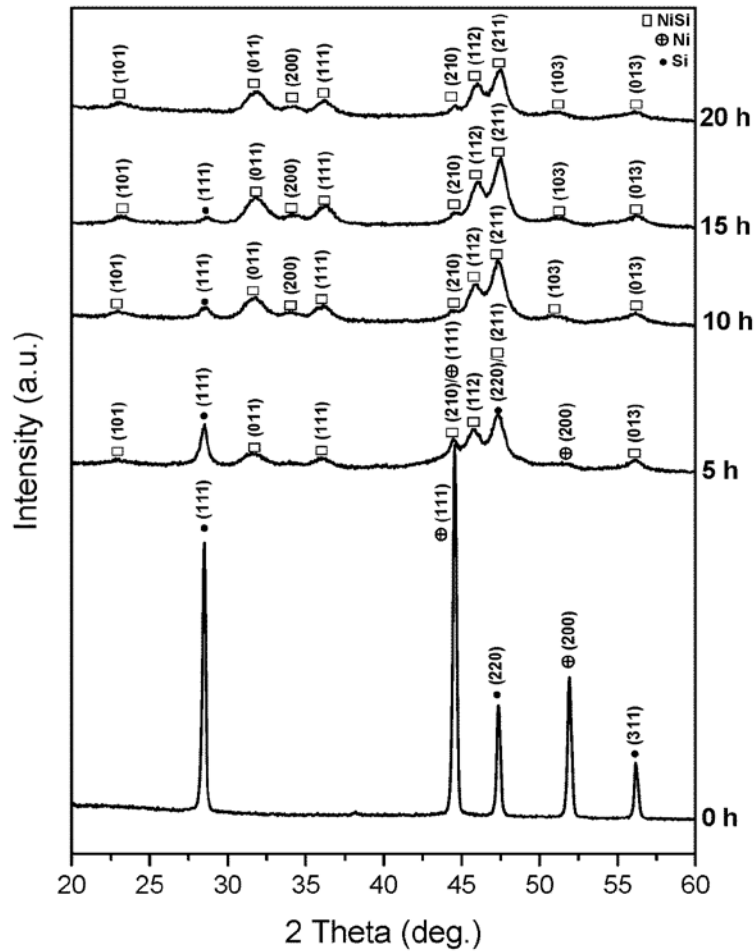


Figure 4.2: XRD patterns of the Ni-60 at.% Si powder blend milled for different times. The Ni and Si peaks are clearly seen in the unmilled powder (0 h). The equilibrium NiSi intermetallic started to form at 5 h of milling time, and its amount increased with milling time.

The crystallite size and lattice strain were calculated from the peak widths using JADE7 X-ray analysis software package. Figure 4.3 shows a plot of the crystallite size and lattice strain (calculated from Si peaks) as a function of milling time in the Ni-60 at.% Si powder blend. In the initial stage of milling, the crystallite size decreased rapidly with time and then reached a saturation value of around 11 nm at 10 h of milling. On the other hand, the lattice strain increased continuously with milling time due to generation and multiplication of dislocations and other crystal defects as a result of plastic deformation of the powder. The strain reached a maximum value of 1.3 % at 15 h of milling.

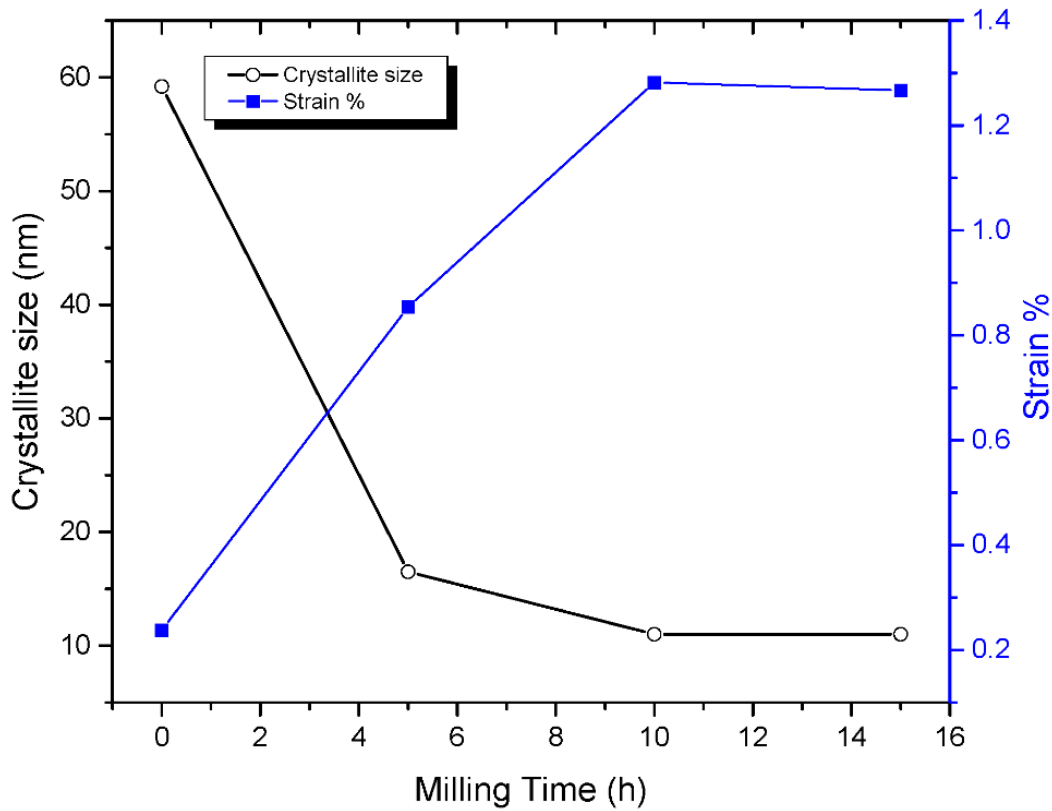


Figure 4.3: Plot of crystallite size and lattice strain for Ni-60 at.% Si as a function of milling time.

The NiSi phase has formed homogeneously after 20 h of milling time and no other phases were detected in the XRD patterns. It has been reported in the literature that the NiSi phase has an orthorhombic crystal structure with the lattice parameters $a = 0.562$ nm, $b = 0.518$ nm, and $c = 0.334$ nm and belonging to the space group *Pnma* (No. 62) (ICDD-PDF # 70-2626) [39, 52, 84]. The lattice parameters of the NiSi phase synthesized by MA in this study were calculated to be $a = 0.566$ nm, $b = 0.524$ nm, $c = 0.322$ nm. Thus, the lattice parameters of the NiSi phase produced in this investigation are only slightly different from the values reported in the literature.

Figure 4.4 shows the XRD patterns of the Ni-67 at.% Si powder blend as a function of the milling time. The structural evolution in this powder blend is somewhat similar to that reported above for the Ni-60 at.% Si powder blend, with some minor differences. Like in the Ni-60 at.% Si powder blend, the diffraction peaks of both Ni and Si in the Ni-67 at.% Si powder blend also broadened and their intensities decreased, again due to a decrease in crystallite size and increase in lattice strain. The NiSi phase started to form after 2 h of milling.

The XRD patterns remained unchanged with continued milling up to 30 h. Both the Ni-60 at.% Si and Ni-67 at.% Si powder blends have shown similar reaction paths in forming the NiSi phase as shown through the XRD patterns (Figure 4.2 and 4.4). Even though the NiSi compound was formed in both the compositions, a small amount of free Si was detected in the XRD patterns of the Ni-67 at.% Si powder blend even after 30 h of milling. But, as mentioned above, in the case of the Ni-60 at.% Si powder blend the NiSi phase had formed homogeneously, and neither free Si nor free Ni was present.

An important difference between the milling of the two powder blends is that formation of the NiSi equilibrium phase has been detected to start even after 2 h of milling time in the Ni-67

at.% Si powder blend (Figure 4.4), whereas it had started to form after 5 h of milling in the Ni-60 at.% Si powder blend. In both the cases, further milling resulted in an increase in the amount of the NiSi phase formed, and the maximum amount of NiSi phase had formed at 20 h of milling.

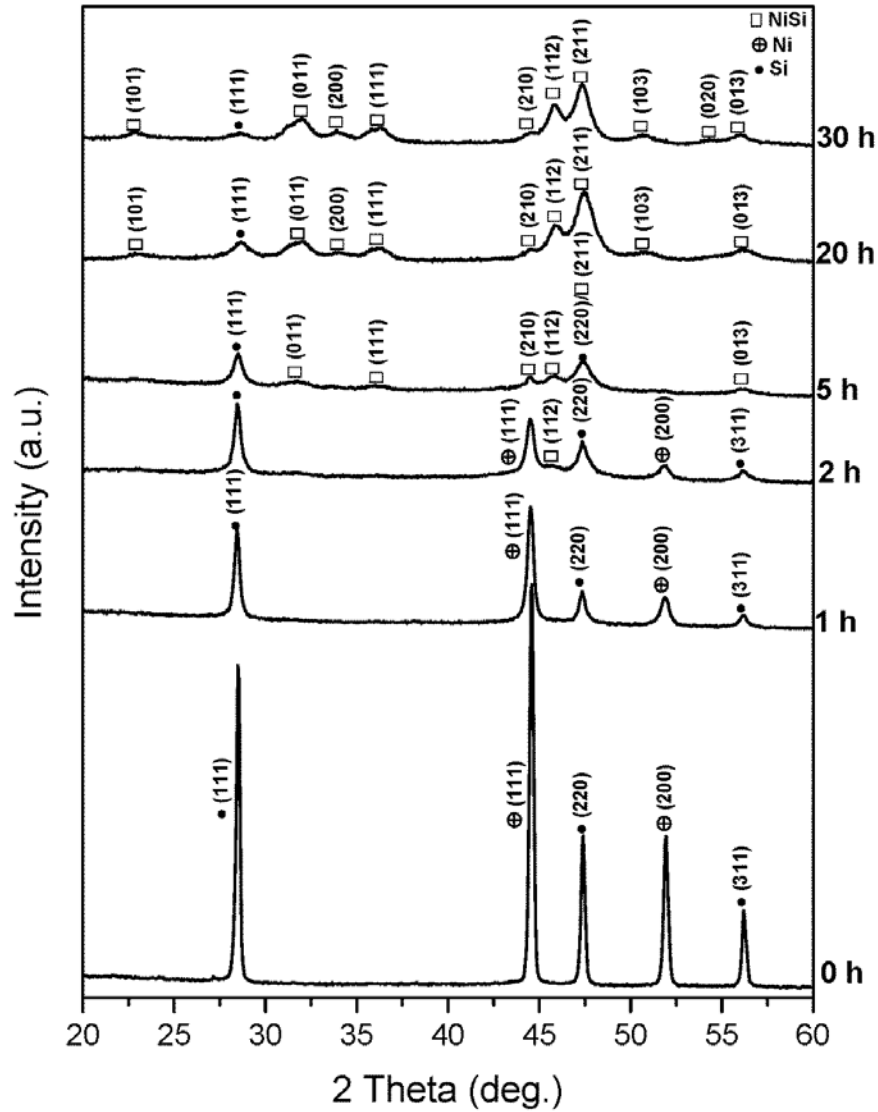


Figure 4.4: XRD patterns of the Ni-67 at.% Si powder blend milled for different times. The Ni and Si peaks are clearly seen in the unmilled powder (0 h). Formation of the equilibrium NiSi phase started at 2 h of milling time. Note that a small amount of Si is present along with NiSi in the powder milled even for 30 h.

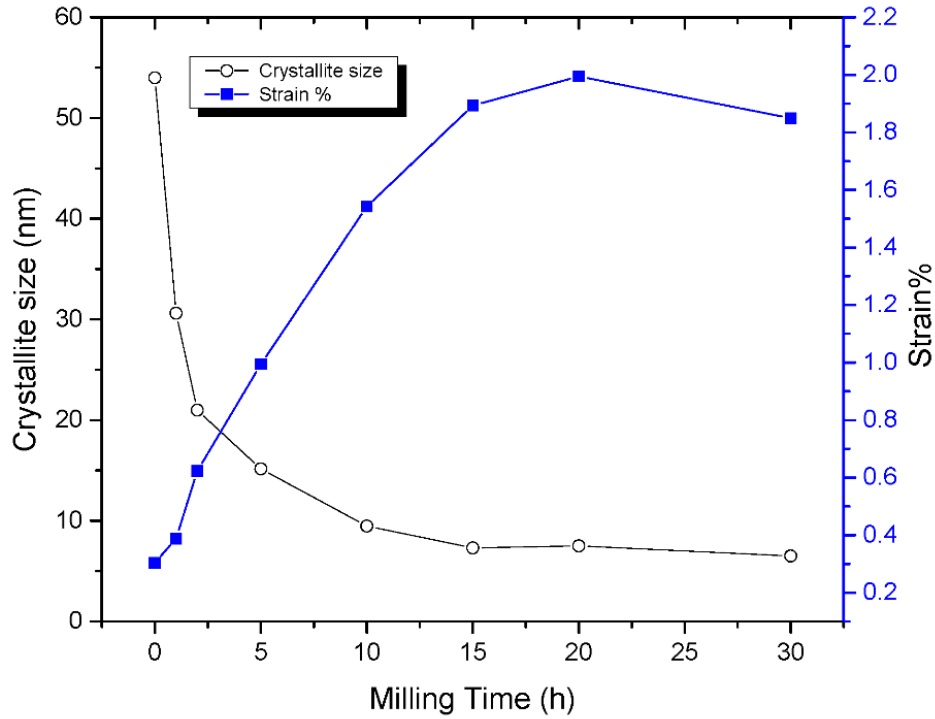


Figure 4.5: Plot of crystallite size and lattice strain for the Ni-67 at.% Si powder blend as a function of milling time.

The variation of crystallite size and lattice strain for the Si peaks in the Ni-67 at.% Si powder blend are plotted in Figure 4.5. It is noted that the NiSi phase started to form at 2 h of milling time after the crystallite size of Si dropped down to around 21 nm. The crystallite size of Si has been estimated as 9 nm at 10 h of milling time and remained virtually constant with further milling. On the other hand, the lattice strain increased continuously with milling time, although at a much slower rate after 10 h of milling, due to generation and multiplication of dislocations and other crystal defects as a result of plastic deformation of the powder. The maximum lattice strain reached was 2% at 20 h of milling time and the lattice strain decreased with increasing milling time. This is possible due to the recovery effects in the milled powders, as reported earlier [6, 85].

Figure 4.6 shows the XRD patterns of the Ni-75 at. % Si powder mixture after milling for different times. The XRD pattern of the unmilled powder blend (for 0 h of milling) shows diffraction peaks corresponding to pure crystalline Ni and Si. The intensity of the Si peaks is higher than that of Ni peaks, a result of the larger amount of Si present in the powder blend. The lattice parameters of Ni and Si calculated from the XRD patterns match very well with those listed in the literature.

After 1 h of milling, the XRD patterns showed that both the Ni and Si peaks became slightly broader and that their peak intensities decreased. Both these effects can be attributed to the reduced crystallite size and increased lattice strain introduced into the powder during milling. A slight shift in the position of the Ni diffraction peaks to higher angles (and therefore smaller lattice parameters) suggests that some solid solubility of Si in Ni has occurred at this stage.

On milling the powder for 2 h, we can notice the presence of new diffraction peaks in the XRD pattern, suggesting possible formation of a new phase. By comparing the peak positions and intensities of these new peaks with those of the possible phases, it could be concluded that these new diffraction peaks correspond to the equilibrium NiSi phase. The number and intensities of the peaks corresponding to the NiSi phase increased with increasing milling time, up to 4 h, while the intensities of the diffraction peaks from both Ni and Si decreased.

On milling the powder for 5 h, the most intense peaks 211_{NiSi} and 112_{NiSi} became more intense with increasing milling time, suggesting an increased amount of the NiSi phase in the milled powder. It may also be noted that the NiSi phase that had formed earlier and the remaining free Si reacted to form the equilibrium NiSi_2 phase. This can be inferred from the formation of the NiSi_2 phase, and simultaneous decrease in the intensity of the 111_{Si} peak, suggesting consumption

of Si in the formation of the NiSi₂ phase. These observations are confirmed by SEM/EDS analyses, described later.

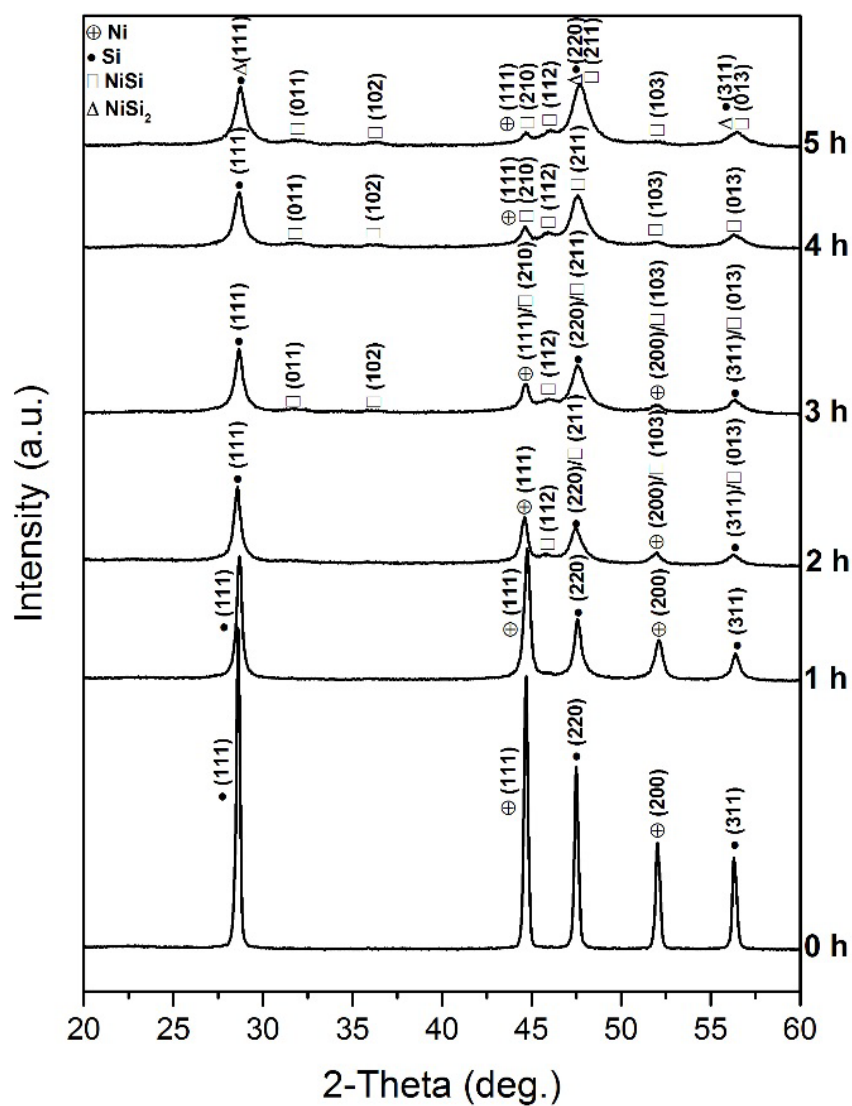


Figure 4.6: XRD patterns of the Ni-75 at.% Si powder blend milled for different times. The Ni and Si peaks are clearly seen in the unmilled powder (0 h). Formation of the equilibrium NiSi phase started to occur at 2 h of milling, and its amount increased with milling time.

The results for the Ni-80 at.% Si powder blend were very similar (Figure 4.7) except for minor differences in the intensities of the diffraction peaks due to the increased amount of Si. After milling for 5 h, the XRD pattern from the powder exhibited the presence of the NiSi, NiSi₂, and Si phases, like in the case of the Ni-75 at.% Si powder blend.

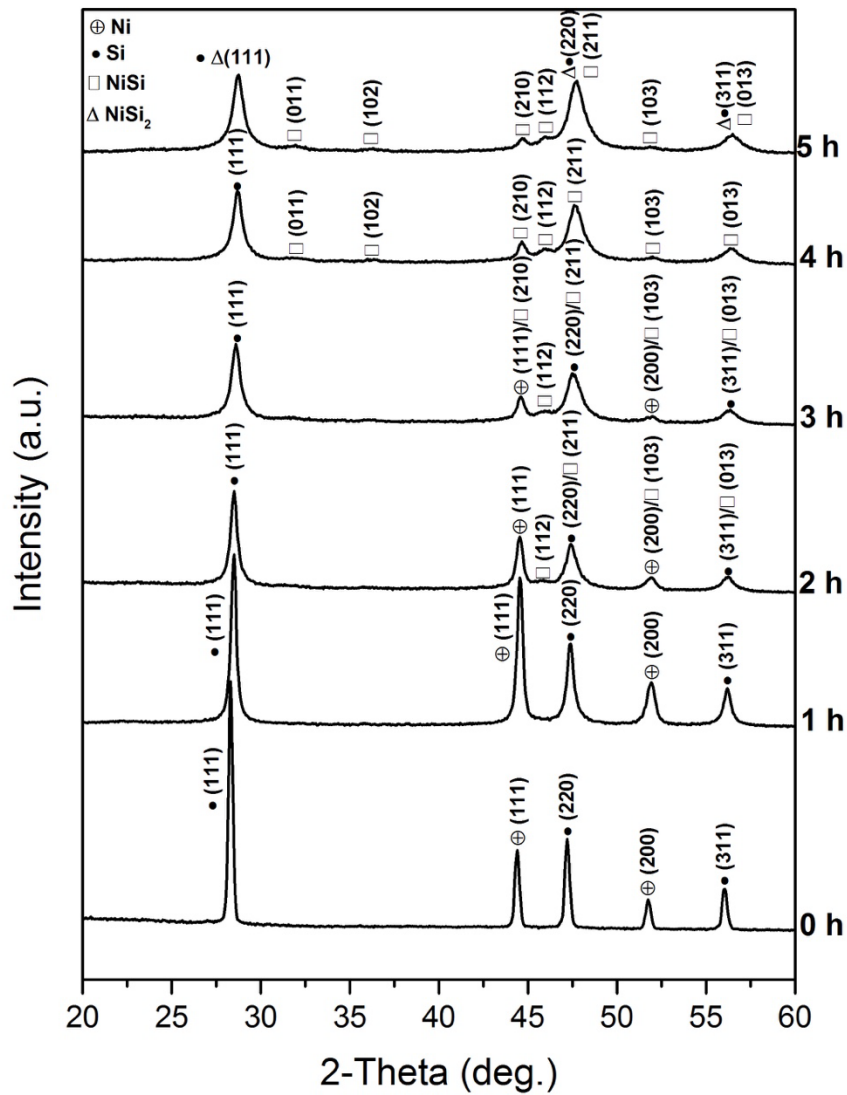


Figure 4.7: XRD patterns of the Ni-80 at.% Si powder blend milled for different times. The Ni and Si peaks are clearly seen in the unmilled powder (0 h). Formation of the equilibrium NiSi phase started to occur at 2 h of milling, and its amount increased with milling time.

The lattice parameter of the Ni(Si) solid solution was calculated from the 111_{Ni} peak position as a function of the milling time. The lattice parameter decreased with milling time and reached 0.35142 nm for Ni-60 at.% Si, 0.35131 nm for Ni-67 at.% Si, 0.35130 nm for the Ni-75 at.% Si powder blend, and to 0.35117 nm for the Ni-80 at.% Si powder blend after 5 h of milling. This is in contrast to the value of 0.3523 nm for pure Ni in the as-blended condition [39]. From the standard variation of the lattice parameter of the Ni(Si) solid solution as a function of Si content in the Ni-Si system, shown in Figure 4.8 [44], the Si content in the solid solutions was estimated to be about 16.4 at.% for Ni-60 at.% Si, 18.2 at.% for the Ni-(67-75) at.% Si and 20.6 at.% for the Ni-80 at.% Si powder blends, respectively. Since the solid solubility of Si in Ni at room temperature under equilibrium conditions was estimated to be only about 2.5 at.% [86], it can be concluded that MA processing has significantly increased the solid solubility limit of Si in Ni in the Ni-Si alloy system.

Increasing the milling time up to 10 h led to a decreased intensity of the NiSi peaks in both the compositions (Ni-75 at. % Si and Ni-80 at.% Si). Even at this stage, it is clear from Figure 4.9 and Figure 4.10 that a small amount of the NiSi phase existed, along with the NiSi₂ phase, in the milled Ni-75 at.% Si powder. It is to be noted from the XRD patterns that the most intense 220_{NiSi_2} peak appears at $2\theta = 47.50^\circ$, next to the most intense 211_{NiSi} peak at $2\theta = 47.22^\circ$. That is the reason why one can clearly notice the splitting of the peak. Moreover, XRD patterns indicated that the NiSi₂ peaks became more prominent on milling the powder for 15 h, as seen in Figure 4.9. and Figure 4.10.

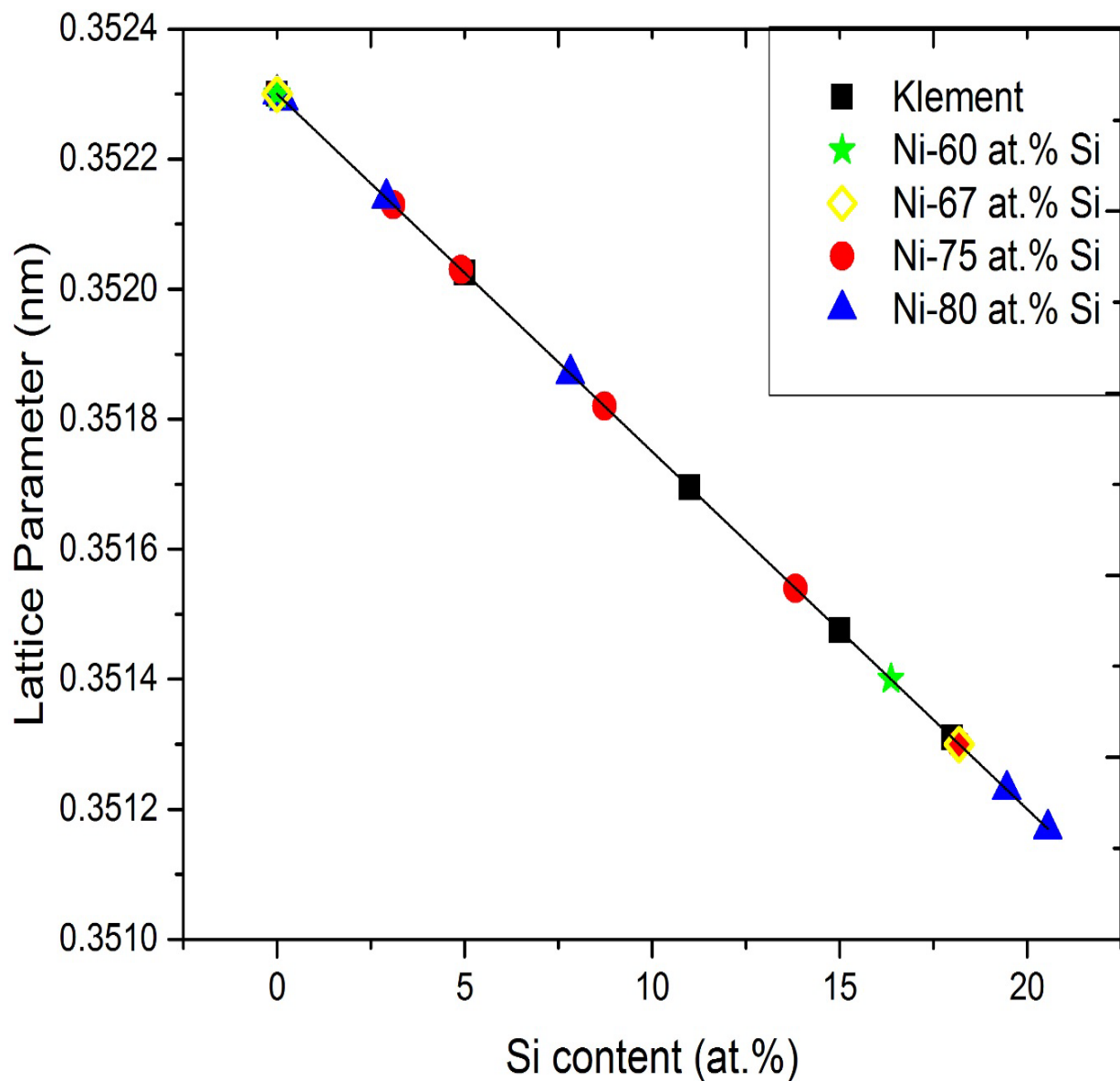


Figure 4.8: Variation of the lattice parameter of Ni(Si) solid solution with Si content based on the results of Klement [44].

It is important to note here that the diffraction peaks for the NiSi_2 and Si phases completely overlap since their crystal structures are similar and the lattice parameters are very close to each other. Also, the XRD patterns clearly indicated that the sharp decrease in the amount of NiSi with

continued milling is associated with an increase in the amount of the NiSi₂ equilibrium phase that has formed as a result of interaction between NiSi and Si. The results are identical for the Ni-80 at.% Si blend. The NiSi₂ phase has been determined to have a cubic structure with the lattice parameter $a = 0.5406$ nm and belonging to the space group $Fm\bar{3}m$ (No. 225) [65, 87]. An almost homogenous NiSi₂ phase had formed on milling the powder for 15 h in both the Ni-75 at.% Si and Ni-80 at.% Si compositions.

It may be noted that the intensity of the peak at $2\theta = 56.49^\circ$ is high at 5 h of milling, decreases at 10 h, and then increases again at 15 h of milling. This can be understood as follows. At 5 h of milling, the powder contains NiSi, NiSi₂, and Si phases. And the 013 planes of NiSi, 311 planes of NiSi₂, and 311 planes of Si diffract at this angle. That is why this peak is a superimposition of all these three phases. But, the amount of NiSi₂ (which has the highest relative intensity among the three phases) at this milling time is relatively small. That is why the peak has a low intensity. On milling for 10 h, Si has disappeared, the NiSi phase continued to exist, and the amount of the NiSi₂ phase has substantially increased and therefore, the relative intensity of this peak is quite high due to superimposition of the peaks from the NiSi and NiSi₂ phases. However, on milling the powder for 15 h, only the NiSi₂ phase is present and so the relative intensity is again high. Quantitatively, the relative intensity of this peak, with respect to 220 of NiSi₂ phase, is 22% at 5 h, 12% at 10h, and 14% at 15 h of milling, confirming the above explanation.

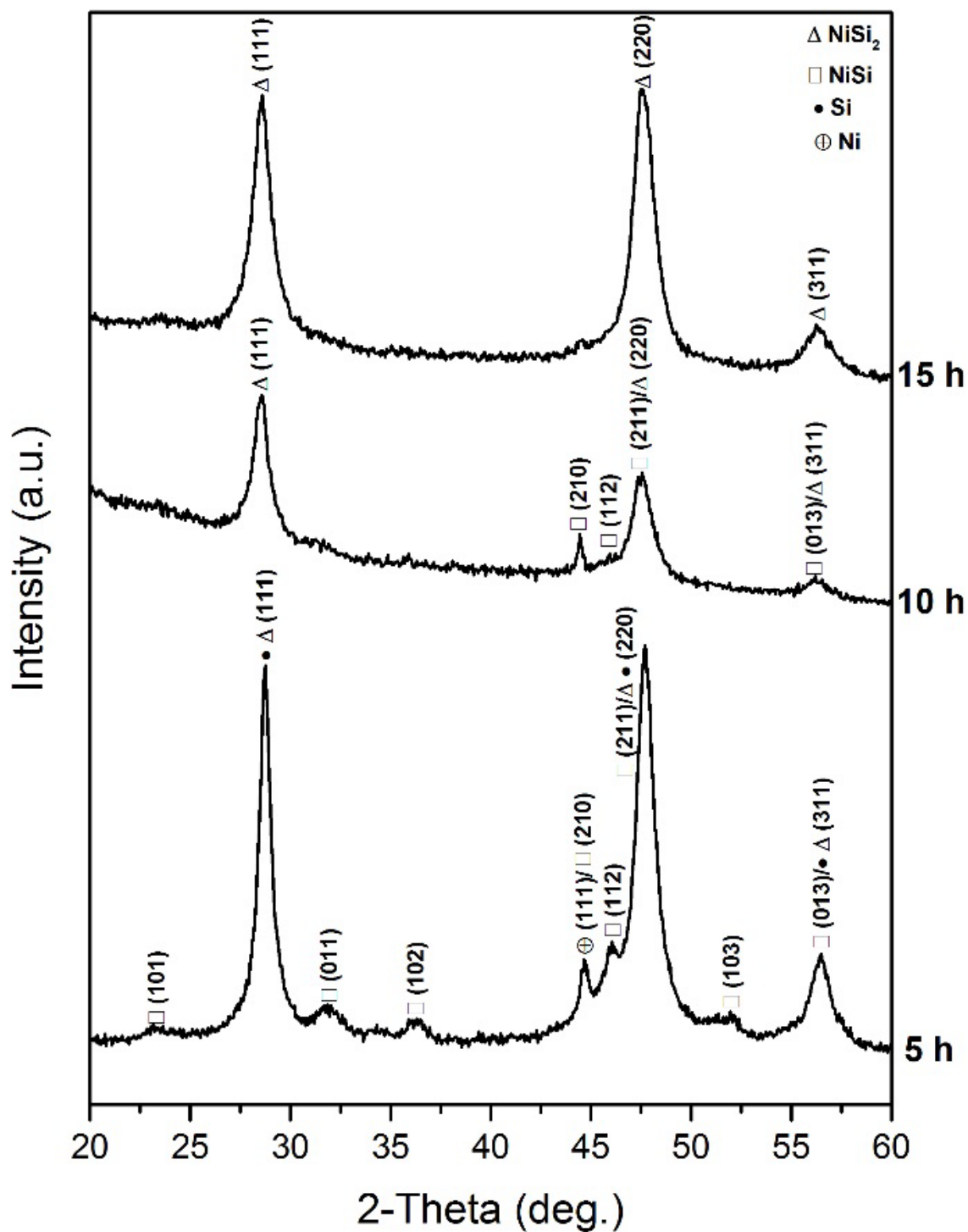


Figure 4.9: XRD patterns of the Ni-75 at.% Si powder blend milled for different times. On milling the powder for 10 h, a new equilibrium intermetallic NiSi_2 started to form. An almost homogenous NiSi_2 phase had formed on milling the powder for 15 h.

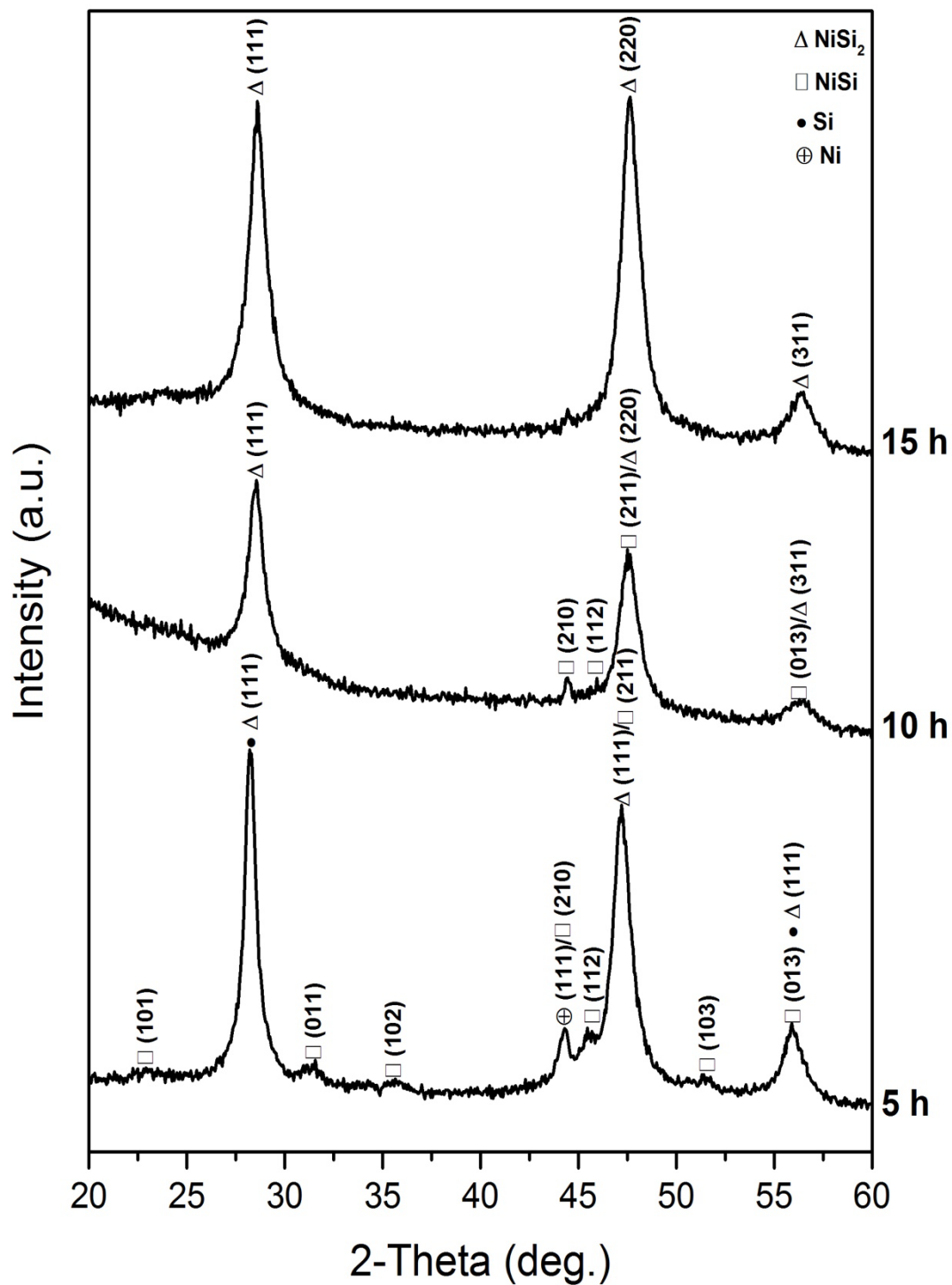


Figure 4.10: XRD patterns of the Ni-80 at.% Si powder blend milled for different times. On milling the powder for 10 h, a new equilibrium intermetallic NiSi_2 started to form. An almost homogenous NiSi_2 phase had formed on milling the powder for 15 h.

The crystallite size and lattice strain were calculated from the peak widths using JADE7 X-ray analysis software package. Figures 4.11 and 4.12 show plots of the crystallite size and lattice strain (calculated from the 111_{Si} peaks) as a function of the milling time in the Ni-75 at.% Si and Ni-80 at.% Si powder blends, respectively. In the initial stages of milling, the crystallite size decreased rapidly with time and then reached a saturation value of around 13 nm and 12 nm at 4 h of milling for Ni-75 at.% Si and Ni-80 at.% Si, respectively. There was no significant change in the crystallite size on continued milling of the powder. On the other hand, the lattice strain increased continuously with milling time due to generation and multiplication of dislocations and other crystal defects as a result of plastic deformation of the powder. The strain reached a maximum value of 1.1 % at 5 h of milling in both the Ni-75 at.% Si and Ni-80 at.% Si powder blends.

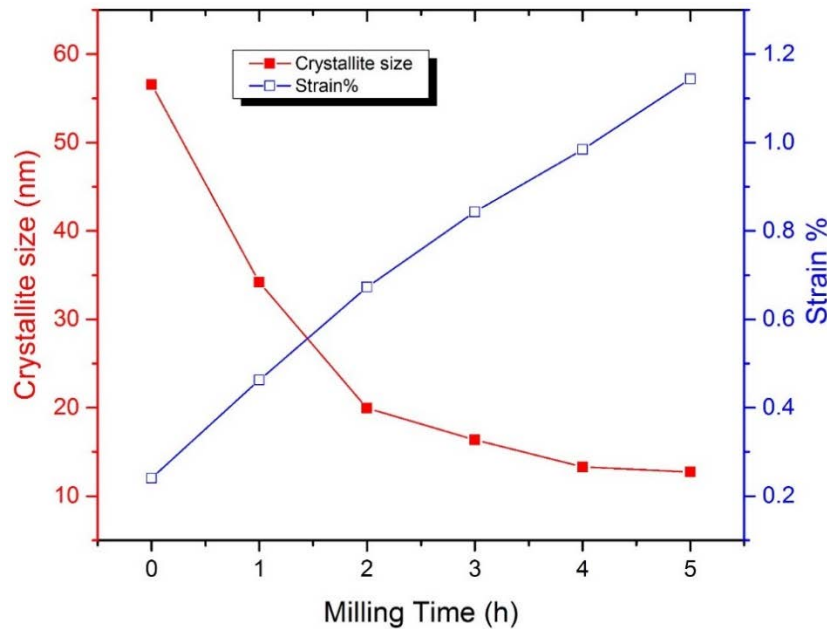


Figure 4.11: Plot of crystallite size and lattice strain for the Ni-75 at.% Si powder blend powder blend as a function of milling time.

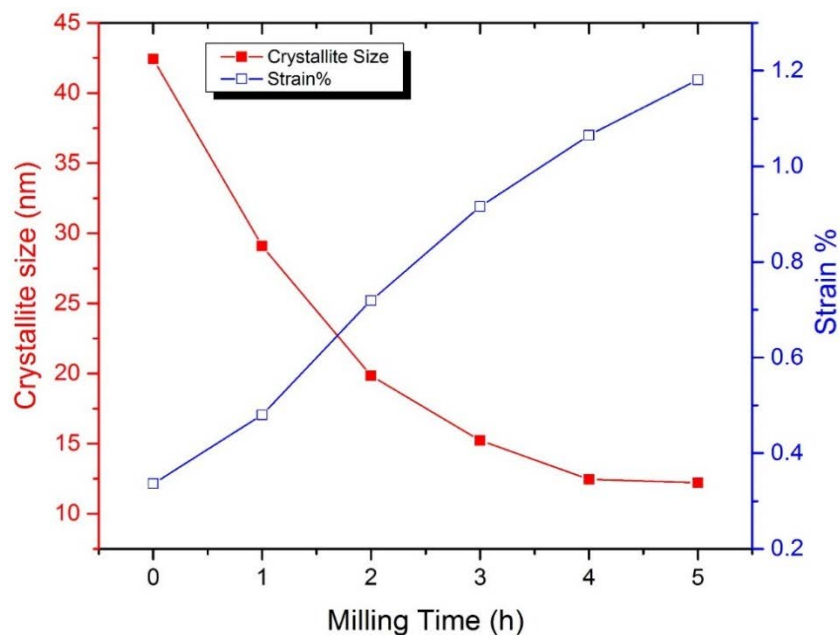


Figure 4.12: Plot of crystallite size and lattice strain for the Ni-80 at.% Si powder blend as a function of milling time.

4.2.2 Scanning Electron Microscopy (SEM)

Figure 4.13 shows the SEM micrographs of the pure Ni and Si powders. The Ni powder was produced by the carbonyl gas refining process and consequently has the spiky needle-like morphology (Figure 4.13(a)). On the other hand, being a semi-metal, Si has the blocky faceted morphology (Figure 4.13(b)).

Figure 4.14 shows the SEM micrographs of the powder blend on milling for different times. Figure 4.14(a) shows the SEM micrograph of the unmilled powder wherein the Ni and Si powder particles could be identified unambiguously. EDS analysis confirmed that the powder particles with smooth surface and dark contrast (about 2 μm) are Si, while the relatively fine roughly spheroidal (but spiky) particles with bright contrast (about 6 μm in size) represent Ni. Interdiffusion between the powder particles and homogenization occur during milling and Figure

4.14(b) represents an SEM micrograph of the powder milled for 5 h, showing the presence of both NiSi and Si phases.

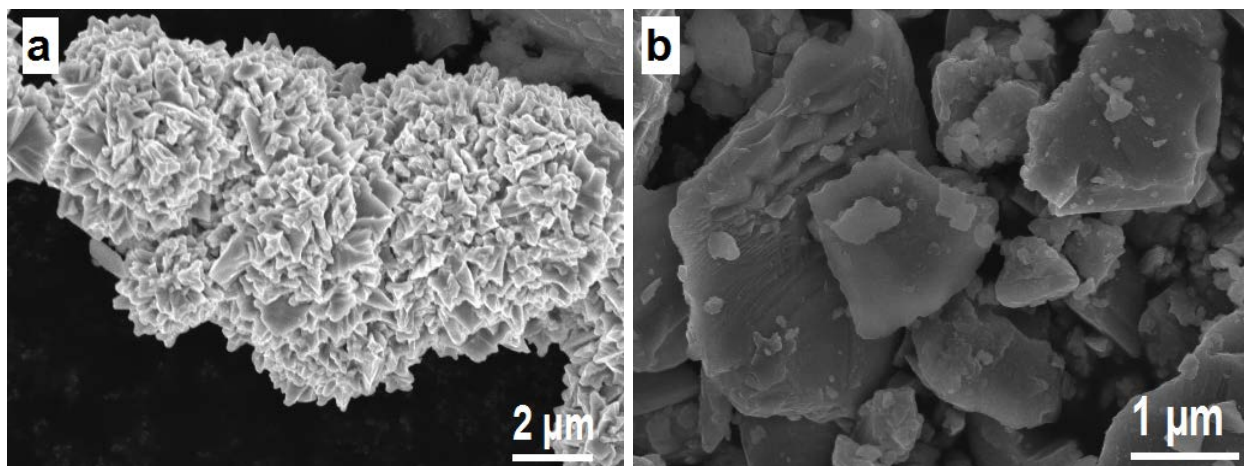


Figure 4.13: (a) and (b): Scanning electron micrographs of pure Ni and Si powders showing the spiky and faceted morphologies, respectively.

By observing the backscattered micrograph (Figure 4.14(c)), which shows the atomic number contrast of one large powder particle, it becomes clear that interdiffusion between Ni and Si has occurred and that structural changes have taken place, resulting in the formation of the NiSi intermetallic phase. In the backscattered image, the phase with a low average atomic number appears darker and the one with a higher atomic number appears brighter. Accordingly, the lighter phase Si appears as dark spots distributed uniformly and the heavier phase NiSi appears brighter as shown in Figure 4.14(c). EDS analysis confirmed that the average chemical composition of the NiSi phase is 55 at.% Si.

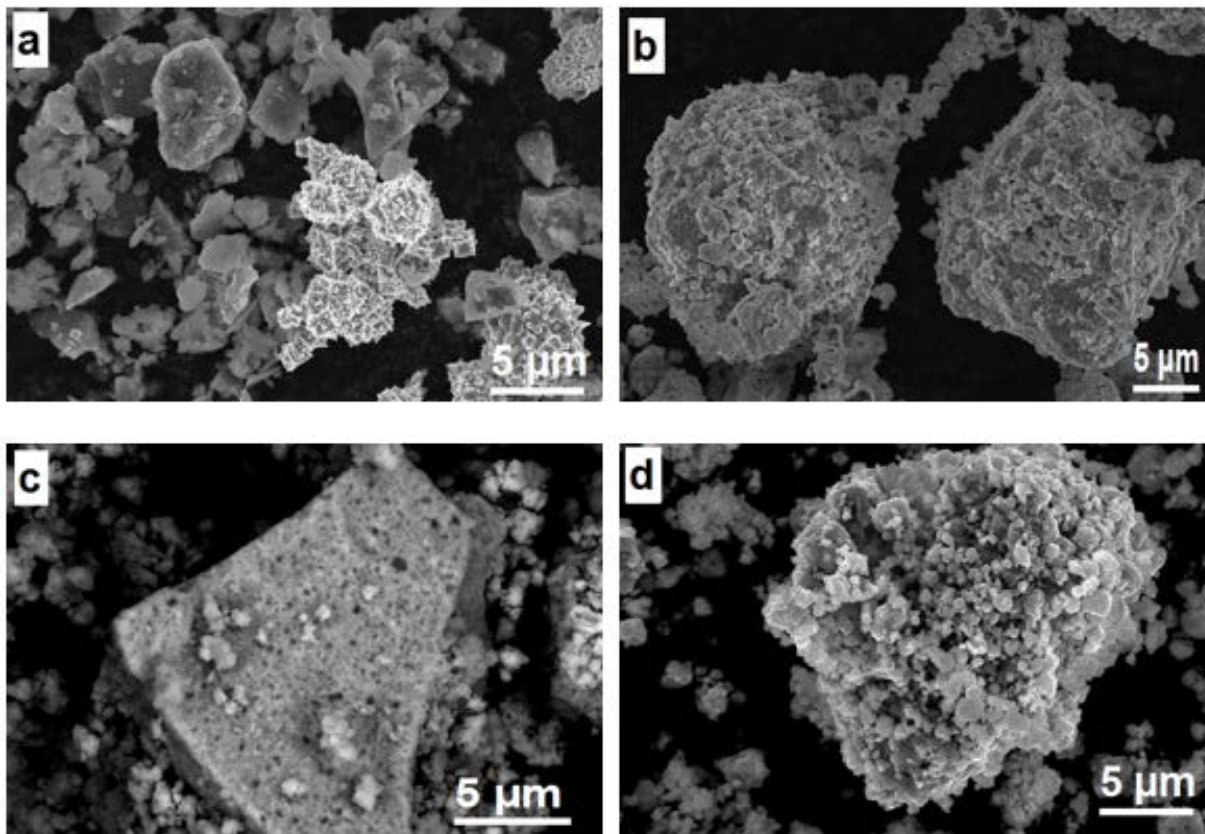


Figure 4.14: (a): Scanning electron micrograph of the Ni-60 at. % Si powder blend in the as-blended (unmilled) condition showing elemental Ni and Si powder particles. (b): Scanning electron micrograph of the Ni-60 at. % Si powder blend after milling for 5 h. showing the presence of both NiSi and Si phases. (c): Backscattered image of the Ni-60 at.% Si powder shows the atomic number contrast where the lighter phase (Si) appears dark and the heavier phase (NiSi) appears bright (d): Scanning electron micrograph of the Ni-60 at. % Si powder blend after milling for 20 h showing uniform grains size of NiSi phase.

On further milling the Ni-60 at.% Si powder to 20 h, the amount of the pure Si phase decreased, as mentioned earlier in the XRD analysis. The powder particles are of intermediate size, about 0.9 μm in size (Figure 4.14(d)) and the chemical composition of these powders was determined by EDS to be very close to that of NiSi (49.1 at.% Si). Thus, it appears that a small amount of Si is lost during MA.

Figure 4.15(a) shows the SEM image of the Ni-67 at.% Si powder mixture milled for 5 h. Due to agglomeration in the early stages of milling, the morphology and distribution of powder particles is inhomogeneous showing large and small sizes of particles distributed non-uniformly. EDS analysis confirmed that the chemical composition is different in different regions of the sample. In some regions of the powder, the Si content in the powder was about 58.9 ± 1.7 at.%, whereas in other regions the Si content in the powder was about 46.9 ± 1.2 at.%. On milling up to 30 h, the powder particle size was very fine reaching a value of about $0.5 \mu\text{m}$ (Figure 4.15(b)). EDS analysis of the Ni-67 at.% Si powder at this stage showed that the NiSi powder particles have about 59.0 ± 0.6 at.% Si. XRD results (Figure 4.4) have also confirmed that the NiSi phase has formed at this stage of milling with a very small amount of excess Si remaining.

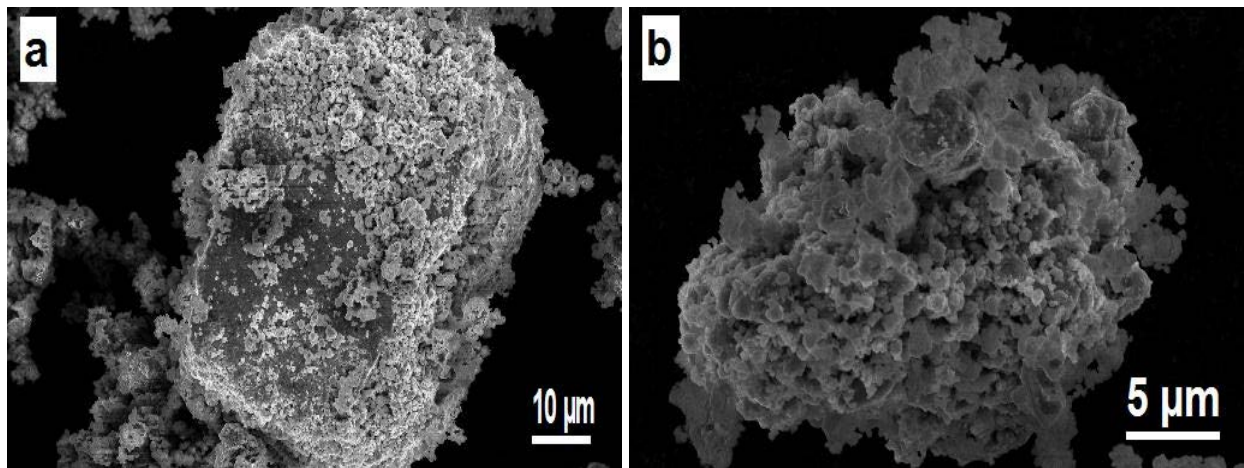


Figure 4.15: Scanning electron micrograph of Ni-67 at. % Si after milling for 5 h. showing the presence of both NiSi and Si phases (b): Scanning electron micrograph of Ni-67 at. % Si after milling for 30 h showing. Showing NiSi and small amount of Si phases.

EDS analyses confirmed that the average chemical composition of the NiSi particles is 51.85 ± 0.66 at.% Si in Ni-75 at.% Si and 49.33 ± 0.44 at.% Si in Ni-80 at.% Si, and for the NiSi₂ phase, the average chemical composition is 67.67 ± 0.60 at.% Si in Ni-75 at.% Si and 68.50 ± 0.59 at.% Si in Ni-80 at.% Si. These values are every close to the values expected for the equilibrium NiSi and NiSi₂ phases. XRD results have also confirmed that both the NiSi and NiSi₂ phases have formed at this stage of milling (5 h).

The powder particle size is also very fine, about 0.4 μm . EDS analyses of the powder milled for 15 h showed that the powder particles now have about 66.18 ± 0.58 at.% Si in the Ni-75 at.% Si powder blend, and 68.65 ± 0.61 at.% Si in the Ni-80 at.% Si powder blend. This composition is what is expected for the NiSi₂ phase, which is confirmed to have formed through XRD patterns (Figure 4.9). The presence of only the NiSi₂ phase at this time in both the powder blends, coupled with the EDS observation of about 67 at. % Si in the milled powder, clearly suggests that there is loss of Si during milling of the Ni-Si powder blends.

4.3 Discussion

4.3.1 Supersaturated Ni(Si) Solid Solutions

The equilibrium solid solubility of Si in Ni was reported to be around 10 at.% at 700 °C and 15 at.% at 1035 °C, the peritectic temperature [65]. Based on their thermodynamic calculations, Nikolaychuk and Tyurin [86] estimated the room temperature solid solubility of Si in Ni to be 2.5 at.%. During MA, it was noted that, in the Ni-Si powder blends, the lattice parameter of Ni decreased with milling time. The reason for this decrease in the lattice parameter is the formation of the Ni(Si) substitutional solid solution. It is also to be noted that the extent of solid

solubility increase is different in the Ni-Si powder blends, viz., 16.36 at.% for the Ni-60 at.% Si, 18.18 at.% for the Ni-67 at.% Si, 18.2 at.% for the Ni-75 at.% Si and 20.6 at.% for the Ni-80 at.% Si, respectively, after 5 h of milling.

Since the silicon atom has a smaller diameter ($d_{\text{Si}} = 0.204$ nm) than that of Ni ($d_{\text{Ni}} = 0.249$ nm), the Si atom can enter into the metal lattice substitutionally and decrease the lattice parameter of Ni. The observed decrease in the lattice parameter of Ni with increasing Si content [44, 52] clearly suggests that Si atoms are dissolving substitutionally in the Ni lattice.

Solid solubility extensions have been reported in many alloy systems by non-equilibrium processing techniques such as rapid solidification processing and MA [5, 6, 88-91]. Even though large solid solubility extensions have been reported in rapidly solidified alloys, the solid solubility extensions in mechanically alloyed powders are rather limited [6]. However, in the case of Ni-Si alloys, the disordering of the L_{12} -Ni₃Si phase results in the formation of a solid solution, and therefore the solid solubility extensions appear to be very large in such systems [92]. But, no systematic investigations have been carried out to determine whether there are large solid solubility extensions in mechanically alloyed powders.

It was mentioned that the extent of supersaturation of Si in Ni is different depending on the initial solute content in the powder mixture. A few such instances have been reported earlier [91, 93, 94]. It is possible that a situation like this could arise during rapid solidification processing of alloys, when the solute concentration at the dendrite tip can be quite high and is determined by the operative solute partition ratio. But, no melting process is involved during MA and therefore this explanation cannot be valid in this case. However, it can be explained on the basis that the concentration gradients are steeper at higher solute contents, which will result in increased

diffusion and consequently higher solid solubility levels. This variation may arise possibly due to kinetic considerations only since thermodynamically the maximum solid solubility is fixed for a given alloy system and temperature. It is also possible that the enhanced grain boundary area due to a reduction in grain size in these powder samples can also contribute to the differences in the solid solubility levels.

4.3.2 Crystallite Size and Lattice Strain

The crystallite size and lattice strain are the most crucial parameters in the MA process. XRD methods are employed to determine the crystallite size or grain size and lattice strain in the mechanically alloyed powders which are very simple as compared to TEM methods. The grain size as obtained by XRD methods is an average length of columns of the unit cells normal to the reflection planes, also known as the column length. As we mentioned earlier, the grain size and lattice strain were calculated by measuring the width of the XRD peaks using standard procedures [26].

The crystallite size of the Ni-60, 67, 75 and 80 at.% Si compositions (Figure 4.3, Figure 4.5, Figure 4.11 and Figure 4.12) decreased exponentially with milling time and then reached the saturation value of about 11 nm. The saturation crystallite size also corresponds to the steady state condition of milling, for a given composition, and will not change even if the powder is milled for a longer time. Simultaneously, the lattice strain increased due to the generation and multiplication of dislocations and other crystal defects. However, beyond about 10 h of milling time in the lower Si content (60 and 67 at.%) when the crystallite size reached the saturation value, continued milling is not expected to produce higher dislocation density due to the difficulty of generating new

dislocations in nanometer-sized grains. Moreover, due to the slight rise in the powder temperature, the existing dislocations may be rearranged or annihilated due to relaxation processes. This effect was obvious from the decreased lattice strain values obtained corresponding to saturation crystallite size.

4.3.3 Formation of Stable NiSi and NiSi₂ Intermetallic Phases

As shown in Figures 4.2 and 4.4, the sequence of structural evolution in the Ni-60 at.% Si and Ni-67 at.% Si was that alloying occurred between Ni and Si resulting in the formation of the Ni(Si) solid solution followed by the formation of the equilibrium NiSi intermetallic phase. Since the MA process is carried out essentially at room temperature, one would expect to observe the equilibrium constitution at room temperature according to that present in the phase diagram. According to the Ni-Si phase diagram, at room temperature, one would expect to observe a mixture of the NiSi and NiSi₂ phases at the Ni-60 at.% Si composition and a homogeneous NiSi₂ phase at the Ni-67 at.% Si composition, if alloying occurred between blended elemental Ni and Si powders and equilibrium phases had formed. However, according to the present result, we ended up with the formation of the NiSi intermetallic phase in both the Ni-60 at.% Si and Ni-67 at.% Si compositions. Note that a small quantity of elemental Si was present in the Ni-67 at.% Si composition and that the NiSi₂ phase did not form in either of the powder blends. Thus, the constitution in the milled powders is:



It is also important to realize here that there are some difficulties in identifying the NiSi_2 phase unambiguously in XRD patterns from mechanically alloyed powders. The crystal structures and lattice parameters of the NiSi_2 and Si phases are very similar and close to each other. Both of them have the cubic structure and the lattice parameters are 0.5406 nm and 0.54306 nm, respectively, for NiSi_2 and Si. Consequently, all the diffraction peaks of these two phases almost overlap. For example, the 2θ value of 111_{NiSi_2} peak is at 28.576° and the 2θ value of 111_{Si} peak is at 28.443° . Additionally, the XRD peaks in the milled powder are also broad. Therefore, the combined effects of peak overlap and peak broadening make it very difficult in unambiguously identifying the formation of the NiSi_2 phase in the milled powders. However, a close look at the XRD patterns at different MA times shows that the intensity of the Si peak decreases with milling time. To confirm that formation of the NiSi_2 phase did not occur up to 30 h of milling, Figure 4.16 shows the integrated intensity, the area under 111_{Si} peak, versus milling time for the Ni-60 at.% Si and Ni-67 at.% Si compositions. It can be seen that the intensity of 111_{Si} peak decreases continuously with increasing milling time suggesting that the amount of elemental Si is decreasing in the milled powder. If we assume that the 111 peak belongs to NiSi_2 , which is the equilibrium stable phase, then the intensity should increase with milling time. The decrease in intensity of the Si peak can be easily understood as due to consumption of Si to react with Ni to form NiSi, and the amount of the NiSi phase was found to increase with increasing milling time. This fact could be inferred from the fact that the integrated intensity of the 112 peak of the NiSi phase increased with milling time (Figure 4.17). The formation of NiSi_2 could not be observed even in the Ni-67 at.% Si composition, in agreement with the result reported by Datta et al. [81, 82]. Even though

the starting powder had 67 at.% Si, due to loss of Si during milling, the milled powder contained a mixture of the NiSi phase and a small amount of free Si.

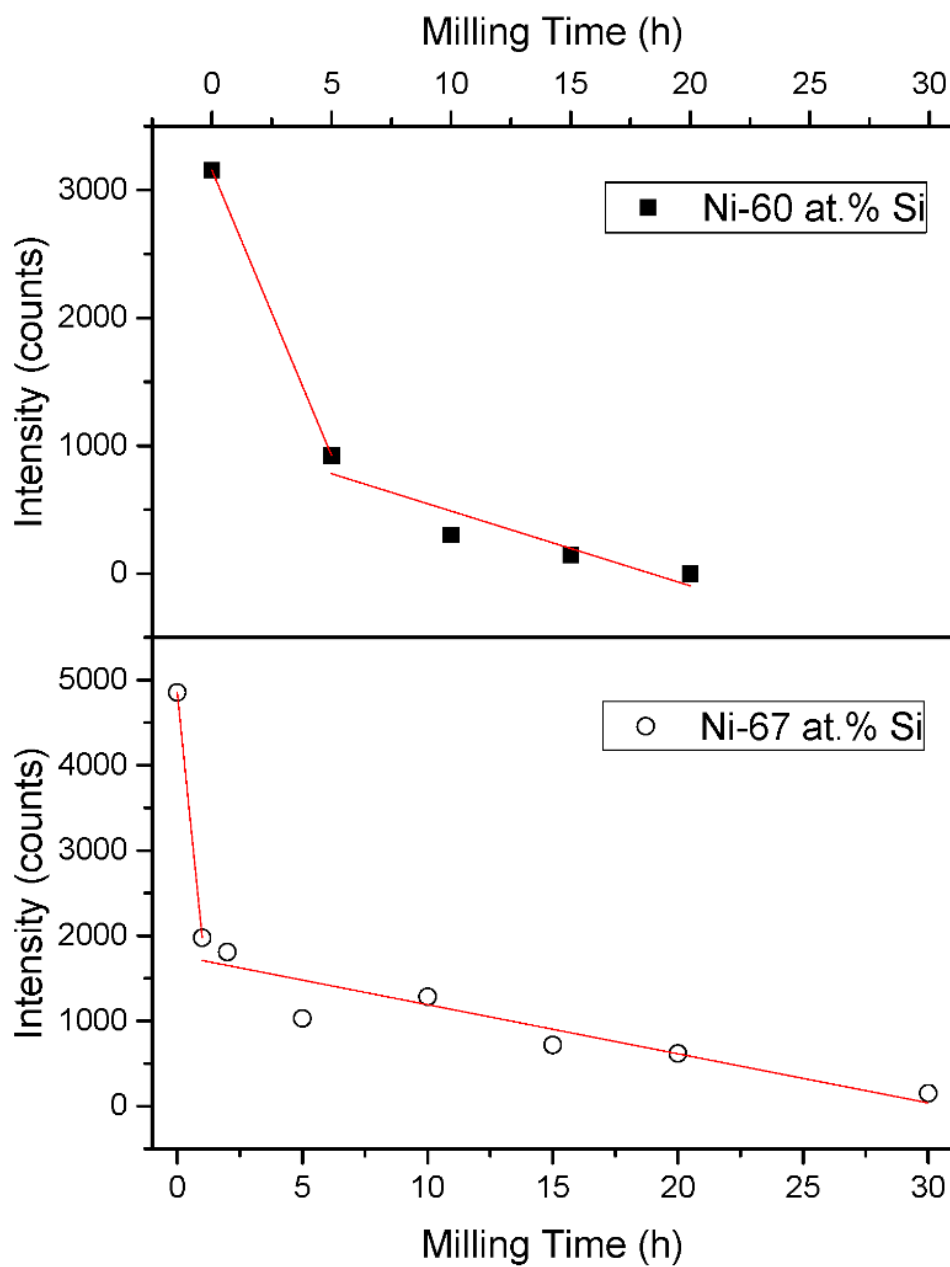


Figure 4.16: Plot of intensity for 111_{Si} peak in Ni-60 at.% Si and Ni-67 at.% Si powder blends as a function of milling time.

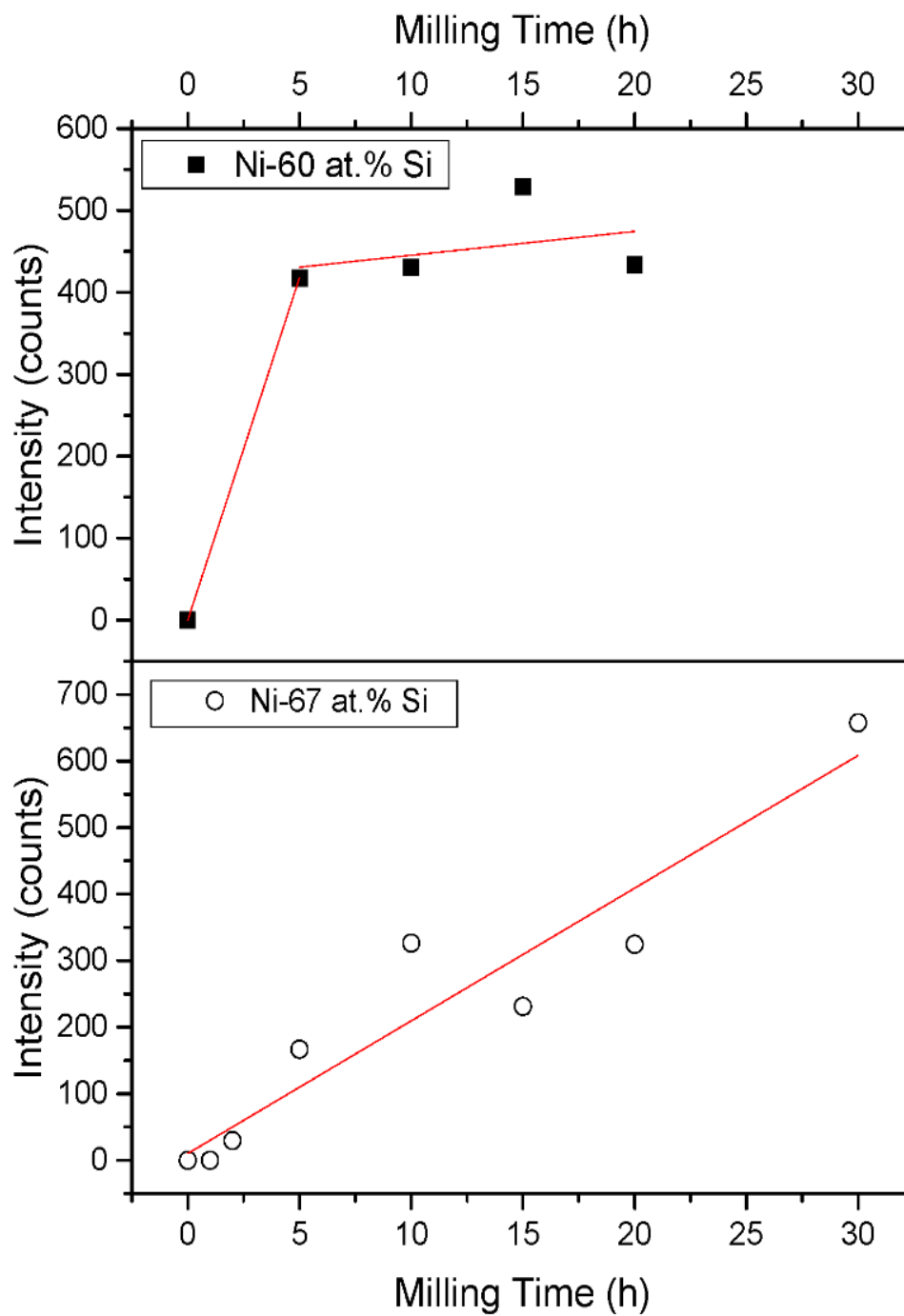


Figure 4.17: Plot of intensity for $^{112}\text{NiSi}$ peak in Ni-60 at.% Si and Ni-67 at.% Si powder blends as a function of milling time.

The Si-rich end of the Ni-Si binary phase diagram (≥ 50 at.% Si) features two equilibrium intermetallics, viz., NiSi and NiSi₂. It is clear from Figure 4.2 and Figure 4.4, that the NiSi phase had started to form at 2 h and 5 h of milling in Ni-67 at % Si and Ni-60 at. % Si powder blends, respectively. The amount of the NiSi phase formed has decreased with increasing Si content; expected from the equilibrium phase diagram, since this composition is farther from the equilibrium composition for NiSi.

The technique of MA has been extensively employed to produce intermetallic phases in a number of alloy systems starting from blended elemental powder mixtures [5]. Therefore, it is not surprising that the equilibrium NiSi phase has formed during MA from blended elemental Ni and Si powders. Similarly, the equilibrium and metastable Ni-Ge intermediate phases have been synthesized through MA starting from blended elemental Ni and Ge powders [95, 96].

The only way the results obtained in the present investigation can be rationalized will be to assume that some amount of Si is lost during the milling process. This is confirmed from EDS analyses of the milled powders because the total amount of Si in the powder was 49.1 at.% in the Ni-60 at.% Si powder blend, and 59.0 at.% Si in the Ni-67 at.% Si powder blend. Since sufficient amount of Si was available in the Ni-60 at.% Si powder blend, only the NiSi phase had formed homogeneously. But, in the Ni-67 at.% Si powder blend, some free Si was present along with the NiSi phase. However, the reaction between NiSi and Si did not lead to the formation of NiSi₂ phase, as evidenced by XRD analysis. Even though, in principle, it is possible to obtain a small amount of the NiSi₂ phase in the Ni-67 at.% Si powder blend, according to the reaction:



Sufficient amount of Si was not present for the completion of the reaction. It is also interesting to note that not even a small amount of NiSi₂ phase was present in the milled Ni-67 at.% Si powder blend. This could be due to kinetic factors, where perhaps the formation enthalpy of NiSi₂ was reasonably high. This could perhaps be the reason why some of the MSi₂ and MGe₂ type phases (where M is a transition metal) are absent under equilibrium conditions [97].

Two intermetallics, viz., NiSi and NiSi₂, had formed on mechanically alloying the Ni-75 at.% Si and Ni-80 at.% Si powder blends for 5 h. It is clear from Figure 4.6 and Figure 4.9 that the NiSi phase had started to form at an early stage of milling (2 h), but a significant amount of the phase had formed on milling the powder for 5 h. Both the milled powders contained a mixture of the NiSi phase and Si, according to the reactions:



However, only the NiSi₂ phase was present in the final stages in both the powder blends. Since the initial powder blends contained 75 and 80 at.% Si, it is expected, according to the equilibrium phase diagram, that the constitution of the powders will be a mixture of NiSi₂ and Si. Since only the NiSi₂ phase is present, it can be surmised that (a) either the NiSi₂ intermetallic has an increased homogeneity range to include these new compositions or (b) that some amount of Si is lost during milling. EDS analyses confirm that the total amount of Si in the two powder blends was 66.18 ± 0.58 at.% Si in the Ni-75 at.% Si powder blend, and 68.65 ± 0.61 at.% Si in the Ni-80 at.% Si powder blend on milling the powder for 15 h. Even though these values may not be very accurate due to the rough surfaces of the mechanically alloyed powders, they are at least

indicative of the fact that there is some loss of Si in the milled powder and/or that there is also some increase in the homogeneity range for the NiSi₂ intermetallic.

The present results show that the NiSi₂ phase composition is slightly different from what is expected under equilibrium conditions. The equilibrium phase diagram shows that NiSi₂ is a line compound. But, in the milled powders, it is noted that it could exist over a small composition range, suggesting that the homogeneity range of the NiSi₂ phase is extended in comparison to the equilibrium composition. Whereas the Si content of the NiSi₂ phase is 66.7 at.% under equilibrium conditions, it could be in the range between 66.2 and 68.7 at.% Si in the mechanically alloyed condition. Such extended homogeneity ranges of intermetallics in the MA condition have been reported earlier [5, 6, 98].

There have been some examples of loss of Si in the MA literature. Some examples are the Ni-Si [81, 82] and Mn-Si systems on continued milling [99-101]. One reason for the loss of Si during MA is its possible oxidation. According to Ellingham diagrams, the free energies of the oxides of Si and Ni are:



$$\Delta G = -853.25 \text{ kJ mol}^{-1} \text{ at } 299 \text{ K, and}$$



$$\Delta G = -419.625 \text{ kJ mol}^{-1} \text{ at } 299 \text{ K.}$$

Since oxidation of Si is so much easier (due to its lower free energy of formation of SiO₂) than that of Ni, it is relatively easy for Si to get oxidized during MA. Even though milling was carried out under nominal argon atmosphere, it is relatively easy for ambient air to get into the container during milling. Such an ingress of air and oxygen into the powder during MA has been

demonstrated earlier [102, 103]. In this context, it is useful to recall that no loss of Ge was detected during milling of Ni-Ge powder blends [95, 96]. This can be understood in terms of the free energy of formation of GeO_2 ($-417.5 \text{ kJ mol}^{-1}$ at 299 K), which is close to that of NiO formation and much lower than that of SiO_2 formation.

4.4 Conclusions

Mechanical alloying of Ni-(60, 67, 75 and 80) at.% Si powder blends was conducted at room temperature in a high-energy SPEX mill. The supersaturated substitutional solid solution of Si in Ni started to form in the early stages of milling (at 2 h of milling in the Ni-67 at.% Si powder blend and at 5 h in the Ni-60 a.% Si powder blend) followed by the formation of NiSi phase. The amount of the NiSi phase formed increased with increasing milling time and the amount of free Si decreased. Due to loss of Si during MA, formation of the NiSi_2 phase was not observed in both the compositions. However, a small amount of unreacted Si was still observed to be present, even after long milling for 30 h in the case of Ni-67 at.% Si, confirmed by XRD and EDS investigations. In the early stages of milling of Ni- (75 and 80) at.% Si a supersaturated substitutional solid solution of Si in Ni had formed followed by the formation of the NiSi intermetallic phase at 2 h of milling in both compositions. The amount of NiSi increased with increasing milling time. On continued milling, the NiSi intermetallic phase reacted with the free Si to form the NiSi_2 intermetallic phase at 15 h of milling. This NiSi_2 phase appears to have a small homogeneity range in the milled condition, unlike in the equilibrium state where it is a line compound. The presence of only the NiSi_2 phase in the Ni-75 and 80 at.% Si compositions in the milled powders clearly suggests that there is perhaps some loss of Si during milling.

CHAPTER 5: SYNTHESIS OF Fe-C ALLOYS BY MECHANICAL ALLOYING

5.1 Introduction

Iron and its alloys have been used by mankind for at least 3,000 years and since the industrial revolution, they have been the major structural materials for different applications. Their applications have been possible due to their attractive properties of high strength, good ductility, easy manufacturability, availability, and low cost. Additionally, their properties can be significantly modified through alloying, thermo-mechanical processing, and heat treatment. This is possible mainly due to the allotropic transformation of the face-centered cubic (fcc) austenite at temperatures $>910\text{ }^{\circ}\text{C}$ to the body-centered cubic (bcc) ferrite at room temperature [104]. The grain size of the steel produced by conventional processing methods is of the order of micrometers. The mechanical properties of steels will be influenced by many different parameters/processes, for example, oxidation of steel, non-metallic inclusions which are formed during solidification, heat treatment, mechanical processing, and thermo-mechanical processing.

The unconventional properties resulting from grain sizes in the nanometer range ($<100\text{ nm}$) have been attracting considerable interest because of their unique properties compared with conventional materials. Different unusual properties, for instance, ultrahigh strength, and superplasticity were reported for nanocrystalline materials whose grain size is less than 100 nm . Over the past three decades, there have been a large number of researchers working in the area of processing of steel alloys using high-energy mechanical milling technique and subsequent heat treatment.

Mechanical milling was conducted in a planetary ball mill on commercially pure iron by Kimura et al. [105], who noted that the crystallite size of the specimen got refined with a concomitant increase in strain with increasing milling time. They noted that the individual nanocrystalline grains were about 20 nm in size and that the hardness increased to 950 HV on milling the powder for 100 h. On the other hand, on milling pure iron powder in a SPEX shaker mill, Jang and Koch [106] observed a smaller grain size of about 10 nm, a result of the higher energy input employed. And, Jia et al. [107] reported that unusual deformation and failure modes in nanograined materials obtained by milling of pure Fe in a SPEX 8000 mill for 15 h. These deformation modes were similar to those in amorphous materials.

Processing of pure Fe in an attritor mill under argon or nitrogen gas resulted in different phases. Cook et al. [108] observed that processing in argon gas environment led to production of nanocrystalline bcc-Fe. During milling under nitrogen atmosphere, nitrogen was alloyed into the Fe powder and a bct-Fe phase was produced on the surface as a result of cold work induced stress and the existence of nitrogen at the grain boundaries. However, investigations by Rawers and Doan [109] showed that mechanical milling of pure Fe in nitrogen or argon did not show any change in lattice dimensions and the bct-Fe phase was not observed.

While the hardness of these materials is reasonably high, it is doubtful if these would exhibit any plasticity. Therefore, to induce some plasticity into these materials, Srinivasarao et al. [110] produced iron with a bimodal grain size distribution through mechanical milling and spark plasma sintering. In the first stage, the milled powder was sintered at 600 °C and 254 MPa for 2 min, when the grain size obtained was different in different regions, with an average grain size of 800 nm. Subsequently, this material was subjected to step sintering. In this method, the previously

sintered sample was heated to 690, 700, and 720 °C at a stress of 484 MPa for 6 min. Unlike the samples subjected to equal channel angular pressing (ECAP) which exhibited a grain size of 150–300 nm, and a strength of about 700 MPa and only about 20% plastic strain, the samples with a bimodal grain size distribution exhibited much higher strength reaching 2.6 GPa and a plastic strain of 0.4, although not together. Obviously, this is a profitable route to pursue to achieve both strength and ductility.

Several investigators have also studied the mechanical alloying behavior of Fe-C powder blends with different C contents ranging from 0 to 4.9 wt.%. By mechanically alloying mixtures of Fe and C, it was possible to obtain a fully ferritic structure with 0 to 2 wt.% C, and a two-phase mixture of ferrite and cementite when the carbon content was in the range of 2 to 4 wt.% C. The hardness of the mechanically milled Fe-C alloys deviated from the expected Hall-Petch relationship to lower hardness side when the grain size was below 100 nm [111]. The carbon content was measured using three-dimensional atom probe (3DAP). Zhang et al. [112] reported that around 1.0 at.% C was dissolved within the ferrite grains, and that carbon strongly segregated at the grain boundaries. The properties of the compact were measured after spark plasma sintering of the milled powder. The measured yield and fracture strength were 2000 MPa and 3500 MPa, respectively. Moreover, a plastic strain of over 40 % was obtained. Oh-ishi et al. [113] showed that after milling the Fe-0.8 wt.% C powder blend, the microstructure showed a bimodal structure consisting of fine equiaxed ferrite and cementite phase grains, and coarse-grained regions. The bimodal grain structure exhibited excellent combination of high strength and high plastic strain.

Tanaka et al. [114] investigated the synthesis of Fe and graphite in the composition range of 0.79 – 4.1 at. % C. They noted that TEM showed the fine lamellar structure for MA powder of

0.79, 1.15 and 1.38 at.% C after 200 h of milling time which confirmed alloying at the nano-level size. They also reported that the Fe_3C phase had formed after 2000 h of MA for a carbon content of 0.79 – 1.15 at.%. On the other hand, the Fe_7C_3 phase had formed after 2000 h of MA for carbon content of 0.3 wt.% C. They reported formation of fine paramagnetic particles by the Mossbauer spectroscopy method for powder mixtures having 3.6 – 4.1 at.% C after 2000 h of milling time.

Fe- Fe_3C composites with a carbon content of 4.5 at. % C were also synthesized by Arik and Turker [115]. They had started with an elemental blend of Fe and C powders and mechanically alloyed them for 5 h. From the SEM images, they noted that the Fe powder which was spherical in shape with an average particle size of about 142 μm had changed into flake-like shape after 2.5 h of milling. Subsequent milling for up to 5 h resulted in a refined and homogenized structure. They reported that the powders showed an increase in Fe_3C content with increasing sintering temperatures. At a sintering temperature of 1125 °C, only 10 % of Fe_3C was present, compared to 40% and 50% on increasing the temperatures to 1150 and 1175 °C, respectively. Since MA is a common method for the synthesis of nanocrystalline or amorphous microstructures, Chen et al. [116] synthesized Fe-C alloys starting from elemental Fe and graphite powders. On milling the powder mixtures with 0.93 – 6.19 at. % C, the authors noted that only the peaks corresponding to ferrite were observed after 100 h of milling. By measuring the lattice parameters of the ferrite phase using XRD methods, the authors reported that the carbon content within the grain interiors of ferrite was ranging from 0.4 to 0.9 at. % . Rochman and Sueyoshi [117] mechanically alloyed pure Fe and graphite with hypo-eutectoid compositions (1.84 and 2.74 at. %C) up to 300 h of milling. The authors noted that during MA, refinement of crystallite size, formation of supersaturated Fe solid solution and Fe-C amorphous phase occurred first up to 200 h of milling.

Moreover, with increasing milling time, these phases started to transform to more stable phases such as carbides. On subsequent consolidation using the hot pressing (HP) method at different temperatures (610, 730 and 800 °C), they noted that at 610 °C, very fine Fe₃C phase, with sub-micron size, precipitated in the fine ferrite grains. This compact exhibited low mechanical properties because of low sinterability. With further increase in the sintering temperature (e.g., at 730 °C), the strength reached the maximum value. At 800 °C, the strength decreased because coarsening of the microstructure had occurred.

Cementite is one of the most important phases in steels determining its mechanical properties. Even though it is known to be a metastable phase at all temperatures with respect to graphite, it is quite “stable” and does not decompose to its constituent elements. Therefore, its synthesis and mechanical characterization have been attempted through MA [118-126]. By mechanically alloying a mixture of Fe and 25 at.% C, it was possible to obtain the cementite phase. The time required for the formation of the cementite phase was longer in low-energy mills and shorter in high-energy mills. Depending on the milling conditions, the reported crystallite size varied from as small as 3 nm [126], or 4 nm [125] to about 0.5 µm [121]. Occasionally, other minor phases such as ferrite and graphite were also noted. The properties of the compact were measured after spark plasma sintering of the milled powder. The measured microhardness was 1000 HV. The room temperature compression strength was measured as 2.76 GPa, and continued at the same level up to 300 °C, beyond which it showed a decrease to 1.39 GPa at 500 °C. Other physical properties were also measured [119]. The hardness and Young’s modulus of the cementite increased with alloying additions in the order of V, Cr, Mn, and Mo [120, 121]. Yelsukov et al. [123] showed that an amorphous Fe-C phase had formed prior to formation of the Fe₃C phase.

Tokumitsu et al. [122] reported that milling of Fe-C powder blends in the composition range of 25 to 50 at.% C resulted first in the formation of a supersaturated solid solution of α -Fe with the bcc structure. On continued milling, the Fe_3C phase with the orthorhombic structure had formed, which on further milling transformed to the hcp structure, which is a high-pressure phase stable at over 11.54 GPa pressure at room temperature.

In this chapter we describe the results on the synthesis of Fe-0.8 wt.% C (eutectoid steel) and Fe_3C (cementite) through MA methods.

5.2 Results

5.2.1 X-Ray Diffraction Investigations

The sequence of X-ray diffraction patterns after milling of Fe-0.8 wt.% C powder blend, as a function of milling time, is shown in Figure 5.1. The XRD pattern of the unmilled powder blend (0 h of milling) shows the presence of diffraction peaks of pure C, i.e., 002 and 100, and the peaks of pure Fe, viz., 110, 200 and 211. It may be noted in the XRD patterns that the Fe diffraction peaks broadened and their intensity decreased with increasing milling time. These two effects can be ascribed to the severe plastic deformation experienced by the powder particles during MA, which leads to a decrease in the particle and crystallite size and increase in the lattice strain with increasing milling time. It was observed that the C diffraction peaks could not be detected after milling the powder for 15 h. Also, the Fe peak positions shifted to lower angles with increasing milling time. For example, the 110_{Fe} peak angle (2θ) shifted from 44.757° at 0 h to 44.698° at 5 h, and then to 44.600° at 15 h and finally to 44.500° at a milling time of 30 h.

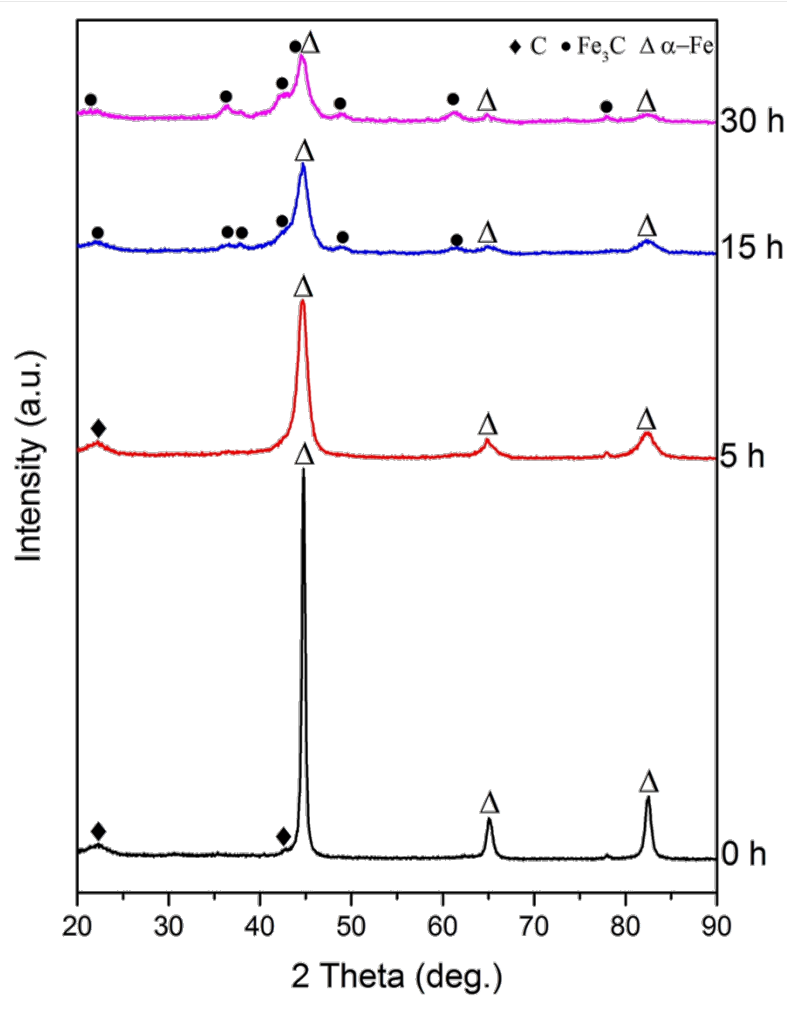


Figure 5.1: XRD patterns of Fe-0.8 wt.% C powder blend as a function of the milling time.

New XRD peaks started appearing at 15 h of milling, identified as the Fe₃C phase. Further, the amount of the Fe₃C phase increased with increasing milling time as shown by the increasing number of diffraction peaks. Figure 5.2 shows an enlarged view of the XRD pattern of the powder milled for 30 h, from which it is obvious that the Fe₃C phase coexisted with α-Fe. The Fe₃C phase has the orthorhombic crystal structure with the lattice parameters $a = 0.50896$ nm, $b = 0.67443$ nm, and $c = 0.45248$ nm [127].

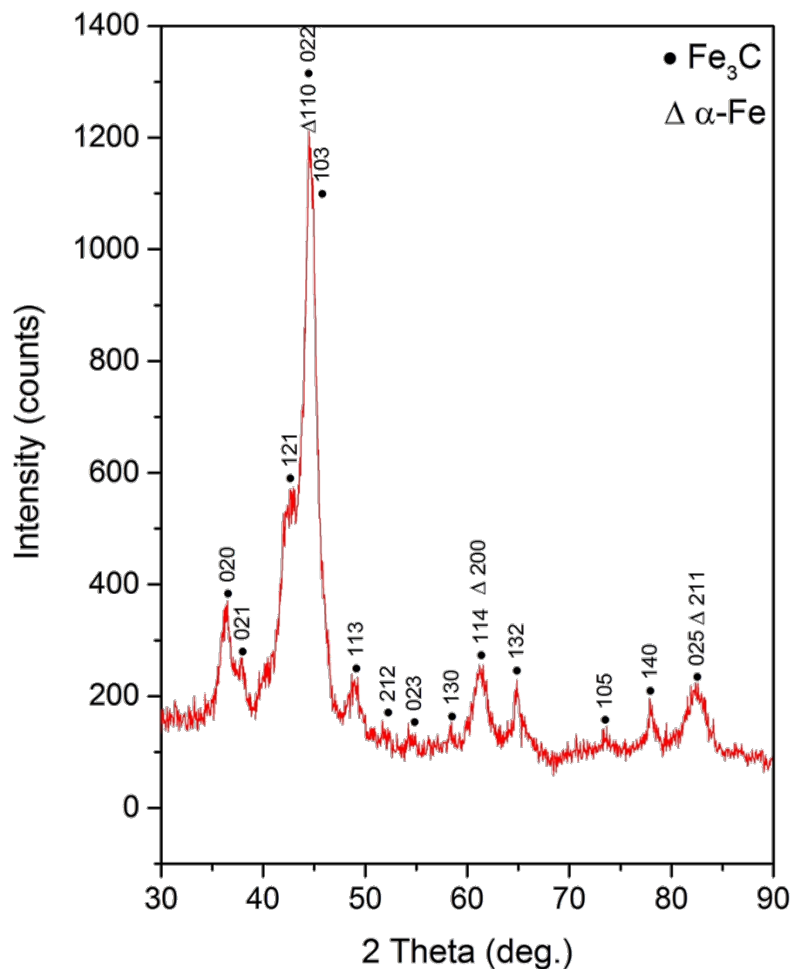


Figure 5.2: XRD pattern of the Fe-0.8 wt.% C powder blend milled for 30h, showing formation of the Fe_3C phase coexisting with $\alpha\text{-Fe}$.

Figure 5.3 shows the XRD patterns of the Fe-7.0 wt. % C powder blend after milling for different times. Again, the XRD pattern of the unmilled powder blend (for 0 h of milling) indicates the presence of diffraction peaks of pure C and Fe. The results for the Fe-7.0 wt.% C powder blend were very similar to the Fe-0.8 wt.% C powder blend, except for more Fe_3C diffraction peaks after milling the powder for 15 h. Furthermore, the XRD patterns indicated that the Fe_3C peaks became more prominent on milling for 30 h as shown in Figure 5.4.

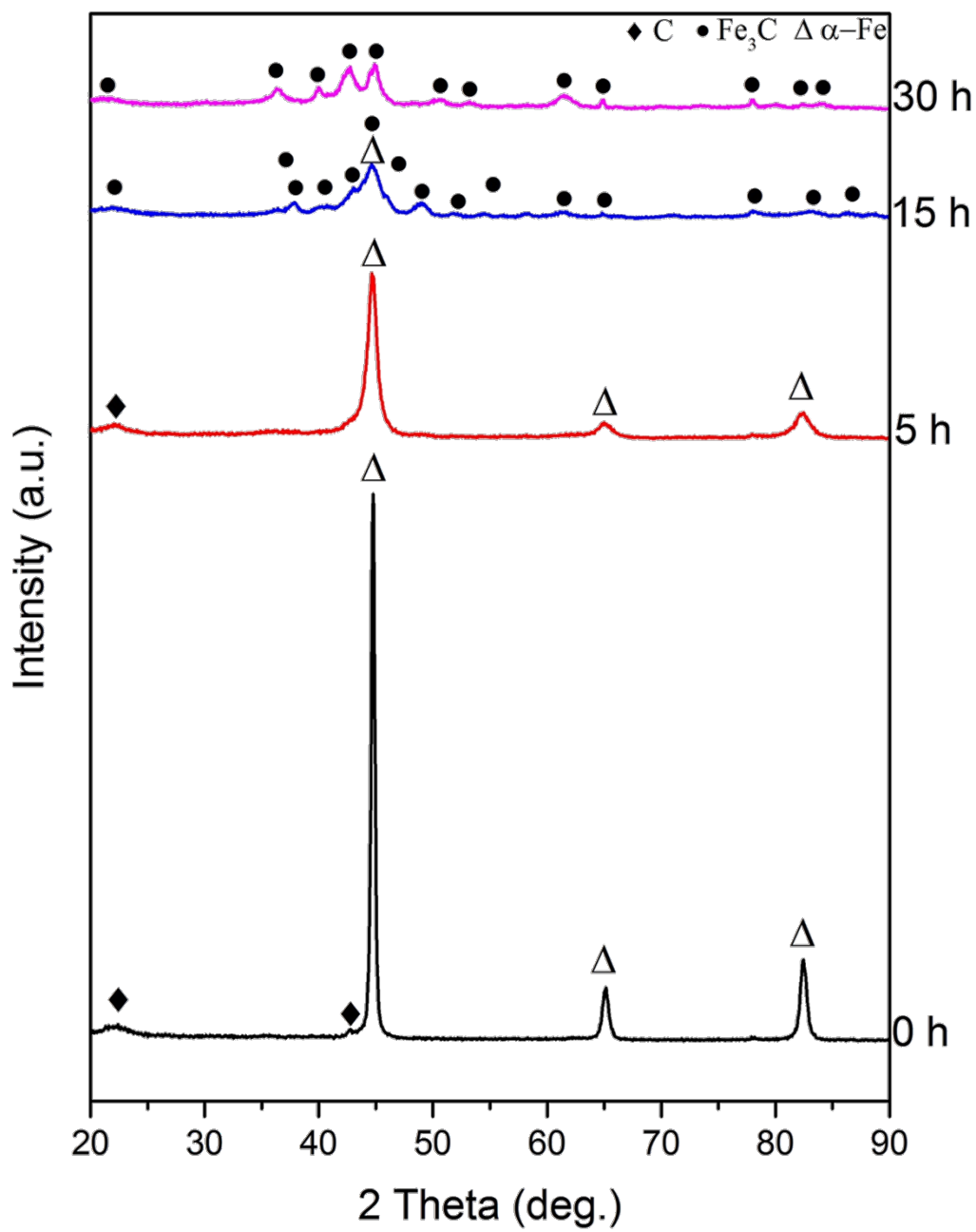


Figure 5.3: XRD patterns of the Fe-7.0 wt.% C powder blend as a function of the milling time.

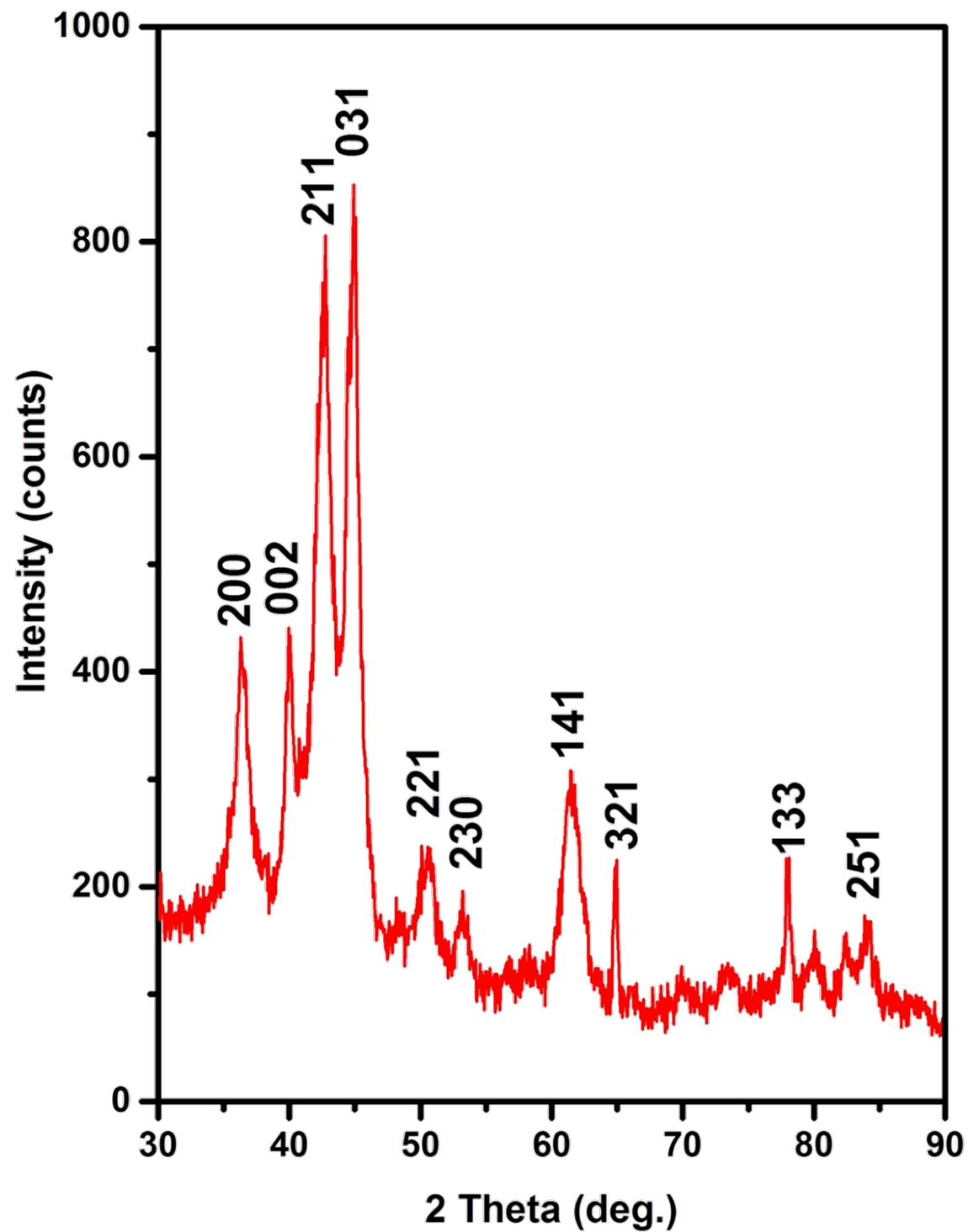


Figure 5.4: XRD pattern of the Fe-7.0 wt.% C powder blend milled for 30 h, showing homogenous formation of the Fe₃C phase.

Figure 5.5 shows the plot of the crystallite size and lattice strain vs. milling time for both Fe-0.8 wt. % C and Fe-7.0 wt. % C powder blends. In the initial stages of milling, the crystallite size in both the compositions decreased rapidly with time and then reached a saturation value of around 7 nm for the Fe-0.8 wt. % C powder blend and about 9.5 nm for the Fe-7 wt. % C powder blend. On the other hand, the lattice strain increased continuously with milling time due to generation of dislocations and other crystal defects as a result of plastic deformation of the powder. The maximum lattice strain reached was 1.6 % at 20 h and 1.3 % at 10 h of milling time for Fe-0.8 wt. % C and Fe-7.0 wt. % C, respectively.

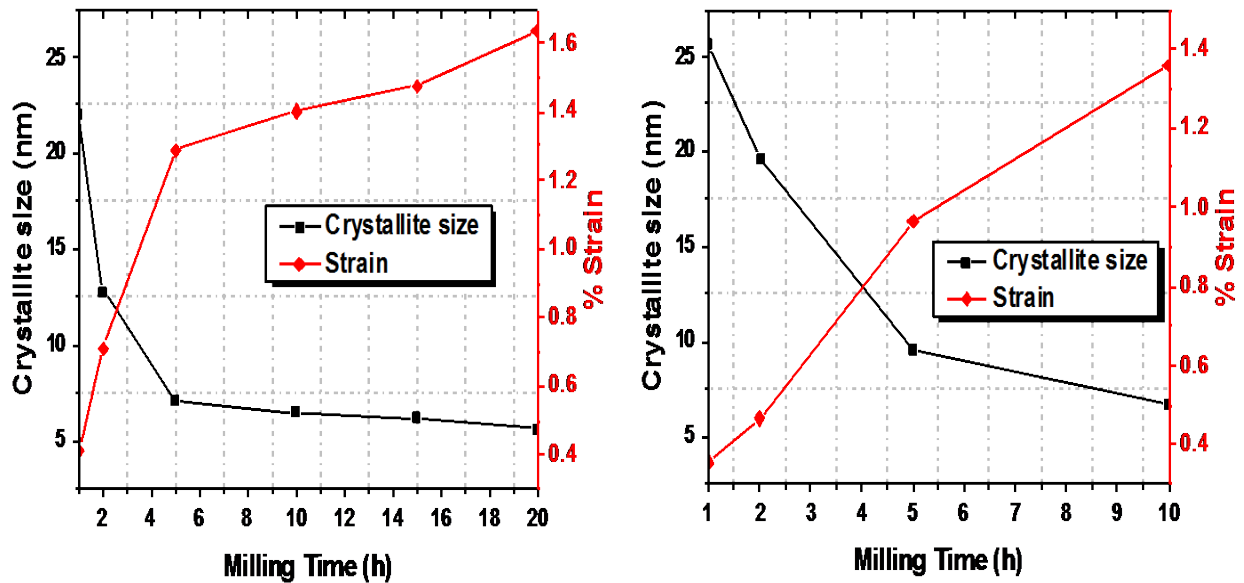


Figure 5.5: Plot of crystallite size and lattice strain for (a) Fe-0.8 wt. % C and (b) Fe-7.0 wt. % C powder blends as a function of milling time.

Figure 5.6 presents the XRD patterns of the Fe-0.8 wt.% C powder milled for 30 h, after sintering at 600 °C for 15 min. The α -Fe and Fe₃C peaks were found to be sharper indicating the

presence of larger grains in the sintered sample. This also suggests that the nature of the phases present is not different between the as-milled and sintered conditions.

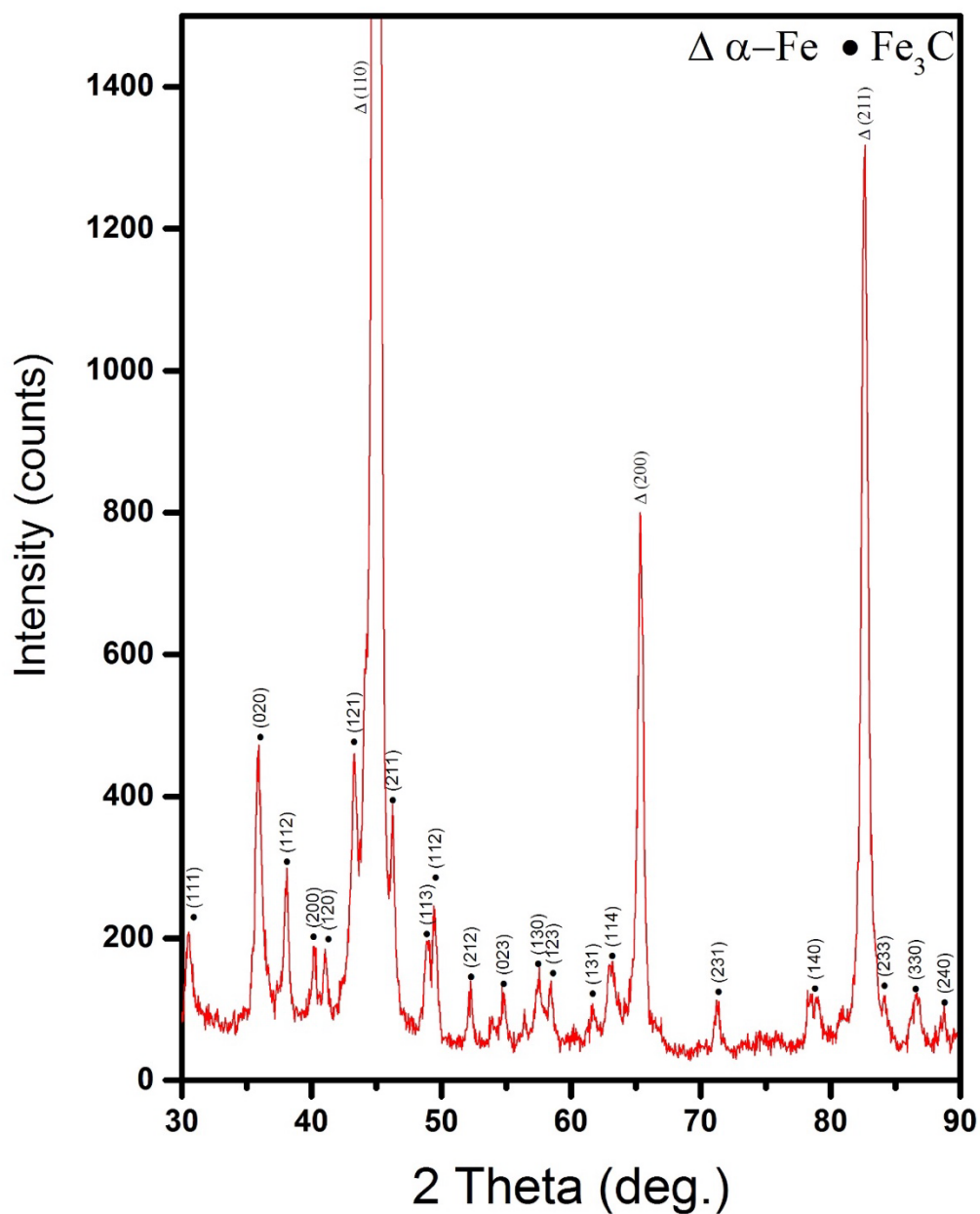


Figure 5.6: XRD pattern of the Fe-0.8 wt.% C powder milled for 30 h after sintering at 600 °C for 15 min under a pressure of 70 MPa showing formation of the Fe_3C phase coexisting with α -Fe.

As mentioned above, the Fe 110 peak positions changed as a function of the milling time, suggesting that a solid solution of C in Fe had formed. The lattice parameter of the solid solution was calculated from the peak positions. Using the relationship between the lattice parameter and carbon content, proposed by Fasiska and Jeffrey [127], the carbon content in the solid solution was estimated [128]:

$$a = (0.28664 \pm 0.0001) + (8.4 \pm 0.8) \times 10^{-4}C \quad (5.1)$$

where a is the lattice parameter (nm) and C is the carbon content (wt.%) in the iron solid solution.

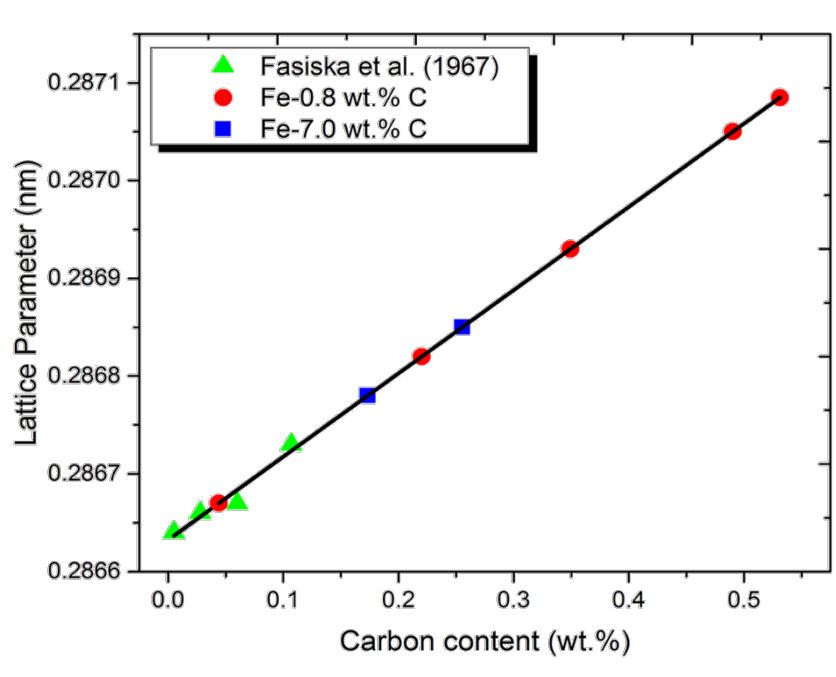


Figure 5.7: : Variation of the lattice parameter of the Fe (C) solid solution with C content based on ref. [128].

Figure 5.7 shows the plot of the the lattice parameter as a function of the carbon content for the Fe-0.8 wt.% C powder blend milled for 1 to 15 h and for the Fe-7.0 wt.% C powder blend

milled for 1 to 2 h. In both the cases, the lattice parameter increased with increasing milling time, in the case of Fe-0.8 wt.% C, from 0.28664 nm for pure Fe to 0.28708 nm after 15 h of milling whereas the lattice parameter of α -Fe in the Fe-7.0 wt.% C increased up to 0.28685 nm after 2 h of milling. As shown in Figure 5.7, the C content in the solid solution was estimated to be about 0.53 wt.% in the Fe-0.8 wt.% C composition after 15 h of milling and about 0.26 wt.% in the Fe-7.0 wt.% C composition after 2 h of milling. It can be concluded that mechanical processing has increased the solid solubility limit of the Fe-C system because the maximum solid solubility of C in Fe under equilibrium conditions is about 0.006 wt.%. It is clear from Figure 5.8(a) and (b) that the lattice parameters (and hence the C content) increased with increasing milling time due to the severe plastic deformation experienced by the powder particles during MA, which leads to an increase of more C atoms dissolved in the Fe lattice.

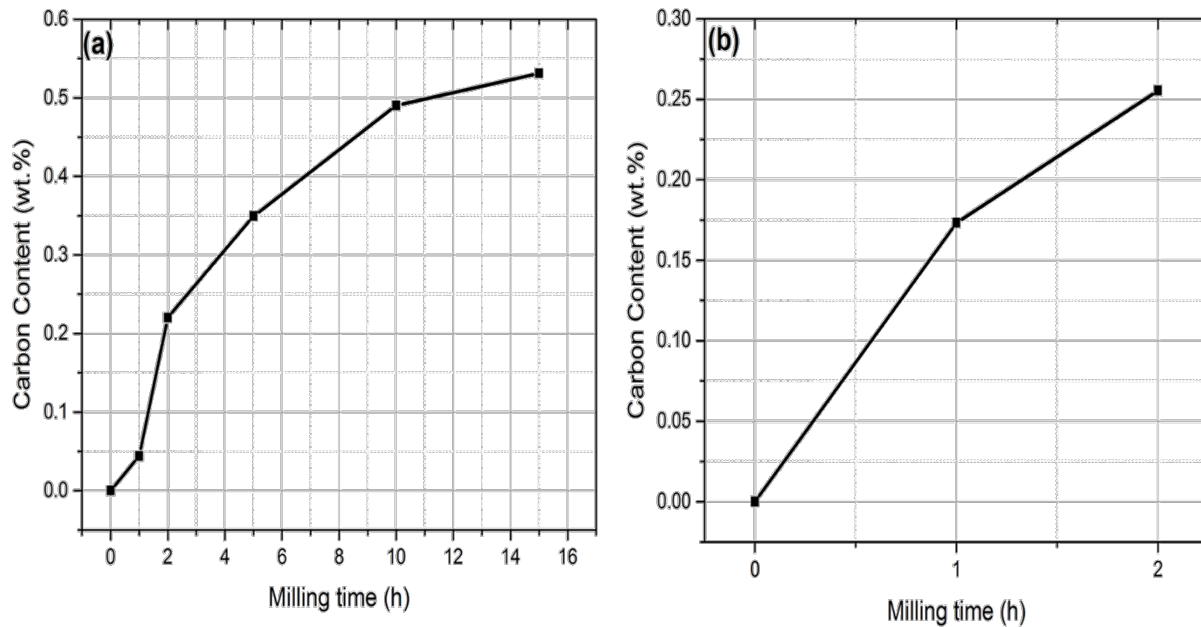


Figure 5.8: Changes in the carbon content with milling time for (a) Fe-0.8 wt.% C powder blend and (b) Fe-7.0 wt.% C powder blend, as a function of milling time.

The Fe_3C peaks were found to be sharper after sintering of Fe-7.0 wt.% C powder (Figure 5.9). indicating the presence of larger grains in the sintered sample. Again, the phases present are not different between the as-milled and sintered conditions. It is interesting to report that the α -Fe peaks have completely disappeared in the Fe-7.0 wt.% C composition which means only a single phase of Fe_3C phase had formed.

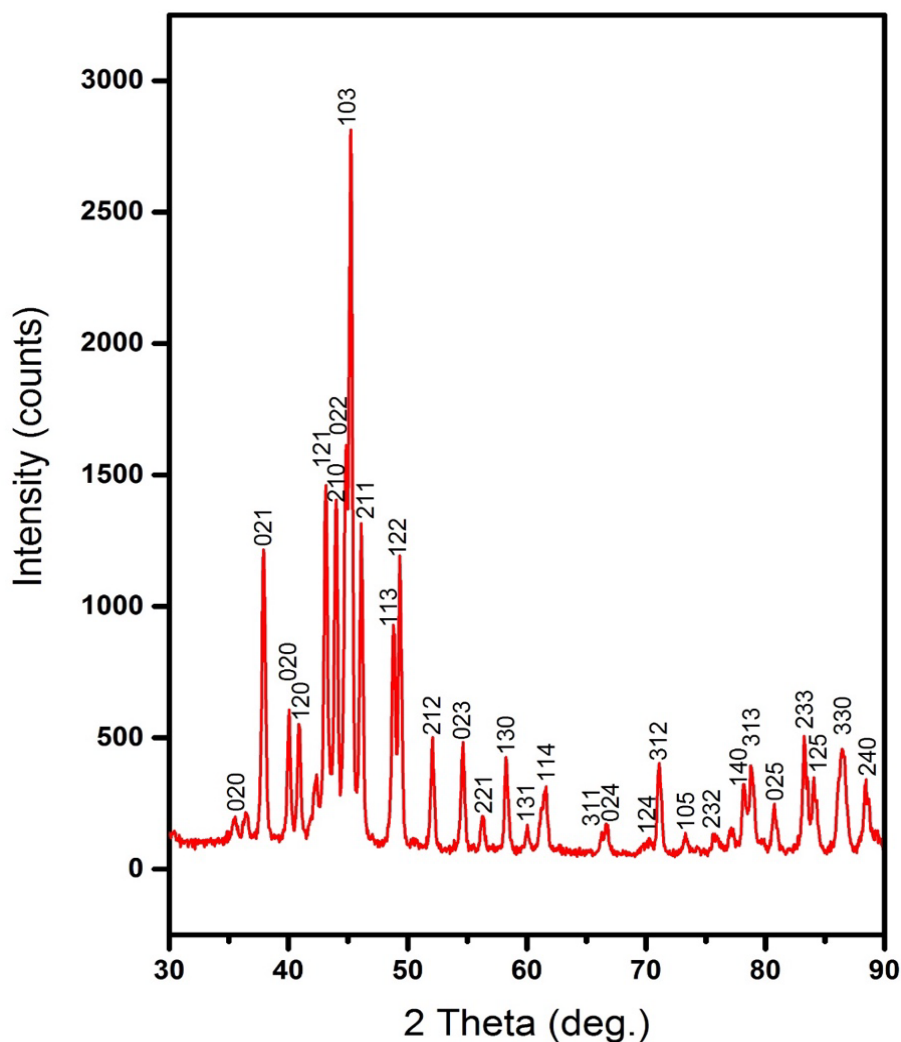


Figure 5.9: XRD pattern of the Fe-7.0 wt.% C powder milled for 30 h, after sintering at 600 °C for 15 min under a pressure of 70 MPa showing formation of only the Fe_3C phase.

The sintered samples of both Fe-0.8 wt.% C and Fe-7.0 wt.% C were put into a sealed quartz tube and heat treated at 900 °C for 1 h. The XRD pattern of Fe-0.8 wt.% C annealed at 900 °C for 1 h, Figure 5.10, shows that the peak widths of α -Fe and Fe_3C phases have decreased, due to grain growth during annealing at high temperatures.

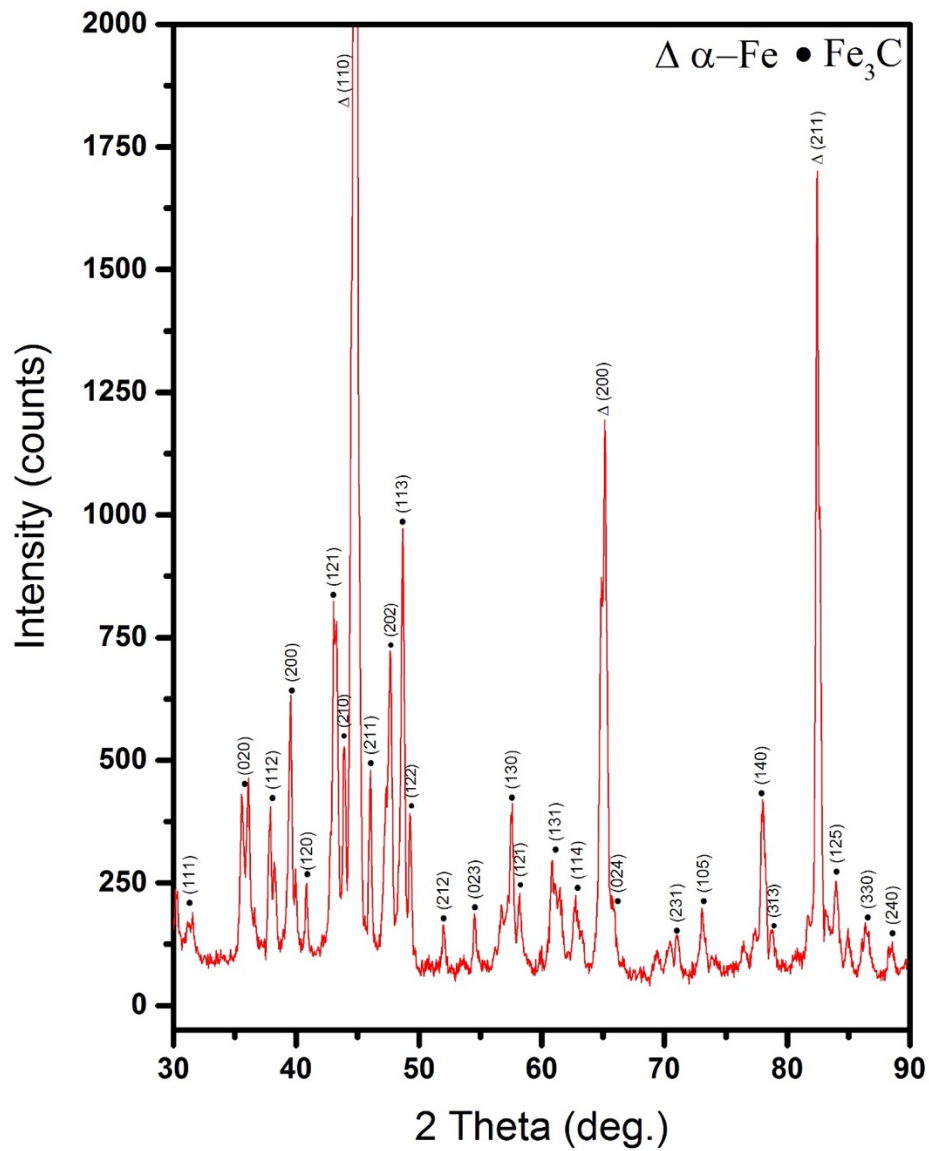


Figure 5.10: XRD pattern of the Fe-0.8 wt.% C after annealing at 900 °C for 1 h showing increase in the sharpness of the α -Fe and Fe_3C phase peaks.

Figure 5.11 presents the XRD pattern of Fe-0.8 wt.% C after heating up to 900 °C for 1 h and quenching into water. It is clear that the martensite phase has formed on quenching and the martensite peaks 101, 110, 002, 200, 112 and 211 are clearly present. The martensite phase has the body-centered tetragonal (BCT) crystal structure with $c/a = 1.0102$ and based on the results in Figure 5.12 [129], the carbon content should be about 0.35 wt.%.

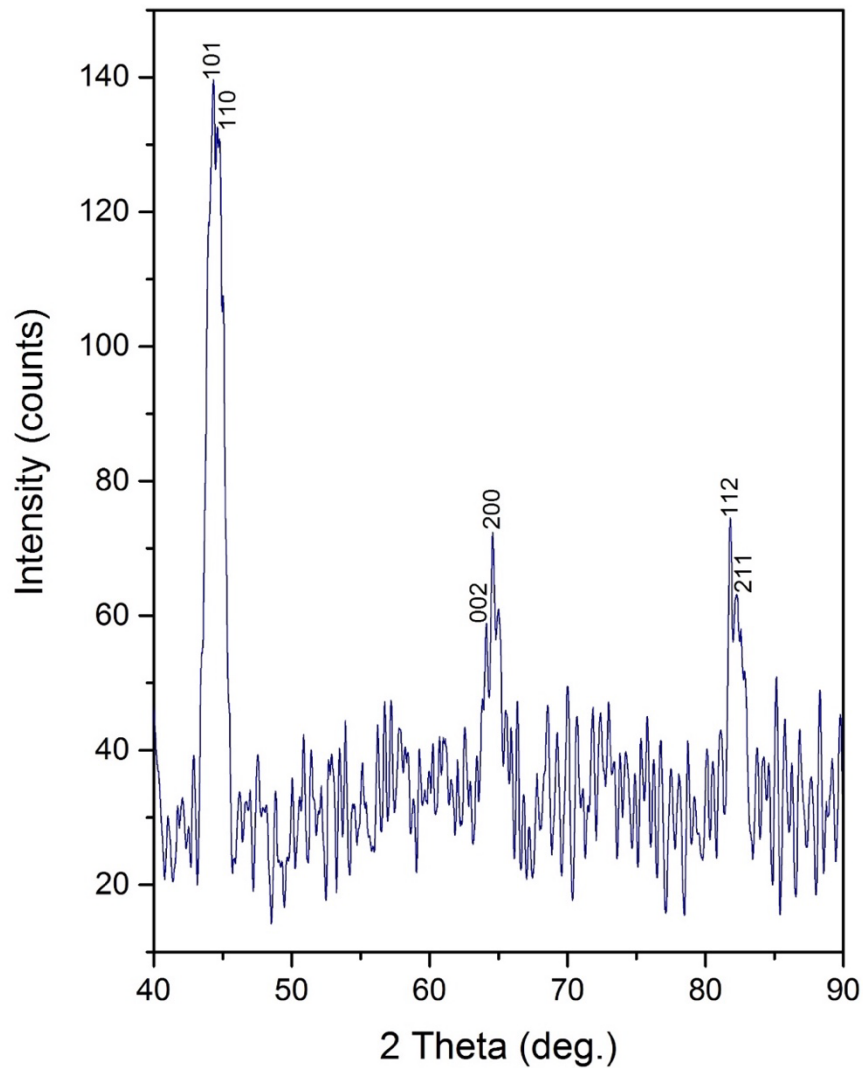


Figure 5.11: XRD pattern of the Fe-0.8 wt.% C after quenching in water showing only the martensite phase.

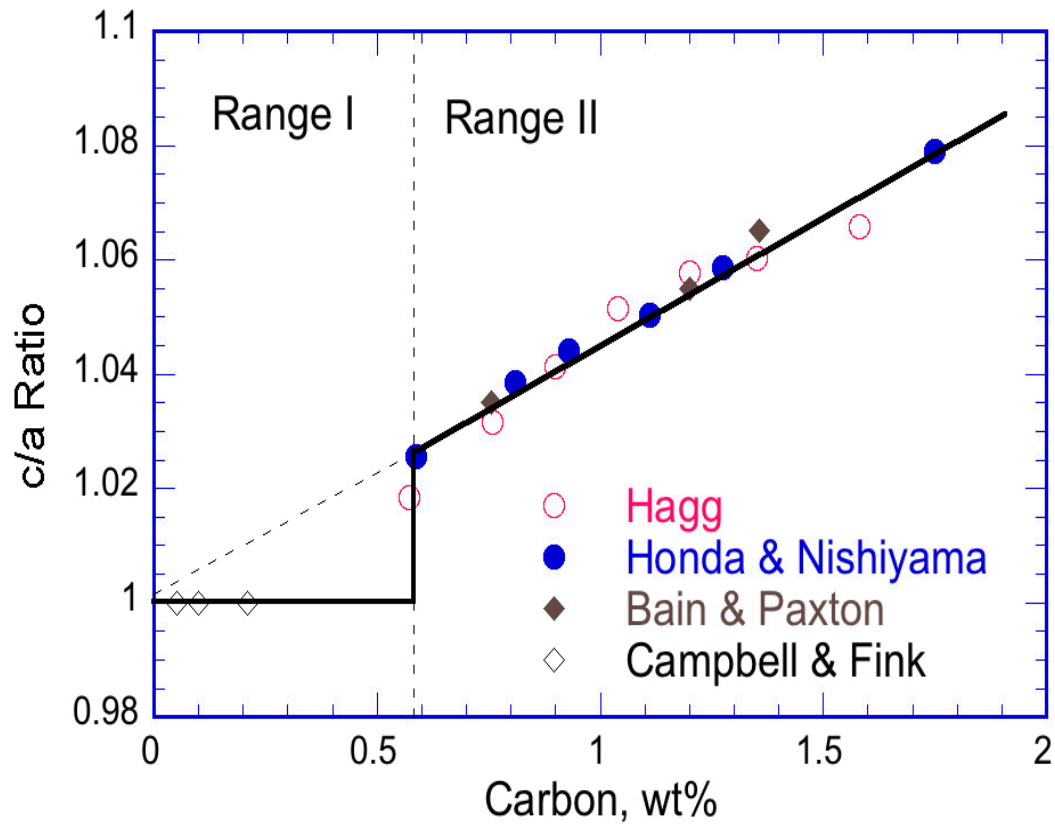


Figure 5.12: c/a ratio vs. carbon content of quenched martensite in Fe-C steels [129].

Figure 5.13 presents the XRD pattern of Fe-7.0 wt.% C of sintered sample after annealing at 900 °C for 1 h. Similar behavior was found during heat treatment of Fe-7.0 wt.% C sintered sample. The sharp diffraction peaks of the α -Fe phase increased during heat treatment, suggesting that the Fe_3C phase started to decompose at high temperature. Such a decomposition has been seen in other studies also [130, 131].

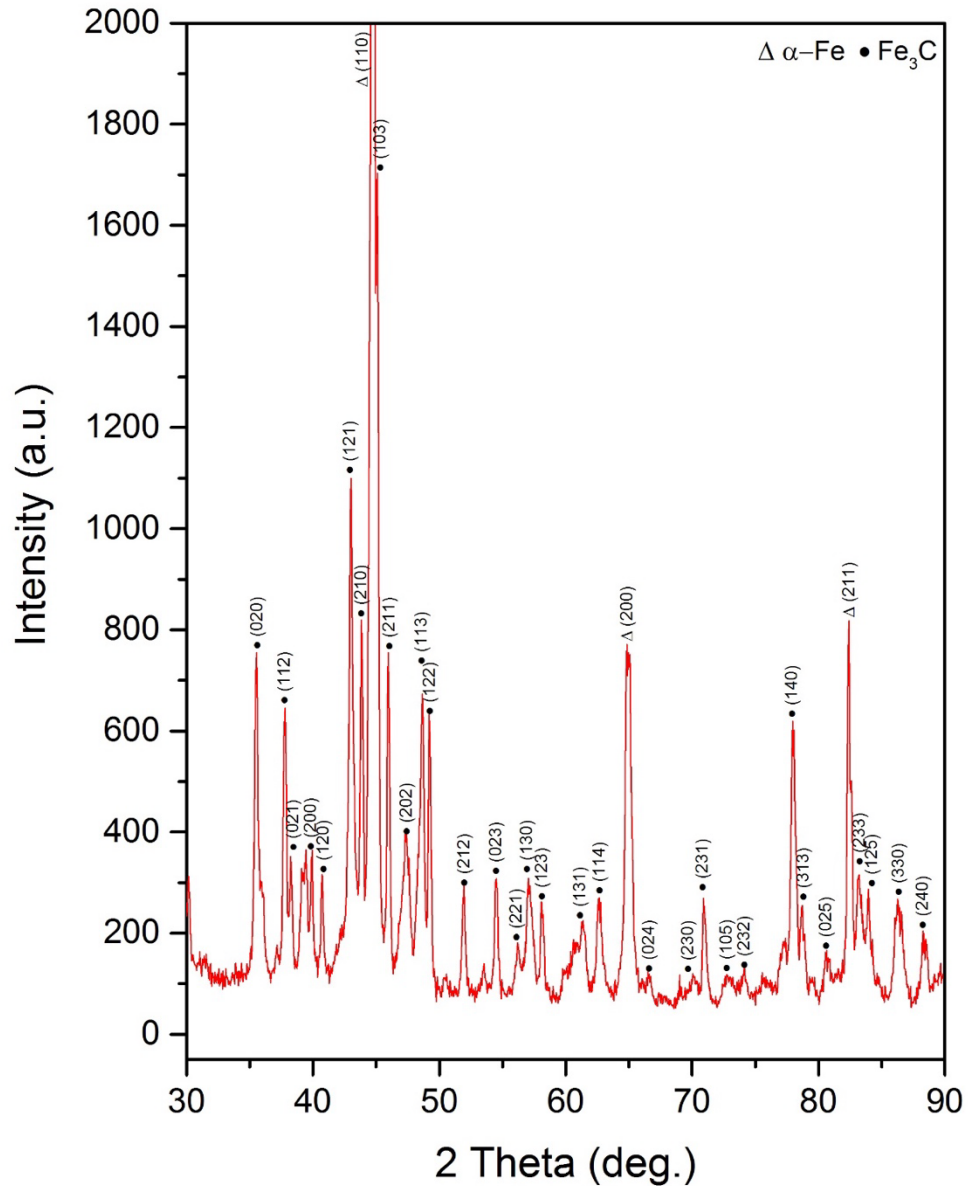


Figure 5.13: XRD pattern of the Fe-7.0 wt.% C of sintered sample after annealing at 900 °C for 1 h showing decomposition of the Fe_3C phase to form $\alpha\text{-Fe}$.

5.2.2 Microstructural Investigation

Figure 5.14 shows the SEM micrographs of the powder blend on milling for different times. Figure 5.14(a) shows the SEM micrograph of the unmilled powder (0 h) wherein the Fe and C powder particles could be identified clearly. It is clear from the micrograph that the pure Fe

particles are spheroidal in shape with an average size of about 10 μm whereas the C particles are irregular and random in size. After 5 h of milling, as shown in Figure 5.14(b), the morphology and distribution of the powder particles is inhomogeneous showing both large and small sized particles distributed non-uniformly due to agglomeration in the initial stages of milling. Figure 5.14(c) shows that the powder particle morphology became more homogeneous after 30 h of milling. The powder particles are of small size, about 2-6 μm .

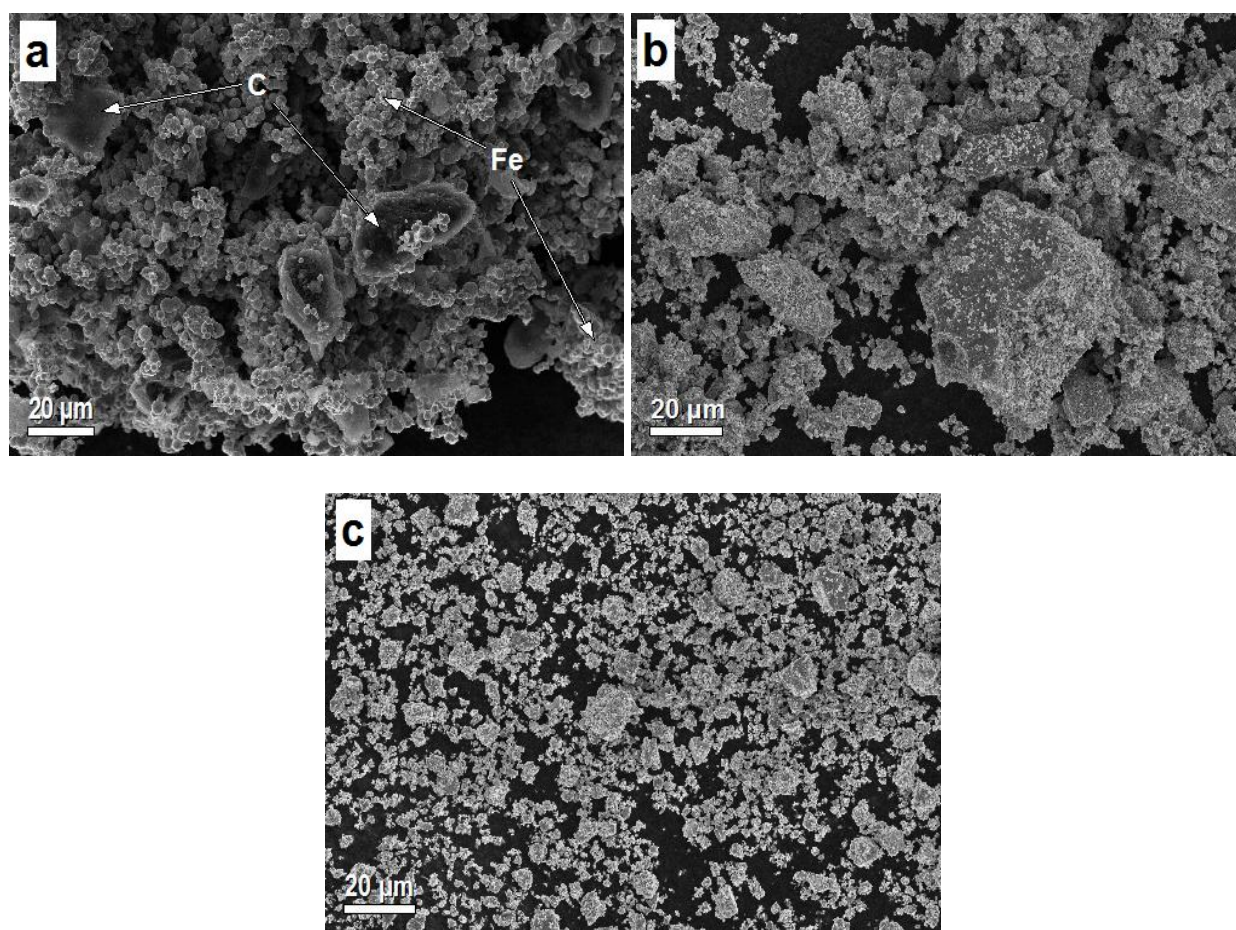


Figure 5.14: Scanning electron micrographs of the powder blend in the (a) as-blended (unmilled condition) showing elemental Fe and C powder particles, (b) after milling for 5 h, showing both large and small sized particles distributed non-uniformly, and (c) after 30 h of milling, when the powder particles became more homogeneous.

Figure 5.15 shows the SEM micrographs of the sintered compact of Fe-0.8 wt.% C after polishing and etching. Figure 5.15(a) represents the low magnification SEM micrograph, showing fully dense sample after spark plasma sintering at 600°C and a pressure of 70 MPa for 15 min, in a vacuum controlled environment. Figure 5.15(b) shows the high magnification SEM in which fine of α -Fe and Fe₃C particles distributed uniformly can be seen. Due to the fact that MA resulted in the formation of finer powder particles with C content distributed homogeneously, it is difficult to see the lamellar structure of α -Fe and Fe₃C phases.

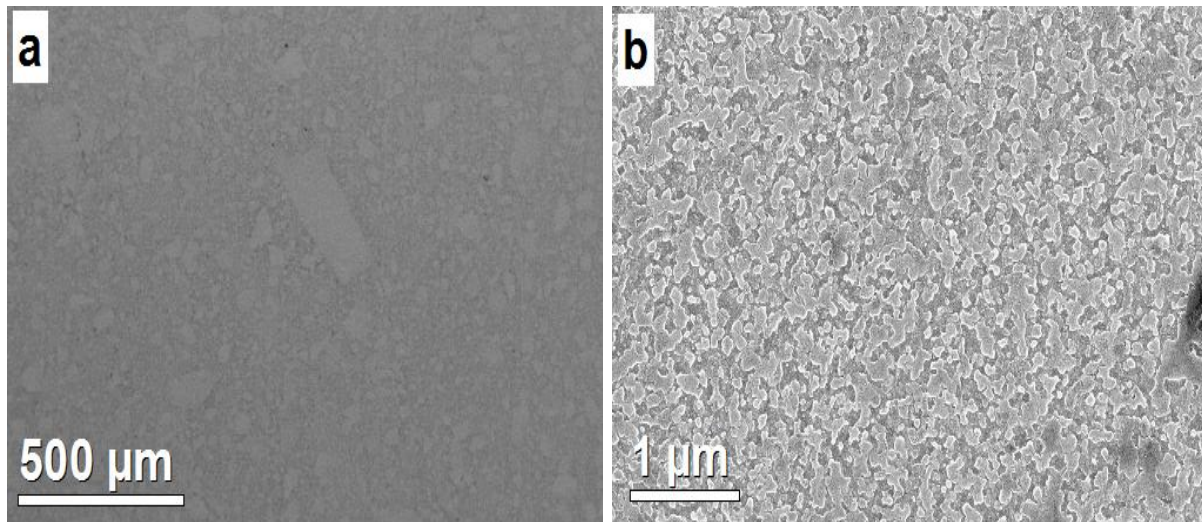


Figure 5.15: (a) Low magnification scanning electron micrograph of Fe-0.8 wt.%C after spark plasma sintering showing fully dense sample (b) high magnification scanning electron micrograph showing α -Fe and Fe₃C phases.

Figure 5.16 shows TEM micrographs of Fe-0.8 wt.% C after sintering. Figure 5.16(a) and (b) represent the bright-field and dark-field TEM images, respectively with low magnification whereas Figure 5.16(c) and (d) at a high magnification. It is clear that the sample has very fine equiaxed grains of about 30 nm of α -Fe and Fe₃C phases.

Figure 5.17 shows the selected area diffraction pattern of Fe-0.8 wt.% C after sintering. The micrograph clearly shows the presence of both the α -Fe and Fe_3C phases, confirming the XRD results.

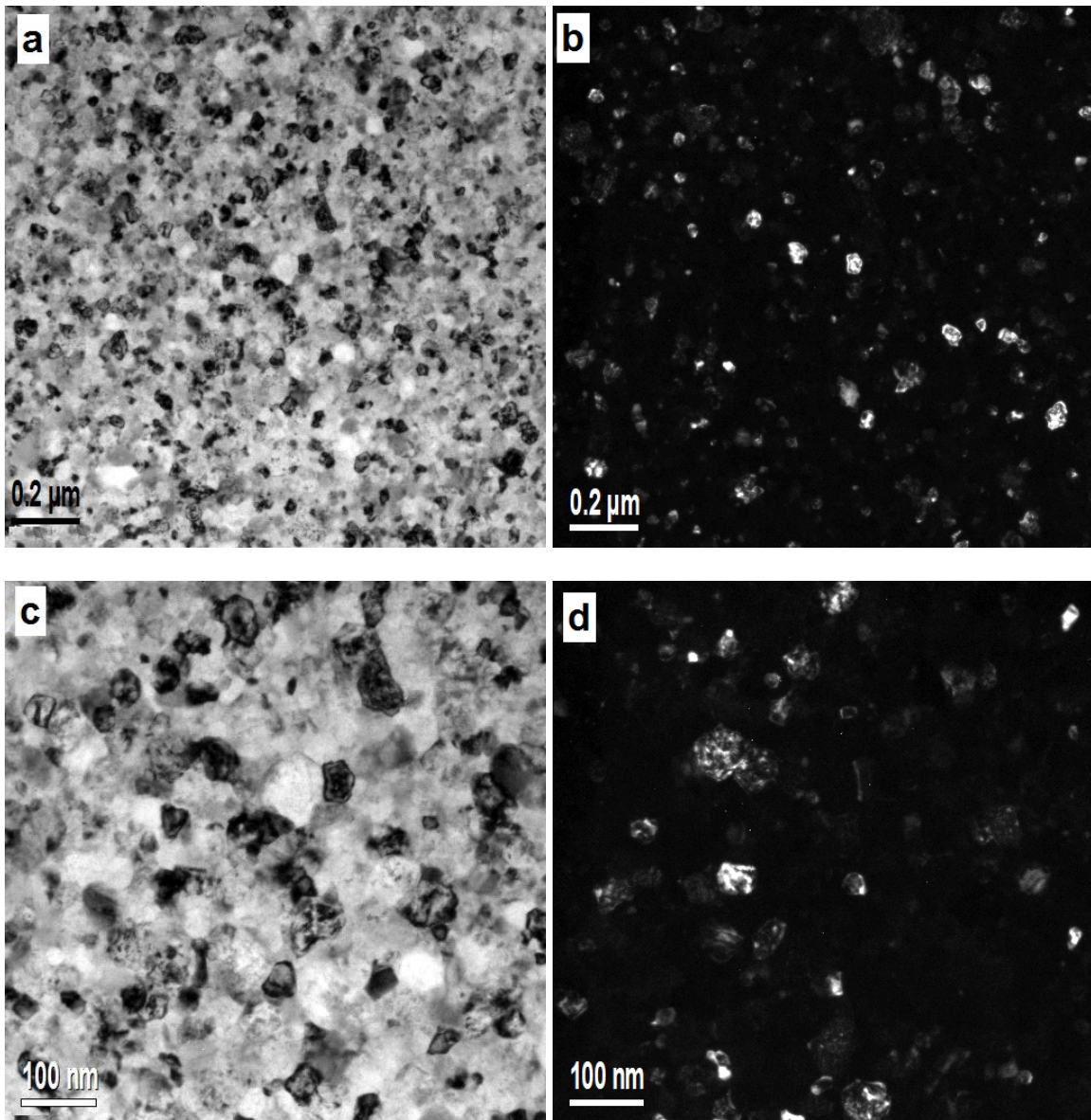


Figure 5.16: Low magnification (a) bright field and (b) dark field TEM micrograph of sintered Fe-0.8 wt.% C. High magnification (c) bright field and (d) dark field TEM micrograph of sintered Fe-0.8 wt.% C sample.

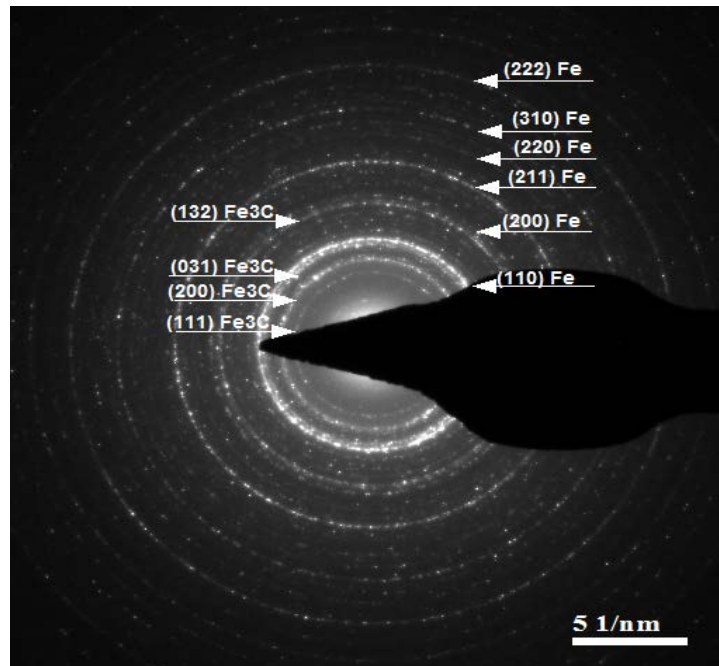


Figure 5.17: Selected area diffraction pattern of Fe-0.8 wt.% C after sintering, showing the presence of the α -Fe and Fe_3C phases.

Figure 5.18 shows the SEM micrographs of Fe-0.8 wt.% C after annealing at 900 °C for 1 h. It can be seen that recovery and recrystallization mechanisms as well as grain growth have occurred during annealing and that the pearlitic structure (eutectoid structure) which consists of alternate layers of ferrite (α -Fe) and cementite (Fe_3C) phases that formed simultaneously during transformation appeared in the sample (Figure 5.18(a) and (b)). The results show a big difference between the as-sintered condition and after annealing, in terms of the microstructure. The as-sintered sample shows the Fe_3C dissolved in α -Fe whereas the redistribution of C atoms by diffusion led to change the microstructure.

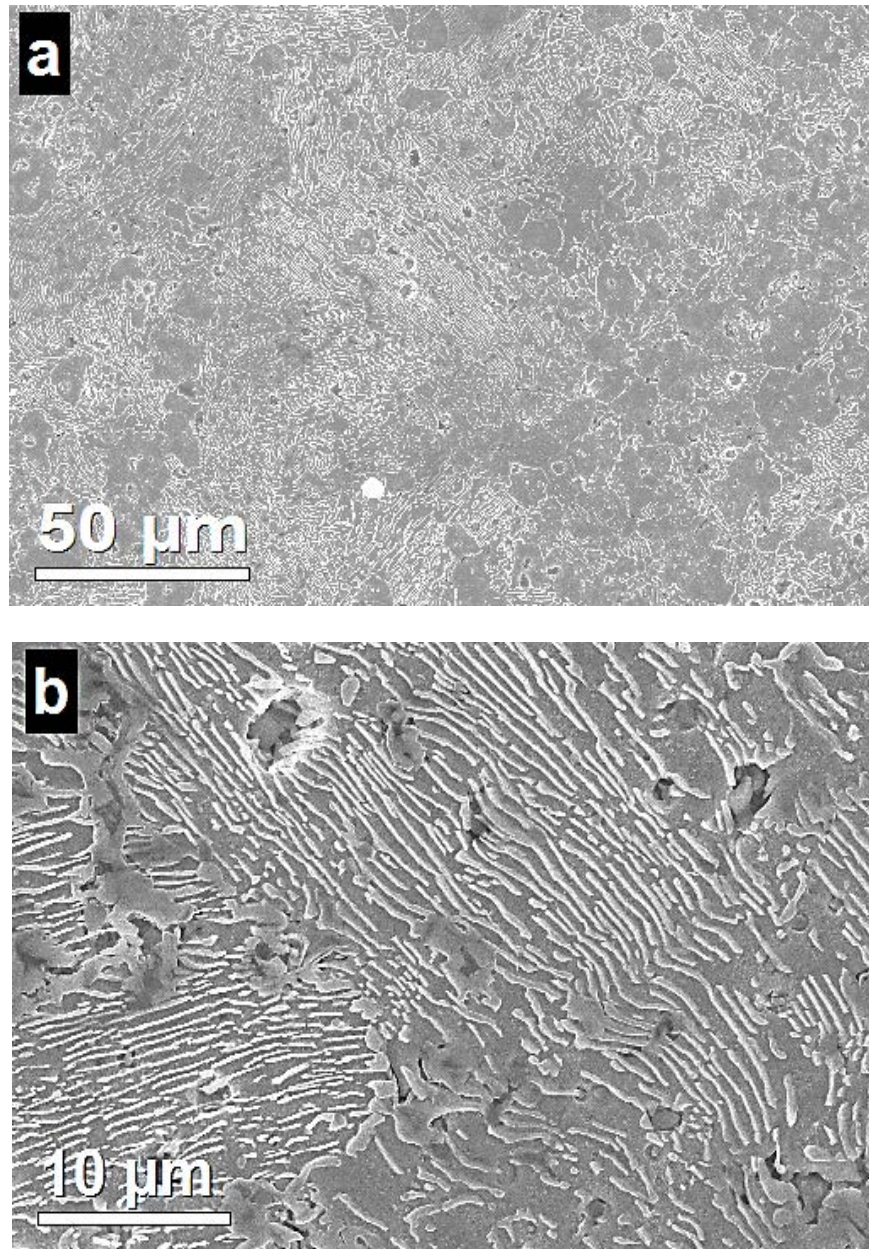


Figure 5.18: Scanning electron micrographs of Fe-0.8 wt.% C after annealing at 900 °C for 1 h (a) Low magnification micrograph with large area of pearlitic structure, and (b) high magnification micrograph clearly showing the lamellar structure of pearlite.

Figure 5.19 shows the EDS scan line of the Fe-0.8 wt.% C sample after annealing when the lamellar structure had appeared. The C and Fe profiles clearly show that the C content is higher

in the cementite lamellae and that it is low in the ferrite lamellae. And, these patterns get repeated frequently because of the presence of alternating layers of ferrite and cementite, that have grown during the annealing process. The layer thickness of Fe_3C is very fine, about $0.13\text{ }\mu\text{m}$.

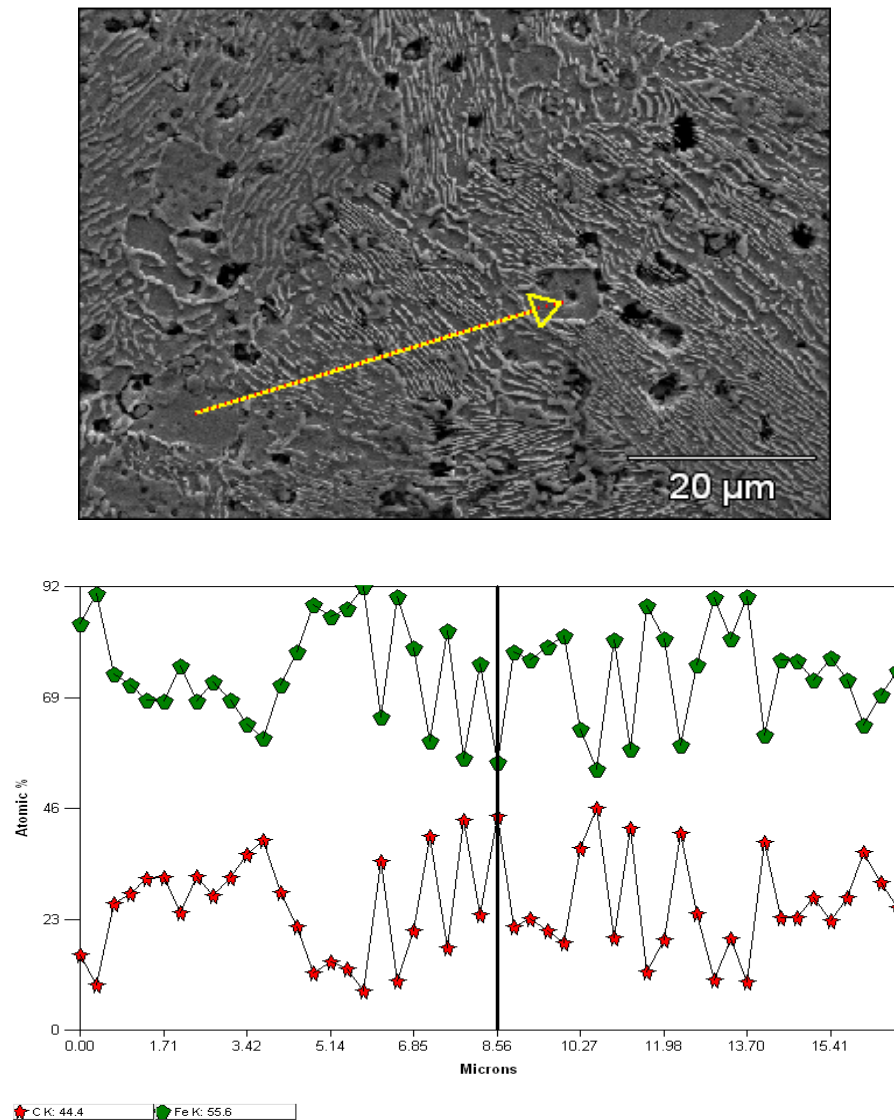


Figure 5.19: EDS elemental concentration profiles along with scan line of the Fe-0.8 wt.% C sample after annealing at $900\text{ }^{\circ}\text{C}$ for 1 h. Increasing and decreasing C contents can be clearly identified in the lamellar structure of pearlite (Fe_3C and $\alpha\text{-Fe}$, respectively).

The bright-field and dark-field TEM micrographs (Figure 5.20(a) and (b)), respectively, show the lamellar structure of α -Fe and Fe_3C phases after annealing 900 °C for 1 h. The thickness of α -Fe phase and Fe_3C phase are about 0.13 μm and 0.15 μm , respectively. This TEM observation confirms the XRD, SEM and EDS analyses.

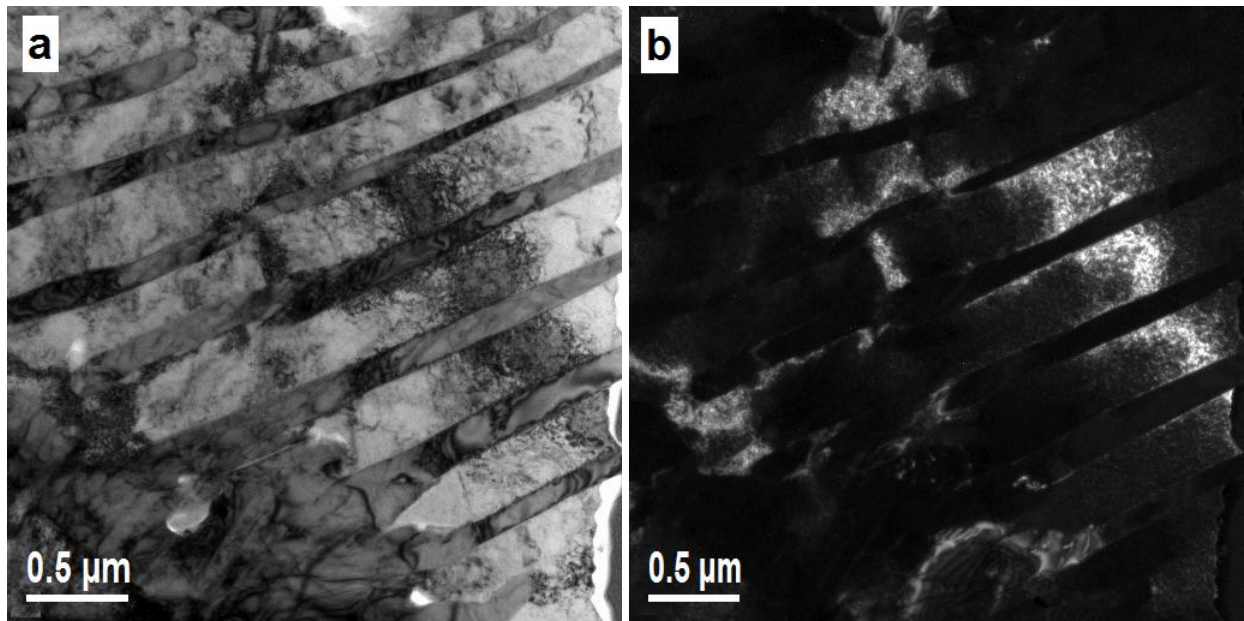


Figure 5.20: TEM micrographs of the Fe-0.8 wt.% C sample after annealing at 900 °C for 1 h (a) bright field (b) dark field, showing the lamellar structure of pearlite (α -Fe and Fe_3C).

Figure 5.21 shows the SEM images of Fe-0.8 wt.% C after quenching in water. It is clear that martensite had formed during quenching. Figure 5.21(a) and (b) show the lenticular structure of martensite. This is because the steel was quenched rapidly from the austenitic zone (900 °C), and there was not enough time for the eutectoidal diffusion-controlled decomposition process to take place. Instead, the steel transformed to martensite by a diffusionless transformation. The

cooling rate is such that majority of C atoms in solution in the γ -Fe remain in solution in the α' -Fe (martensite) phase.

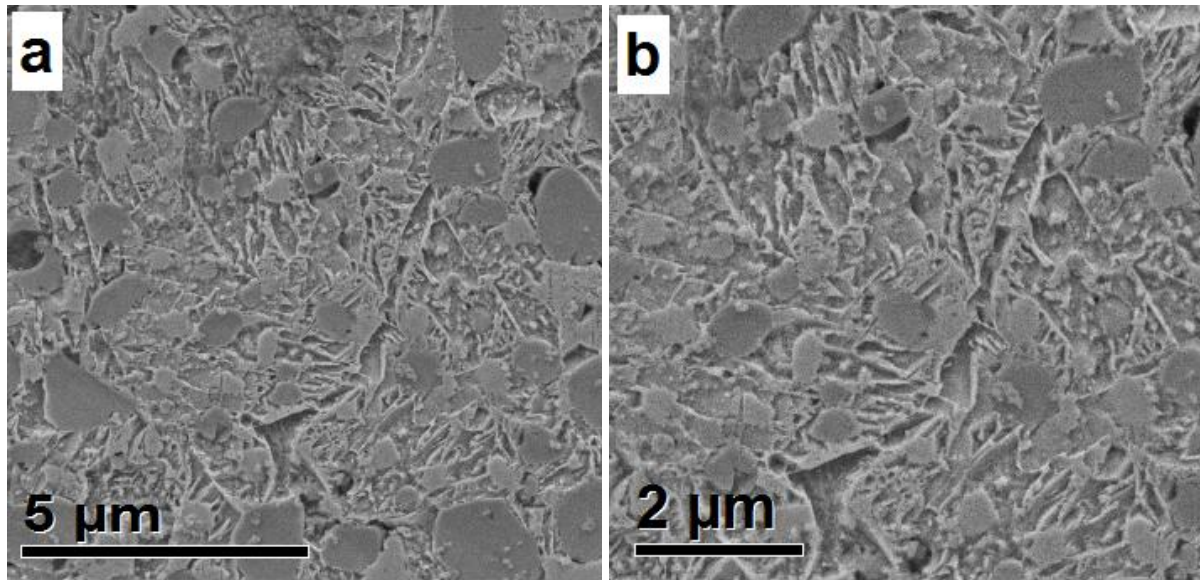


Figure 5.21: Scanning electron micrographs of Fe-0.8 wt.% C after quenching in water (a) Low magnification micrograph and (b) high magnification micrograph showing the lenticular structure of martensite.

Figure 5.22 shows the TEM micrograph of Fe-0.8 wt.% C after quenching in water. The micrograph shows the lenticular structure of martensite. Bright field and dark field images (Figure 5.22 (a) and (b), respectively,) show that the width of the martensite plate is about 0.16 μm.

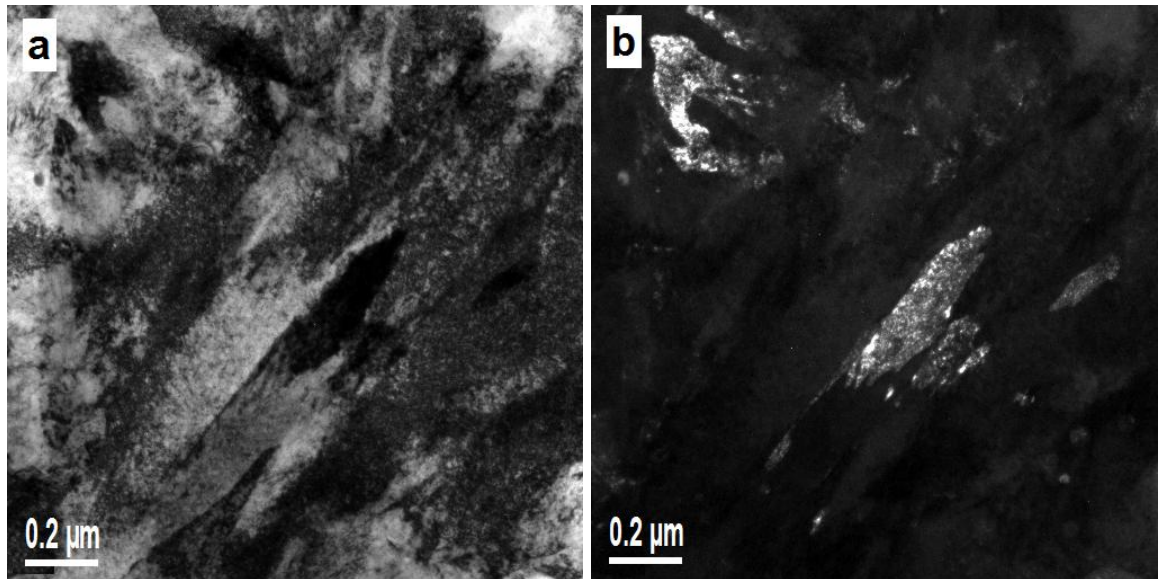


Figure 5.22: TEM micrograph of Fe-0.8 wt.% C after quenching in water (a) bright field (b) dark field micrographs showing the lenticular structure of martensite.

Figure 5.23 shows the SEM micrographs of a sintered compact of Fe-7.0 wt.% C after polishing and etching. Figure 5.23(a) represents the low magnification SEM, showing that the sample is fully dense after spark plasma sintering at 600°C and a pressure of 70 MPa for 15 min, in a vacuum controlled environment. Figure 5.23(b) shows a high magnification secondary-electron micrograph of single phase of Fe_3C . It is well-known that nital does not attack the cementite phase, and therefore the microstructural features are revealed only when the sample contained the two phases of ferrite and cementite due to etching of the ferrite phase. This is the reason why we could not see the grain boundaries in the sample after etching and this supports the XRD results of synthesis of pure Fe_3C through MA and SPS.

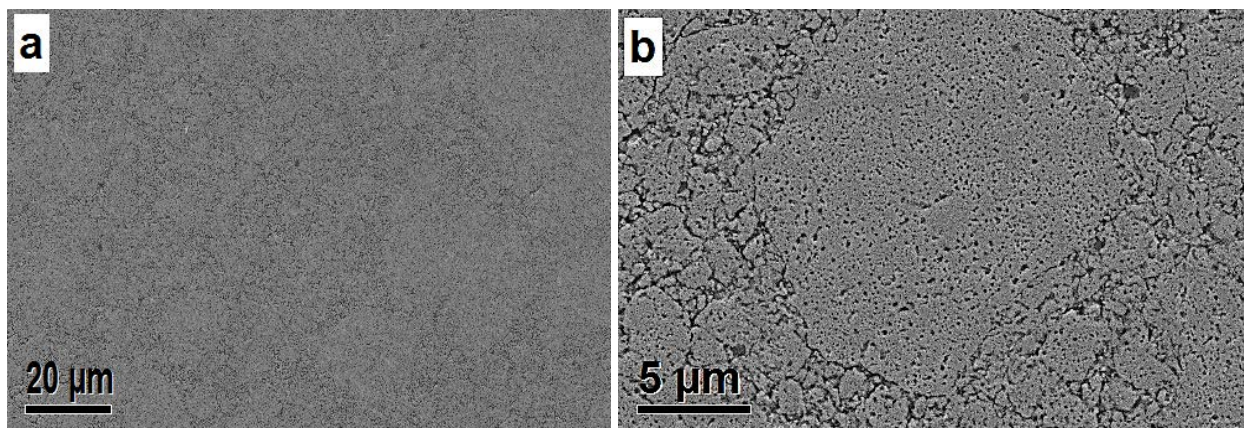


Figure 5.23: (a) Low magnification scanning electron micrograph of Fe-7.0 wt.% C after spark plasma sintering showing fully dense sample (b) high magnification secondary-electron image showing the general morphology.

Figure 5.24(a) shows the low magnification TEM micrograph and (b) the selected area diffraction pattern of the Fe-7.0 wt.% C sample after sintering. The micrograph shows the presence of fine grains 40-60 nm in size, and the selected area diffraction pattern clearly shows the presence of Fe_3C , confirming the results of XRD and SEM. However, on annealing the Fe-7.0 wt.% C sample at 900 °C for 1 h, the TEM micrograph (Figure 5.24(c)) shows that grain growth has occurred during annealing (the grain size now is in the range of 200-500 nm). The selected area diffraction pattern (Figure 5.24 (d)) shows the presence of both the $\alpha\text{-Fe}$ and Fe_3C phases. The effect of grain growth may also be seen in the diffraction pattern where the rings are very spotty.

Electron energy loss spectroscopy (EELS) was used to investigate the chemistry of the as-sintered sample and also after annealing of Fe-7.0 wt.% C. The results show that there is loss of C during annealing. The Fe and C contents are about 68.53 at.% and 31.47 at.%, respectively in the as-sintered sample, which is somewhat similar to what we started with as a powder blend. On the other hand, the EELS analysis of the annealed sample, shows 80.15 at.% Fe and 19.85 at.% C.

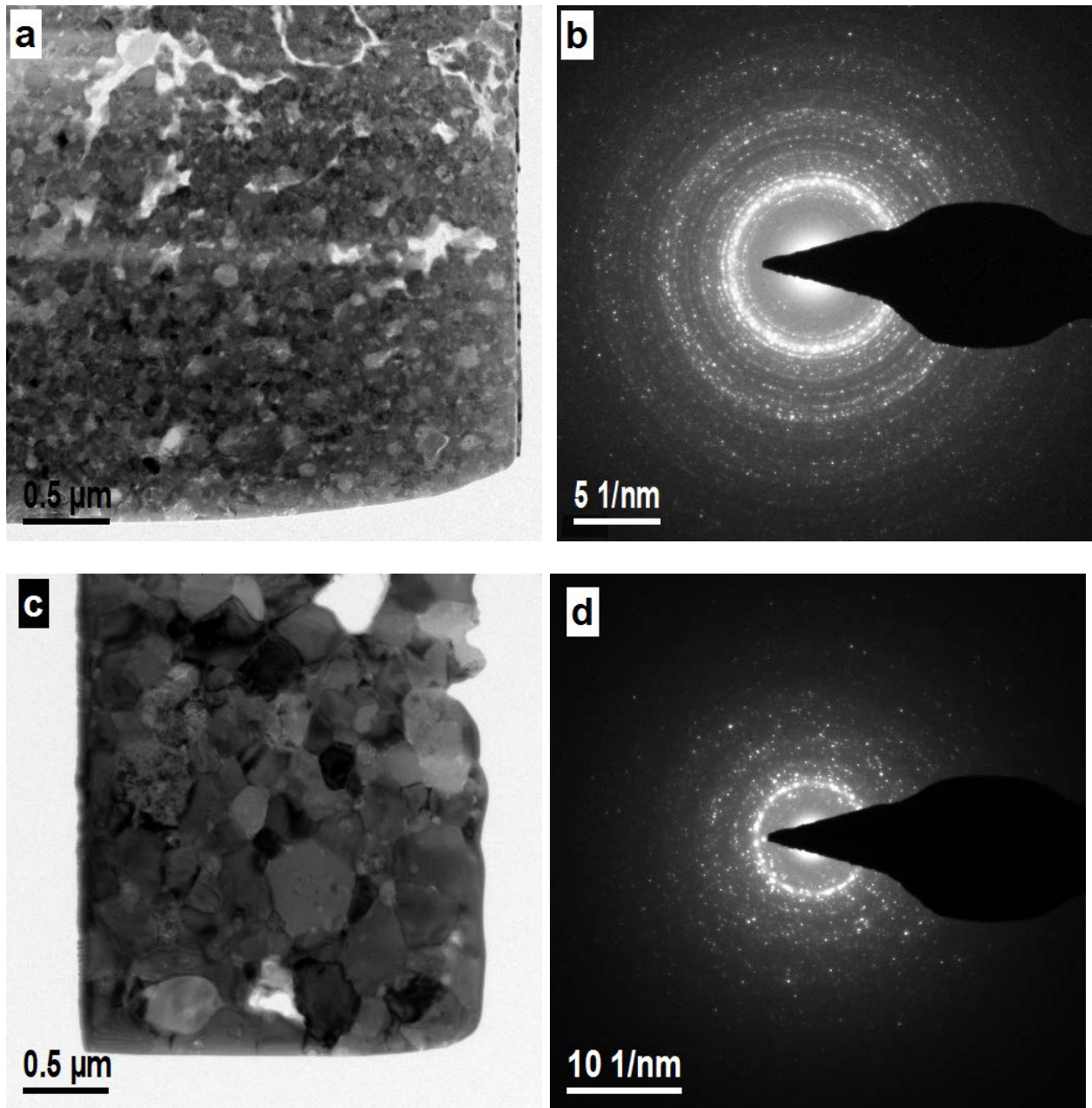


Figure 5.24: (a) TEM micrograph of sintered Fe-7.0 wt.% C, (b) selected area diffraction pattern, showing only the Fe₃C phase, (c) TEM micrograph of Fe-7.0 wt.% C after annealing at 900 °C for 1 h, and (d) selected area diffraction pattern after annealing, showing the both α-Fe and Fe₃C phases.

5.2.3 Microhardness Investigation

The microhardness measurements were performed on samples of Fe-0.8 wt. % C and Fe-7.0 wt.% C in the as-sintered condition and after heat treatment also. Table 5.1 shows the microhardness measurement of Fe-0.8 wt.% C in different conditions and compared with normal values of steel of 0.8 wt.% C content. The sintered sample shows a high hardness value, suggesting that grain refinement and the presence of a larger amount of grain boundaries, due to MA, raises the hardness and also because the Fe_3C was completely dissolved in $\alpha\text{-Fe}$. That is, no lamellar structure appears on the polished and etched surface. This result almost agrees with that of Umemoto et al. [132], who reported that the hardness of deformed pearlite was less than 700 HV. On the other hand, the hardness value decreased after annealing the sample at 900 °C for 1 h. This suggests that recrystallization and grain growth reduce the hardness value. However, the hardness of the quenched sample is relatively lower than normal, indicating that the low carbon content in the sample prevents full phase transformation of $\gamma\text{-Fe}$ to martensite.

Table 5.1: Microhardness measurements of Fe-0.8 wt.% sample.

Condition	This study	Typical values
Sintered	638	-
Annealed	240	260
Quenched	400	511

Table 5.2 shows comparison of hardness measurement in the Fe-7.0 wt.% C in the sintered and annealed conditions. It shows clearly that the hardness value of pure Fe_3C is very high.

However, after annealing at a high temperature some amount of C was lost, confirmed by XRD and EELS, and so the hardness of Fe_3C had decreased. Thus, the hardness value looks lower after annealing. Figure 5.25 shows the optical microscopy images of the hardness indentations of sintered Fe-7.0 wt.% C and Fe-0.8 wt.% C. It is clear from Figure 5.25(a) that the Fe-7.0 wt.% sample behaves in a brittle manner, as indicated by the presence of cracks along the diagonals of the indentation, whereas the Fe-0.8 wt.% C (Figure 5.25 (b)) shows more ductility, suggested by the absence of indentation cracks.

Table 5.2: Microhardness measurements of Fe-7.0 wt.% sample.

Condition	This study	Normal
Sintered	907	800
Annealed	743	-

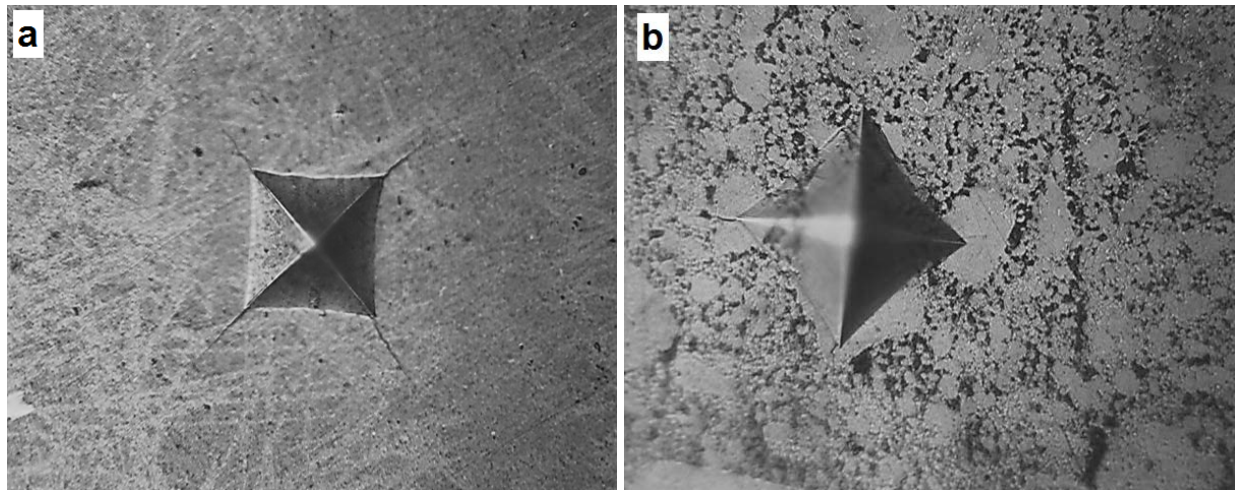


Figure 5.25: Optical microscope images of Vickers hardness impressions of as-sintered samples in (a) Fe-7.0 wt.% C and (b) Fe-0.8 wt.% C.

5.3 Discussion

As shown in Figure 5.1, the sequence of phase evolution in the Fe-0.8 wt.% C composition was that the Fe peak positions changed as a function of milling time, suggesting that a solid solution of C in Fe had formed in the early stages of milling, followed by the formation of Fe₃C phase at 15 h of milling. A similar behavior was seen during MA of Fe-7.0 wt.% C powder blend composition (Figure 5.3) at the early stage of MA. But, the solid solution of C in the Fe was transformed to Fe₃C phase after 5 h of milling time. Furthermore, the amount of the Fe₃C phase increased with milling time up to 30 h in both cases. The solid solution of α -Fe and Fe₃C phase had formed due to the generation a variety of crystal defects including dislocations, grain boundaries, stacking faults, vacancies etc., which induce lot of lattice strain. These formed because of intense plastic deformation experienced by the powder particles using MA method.

The sharpness of the diffraction peaks after sintering can be attributed to removal of lattice strain and grain growth. The grains were still equiaxed and very fine grained with about 30 nm in size. Furthermore, it is clear from the XRD patterns of both the annealed samples of Fe-0.8 wt.% C and Fe-7.0 wt.% C (Figure 5.10 and Figure 5.13) that the Fe₃C peaks, which existed as a homogeneous phase in the Fe-7.0 wt.% C sample and a small fraction in the other one (Fe-0.8 wt.% C), are significantly decreased after annealing at 900 °C for 1 h, suggesting decomposition/loss of C during heat treatment which was confirmed by EELS analysis. This loss of C content was also noted during quenching of the Fe-0.8 wt.% C sample to room temperature.

The microstructure of the investigated sample Fe-0.8 wt.% C strongly depended on the heat treatment given to the samples. For example, in the case of the as-sintered condition, the microstructure was very fine grained since the SPS is a very fast sintering process and

consequently there was no grain growth. Moreover, after annealing at a high temperature and due to the recovery and recrystallization mechanisms as well as grain growth, the lamellar structure of pearlite was clearly seen on the polished and etched surface. On the other hand, the quenched sample had shown lenticular structure of martensite even though, the carbon content was low, around 0.35 wt.%, with the expected bcc structure. Since nital did not attack the Fe_3C phase even at 5% concentration, the microstructure of Fe-7.0 wt.% C seems to be similar in both the as-sintered and annealed conditions.

The microhardness measurements of the sintered samples show high values. This is due to nanograin structure that had formed through MA. On the other hand, the annealed samples showed lower hardness values.

5.4 Conclusions

The results of the investigation show that MA can be successfully used for milling of pure Fe and C to synthesize nanocrystalline eutectoid steel and pure Fe_3C with good mechanical properties. In the early stages of milling, supersaturated solid solution of Fe(C) had formed, 0.53 wt.% in Fe-0.8 wt.% composition and 0.26 wt.% in Fe-7.0 wt.% C composition, and this transformed to α -Fe and Fe_3C phases after 15 h of milling, in the Fe-0.8 wt.% C, and to fully Fe_3C phase in the case of Fe-7.0 wt.% C after 5 h of milling. Sintering of the powders at 600 °C and 70 MPa for 15 min using spark plasma sintering led to fabrication of nanocrystalline bulk steel (Fe-0.8 wt.% C) with Fe_3C phase completely dissolved in α -Fe phase with a high hardness value 638 HV. Also, single phase bulk Fe_3C , with a very high hardness value 907 HV, could also be produced. Annealing the Fe-0.8 wt.% C sample at 900 °C for 1 h promoted grain growth resulting

in reduced hardness value. In contrast, annealing the Fe-7.0 wt.% C sample led to decomposition of Fe_3C to $\alpha\text{-Fe}$ and reduced the hardness value.

CHAPTER 6: SYNTHESIS OF AUSTENITIC STAINLESS STEEL ALLOY POWDERS THROUGH MECHANICAL ALLOYING

6.1 Introduction

Stainless steel alloys are used in the chemical, nuclear, petrochemical and food industries due to the excellent combination of high strength, good corrosion resistance, weldability and biocompatibility [133, 134]. Austenitic stainless steels are non-magnetic in nature and contain around 16-25 wt.% of Cr, and also N in solid solution, both of which confer high corrosion resistance. Further, the presence of 8-25 wt.% Ni helps to stabilize their austenitic face-centered cubic (fcc) structure. Austenitic stainless steels are the most widely used grade due to their excellent formability, high resistance to corrosion, low thermal expansion, high mechanical strength and toughness.

Traditionally, austenitic stainless steels are manufactured by melting the raw materials - Fe, Cr and Ni together in an electric furnace which requires 8 to 12 h of intense heat. The molten metal is refined and decarburized by blowing oxygen, argon and nitrogen into the molten steel. The refined molten steel is then processed through a continuous casting machine [5, 6].

There have been many investigations on the synthesis of stainless steel alloys through MA, mostly to synthesize austenitic stainless steel alloys. Several researchers [135-138] have synthesized duplex and ferritic stainless steel powders using dual-drive planetary and Fritsch Pulverisette planetary mills. They studied the structure of Fe-Cr-Ni elemental powder blends with the compositions Fe-18Cr-13Ni and Fe-17Cr-1Ni after milling them, separately, up to 40 h.

Shashanka and Chaira [135] reported that formation of austenitic and ferritic (duplex) stainless steel required 10 h of milling in a dual-drive planetary mill due to the high impact energy,

whereas milling in the Fritsch Pulverisette planetary mill required 40 h to synthesize the duplex stainless steel. They also investigated the phase transformation that occurs in the annealed stainless steel powders synthesized from dual-drive planetary mill under argon and nitrogen atmospheres after 10 h of milling. It was reported that annealing of the stainless steel powders at 750 °C enhanced the ferrite → austenite transformation under both atmospheres. But, nitrogen favored austenitic transformation to a greater extent than argon because nitrogen atoms diffuse into interstitial sites of austenite which are larger than in ferrite; thus the nitrogen atoms create less distortion and volume mismatch. Moreover, with milling time, the concentration of lattice defects increased due to severe plastic deformation, which refined the particles and grain sizes with a concomitant increase in the grain boundary area, suggesting that these are preferable sites for nitrogen absorption [139]. Therefore, it was concluded that nitrogen acted as an austenitic stabilizer.

Further, the authors [138] also studied the effect of milling parameters, for example, milling speed, process control agent (PCA), and ball to powder weight ratio (BPR), on the synthesis of duplex and ferritic stainless steel powders. They reported that larger PCA amount, higher BPR, and faster milling speed were more effective in the formation of duplex and ferritic stainless steel powder and reducing the particle size after 10 h of milling.

Enayati et al. [140] investigated MA of Fe-Cr-Ni powder blends with the nominal compositions of Fe-18Cr-8Ni, Fe-15Cr-15Ni, and Fe-15Cr-25Ni. They reported that MA of Fe-18Cr-8Ni and Fe-15Cr-15Ni elemental powder blends led to formation of fully ferritic solid solution (α) even at 60 h and 50 h of milling, respectively. However, both austenite and ferrite phases were found to form after the milled powders were annealed at 700 °C for 1 h. On the other

hand, the structure of the as-milled Fe-15Cr-25Ni powder blend, at 50 h of milling, and after annealing, was fully austenite (γ) due to the higher content of austenite stabilizing element (Ni).

Other work by Enayati et al. [141] reported that the austenitic stainless steel (Fe-20Cr-7.03Ni-1.62Mn-0.4S-0.05C) chips transformed partially to the martensite phase during milling and that the particles had dual structure consisting of austenite and martensite phases. However, the austenite did not completely transform to the martensite phase even after 100 h of milling. On the other hand, the chips milled for 100 h were annealed at 700 °C for 1 h, when the martensite phase transformed back to the austenite phase.

Oleszak et al. [142] milled 316L (Fe-17Cr-13Ni-2.2Mo-0.2Mn-0.8Si-0.02C) austenitic stainless steel powder using Fritsch P5 Planetary ball mill. They reported that formation of austenite and martensite phases depended on the milling time. They also reported formation of a two-phase nanocrystalline structure of austenite and martensite at 10 h of milling. Increasing the milling time up to 100 h led to a decrease in the martensite fraction down to 46% from 66%.

El-Eskandarany and Ahmed [143] studied the synthesis of austenitic stainless steel (Fe-18Cr-8Ni) by the rod-milling technique. When the powder blend was subjected to MA for different milling times, the authors reported formation of (bcc) FeCrNi solid solution at around 48 h of milling, as concluded by the absence of Cr and Ni peaks in the XRD pattern, and increase in the lattice parameter of pure Fe, suggesting solubility of Cr and Ni in the Fe lattice to form a solid solution. Further, after milling for 300 h, they reported that the (bcc) FeCrNi solid solution had completely transformed to a homogenous amorphous phase. Other researchers [144, 145] also investigated the synthesis of high-nitrogen austenitic Fe-Cr-Ni-N alloys through MA.

In this investigation, we report on the successful synthesis of a homogeneous austenitic stainless steel by MA starting from blended elemental powders by optimizing the chemical composition and process parameters. We show that austenitic stainless steel can be synthesized at lower Ni content than reported earlier with nanometer-sized grains that are thermally stable even on annealing at relatively high temperatures.

6.2 Results

6.2.1 Evolution of X-Ray Diffraction Patterns

In order to understand the phase evolution of Fe-Cr-Ni alloy powders at different stages of milling, X-ray diffraction (XRD) analyses were performed. Figure 6.1 shows the XRD patterns of Fe-18Cr-8Ni alloy powder after milling for different times. The XRD pattern of the unmilled powder blend (0 h of milling) shows the presence of diffraction peaks of pure crystalline bcc Fe, fcc Cr and fcc Ni. It may be noted that the 110_{Fe} and 110_{Cr} peaks and the 111_{Ni} peak completely overlap because the lattice spacings are the same for all these reflections. After 5 h of MA all the XRD peaks of Cr and Ni have completely disappeared. Additionally, the Fe peaks have become broader and their intensities decreased, a result of the reduced crystallite size and increased lattice strain introduced into the powder during MA. Furthermore, it was noted that the Fe peak positions have shifted to the lower angle side, indicating formation a new solid solution phase of FeCrNi.

It is worth noting that after 15 h and 10 h (in the case of Fe-18Cr-8Ni and Fe-18Cr-12Ni, respectively), new peaks representing the γ phase started appearing along with the α phase at this stage. These peaks are very clear at this stage, even though it may be noted that the γ phase peaks started appearing even at 10 h of milling in the case of Fe-18Cr-8Ni powder blend.

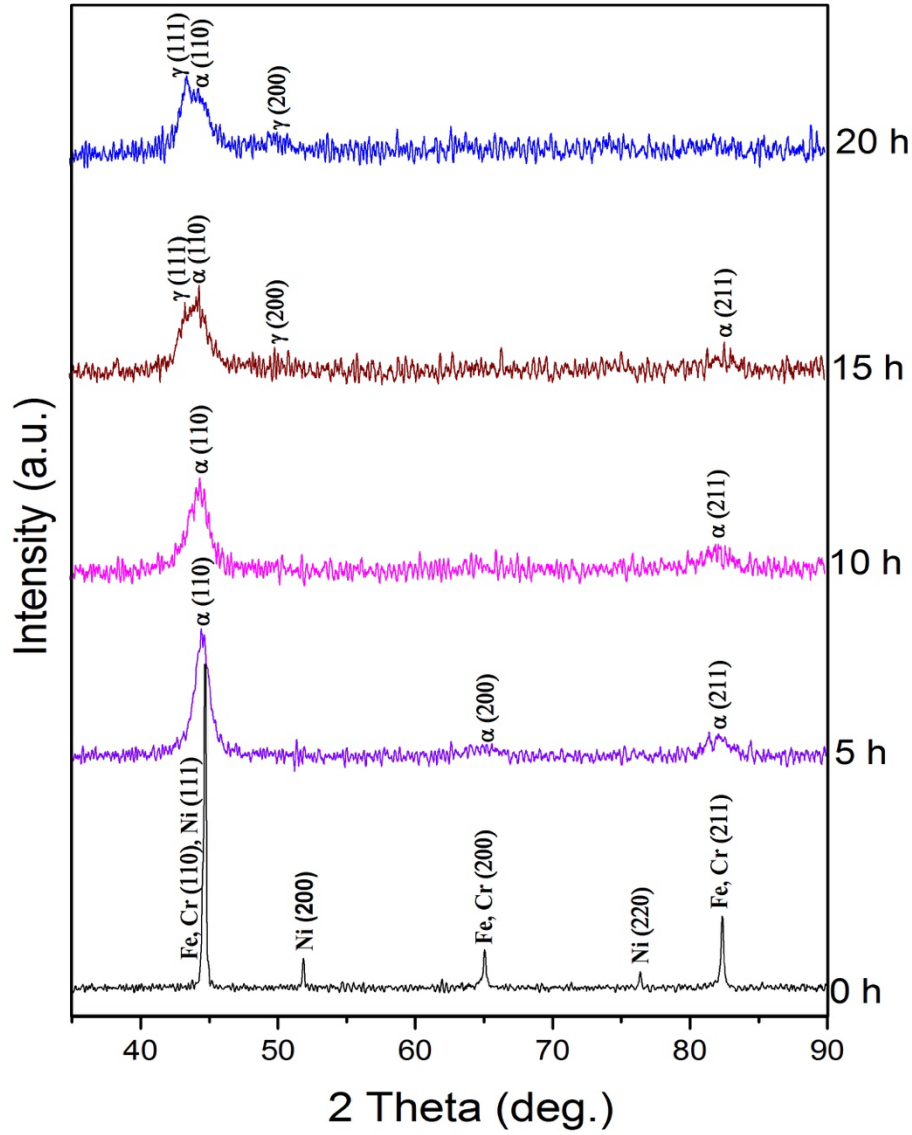


Figure 6.1: XRD patterns of the Fe-18Cr-8Ni powder blend milled for different times. The Fe, Cr and Ni peaks are clearly seen in the unmilled powder (0 h). Formation of the metastable α phase started to form at 5 h of milling. After 15 h of milling, the metastable α phase transforms to the γ phase, and its amount increased with increasing milling time.

With continued milling, the fraction of the γ phase increased and this continued up to 30 h of milling time (Figure 6.2). However, both the γ phase and the α phase still coexisted in both

the Fe-18Cr-8Ni and Fe-18Cr-12Ni powder blends. In the 18Cr-8Ni composition investigated, the γ (austenite) phase formed has eventually transformed to the α (bcc) phase at 40 h of milling.

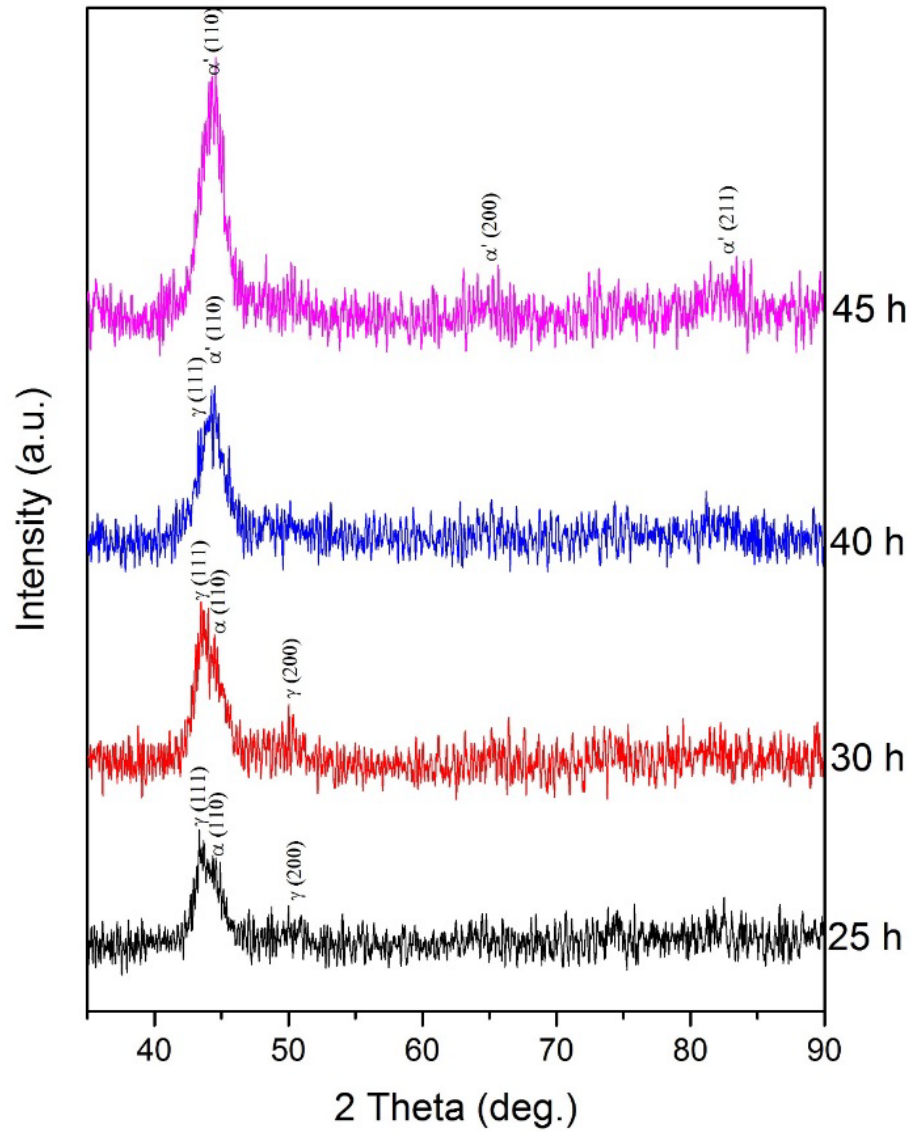


Figure 6.2: XRD patterns of the Fe-18Cr-8Ni powder blend milled for different times. After 40 h of milling, the γ (austenite) phase has transformed to the α phase. On continued milling of the powder to 45 h, only the α phase (martensite) is present.

This α phase can be either the ferrite phase or the stress-induced martensite phase, and both have the same crystal structure and lattice parameters and so it will be difficult to differentiate between these two cases. However, this phase is frequently referred to as the martensite phase in the literature [140, 142, 146-148]. Thus, the milled powders, at sufficiently long times (45 h), showed the presence of only the martensite phase in the 18Cr-8Ni composition; while only the 18Cr-20Ni composition contained the homogeneous austenite phase.

The Fe-18Cr-12Ni powder blend also behaved in a similar manner (Figure 6.3), except that the times for the transformations were slightly different. For example, the austenite phase started to form at 10 h of milling in the 18Cr-12Ni powder blend.

Figure 6.4 shows the XRD patterns of Fe-18Cr-20Ni alloy powder after milling for different times. Again, the XRD pattern of the unmilled powder blend (for 0 h of milling) indicates the presence of diffraction peaks of pure crystalline bcc Fe, bcc Cr and fcc Ni, with the Ni peaks showing higher intensity than those in the other compositions i.e. Fe-18Cr-8Ni and Fe-18Cr-12Ni, a consequence of higher amount of Ni present in the powder blend. On milling the powder blend for 5 h, diffraction peaks of the elements (Fe, Cr and Ni) showed broadening and a decrease in their intensities. At this stage of milling, we still noted the Ni peaks whereas in the case of the Fe-18Cr-8Ni and Fe-18Cr-12Ni, the Ni peaks have completely disappeared after 5 h of MA.

The Ni peaks completely disappeared on milling the powder blend for 10 h, and at this stage we noted that new peaks of the γ phase 111_γ and 200_γ started appearing along with the α phase. Increasing milling time up to 30 h, all the α phase was converted to γ phase.

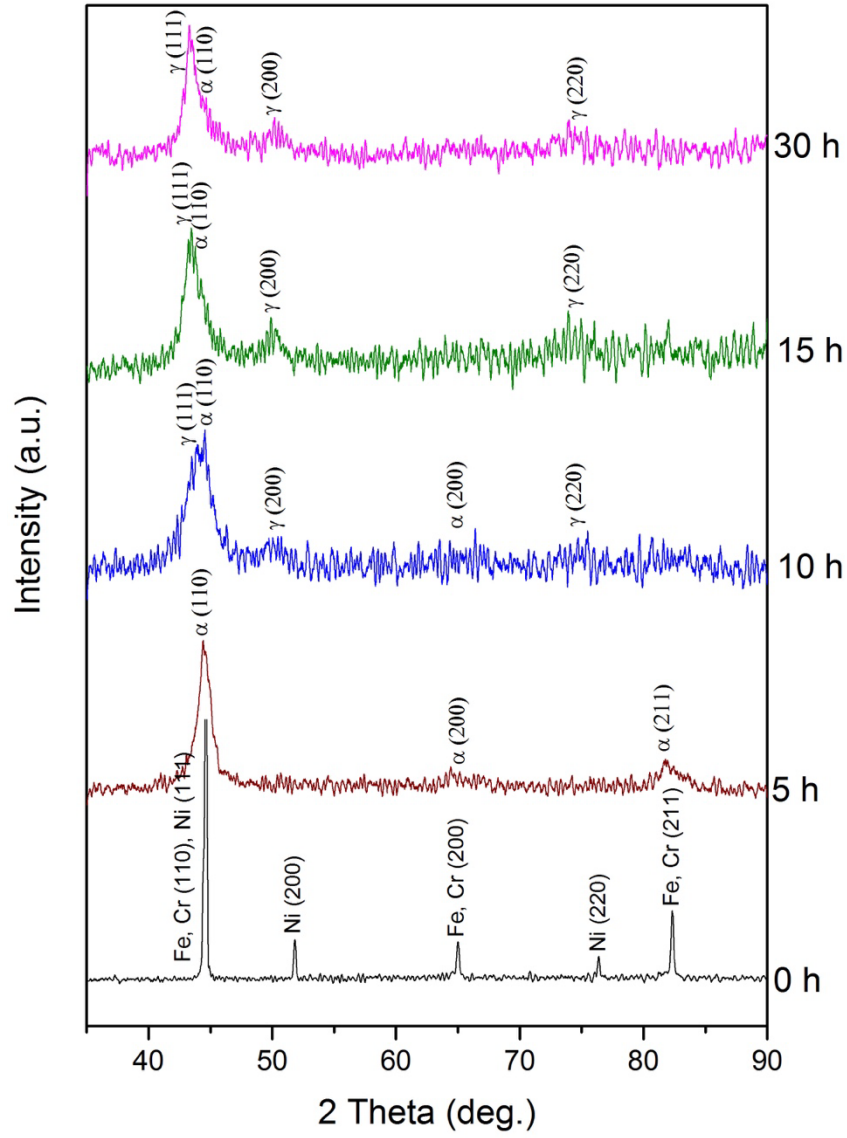


Figure 6.3: XRD patterns of the Fe-18Cr-12Ni powder blend milled for different times. The Fe, Cr and Ni peaks are clearly seen in the unmilled powder (0 h). The γ phase started to form at 10 h of milling. After 15 h of milling, the metastable α phase transforms to the γ phase, and its amount increased with milling time.

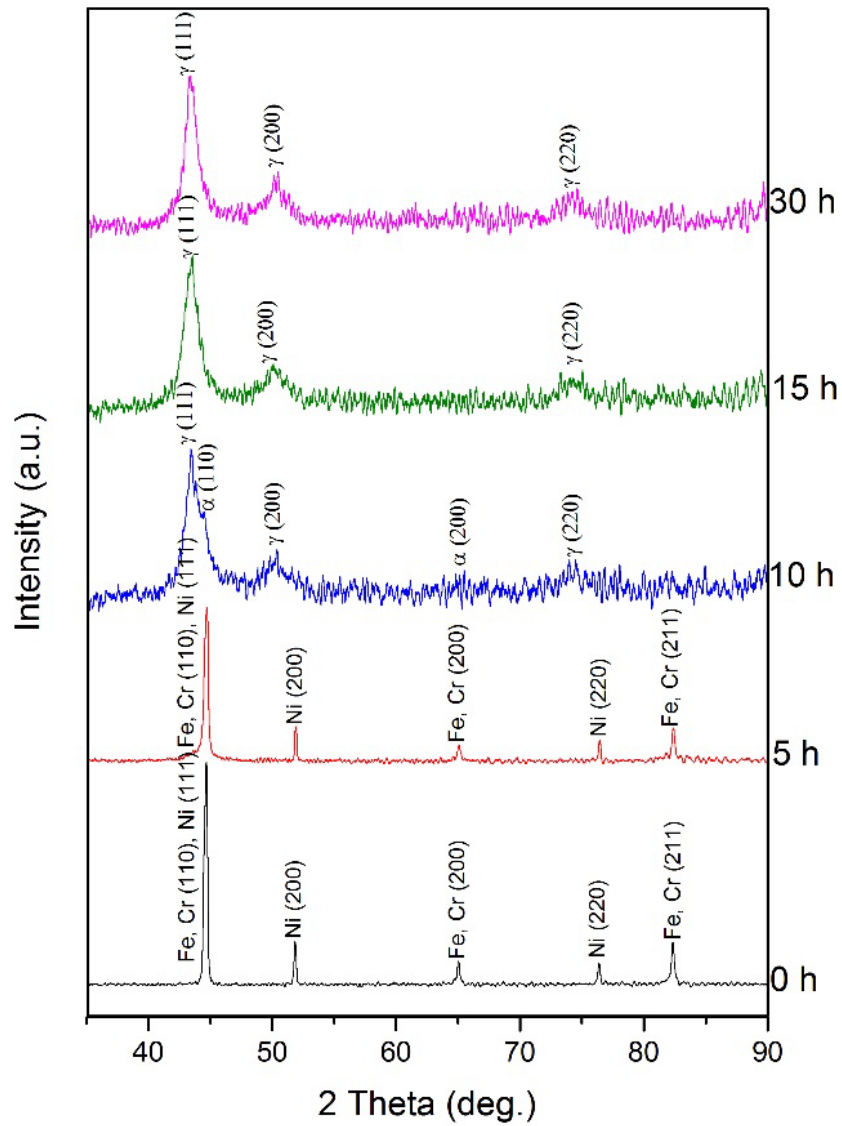


Figure 6.4: XRD patterns of the Fe-18Cr-20Ni powder blend milled for different times. The Fe, Cr and Ni peaks are clearly seen in the unmilled powder (0 h). The γ phase started to form at 10 h of milling. After 15 h of milling, the metastable α phase transforms to the γ phase, and its amount increased with milling time.

Figure 6.5 shows the XRD patterns of the three powders milled for 30 h. Similar to the milled powders, in the annealed condition at 600 °C for 1 h in Ar atmosphere also (Figure 6.6), only the 18Cr-20Ni composition showed the austenite phase fully and the other two compositions

showed the presence of both the austenite and martensite phases. But, the important difference is that the proportion of the two phases is different in the as-milled and annealed conditions, as listed in Table 6.1. The amount of the austenite phase is higher in the annealed powder, showing a trend towards equilibration.

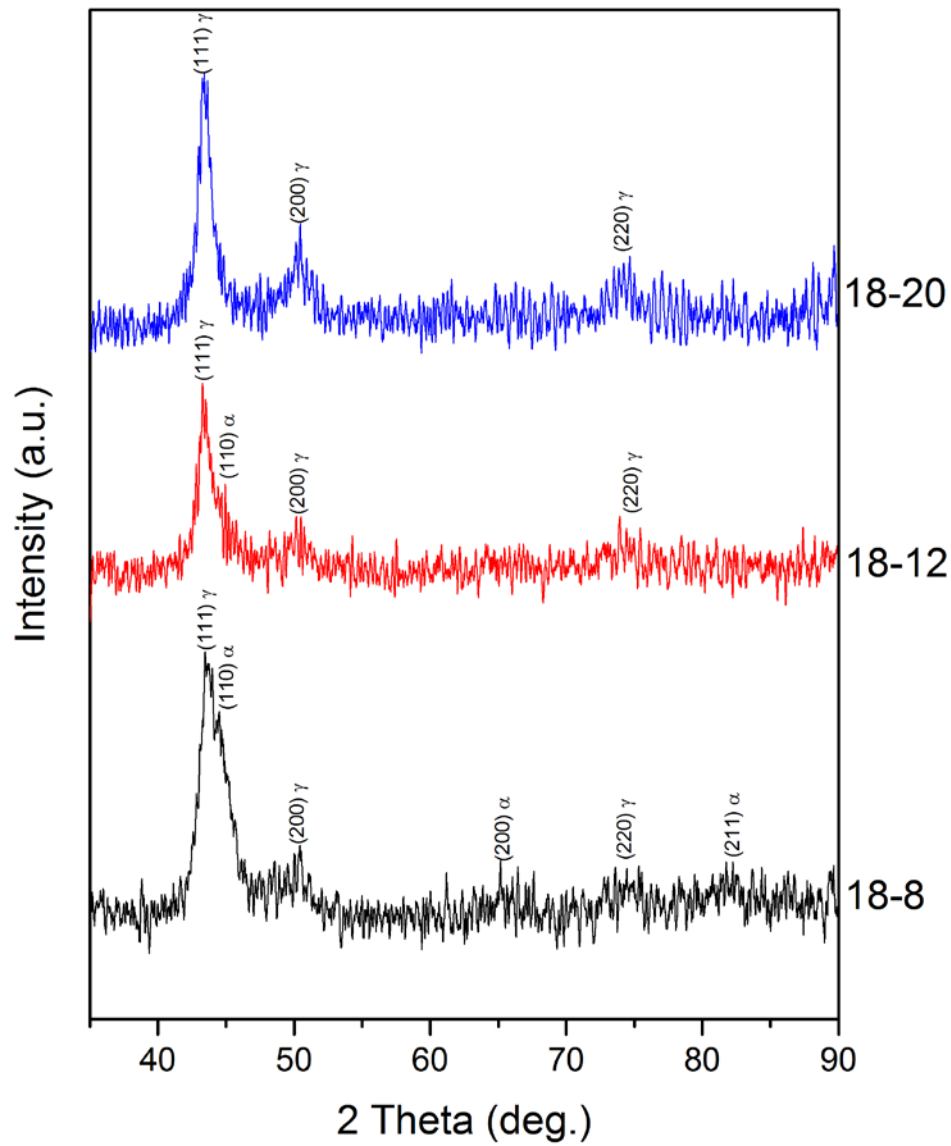


Figure 6.5: XRD patterns of Fe-18Cr-8Ni, Fe-18Cr-12Ni, and Fe-18Cr-20Ni powders milled for 30 h.

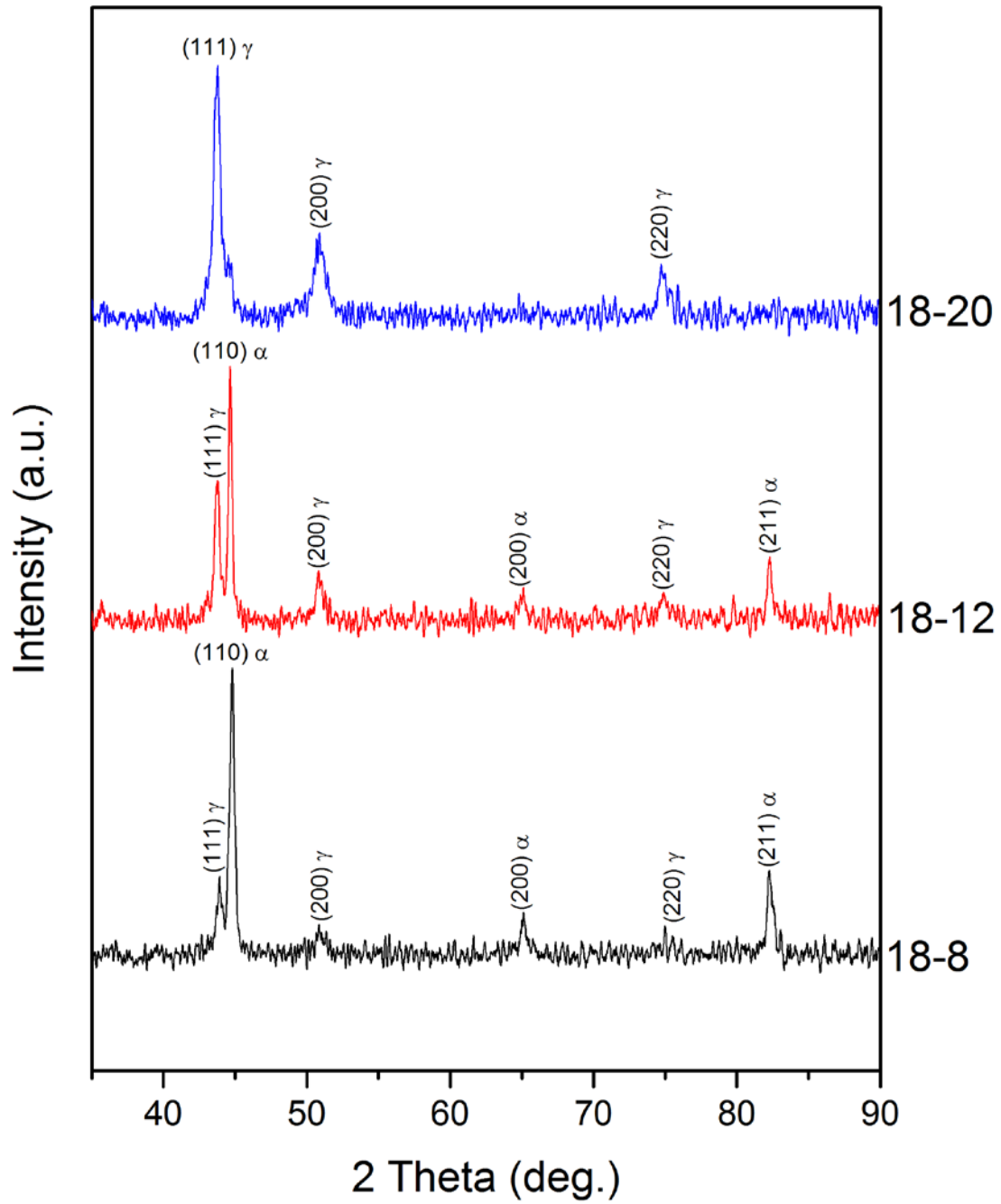


Figure 6.6: XRD patterns of Fe-18Cr-8Ni, Fe-18Cr-12Ni, and Fe-18Cr-20Ni powders after annealing the milled powders at 600 °C for 1 h.

Table 6.1: Proportions of the different phases in the as-milled and annealed (600 °C/1 h) Fe-18Cr-xNi (x = 8, 12, and 20) powders.

Nominal composition	As-milled Powders		Annealed Powders	
	% α	% γ	% α	% γ
Fe-18Cr-8Ni	79.6	20.4	69.1	30.9
Fe-18Cr-12Ni	59.4	40.6	46.7	53.3
Fe-18Cr-20Ni	0	100	0	100

6.2.2 Lattice Parameter Calculations

The lattice parameters calculated from the 111_{Ni} and 110_{Fe} planes of Fe-18Cr-8Ni, Fe-18Cr-12Ni and Fe-18Cr-20Ni powder blends at 0 to 30 h of milling were calculated using Nelson-Riley (N-R) extrapolation method [149]. Figure 6.7 shows the lattice parameters of the three compositions versus milling time. It has been observed from the graph that with increasing milling time, the lattice parameter increased due to the existence of a large amount of defects during MA and also diffusion of Cr and Ni atoms into the lattice position of Fe atoms. Also, it is clear that the Ni content plays an important role in the $\alpha \rightarrow \gamma$ phase transformation. For example, in the case of the Fe-18Cr-20Ni and Fe-18Cr-12Ni powder blends, the phase transformation started at 10 h of milling time and continued up to 30 h of milling time. In contrast, the $\alpha \rightarrow \gamma$ phase transformation started at 15 h of milling time in the Fe-18Cr-8Ni powder blend. The lattice parameter values of γ and α present in the powders are 0.3619 nm and 0.2865 nm, respectively. These values are in good agreement with the standard lattice parameter of fcc γ -Fe (0.3659 nm) [150] and bcc α -Fe (0.2866 nm) [151].

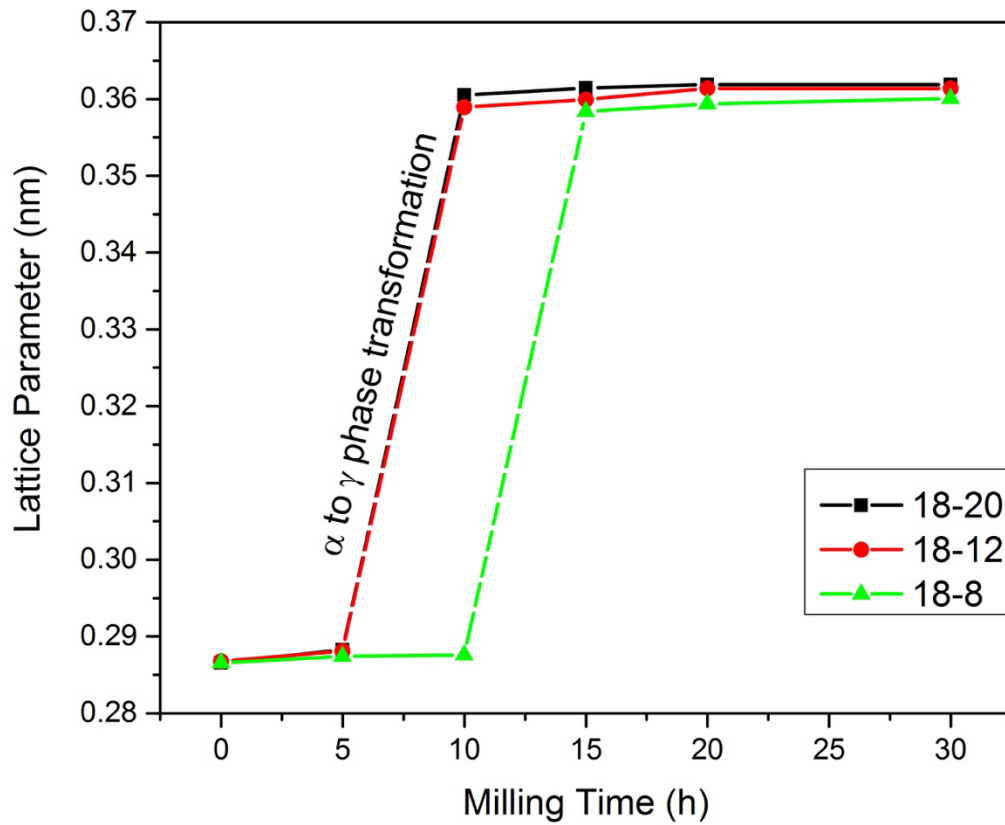


Figure 6.7: Variation of lattice parameter with milling time.

6.2.3 Evolution of Microstructure

Scanning electron microscopy (SEM) was conducted to understand the morphology of the mechanically alloyed Fe-Cr-Ni powders at different stages of milling. Figure 6.8 (a) and (b) show the SEM images of the as-blended Fe-18Cr-8Ni powder mixture. It is clear from the images that the pure Fe particles are spheroidal in shape and that the average particle size is about 10 μm whereas Cr particles are bulky and random in size. Further, it can be also seen from the micrograph that the pure Ni particles have spiky needle-like morphology and that the average particle size is around 2 μm . Since pure Ni has a relatively higher atomic number than pure Fe and Cr, the micrograph shows that the Ni particles seem brighter than Fe and Cr particles.

After 5 h of milling, as shown in Figure 6.8 (c), the morphology and distribution of the powder particles is inhomogeneous showing both large and small sized particles distributed non-uniformly, as a result of agglomeration in the early stages of milling. Figure 6.8 (d) shows that the powder particle morphology of Fe-18Cr-8Ni became more homogenous after 30 h of milling time. Similar behavior was found during milling of Fe-18Cr-12Ni and Fe-18Cr-20Ni compositions.

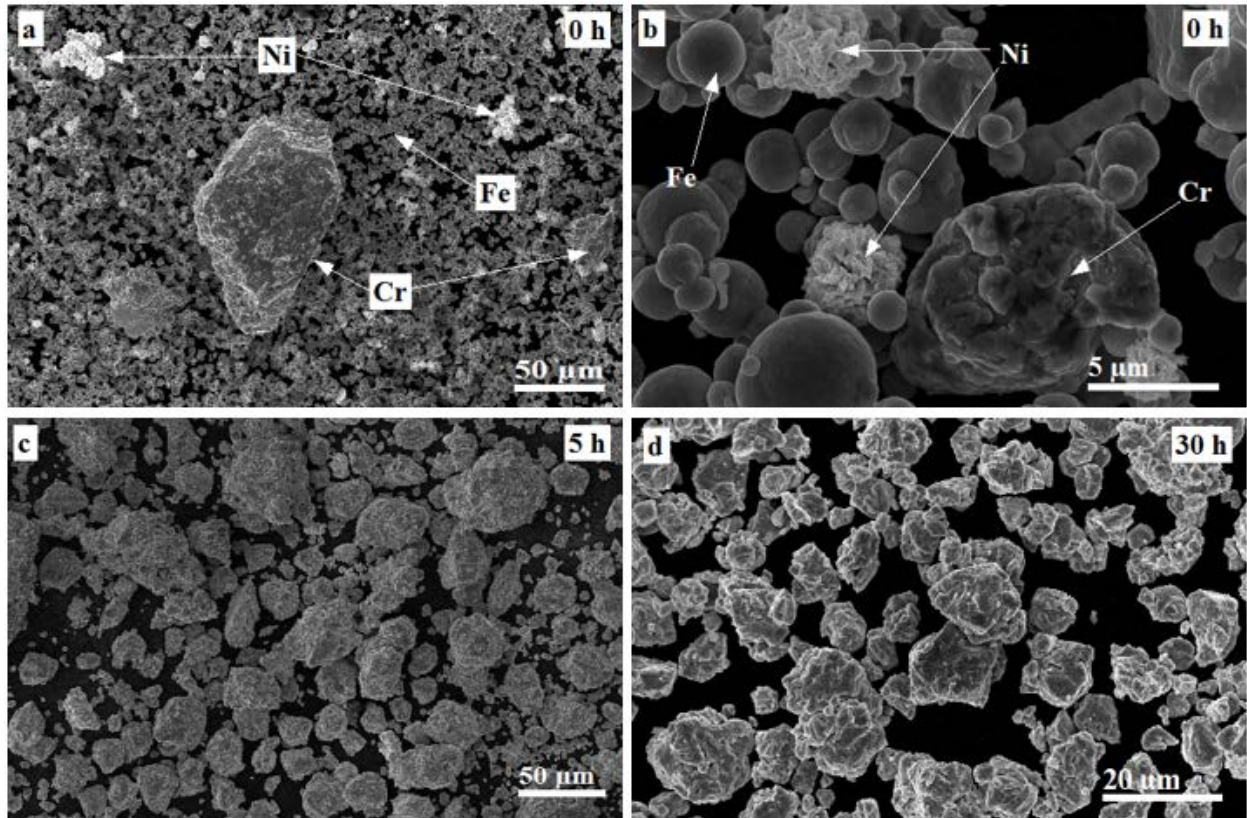


Figure 6.8: Low magnification scanning electron micrograph of the Fe-18Cr-8Ni powder blend in the as blended (unmilled) condition showing elemental Fe, Cr and Ni powder particles. (c): high magnification scanning electron micrograph (unmilled condition) showing the morphology of the pure Fe particles which are spheroidal in shape, Cr particles which are bulky and random in size and pure Ni particles which have spiky needle-like. (c): Scanning electron micrograph of Fe-18Cr-8Ni powder blend after 5 h of milling showing both large and small sizes particle distributed non-uniformly (d): Scanning electron micrograph of the Fe-18Cr-8Ni powder blend after milling for 30 h showing uniform particles.

The energy dispersive spectroscopy (EDS) was also used to investigate the chemistry of the mechanically alloyed Fe-Cr-Ni powders at different stages of milling. Figure 6.9 (a) and (b) show the EDS analyses of Fe-18Cr-8Ni powder blends after 5 h and 30 h of milling, respectively. From the spectra it is clear that there is not much difference between the initial and final compositions.

The energy dispersive spectroscopy (EDS) was used to investigate the chemistry of the mechanically alloyed Fe-Cr-Ni powders at 30 h of milling (Table 6.2).

Table 6.2: Chemical analyses of the Fe-Cr-Ni powder at 30 h of milling.

Compositions	Elements (wt.%)		
	Fe	Cr	Ni
Fe-18Cr-8Ni	72.19 +/- 0.87	17.09 +/- 0.36	9.82 +/- 0.30
Fe-18Cr-12Ni	70.10 +/- 1.64	17.2 +/- 0.71	12.7 +/- 0.67
Fe-18Cr-20Ni	59.70 +/- 0.64	17.5 +/- 0.23	22.8 +/- 0.35

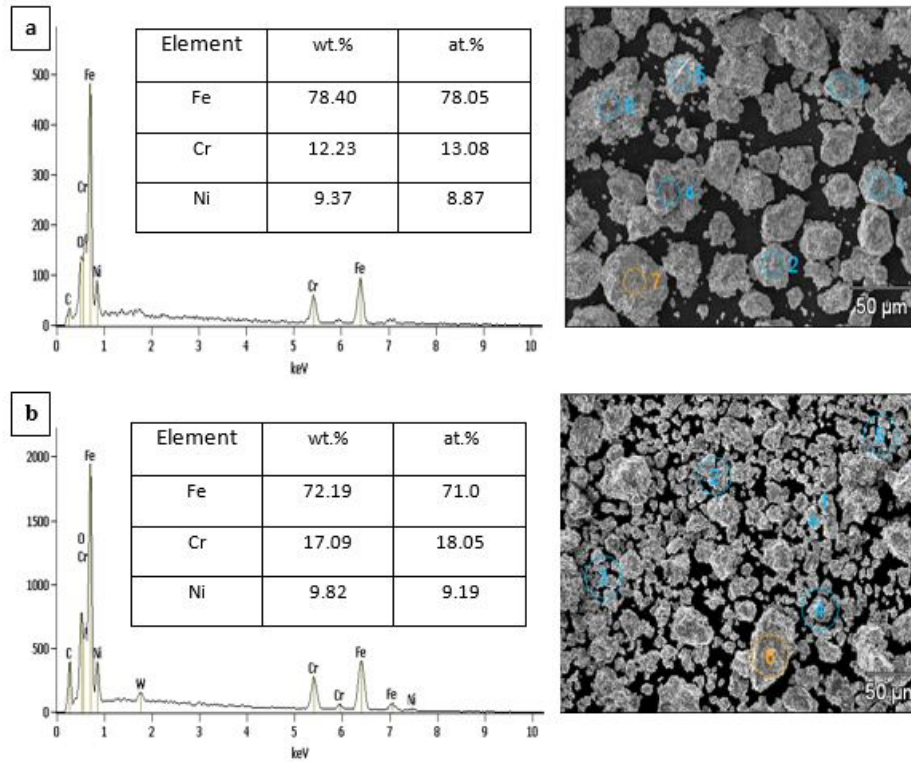


Figure 6.9: SEM images and EDS spectra of the Fe-18Cr-8Ni powder blend milled for (a) 5 h and (b) 30 h.

Figure 6.10(a) shows the TEM micrograph and (b) the selected area diffraction pattern of the Fe-18Cr-8Ni powder milled for 30 h. The micrograph shows the presence of very fine grains of the order of 3-9 nm, while the selected area diffraction pattern clearly shows the presence of both the α and γ phases. High-resolution TEM investigations and the fast Fourier transforms also confirm the presence of both the α and γ phases at this stage of milling (Figure 6.10(c)). On the other hand, the powder containing 20% Ni shows the presence of only the γ phase (Figure 6.11 (a)), confirmed by the diffraction pattern (Figure 6.11 (b)), and the high-resolution micrograph (Figure 6.11 (c)), confirming what was observed through XRD investigations.

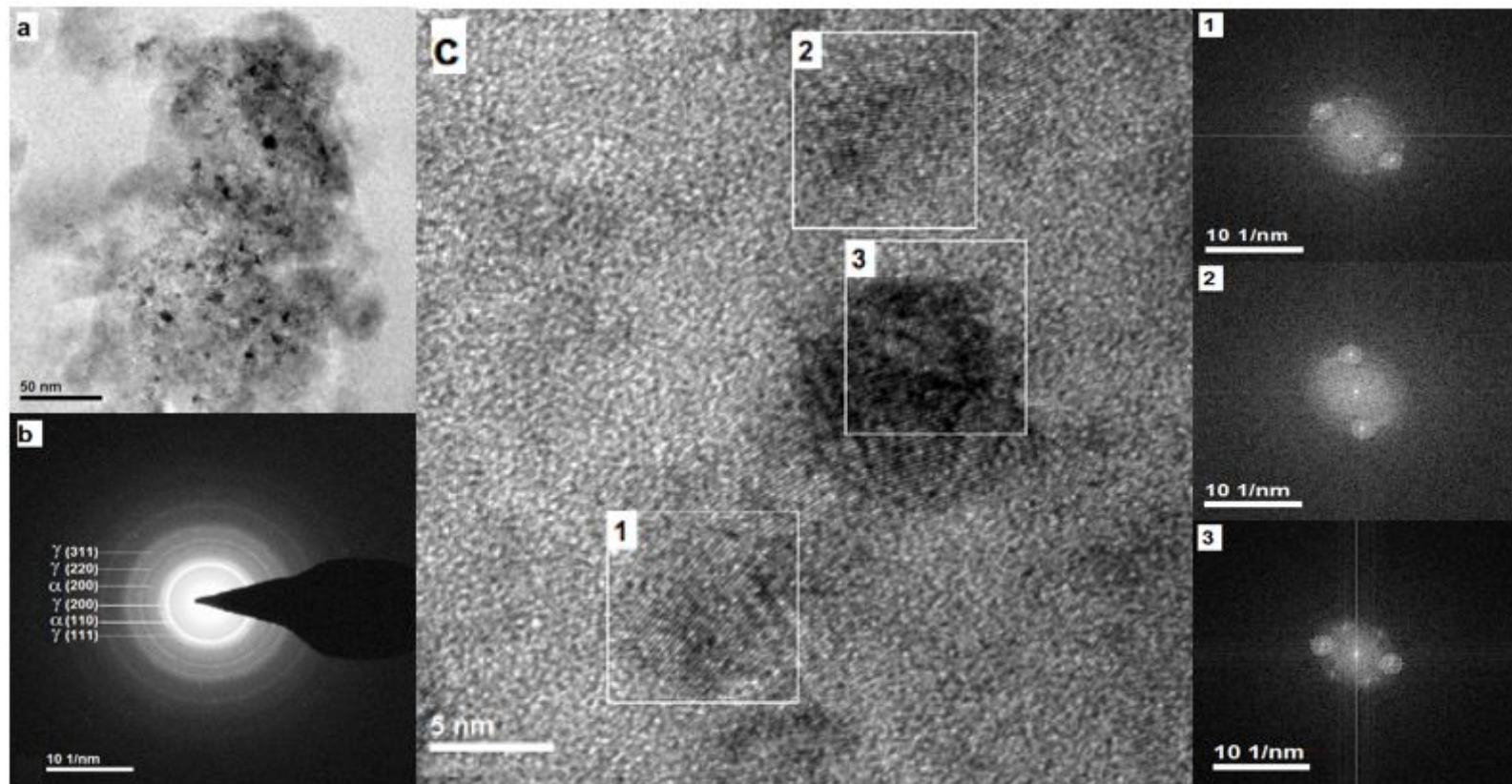


Figure 6.10: (a) Low magnification transmission electron micrograph, (b) selected area diffraction pattern, and (c) high-resolution transmission electron micrograph of Fe-18Cr-8Ni powder blend milled for 30 h. Both the austenite and martensite phases are present. The fast Fourier transformation diagrams (as insets in (c)) show that regions 1 and 2 represent the austenite phase and region 3 the martensite phase.

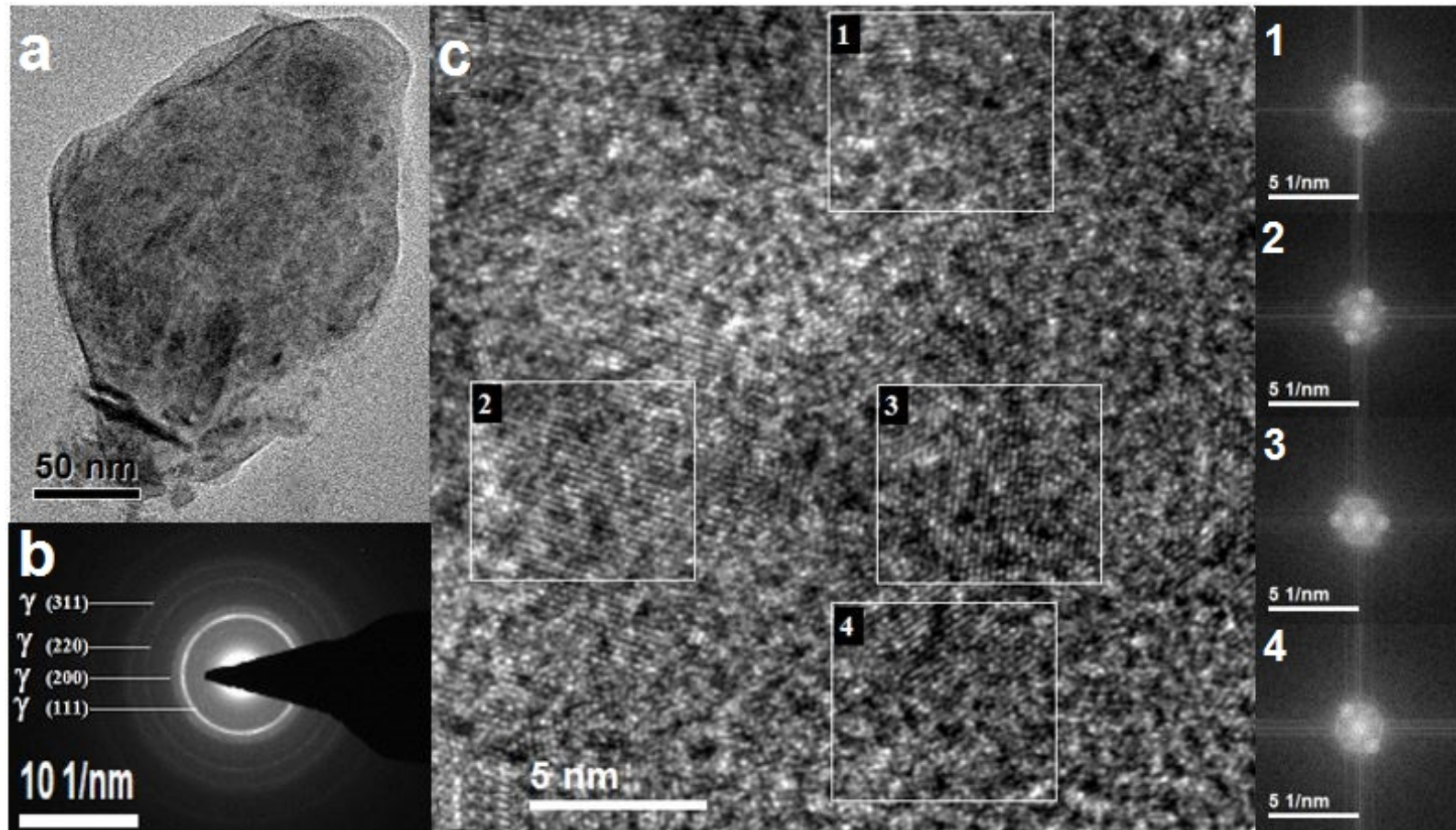


Figure 6.11: (a) Low magnification transmission electron micrograph, (b) selected area diffraction pattern, and (c) high-resolution transmission electron micrograph of the Fe-18Cr-20Ni powder blend milled for 30 h. Only the austenite phase is present in this powder.

6.3 Discussion

As shown in Figures 6.1 and 6.2, the sequence of phase evolution in the Fe-18Cr-8Ni composition was that alloying took place among Fe, Cr and Ni resulting in the formation of a single-phase bcc FeCrNi (α) solid solution in the early stages of milling (5 h), followed by the formation of fcc (γ) phase at 15 h of milling, and finally new peaks of bcc (α') martensite started appearing after milling the powder for 45 h. A similar behavior was seen during MA of Fe-18Cr-12Ni powder blend composition. But, the MA behavior of Fe-18Cr-20Ni powder blend composition was shown to be different. As shown in Figure 6.4, milling the Fe-18Cr-20Ni powder blend up to 10 h led to the formation of fcc (γ) phase coexisting with the bcc (α) phase. Furthermore, the metastable bcc (α) solid solution transformed completely to the fcc (γ) phase with increasing milling time due to higher Ni content, which is an austenite stabilizing element. As mentioned in the Introduction part, MA is a high-energy ball milling process involving repeated cold welding, fracturing and rewelding of powder particles. During MA, the powder particles store a lot of energy due to the intense plastic deformation at extremely high strain rate experienced by the powder particles, thereby creating a variety of a high density of crystalline defects such as dislocations, vacancies, stacking faults and grain boundaries, which induce lot of lattice strain [5, 6]. Furthermore, due to the process of cold working and recovery, grain refinement takes place leading to the formation nanostructured grains, which favor the stabilization of austenite [152-154]. Formation of a bcc (α) phase was also reported in steels processed by non-equilibrium processing techniques such as rapid solidification processing [155-157].

As mentioned above, in comparison to the milled powders, the amount of the austenite phase was higher in the powders that were annealed at 600 °C for 1 h. Also, the amount of the austenite phase was higher at higher Ni contents in the initial powder blend. These observations clearly suggest that the powders were approaching the equilibrium constitution. But, complete equilibrium was not achieved as indicated by the presence of some amount of the martensite phase. This situation may be due to the fine grain structure of the martensite phase and also perhaps due to the presence of increased defect structure.

But, based on the results presented in Figure 6.12 [158], the three compositions should be placed in the austenite region whereas in this study the results show that the Fe-18Cr-8Ni and Fe-18Cr-12Ni powder blends contain a mixture of bcc (α) phase along with fcc (γ) phase at the early stages of milling and only the bcc (α) phase at the end of milling. However, the energy associated with defects which are developed during MA, especially grain boundaries, could influence the thermodynamic stability of the different phases by increasing the free energies - ΔG_α and ΔG_γ and thus change the stability range of the bcc (α) and fcc (γ) phases with respect to the equilibrium condition. Even though one can argue that MA can always stabilize metastable phases, this constitution continued to be present in the annealed powders as well. Thus, it appears that the phase boundaries need to be redefined by introducing a two-phase region in this figure. Hence, we propose that the phase stability diagram be tentatively modified as shown by the thick (red) line in Figure 6.12. The exact positions of the boundaries need to be worked out by conducting the experiments at smaller composition intervals.

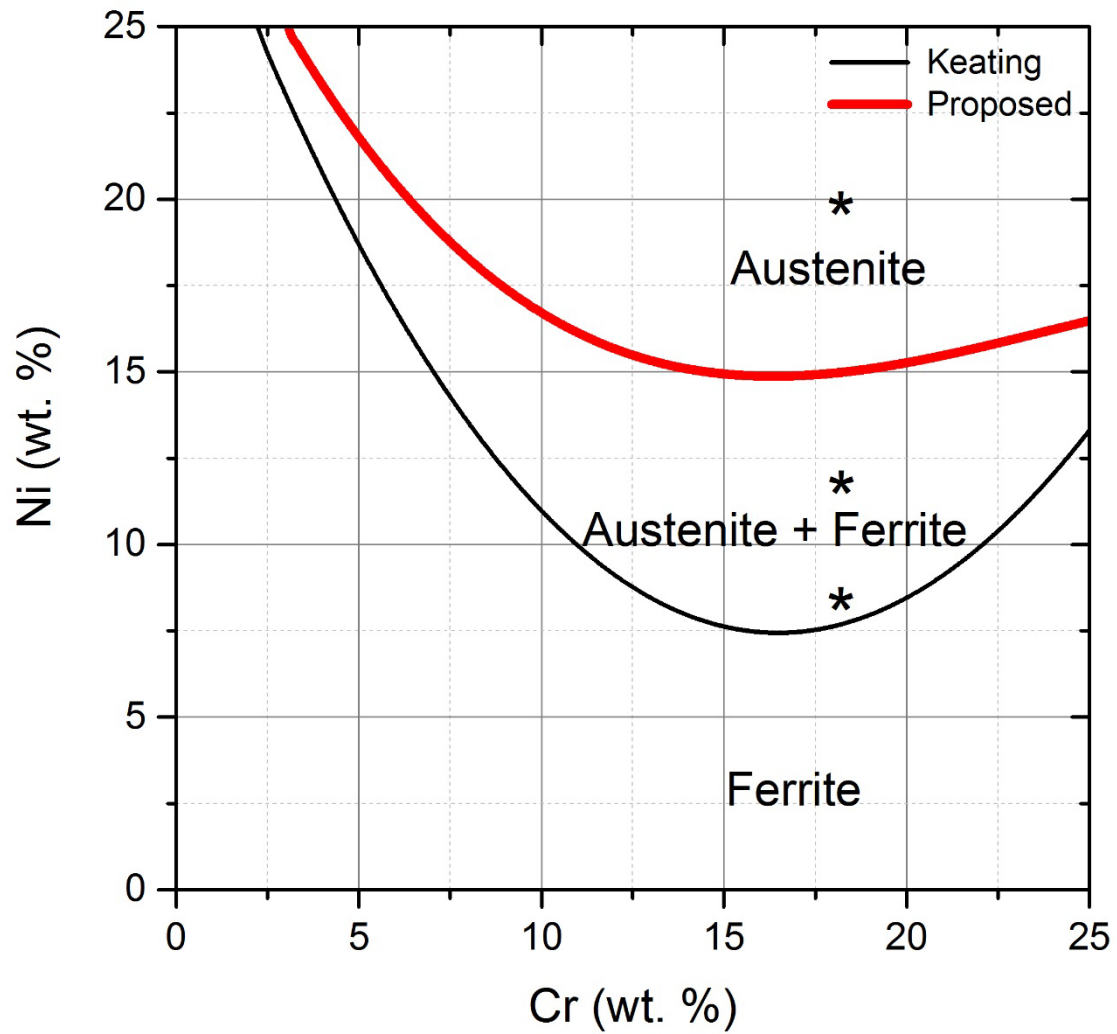


Figure 6.12: The effect of Cr and Ni contents on the stability of the austenite phase in Fe-Cr-Ni alloys, thin (black) line according to [158] and the proposed boundary as indicated by the thick (red) line. The compositions investigated in the present investigation are indicated by asterisks.

6.4 Conclusions

Three different compositions of austenitic stainless steel (Fe-18Cr-8Ni, Fe-18Cr-12Ni and Fe-18Cr-20Ni) elemental powder blends were mechanically alloyed using a high-energy ball mill. In the early stages of MA, the three compositions showed the presence of bcc (α) structure, and with continued milling the bcc (α) phase transformed to fcc (γ). The time for this phase transformation was strongly dependent on the Ni content in the initial blend, decreasing with an increase in the Ni content. After 30 h of milling, a fully homogenous austenite phase could only be obtained in the 18-20 powder blend, while in the 18-8 and 18-12 powder blends, both the austenite and (ferrite or martensite) phases were present at intermediate stages of milling and only the bcc (α') martensite phase in the final stages of Fe-18Cr-18Ni powder blend. Annealing of the powders at 600 °C for 1 h promoted the martensite to austenite transformation in both Fe-18Cr-8Ni and Fe-18Cr-12Ni compositions. In contrast, the structure of the Fe-18Cr-20Ni composition after annealing also was fully austenitic.

CHAPTER 7: CONCLUSIONS

Synthesis of stable and metastable phases was investigated in the Ni- and Fe-based alloy systems using mechanical alloying (MA) process, and these phases were characterized using X-ray diffraction (XRD), scanning electron microscopy (SEM) equipped with energy dispersive spectroscopy (EDS), transmission electron microscopy (TEM) attached with electron energy loss spectroscopy (EELS) techniques.

A supersaturated solid solution of Ge in Ni had formed in the early stages of milling followed by the formation of the NiGe intermetallic phase at 5 h of milling. It was estimated that the maximum Ge content in the Ni solid solution increased to about 12 at.% on milling the powder for about 5 h. The amount of the NiGe phase formed increased with increasing milling time. On continued milling up to 40 h, the NiGe intermetallic and remaining Ge reacted to form the metastable NiGe₂ phase; the NiGe₂ phase is not shown in the equilibrium phase diagram of the Ni-Ge system. However, it could be normally synthesized at a high temperature of 700 °C and a high pressure of 5.5 GPa. Another important finding of this study was that on milling the powder containing the NiGe₂ phase for a longer period of time, this metastable NiGe₂ phase started to decompose to form the equilibrium NiGe phase, thus moving toward equilibrium.

Stable and metastable phases were found also in the Ni-x at.% Si (x= 60, 67, 75 and 80) alloys during MA of the powders. A supersaturated substitutional solid solution of Si in Ni had formed in the early stages of milling followed by the formation of the NiSi intermetallic in these compositions. The amount of the NiSi phase increased with increasing milling time. On continued milling, the NiSi intermetallic phase reacted with the free Si to form the NiSi₂ intermetallic phase.

The significant finding of this study in the Ni-Si system was the NiSi_2 phase appears to have a small homogeneity range in the milled condition, unlike in the equilibrium state where it is a line compound.

In the MA of pure Fe and C powders, a supersaturated solid solution of $\text{Fe}(\text{C})$ had formed, with 0.53 wt.% C, after 15 h of milling in the Fe-0.8 wt.% composition and 0.26 wt.% after 2 h of milling, in Fe-7.0 wt.% C composition, and this has transformed to a mixture of α -Fe and Fe_3C phases after 15 h of milling, in the Fe-0.8 wt.% C, and to fully Fe_3C phase in the case of Fe-7.0 wt.% C after 5 h of milling. A crucial finding of this investigation was that single-phase bulk Fe_3C could be synthesized after sintering the pure Fe_3C powder which was milled for 30 h. Due to loss of C during heat treatment of the steel, the mechanical properties decreased.

Another critical point that the present study identified was in the mechanical alloying of Fe-18Cr-xNi (8, 12 and 20). The three compositions showed the presence of bcc (α) structure, and with continued milling the bcc (α) transformed to fcc (γ). The time for bcc (α) to fcc (γ) transformation decreased with an increase in the Ni content in the initial powder blend. A fully homogenous austenite phase could only be obtained in the 18Cr-20Ni powder blend on milling up to 30 h, whereas both austenite and (ferrite or martensite) phases were coexisting at intermediate stages of milling and only the bcc (α') phase in the final stages for the 18Cr-8Ni powder blend. Annealing of the powders at 600 °C for 1 h promoted the martensite to austenite transformation in both the Fe-18Cr-8Ni and Fe-18Cr-12Ni compositions. In contrast, the structure of the Fe-18Cr-20Ni composition after annealing was fully austenitic.

APPENDIX:
LIST OF PUBLICATIONS BY AHMED AL-JOUBORI

- C. Suryanarayana and A. Al-Joubori, “Reversible Transformation of NiGe in Mechanically Alloyed Ni-Ge Powders”, J. Mater. Res., 30, Issue 13 (July 2015) 2124-2132. DOI: [10.1557/jmr.2015.161](https://doi.org/10.1557/jmr.2015.161)
- A. Al-Joubori and C. Suryanarayana, “Synthesis of Metastable NiGe₂ by Mechanical Alloying”, Materials & Design, 87 (December 2015) 520-526. DOI: [10.1016/j.matdes.2015.08.051](https://doi.org/10.1016/j.matdes.2015.08.051)
- C. Suryanarayana and A. Al-Joubori, “Alloyed Steels: Mechanically”, in “Encyclopedia of Iron, Steel, and Their Alloys”, edited by Rafael Colás and George Totten, Taylor & Francis LLC, (March 2016) pp.159-177. DOI: [10.1081/E-EISA-120053049](https://doi.org/10.1081/E-EISA-120053049)
- A. Al-Joubori and C. Suryanarayana, Synthesis and Stability of the Austenite Phase in Mechanically Alloyed Fe-Cr-Ni Alloys, Mater. Letters (In Press).
- A. Al-Joubori and C. Suryanarayana, Synthesis of Fe-C alloys by mechanical alloying, Materials Science and Technology MS&T14, Pittsburgh, U.S.A. (2014), pp. 509-516- Conference paper.
- A. Al-Joubori and C. Suryanarayana, Synthesis of stable and metastable phases in the Ni-Si system by mechanical alloying, J. Powder Technology (In Review).
- A. Al-Joubori and C. Suryanarayana, Synthesis of nickel silicide phases by mechanical alloying, Advanced Powder Technology (In Review).

Conference Presentations

- A. Al-Joubori and C. Suryanarayana, Synthesis of Fe-C alloys by mechanical alloying, Materials Science and Technology 2014, (MS&T14), Pittsburgh, PA, U.S.A. (Oct. 12-16, 2014).
- A. Al-Joubori and C. Suryanarayana, Synthesis of metastable NiGe₂ by mechanical alloying, 144th annual meeting and exhibition, (TMS2015), Orlando, FL, U.S.A. (Mar. 15-19, 2015).
- A. Al-Joubori and C. Suryanarayana, Synthesis of stable and metastable phases in the Ni-Si system by mechanical alloying, 145th annual meeting and exhibition, (TMS2016), Nashville, TN, U.S.A. (Feb. 14-18, 2016).
- A. Al-Joubori and C. Suryanarayana, Synthesis and characterization of austenitic stainless steel powder alloys through mechanical alloying, Materials Science and Technology 2016, (MS&T16), Salt Lake City, UT, U.S.A. (Oct. 23-27, 2016).

REFERENCES

1. J. S. Benjamin, *Scientific American* 1976, vol. 234, pp. 40-48.
2. J. S. Benjamin, *Metal Powder Report* 1990, vol. 45, pp. 122-127.
3. J. S. Benjamin, *Adv. Powder. Metall. Part. Mater.* 1992, vol. 7, pp. 155-155.
4. H. K. D. H. Bhadeshia, *Mater. Sci. Eng. A* 1997, vol. 223, pp. 64-77.
5. C. Suryanarayana, *Prog. Mater. Sci.* 2001, vol. 46, pp. 1-184.
6. C. Suryanarayana: *Mechanical Alloying and Milling*. (Marcel Dekker, New York, 2004).
7. M. Sopicka-Lizer: *High-Energy Ball Milling: Mechanochemical Processing of Nanopowders*. (Woodhead Publishing Ltd., Cambridge, UK, 2010).
8. C. Suryanarayana and N. Al-Aqeeli, *Prog. Mater. Sci.* 2013, vol. 58, pp. 383-502.
9. E. Arzt and L. Schultz, In *D. G. M. Conference New Materials by Mechanical Alloying Techniques*, (DGM Informationsgesellschaft: Clausthal-Zinc, Germany, 1988).
10. A. E. Ermakov, E. E. Yurchikov and V. A. Barinov, *Fiz. Met. Metalloved.* 1981, vol. 52, pp. 1184-1193.
11. C. C. Koch, O. B. Cavin, C. G. McKamey and J. O. Scarbrough, *Appl. Phys. Lett.* 1983, vol. 43, pp. 1017-1019.
12. S. J. Campbell and W. A. Kaczmarek, In *Mössbauer Spectroscopy Applied to Magnetism and Materials Science*, ed. G. J. Long and Grandjean F. (Plenum Press: New York, 1996), pp 273-330.
13. D. R. Maurice and T. H. Courtney, *Metall. Trans. A* 1990, vol. 21, pp. 289-303.
14. A. R. West: *Solid State Chemistry and Its Applications*. (John Wiley & Sons, 2007).

15. P. Hagenmuller: *Preparative Methods in Solid State Chemistry*. (Academic Press, Inc., New York, 1972).
16. L. Lu, M. O. Lai and S. Zhang, *J. Mater. Process. Technol.* 1997, vol. 67, pp. 100-104.
17. Z. H. Chin and T. P. Perng, *Mater. Sci. Forum* 1997, vol. 235-238, pp. 121-126.
18. M. Umemoto, Z. G. Liu, K. Masuyama and K. Tsuchiya, *Mater. Sci. Forum* 1999, vol. 312-314, pp. 93-102.
19. L. Lü and M. O. Lai: *Mechanical Alloying*. (Kluwer Academic Publishers, Boston, 1998).
20. R. A. Dunlap, D. A. Small and G. R. Mackay, *J. Mater. Sci. Lett.* 1999, vol. 18, pp. 881-883.
21. M. Miki, T. Yamasaki and Y. Ogino, *Mater. Trans. Japan Inst. Metals* 1992, vol. 33, pp. 839-844.
22. A. Calka and J. S. Williams, *Mater. Sci. Forum* 1992, vol. 88-90, pp. 787-794.
23. D. Gavrilov, O. Vinogradov and W. Shaw, *Proc. Int. Conf. on Composite Materials, ICCM-10* 1995, pp. 299-307.
24. L. Takacs and M. Pardavi-Horvath, *J. Appl. Phys.* 1994, vol. 75, pp. 5864-5866.
25. B. D. Cullity and S. R. Stock: *Elements of X-Ray Diffraction*. 3rd ed. (Prentice Hall, Upper Saddle River, NJ, 2001).
26. C. Suryanarayana and M. Grant Norton: *X-Ray Diffraction: A Practical Approach*. (Plenum Press, New York, 1998).
27. A. J. C. Wilson: *Mathematical Theory of X-Ray Powder Diffractometry*. (Philips Technical Library Eindhoven, The Netherlands, 1963).
28. G. K. Williamson and W. H. Hall, *Acta Metall.* 1953, vol. 1, pp. 22-31.

29. D. Brandon and W. D. Kaplan: *Microstructural Characterization of Materials*. (John Wiley & Sons, Chichester, UK, 1999).
30. B. De Schutter, W. Devulder, A. Schrauwen, K. van Stiphout, T. Perkisas, S. Bals, A. Vantomme and C. Detavernier, *Microelectron. Eng.* 2014, vol. 120, pp. 168-173.
31. Y. Deng, O. Nakatsuka, N. Taoka and S. Zaima, In *Silicon-Germanium Technology and Device Meeting (ISTDM), 2014 7th International*, (IEEE: 2014), pp 85-86.
32. F. Nemouchi, V. Carron, J. Lábár, L. Vandroux, Y. Morand, T. Morel and J. Barnes, *Microelectron. Eng.* 2013, vol. 107, pp. 178-183.
33. B.-Y. Tsui, J.-J. Shih, H.-C. Lin and C.-Y. Lin, *Solid State Electron.* 2015, vol. 107, pp. 40-46.
34. N. S. Dellas, S. Minassian, J. M. Redwing and S. E. Mohny, *Appl. Phys. Lett.* 2010, vol. 97, p. 263116.
35. P. S. Lim, D. Z. Chi, P. C. Lim, X. C. Wang, T. K. Chan, T. Osipowicz and Y.-C. Yeo, *Appl. Phys. Lett.* 2010, vol. 97, p. 182104.
36. S. Neumeier, M. Dinkel, F. Pyczak and M. Göken, *Mater. Sci. Eng. A* 2011, vol. 528, pp. 815-822.
37. T. B. Massalski, H. Okamoto, P. R. Subramanian and L. Kacprzak: *Binary Alloy Phase Diagrams*. 2nd ed. (ASM International, Materials Park, Ohio, 1990).
38. A. Nash and P. Nash, *Bull. Alloy Phase Diagr.* 1987, vol. 8, pp. 255-264.
39. P. Villars and L. D. Calvert: *Pearson's Handbook of Crystallographic Data for Intermetallic Phases*. 2nd ed. (ASM International, Materials Park, OH, 1991).
40. Y. Ma and A. J. Ardell, *J. Phase Equilib. Diffus.* 2011, vol. 33, pp. 4-8.

41. Y. Q. Liu, D. J. Ma and Y. Du, *J. Alloys Compd.* 2010, vol. 491, pp. 63-71.
42. S. Jin, C. Leinenbach, J. Wang, L. I. Duarte, S. Delsante, G. Borzone, A. Scott and A. Watson, *Calphad* 2012, vol. 38, pp. 23-34.
43. H. Takizawa, K. Uheda and T. Endo, *J. Alloys Compd.* 2000, vol. 305, pp. 306-310.
44. W. Klement, *Can. J. Phys.* 1962, vol. 40, pp. 1397-1400.
45. A.F. Polesya and L.S. Slipchenko, *Izv. Akad. Nauk SSSR Metally* 1974, vol. 2, p. 239.
46. T. F. Grigorieva, A. P. Barinova, V. V. Boldyrev and E. Y. Ivanov, *Solid State Ionics* 1997, vol. 101, pp. 17-24.
47. M. Ellner and B. Predel, *J. Less-Common Met* 1980, vol. 76, pp. 181-197.
48. T. Benameur and A. R. Yavari, *J. Mater. Res.* 1992, vol. 7, pp. 2971-2977.
49. T. Benameur, A. R. Yavari, J. Malagelada and M. D. Baro, In *Ordering and Disordering in Alloys*, (Springer: 1992), pp. 317-327.
50. A. Antolak, D. Oleszak, M. Pękała and T. Kulik, *Mater. Sci. Eng. A* 2007, vol. 449, pp. 440-443.
51. S. Ly, L. L. Miller and D. C. Johnson, In *APS Northwest Section Meeting Abstracts*, (2004), p 1006.
52. W. B. Pearson: *A Handbook of Lattice Spacings and Structures of Metals and Alloys*. (Pergamon Press, New York, 1967).
53. I. R. Brahman, A. K. Jena and M. C. Chaturvedi, *Scripta Metall.* 1989, vol. 23, pp. 1281-1284.
54. P. Lecocq, *Annales de Chimie (Paris)* 1963, vol. 8, pp. 85-116.

55. S. Sharma, R. Vaidyanathan and C. Suryanarayana, *Appl. Phys. Lett.* 2007, vol. 90, p. 111915.
56. R. M. Davis, B. McDermott and C. C. Koch, *Metall. Trans. A* 1988, vol. 19, pp. 2867-2874.
57. Y. Wang, C. Suryanarayana and L. An, *J. Am. Ceram. Soc.* 2005, vol. 88, pp. 780-783.
58. T. F. Grigor'eva, M. A. Korchagin, A. P. Barinova, E. Yu. Ivanov and V. V. Boldyrev, *Inorg. Mater.* 2000, vol. 36, pp. 1235-1238.
59. M. L. Trudeau, R. Schulz, D. Dussault and A. Van Neste, *Phys. Rev. Lett.* 1990, vol. 64, pp. 99-102.
60. U. Patil, S. J. Hong and C. Suryanarayana, *J. Alloys Compd.* 2005, vol. 389, pp. 121-126.
61. S. Sharma and C. Suryanarayana, *J. Appl. Phys.* 2007, vol. 102, p. 083544.
62. M. Sherif El-Eskandarany, K. Aoki, K. Sumiyama and K. Suzuki, *Appl. Phys. Lett.* 1997, vol. 70, pp. 1679-1681.
63. M. Sherif El-Eskandarany, K. Aoki, K. Sumiyama and K. Suzuki, *Scripta Mater.* 1997, vol. 36, pp. 1001-1009.
64. M. Sherif El-Eskandarany, K. Aoki, K. Sumiyama and K. Suzuki, *Acta Mater.* 2002, vol. 50, pp. 1113-1123.
65. P. Nash and A. Nash, *Bull. Alloy Phase Diagr.* 1987, vol. 8, pp. 6-14.
66. J. Fouet, M. Texier, M. I. Richard, A. Portavoce, D. Mangelinck, C. Guichet, N. Boudet and O. Thomas, *Mater. Lett.* 2014, vol. 116, pp. 139-142.
67. L. A. Clevenger and C. V. Thompson, *J. Appl. Phys.* 1990, vol. 67, pp. 1325-1333.
68. J. E. Masse, P. Knauth, P. Gas and A. Charäi, *J. Appl. Phys.* 1995, vol. 77, pp. 934-936.

69. J. W. Mayer and S. S. Lau: *Electronic Materials Science: For Integrated Circuits in Si and Gaas*. (Macmillan; London: Collier Macmillan, New York, 1990).
70. W. H. Wang, H. Y. Bai and W. K. Wang, *Mater. Sci. Eng. A* 1994, vol. 179-180, pp. 229-237.
71. W. H. Wang and W. K. Wang, *J. Mater. Res.* 1994, vol. 9, pp. 401-405.
72. L. Cao, R. F. Cochrane and A. M. Mullis, *Metall. Mater. Trans. A* 2015, vol. 46, pp. 4705-4715.
73. K. Omuro and H. Miura, *Appl. Phys. Lett.* 1992, vol. 60, pp. 1433-1435.
74. J. S. C. Jang, C. H. Tsau, W. D. Chen and P. Y. Lee, *J. Mater. Sci.* 1998, vol. 33, pp. 265-270.
75. Y. S. Cho and C. C. Koch, *J. Alloys Compd.* 1994, vol. 194, pp. 287-294.
76. G. F. Zhou and H. Bakker, *Acta Metall. Mater.* 1994, vol. 42, pp. 3009-3017.
77. J. S. C. Jang and C. H. Tsau, *J. Mater. Sci.* 1993, vol. 28, pp. 982-988.
78. J. Lagerbom, T. Tiainen, M. Lehtonen and P. Lintula, *J. Mater. Sci.* 1999, vol. 34, pp. 1477-1482.
79. K. Okadome, K. Unno and T. Arakawa, *J. Mater. Sci.* 1995, vol. 30, pp. 1807-1810.
80. K. Omuro and H. Miura, *Jpn. J. Appl. Phys.* 1991, vol. 30, pp. L851-L853.
81. M. K. Datta, S. K. Pabi and B. S. Murty, *J. Appl. Phys.* 2000, vol. 87, pp. 8393-8400.
82. M. K. Datta, S. K. Pabi and B. S. Murty, *Mater. Sci. Eng. A* 2000, vol. 284, pp. 219-225.
83. N. Iwamoto and S. Uesaka, *Mater. Sci. Forum* 1992, vol. 88, pp. 763-770.
84. K Toman, *Acta Crystallogr.* 1951, vol. 4, pp. 462-464.

85. E. Hellstern, H. J. Fecht, C. Garland, W. L. Johnson and W. M. Keck, In *MRS Proceedings*, (Cambridge Univ Press: 1988), pp 137-142.
86. P. A. Nikolaychuk and A. G. Tyurin, *Corros. Sci.* 2013, vol. 73, pp. 237-244.
87. H. Pfisterer and K. Schubert, *Naturwissenschaften* 1950, vol. 37, pp. 112-113.
88. C. Suryanarayana and T. R. Anantharaman, *J. Mater. Sci.* 1970, vol. 5, pp. 992-1004.
89. Z. A. Chaudhury and C. Suryanarayana, *J. Mater. Sci.* 1983, vol. 18, pp. 3011-3022.
90. D. K. Mukhopadhyay, C Suryanarayana and F. H. Froes, *Scripta Metall. Mater.* 1994, vol. 30, pp. 133-137.
91. C. R. Clark, C. Suryanarayana and F. H. Froes, In *Synthesis/Processing of Lightweight Metallic Materials.*, ed. F. H. Froes, Suryanarayana C.; and Ward-Close C.M. (TMS: Warrendale, 1995), pp 175-182.
92. H. Bakker, G. F. Zhou and H. Yang, *Prog. Mater. Sci.* 1995, vol. 39, pp. 159-241.
93. A. P. Radlinski, A Calka, B. W. Ninham and W. A. Kaczmarek, *Mater. Sci. Eng. A* 1991, vol. 134, pp. 1346-1349.
94. M. V. Zdujic, K. F. Kobayashi and P. H. Shingu, *J. Mater. Sci.* 1991, vol. 26, pp. 5502-5508.
95. Ahmed A. Al-Joubori and C. Suryanarayana, *Mater. Des.* 2015, vol. 87, pp. 520-526.
96. C. Suryanarayana and Ahmed Al-Joubori, *J. Mater. Res.* 2015, vol. 30, pp. 2124-2132.
97. T. B. Massalski, H. Okamoto, PR Subramanian and Linda Kacprzak: *Binary Alloy Phase Diagrams*. 2nd ed. ed. (ASM International, Materials Park, Ohio, 1990).
98. D. Singh, C. Suryanarayana, L. Mertus and R. H. Chen, *Intermetallics* 2003, vol. 11, pp. 373-376.

99. M. Umemoto, Z. G. Liu, R. Omatsuzawa and K. Tsuchiya, *J. Metastab. Nanocryst. Mater.* 2000, vol. 8, pp. 918-923.
100. A. J. Zhou, X. B. Zhao, T. J. Zhu, T. Dasgupta, C. Stiewe, R. Hassdorf and E. Mueller, *Intermetallics* 2010, vol. 18, pp. 2051-2056.
101. Y. Sadia, L. Dinnerman and Y. Gelbstein, *J. Electron. Mater.* 2013, vol. 42, pp. 1926-1931.
102. P.S. Goodwin, D.K. Mukhopadhyay, C.Suryanarayana, F. H. Froes and C.M. Ward-Close, In *Titanium 95*, ed. P.A. Blenkinsop, Evans W.J. and Flower H.M (Inst. of Materials: London, UK, 1996), pp 2626-2633.
103. P.S. Goodwin, C.R. Powell, C.Suryanarayana, F.H. Froes and C.M. Ward-Close, In *Processing and Fabrication of Advanced Materials V*, ed. T.S. Srivatsan and Moore J.J. (TMS, Warrendale, PA, 1996), pp 391-398.
104. G. Krauss: *Steels: Processing Sturcture and Performance*. (ASM International, Materials Park, OH, 2005).
105. Y. Kimura, H. Hidaka and S. Takaki, *Mater. Trans., JIM* 1999, vol. 40, pp. 1149-1157.
106. J. S. C. Jang and C. C. Koch, *Scripta Metall. Mater.* 1990, vol. 24, pp. 1599-1604.
107. D. Jia, K. T. Ramesh and E. Ma, *Scripta Mater.* 2000, vol. 42, pp. 73-78.
108. D. C. Cook, T. H. Kim and J. C. Rawers, In *Mater. Sci. Forum*, (Trans Tech Publ: 1996), pp 533-538.
109. J. C. Rawers and R. C. Doan, *Metall. Mater. Trans. A* 1994, vol. 25, pp. 381-388.
110. B. Srinivasarao, K. Oh-Ishi, T. Ohkubo, T. Mukai and K. Hono, *Scripta Mater.* 2008, vol. 58, pp. 759-762.
111. H. Hidaka, T. Tsuchiyama and S. Takaki, *Scripta Mater.* 2001, vol. 44, pp. 1503-1506.

112. H. W. Zhang, R. Gopalan, T. Mukai and K. Hono, *Scripta Mater.* 2005, vol. 53, pp. 863-868.
113. K. Oh-ishi, H. W. Zhang, T. Ohkubo and K. Hono, *Mater. Sci. Eng. A* 2007, vol. 456, pp. 20-27.
114. T. Tanaka, S. Nasu, K. N. Ishihara and P. H. Shingu, *J. Less-Common Met.* 1991, vol. 171, pp. 237-247.
115. H. Arik and M. Turker, *Mater. Des.* 2007, vol. 28, pp. 140-146.
116. Y. Z. Chen, A. Herz, Y. J. Li, C. Borchers, P. Choi, D. Raabe and R. Kirchheim, *Acta Mater.* 2013, vol. 61, pp. 3172-3185.
117. N. T. Rochman and H. Sueyoshi, *IPTEK J. Techolo Sci.* 2008, vol. 19, pp. 7-11.
118. E. P. Yelsukov, V. A. Barinov and L. V. Ovetchkin, *J. Mater. Sci. Lett.* 1992, vol. 11, pp. 662-663.
119. M. Umemoto, Z. G. Liu, H. Takaoka, M. Sawakami, K. Tsuchiya and K. Masuyama, *Metall. Mater. Trans. A* 2001, vol. 32, pp. 2127-2131.
120. M. Umemoto, Z. G. Liu, K. Masuyama and K. Tsuchiya, *Scripta Mater.* 2001, vol. 45, pp. 391-397.
121. M. Umemoto, Y. Todaka, T. Takahashi, P. Li, R. Tokumiya and K. Tsuchiya, *J. Metastab. Nanocryst. Mater.* 2003, vol. 15, pp. 607-614.
122. K. Tokumitsu, K. Majima and R. Yamamoto, *Solid State Ionics* 2004, vol. 172, pp. 211-214.
123. E. P. Yelsukov, G. A. Dorofeev, A. V. Zagainov, N. F. Vildanova and A. N. Maratkanova, *Materials Science and Engineering: A* 2004, vol. 369, pp. 16-22.

124. R. Nowosielski and W. Pilarczyk, *J. Mater. Process. Technol.* 2005, vol. 162, pp. 373-378.
125. D. Chaira, B. K. Mishra and S. Sangal, *Powder Technology* 2009, vol. 191, pp. 149-154.
126. B. Ghosh and S. K. Pradhan, *J. Alloys Compd.* 2009, vol. 477, pp. 127-132.
127. E. J. Fasiska and G. A. Jeffrey, *Acta Crystallogr.* 1965, vol. 19, pp. 463-471.
128. E. J. Fasiska and H. Wagenblast, *Trans. Met. Soc. AIME* 1967, vol. 239, pp. 1818-1820.
129. O. D. Sherby, J. Wadsworth, D. R. Lesuer and C. K. Syn, In *Mater. Sci. Forum*, (Trans Tech Publ: 2007), pp 215-222.
130. A. Tsuzuki, S. Sago, S-I Hirano and S. Naka, *J. Mater. Sci.* 1984, vol. 19, pp. 2513-2518.
131. I. G. Wood, L. Vočadlo, K. S. Knight, D. P. Dobson, W. G. Marshall, G. D. Price and J. Brodholt, *J. Appl. Crystallogr.* 2004, vol. 37, pp. 82-90.
132. M. Umemoto, Y. Todaka and K. Tsuchiya, *Mater. Sci. Forum* 2003, vol. 426-432, pp. 859-864.
133. Kin Ho Lo, Chan Hung Shek and JKL Lai, *Mater. Sci. Eng., R* 2009, vol. 65, pp. 39-104.
134. NR Baddoo, *J. Constr. Steel Res.* 2008, vol. 64, pp. 1199-1206.
135. R. Shashanka and D. Chaira, *Powder Technology* 2014, vol. 259, pp. 125-136.
136. R. Shashanka and D. Chaira, *Materials Characterization* 2015, vol. 99, pp. 220-229.
137. S. Gupta, R. Shashanka and D. Chaira, In *IOP Conference Series: Materials Science and Engineering*, (IOP Publishing: 2015), p 012033.
138. R. Shashanka and D. Chaira, *Powder Technology* 2015, vol. 278, pp. 35-45.
139. F. Tehrani, M. H. Abbasi, M. A. Golozar and M. Panjepour, *Mater. Sci. Eng. A* 2011, vol. 528, pp. 3961-3966.
140. M. H. Enayati and M. R. Bafandeh, *J. Alloys Compd.* 2008, vol. 454, pp. 228-232.

141. M. H. Enayati, M. R. Bafandeh and S. Nosohian, *J. Mater. Sci.* 2007, vol. 42, pp. 2844-2848.
142. D. Oleszak, A. Grabias, M. Pękała, A. Świdarska-Środa and T. Kulik, *J. Alloys Compd.* 2007, vol. 434–435, pp. 340-343.
143. M. Sherif El-Eskandarany and H. A. Ahmed, *J. Alloys Compd.* 1994, vol. 216, pp. 213-220.
144. V. A. Shabashov, K. A. Kozlov, K. A. Lyashkov, N. V. Kataeva, A. V. Litvinov, V. V. Sagaradze and A. E. Zamatovskii, *Phys. Metals Metallogr.* 2014, vol. 115, pp. 392-402.
145. A. A. Popovich, N. G. Razumov, A. O. Silin and E. L. Gulihandanov, *Open Journal of Metal* 2013, vol. 3, pp. 25-29.
146. A. Etienne, B. Radiguet, C. Genevois, J-M. Le Breton, R. Valiev and P. Pareige, *Mater. Sci. Eng. A* 2010, vol. 527, pp. 5805-5810.
147. C. Sun, Y. Yang, Y. Liu, K. T. Hartwig, H. Wang, S. A. Maloy, T. R. Allen and X. Zhang, *Mater. Sci. Eng. A* 2012, vol. 542, pp. 64-70.
148. S. S. M. Tavares, D. Fruchart and S. Miraglia, *J. Alloys Compd.* 2000, vol. 307, pp. 311-317.
149. R. Jenkins and R. L. Snyder: *Introduction to X-Ray Powder Diffractometry*. (Wiley, New York, 1996).
150. R. Kohlhaas, P. Dunner and N. Schmitz-Pranghe, *Z. Angew. Phys.* 1967, vol. 23, p. 245.
151. H. E. Swanson, R. K. Fuyat and G. M. Ugrinic: *Standard X-Ray Diffraction Powder Patterns*. (Natal Burean of Standards Circular 539, Washington 25, D.C., 1955).
152. W. C. Leslie and R. L. Miller, *ASM Trans. Q.* 1964, vol. 57, pp. 972-979.

- 153. S. D. Kaloshkin, V. V. Tcherdyntsev, I. A. Tomilin, Yu V. Baldokhin and E. V. Shelekhov, *Physica B: Condensed Matter* 2001, vol. 299, pp. 236-241.
- 154. C. Kuhrt and L. Schultz, *J. Appl. Phys.* 1993, vol. 73, pp. 1975-1980.
- 155. T. F. Kelly, M. Cohen and J. B. Vander Sande, *Metall. Trans. A* 1984, vol. 15, pp. 819-833.
- 156. T. Koseki and M. C. Flemings, *Metall. Mater. Trans. A* 1995, vol. 26, pp. 2991-2999.
- 157. J. W. Elmer, T. W. Eagar and S. M. Allen, In *Proceedings of the Materials Weldability Symposium, Detroit*, (1990), pp 8-12.
- 158. F. H. Keating: *Chromium-Nickel Austenitic Steels*. (Butterworths Scientific Publications, London, 1956).